EPITAXIAL OXIDE SPINTRONIC STRUCTURES

FERROMAGNETS AND SEMICONDUCTORS

Promotiecommissie

Prof. dr. ir. Mouthaan	(chairman)
Prof. dr. J.C. Lodder	Univ. Twente (promotor)
Dr. R. Jansen	Univ. Twente (co-promotor)
Prof. dr. D.H.A. Blank	Univ. Twente
Prof. dr. ir. R.A.M. Wolters	Univ. Twente / Philips
Prof. dr. J. Aarts	Univ. Leiden
Prof. dr. A. Schuhl	Univ. H. Poincare, FR
Prof. dr. G. Bayreuther	Univ. Regensburg, DE

The work was performed in the Systems and Materials for Information storage group (SMI) of the MESA$^+$ Institute for Nanotechnology, University of Twente.

Printed by Wöhrmann Print Service, Zutphen

ISBN 90-365-2222-6

EPITAXIAL OXIDE SPINTRONIC STRUCTURES

FERROMAGNETS AND SEMICONDUCTORS

PROEFSCHRIFT

ter verkrijging van
de graad van doctor aan de Universiteit Twente,
op gezag van de rector magnificus,
prof. dr. W.H.M. Zijm,
volgens besluit van het College voor Promoties,
in het openbaar te verdedigen
op vrijdag 1 juli 2005 om 15.00 uur

door

Ferry Michael Postma

geboren op 26 mei 1975
te Oldenzaal

Dit proefschrift is goedgekeurd door
promotor: Prof. dr. J.C. Lodder
co-promotor: Dr. R. Jansen

Contents

Chapter 1

Introduction

In this chapter theory and experiments are presented to motivate the research on an Epitaxial Magnetic Tunnel Transistor (MTT) based on the half-metallic ferromagnet $La_{0.67}Sr_{0.33}MnO_3$. In section 1.1 the relevance of spintronics for the information storage industry is discussed. Section 1.2 explains the principle of magneto resistance with a focus on Tunnel Magneto Resistance (TMR). Two spintronic devices that are based on hot electron transport are described in section 1.3. In section 1.4 the use of $La_{0.67}Sr_{0.33}MnO_3$ in spintronic devices is discussed. The chapter is concluded by the section that gives the motivation for this work and an outline of the thesis.

1.1 Spintronics

The work described in this thesis is in the field of spintronics. In spintronics not only the charge of an electron, but also its spin is used. This spin is a quantum mechanical property of an electron that gives it a magnetic moment. There are two spin directions called spin up and spin down. In non magnetic materials both spin directions will be present in equal amounts, but in magnetic materials both spins do not balance each other. An electrical current that flows through a magnetic material will have a spin imbalance as well and this imbalance can be continued when the current flows into a non magnetic material. Both type of electrons will react differently to the application of a magnetic field or to transport through a magnetic material. This forms a new way in which to manipulate a current. Magnetic materials can show hysteresis, which means that there is a memory effect. The magnetic moment of the material can be oriented in a certain direction by applying a magnetic field and it stays in that direction when the field is removed. This memory effect can be used to

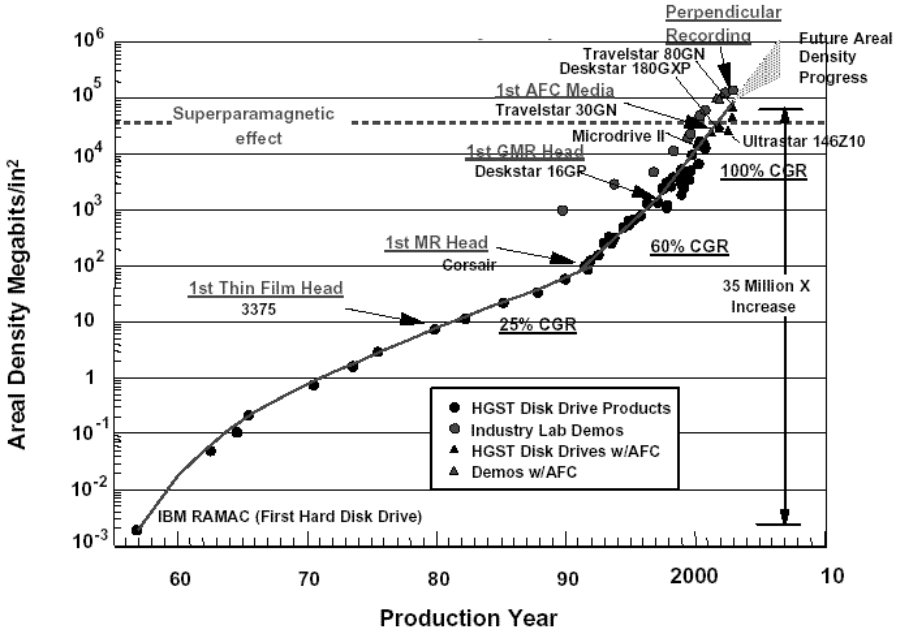

Figure 1.1: *The roadmap for hard disc drives shows the enormous increase in the bit-density in the last years. Reported by Grochowski. [1]*

store information. In the information storage industry, spintronic devices are used to store information and to read information. Ever increasing demands of the public make information storage a billion dollar industry that is evolving extremely fast. Figure 1.1 shows the roadmap for the bit density in hard-disc drives. It shows that in the last 50 years, the bit-density has increased with the incredible factor of 35 million. Support of this large industry makes research in the field of spintronics grow very fast.

1.2 Giant magneto resistance and tunnel magneto resistance

The magnetic field induced change of the resistance in a solid state device is generally referred to as magneto resistance. Magneto resistive devices are the first devices that can be called spintronic. One example of such a magneto-resistive device is a spin valve. Figure 1.2 schematically shows such a spin valve. The attenuation length of an electron in a magnetic material as well as the interface resistance of the metal/ferromagnet interface depend on the

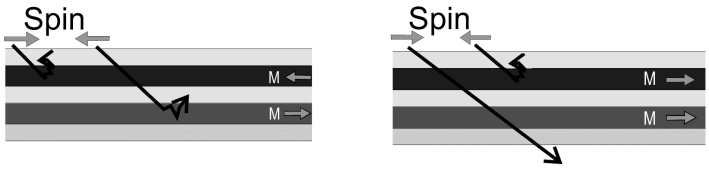

Figure 1.2: *Schematic diagram of magneto resistance in a spin valve structure. In the anti-parallel alignment (left) both type of electrons encounter magnetic layers with a high resistance. In the parallel orientation (right) only one type of electrons encounters a high resistent magnetic film.*

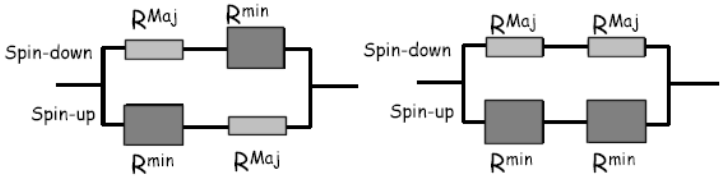

Figure 1.3: *The electrical scheme of the two current model shows that anti-parallel alignment (left) results in a higher resistance then parallel alignment. (right) Rmaj (Rmin) is the resistance for the majority (minority) electrons.*

relative orientation of the spin of the electron and the magnetic moment of the material. This causes the resistance of the multi-layer to depend on the relative orientation of the two ferromagnetic layers. If the magnetic layers are oriented parallel, one type of electron will experience a high resistance in both of the magnetic layers while the other type will experience a low resistance in both of the magnetic layers. When the magnetic moments of both layers are oriented anti-parallel, both electrons will experience a high resistance in one of the layers. Figure 1.3 shows the two current model that explains that this results in a low resistance for parallel alignment and a high resistance for anti-parallel alignment. In the anti-parallel alignment both the spin up and the spin down electrons will be a majority spin in one electrode and a minority spin in the other electrode. For parallel alignment one spin direction will be a majority spin for both electrodes and the other spin direction will be a minority spin in both electrodes. The resistances for majority (minority) spins is denoted in the figure as R^{maj} (R^{min}). The model assumes that spin up electrons travel in one leg and spin down electrons in the other. That means that in this model there is no spin flip. In practice electrons will change their spins due to magnon or spin-orbit scattering.

In a spin valve both magnetic layers have a different coercivity which allows the magnetization in the two layers to be aligned anti-parallel. The anti-parallel alignment can also be achieved by an anti-ferromagnetic coupling between the magnetic layers. This results in an anti-parallel alignment at zero field. When a field is applied to overcome this coupling, the magnetization of both layers will be parallel. Magneto-resistance is not only found in thin film stacks. In a granular magnetic system the grains can be magnetized either randomly or parallel. This also results in a field dependent resistance which is called granular magneto resistance.

The magnetic layers in a spin valve stack are separated by non-magnetic metals, so transport from one electrode to the other is by conduction through this metal. Electrons can also tunnel from one magnetic layer through a thin insulating layer to another ferromagnetic layer. Electron tunneling is a quantum mechanical phenomenon by which an electric current can flow from one electrode through an insulating barrier to another electrode. This tunneling is possible if the insulating barrier is thin enough for the wave-functions in one electrode to spatially overlap with the wave function of the other electrode. Let us consider the simplest case of tunneling in which energy and spin are conserved. In that case, an electron that occupies a certain state in the density of states of electrode 1 will tunnel to a free state in the density of states of electrode 2 with the same energy and spin. Since the electrons tunnel from a filled state in electrode 1 to an empty state in electrode 2 with conservation of energy, the tunnel current will depend on the density of states in both electrodes. The conservation of spin is important if both electrodes have a spin-split density of states, like in the case of two ferromagnetic electrodes. It results in a resistance that depends on the relative orientation of the magnetic moments of the two electrodes. This is generally referred to as tunnel magneto-resistance (TMR). Figure 1.4 shows a simplified model of how the density of states of the two ferromagnetic materials results in the TMR effect. In the parallel alignment shown in the image on the left we see that the majority electrons in electrode 1 can find plenty of free states to tunnel into in electrode two, which gives a low resistance. When the magnetizations in the electrodes are aligned anti-parallel (image on the right) the majority electrons in electrode one have a smaller amount of states in the other electrode to tunnel into. This gives the tunnel barrier a higher resistance. Since electron tunneling plays an important role in the work presented in this thesis, we will discuss some aspects of tunneling that are important for good understanding of the tunnel junction behavior. For more details about magnetic tunnel junctions we refer to the recent review article by Tsymbal *et al.*[2]. The available states in electrode 1 is given by the product of the density of states (φ)and the filling factor (f):

$$\varphi_1(E)f(E) \tag{1.1}$$

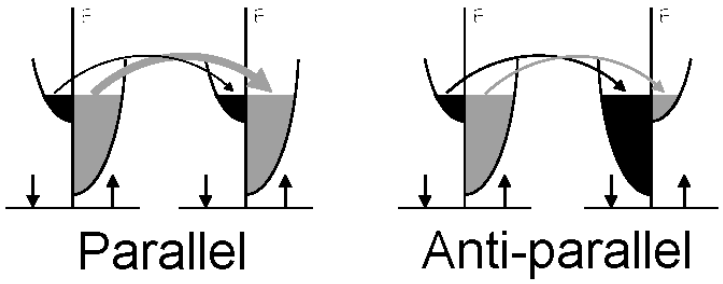

Figure 1.4: *Role of the density of states in spin polarized tunneling. In the parallel alignment (left-picture) the majority electrons in the electrode on the left find more states to tunnel to then in the anti-parallel alignment. (right-picture)*

In which E is the energy. The available states in electrode 2 to tunnel to is given by:

$$\varphi_2(E)(1 - f(E)) \tag{1.2}$$

when a bias voltage V is applied over the junction, the Fermi-level in one electrode will shift by $e \cdot V$ with respect to the other. (e=electron charge) The available states to tunnel into will then be:

$$\varphi_2(E + eV)(1 - f(E + eV)) \tag{1.3}$$

The current from electrode 1 to electrode 2 can be obtained by multiplying the filled states in electrode 1 with the empty states in electrode 2, adding a factor ($|M|^2$) for the probability of transmission through the barrier and integrating over the energy.

$$I_{1\to 2}(V) = \int_{-\infty}^{\infty} \varphi_1(E)\varphi_2(E + eV)|M|^2 f(E)(1 - f(E + eV))dE \tag{1.4}$$

Simmons [3] obtained $|M|^2$ using the WKB (Wentzel-Kramers-Brillioun) approximation for a barrier with average height ϕ above the Fermi-level. The free electron relation for $\varphi_1$andφ_2 and a step function for the filling factor ($T = 0$) are used. The following relation is obtained:

$$J(V) = \frac{J_0}{d^2}(\overline{\phi} - \frac{eV}{2})e^{(-Ad\sqrt{\overline{\phi} - \frac{eV}{2}})} - \frac{J_0}{d^2}(\overline{\phi} + \frac{eV}{2})e^{(-Ad\sqrt{\overline{\phi} + \frac{eV}{2}})} \tag{1.5}$$

In which: $A = 4\pi\sqrt{\frac{2m_e^*}{h}}$, $J_0 = \frac{e}{2\pi h}$, d is the thickness of the tunnel barrier in Å and $\overline{\phi}$ is the average barrier height above the Fermi-level. The equation shows that:

- For $eV \ll \overline{\phi}$, $J(V)$ is linear.
- For higher voltages $J(V)$ becomes non linear.
- For moderate voltages the conductance $\frac{dI}{dV}$ depends parabolically on the voltage. ($J \propto \alpha V + \beta V^3$)
- J depends exponentially on the barrier thickness and on $\sqrt{\overline{\phi}}$

For asymmetric barriers having two different electrode materials, Brinkman *et al.*[4] added the barrier asymmetry $\Delta\phi = \phi_1 - \phi_2$.

$$J(V) = 3.16 \cdot 10^{10}(\frac{\phi^{\frac{1}{2}}}{d})e^{(-1.025\phi^{\frac{1}{2}}d)}(V - C_1\frac{d\Delta\phi}{\phi^{\frac{3}{2}}}V^2 + C_2(\frac{d^2}{\phi})V^3) \tag{1.6}$$

in which C_1=0.0213 and C_2=0.0109. The barrier asymmetry is in eV, the barrier thickness in Å and J is in A/cm^2. Still both simplifications do not include the density of states.

The experiments by Giaever *et al.*[5] showed that the density of states is important in tunneling. In these experiments Al/Al_2O_3/Pb junctions are used. It was found that the tunneling conductance as a function of bias voltage was proportional to the density of states in the superconducting Pb electrode.

Meservey and Tedrow introduced the spin-polarized tunneling technique.[6] These were the first experiments in which an insulator tunnel barrier was sandwiched between two electrodes with a spin split density of states. One electrode was a ferromagnet, the other a superconductor. This superconductor has a spin splitting of the quasi-particle density of states that is induced by a magnetic field. These structures are used to measure the spin polarization of the tunnel current of magnetic materials. This spin polarization is the imbalance of the spin orientation of the tunneling electrons and is given by:

$$P = \frac{I_\uparrow - I_\downarrow}{I_\uparrow + I_\downarrow} \tag{1.7}$$

Another configuration that sandwiches an insulator between two materials with a spin split density of states is formed when two ferromagnets are situated on both sides of the tunnel barrier. This is known as a magnetic tunnel junction. Due to the fact that spin is conserved in tunneling, equation 1.4. becomes spin dependent and the tunnel current depends on the relative orientation of the two ferromagnets. The relative change of the barrier resistance is called the tunnel magneto resistance (TMR) and is given by:

$$TMR = \frac{\Delta R}{R} = \frac{R_{AP} - R_P}{R_{AP}} = \frac{2P_1P_2}{1 + P_1P_2} \tag{1.8}$$

In which R_{AP}(R_P) is the junction resistance in anti-parallel (parallel) alignment. P_1 and P_2 are the electron spin polarizations of both ferromagnets. The

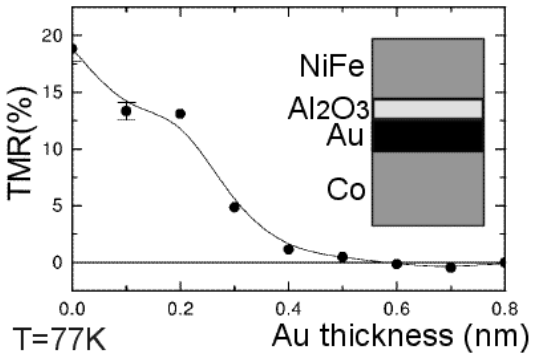

Figure 1.5: *Interface sensitivity of TMR; When a Au layer is inserted between the tunnel barrier and one of the electrodes of a magnetic tunnel junction, the TMR is lowered. This graph shows the TMR as function of the thickness of the inserted Au layer. When the Au thickness is 4 Å, the TMR has vanished. This shows that the TMR is sensitive to the spin polarization in the first one or two atomic layers in the electrodes at the interface with tunnel barrier. Reported by Moodera* et al.*[7]*

TMR is actually not sensitive to the bulk-polarization of the electrode material but to the polarization of the electrode at the interface with the barrier. This interface sensitivity is reported by Moodera *et al.*[7] and by Tedrow *et al.*[8] Figure 1.5 shows the influence of insertion of a thin Au gold film between the barrier and one of the electrodes. When 4 Å of gold is inserted, the TMR is diminished to almost zero. This shows that the TMR is sensitive to spin polarization of the first one or two atomic layers at the interface with the barrier. Due to the fact that tunneling is interface sensitive and the spin polarization at this interface can deviate from that in the bulk, it is better to call P_1 and P_2 the spin polarization of both ferromagnet interfaces. In fact it is even better to say tunnel spin polarization of the electrode/tunnel barrier combination, as we will explain now.

The difference between the spin polarization at the interface and the tunnel spin polarization of the electrode/tunnel barrier combination lies in the role that the matrix $|M|^2$ plays. For 3d ferromagnetic materials, the tunnel spin polarization was found to be positive (spin-up majority).[6] This seems to contradict the fact that at the Fermi-level in the bulk the density of states of these materials there are more minority spins. (In these spin polarized tunneling experiments with an Al superconducting spin split electrode, it is the Fermi electrons that participate in the tunneling. For magnetic tunnel junctions in

which a higher voltage is applied, electrons that are not at the Fermi-level will contribute to the tunnel current as well) To explain this we have to have a look at this $|M|^2$ as it causes the difference between the polarization of the tunnel current and the real polarization of the material. It is also the reason that the tunnel spin polarization is not the same as spin polarizations measured by other techniques. The latest view on this involves the way in which the electrode is bonded to the insulator. [9] In some bonds (ssσ), the conduction will be dominated by the s-electrons and will give a positive tunnel spin polarization for 3d ferromagnets, in other bonds (sdσ), the d-electrons dominate the tunnel current yielding a negative tunnel spin polarization. The (partial) density of states of FCC Co is shown in section 5.6. For Al_2O_3 for instance it is calculated that the s-electrons of the 3d ferromagnets are involved in the bonding, which results in a positive tunnel spin polarization. [9] So the tunnel barrier material plays an important role in the tunneling, it can even change the sign of the TMR. That's why the P1 and P2 in equation 1.8 are best defined as the tunnel spin polarization of the electrodes in combination with that specific tunnel barrier.

1.3 The spin valve transistor and the magnetic tunnel transistor

In this section we will discuss the main principles behind two hybrid devices that incorporate both a semiconductor and a ferromagnet. The first device of this type was invented at the university of Twente by D. J. Monsma *et al.*[10] and is called the spin valve transistor (SVT). The spin valve transistor consists of a metallic multi-layer (=base) containing two separately switching ferromagnets that is sandwiched between two semiconductors. At both metal/semiconductor interfaces a Schottky barrier is formed. One of them (the emitter) is used to inject hot electrons in the metallic layer stack. As these hot electrons travel through the base, the scattering in the base causes a change of their momentum and k-vector. Electrons that have traversed the base and still have enough energy and the right k-vector to overcome the second Schottky barrier, will be collected. This Schottky barrier is called collector. Since the scattering in the base depends on the relative alignment of both ferromagnets, the collector current becomes highly field dependent. This is schematically depicted in figure 1.6. The change in collected current is called magnetocurrent (MC). The ratio between the collected current and injected current is referred to as transfer ratio (T.R. or α). State of art SVT's consisting of Si/Au(20Å)/NiFe(30Å)/Au(70Å)/Co(30Å)/Cu(40Å)/Si show a transfer ratio of 1.18 $\cdot 10^{-4}$and a MC of 230% at 290 K. See figure 1.7. [11] By making the magnetic layers thicker, the MC can easily be increased, but the T.R. will suffer from it. The SVT was the first device that allowed the study of hot

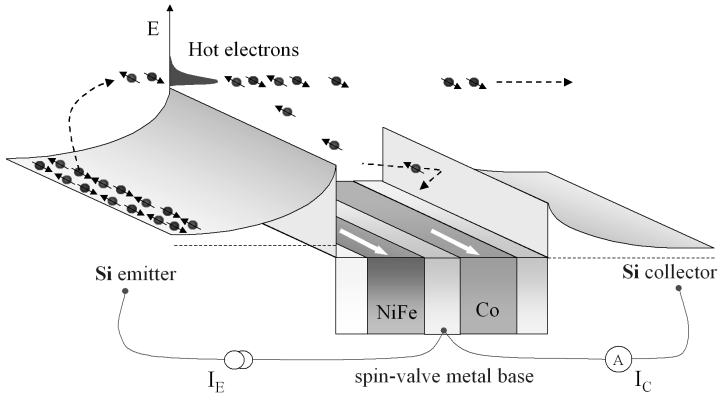

Figure 1.6: *Schematic view of the spin valve transistor; From left to right the picture shows the emitter Schottky barrier that injects hot electrons into the base. The spin valve base in which the hot electrons scatter spin dependently and the collector Schottky barrier that collects the hot electrons.*

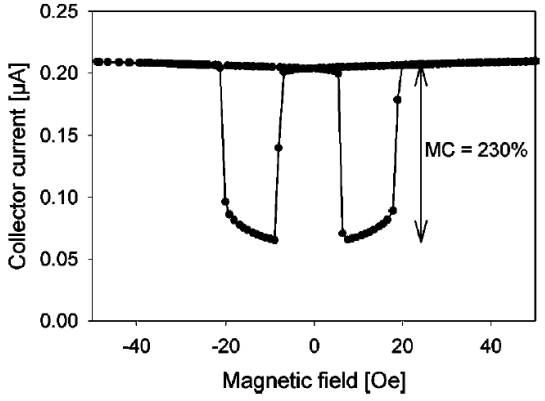

Figure 1.7: *Collector current vs. magnetic field for a Si/Au(20Å)/NiFe(30Å)/Au(70Å)/Co(30Å)/Cu(40Å)/Si SVT. At 290K and an emitter current of 2mA the SVT shows a MC of 230% and a transfer ratio of 1.18 $\cdot 10^{-4}$. Reported by van't Erve* et al.*. [11]*

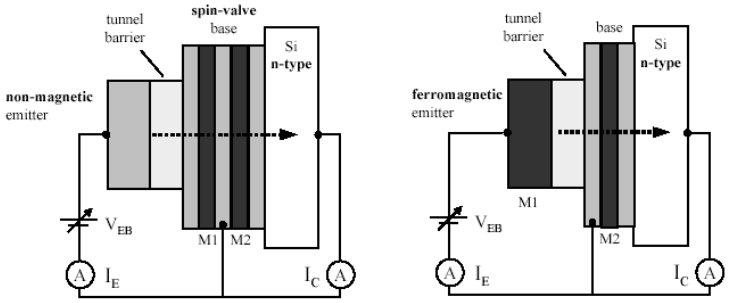

Figure 1.8: *Schematic view of the magnetic tunnel transistor. On the right hand side a magnetic emitter is used to inject spin polarized hot electrons. On the left hand side the polarizer is situated in the base.*

electron scattering in magnetic films and it has indeed given a lot of insight in this topic. For instance two different mean free paths are determined for both spin-up and spin-down hot electrons in Co as well as in $Ni_{80}Fe_{20}$ using spin valve transistors. Further it was established that it is the scattering in the bulk rather then the interface scattering that causes the spin dependence of the scattering. For more details on these topics we refer to the overview paper by Jansen [12]. The height of the Schottky barrier of the emitter determines the energy of the injected electrons. Tuning of this energy has shown to be a precious tool in optimizing properties of the SVT, especially with respect to the transfer ratio. [11] Since this height is determined by the combination of the semiconductor and the adjacent metal, tunability of the energy of the injected electrons is limited. When a tunnel barrier is used as an emitter, the energy of the injected electrons can easily be tuned by the applied emitter voltage. This kind of structure is known as a magnetic tunnel transistor(MTT). It was first proposed by Monsma *et al.*. [10].

The magnetic tunnel transistor knows two configurations. Both of them are shown in figure 1.8. On the left side the base contains two magnetic layers like in the SVT. In the configuration shown on the right hand side of the figure a magnetic emitter is used to inject spin polarized hot electrons. Both configurations have their advantages and disadvantages. When a magnetic emitter is used, the base can consist of just one single layer. When a non-magnetic emitter is used, the minimum of layers in the base is three. This should give a higher transfer for the MTT with a magnetic emitter. On the other hand if one sees the magnetic layers M1 and M2 in the figures as polarizer and analyzer, it is clear that the MTT with a magnetic emitter has a limited polarizer. The polarization of the injected electrons is limited to the tunnel spin polarization of the electrode/tunnelbarrier combination. [13] This directly limits the mag-

neto current. In the MTT with a non magnetic emitter the effectiveness of the polarizer can in principle reach 100% when the magnetic layer is made thick enough.

Mizushima *et al.* were the first to demonstrate the magnetic tunnel transistor. [14] The reported structure consists of (from bottom to top) a Si collector, a Au(10Å)/Fe(10Å)/Au(100Å)/Fe(15Å)/Al(45Å) base, an AlO_x tunnel barrier and an Al emitter. The energy of the injected electrons is now easily tunable. It was expected that the magneto-current as function of injected electron energy would show an anomaly at 1.5 V, where the density of states of Fe has a peak formed by the narrow d-band. This is not observed. Instead the magneto-current decreased monotonously with emitter voltage. [14] This indicates the domination of the collector current by s-electrons. Emitter voltage up to 1.8 V are applied but the transfer ratio does not exceed $1{\cdot}10^{-4}$. A magneto current of 200% is reported. For structures with a magnetic emitter (Si /Au(1.5nm) /Fe(1.5nm) /Al(10nm) /AlO_x /Fe(t)) the magneto current is found to depend strongly on the thickness of the Fe emitter electrode.[15] The maximum of MC is found at a Fe emitter thickness of 0.8 nm and is 100%. The reason that these thin emitters give higher MC then the thicker ones is that the two-dimensionality of the electron states in the 0.8 nm thick Fe emitter decreases spin flip scattering in the tunnel junction. For these emitters a tunnel spin polarization of roughly 40% is deduced.

In 2001 Sato *et al.*[16] reported on a magnetic tunnel transistor with a transfer ratio of 10^{-3}. This is for a MTT with a non-magnetic emitter and a 3-layer base. It consists of GaAs/ Fe(1.5nm)/ Au(7nm)/ Fe(1nm)/ AlO_x(2nm)/ Al/ Au (100 nm). The transfer of 10^{-3} is found for an emitter voltage of 3 V. At this voltage the MC is still 130%. It was found that the MTT's with a tunnel barrier of 2 nm showed a larger transfer ratio then those with a 1.5 nm tunnel barrier. The explanation that is given for this, is that the electrons injected by thicker barriers have a narrower angular distribution, so that a larger part of the injected electrons is in the cone of collection of the collector Schottky barrier.

Magnetic tunnel transistors with a single $Co_{84}Fe_{16}$ base layer consisting of GaAs(111) /$Co_{84}Fe_{16}$25Å/Al_2O_3(50Å) /$Co_{84}Fe_{16}$(300Å)/$Ir_{22}Mn_{78}$ are reported in 2002 by van Dijken *et al.*[17] A MC of 64% and a transfer ratio of around $2{\cdot}10^{-4}$are found for an emitter voltage of 1.4 V. Lower voltages give a lower MC because the ratio between the collected hot electron current and the leakage current of the diode decreases. Above 1.25 V however the collector current is dominated by the collected hot electron current. The transfer ratio increases with increase of the emitter bias. this is attributed to the increase of collector efficiency due to the higher energy of the injected electrons. By varying the thickness of the base-layer the energy dependence of the attenuation length of both spin up and spin down electrons is estimated. The attenuation of minority electrons is found to be nearly energy independent while the at-

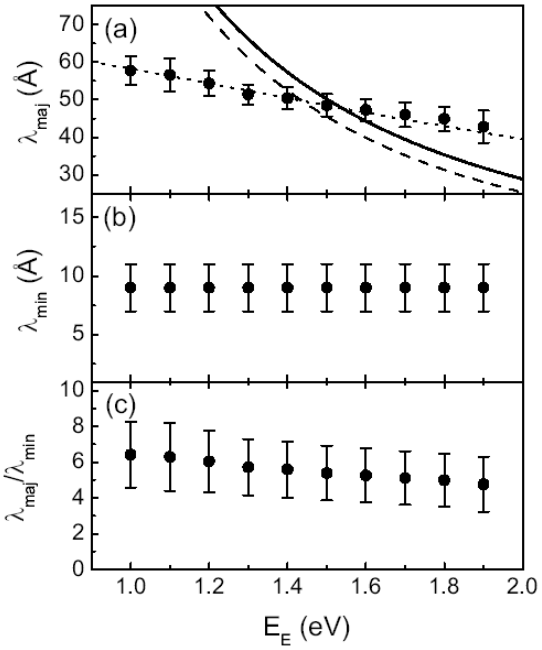

Figure 1.9: *Attenuation length for majority (top panel) and minority (middle panel) electrons in $Co_{84}Fe_{16}$ against the injected electron energy. The bottom panel shows that the ratio of the attenuation lengths of majority and minority electrons decreases as the energy increases. So elevation of the injected electron energy above 1 V decreases the magneto-current. Reported by van Dijken* et al.*[18]*

tenuation length for the majority electrons decreases with increasing electron energy. These findings are shown in figure 1.9. The figure shows the attenuation length for spin up (down) electrons as function of the electron energy in the top (middle) panel. The ratio between these attenuation lengths as function of energy is shown in the bottom panel. The highest value for this ratio is at the lowest energy which is 1 eV in this case. It is calculated that 40 Å of $Co_{84}Fe_{16}$ can filter out minority spins to give spin polarization of 98%. When the thickness of the baselayer is increased, the magneto-current saturates at 75% From this magneto-current a tunnel spin polarization of 27% is determined for the $Co_{84}Fe_{16}$ /$SrTiO_3$ emitter interface. Van Dijken *et al.* also report on magnetic tunnel transistors of the second type with a non-magnetic emitter and a spin valve in the base. [19] It was shown that an extremely high magneto-current (3400%) can be obtained in GaAs based MTT's. Unfortunately this high MC goes at the expense of the output current. State of art

MTT's now show a transfer ratio of $6.5{\cdot}10^{-4}$and a MC of more than 500% for Si/Cu(20Å)/CoFe(50Å)/Cu(40Å)/NiFe(50Å)/Al_2O_3(25Å)/Cu(300Å) operated at 1.4 V. The function of the Cu film on top of the Si is not only to create a good Schottky barrier. It also functions as a seed-layer that promotes crystallinity and smoothness of the spin valve stack. The enhanced smoothness sharpens the switching and furthermore, the improved crystallinity increases the transfer ratio by a factor of 5 to 7 compared to MTT's without a seed-layer, although the base contains an extra layer. This shows that the transfer ratio benefits heavily from improvement of crystal structure. It would therefore be very interesting to study MTT's with an epitaxial base.

1.4 $La_{0.67}Sr_{0.33}MnO_3$ in spintronic devices

The device studied in this thesis has a $La_{0.67}Sr_{0.33}MnO_3$ electrode. That is why we present a short overview of relevant work on $La_{0.67}Sr_{0.33}MnO_3$ and its spin polarization. In 1997 Picket and Singh [20, 21] theoretically predicted the high spin polarization for $La_{2/3}A_{1/3}MnO_3$ (with A = Ca, Sr, or Ba). Soulen *et al.* performed the first measurements of the spin polarization by Andreev reflection for $La_{0.7}Sr_{0.3}MnO_3$ in 1998. [22] A spin polarization of 78% for $La_{0.7}Sr_{0.3}MnO_3$ was determined. These experiments did not involve a tunnel barrier, so this spin polarization is in essence different from the tunnel spin polarization. Later that year, Park *et al.* determined the spin polarization of the $La_{0.7}Sr_{0.3}MnO_3$ surface by spin-resolved photoemission spectroscopy. In this technique photons excite atoms in the $La_{0.7}Sr_{0.3}MnO_3$ and electrons are emitted. The energy and spin of these electrons is detected. [23, 24] 100% spin polarization was found for $T < 60$ K. This polarization decreases gradually upon heating up to T_c. The top panel in figure 1.10 shows the spin resolved photoemission spectra of $La_{0.7}Sr_{0.3}MnO_3$ taken at 40 K. From this the spin imbalance (here defined as spin up - spin down) of LSMO as a function of energy is deduced. This is shown in the bottom panel. Around the Fermi-level, the intensity from the spin down electrons is zero while that from the spin up is not, showing 100% spin polarization.

The first work on magnetic tunnel junctions based on $La_{0.7}Sr_{0.3}MnO_3$ was published in 1996 by Sun and co-workers. [25, 26] 83% TMR at 4.2 K was demonstrated for $La_{0.67}Sr_{0.33}MnO_3$ /$SrTiO_3$ /$La_{0.67}Sr_{0.33}MnO_3$ magnetic tunnel junctions. From this TMR a spin polarization of 54% was deduced. The TMR was present up to 200 K and strongly temperature dependent. In 1997 a TMR of about 400% was measured and a spin polarization of 81% was deduced. [27] In 1997 Viret *et al.* reached 450% TMR in similar structures. [28, 29] This gives a spin polarization of 83% for $La_{0.7}Sr_{0.3}MnO_3$. The dramatic reduction of the TMR above 150 K and the maximum of junction resistance at 190 K are attributed to an oxygen deficiency in the $La_{0.7}Sr_{0.3}MnO_3$ interface layer.

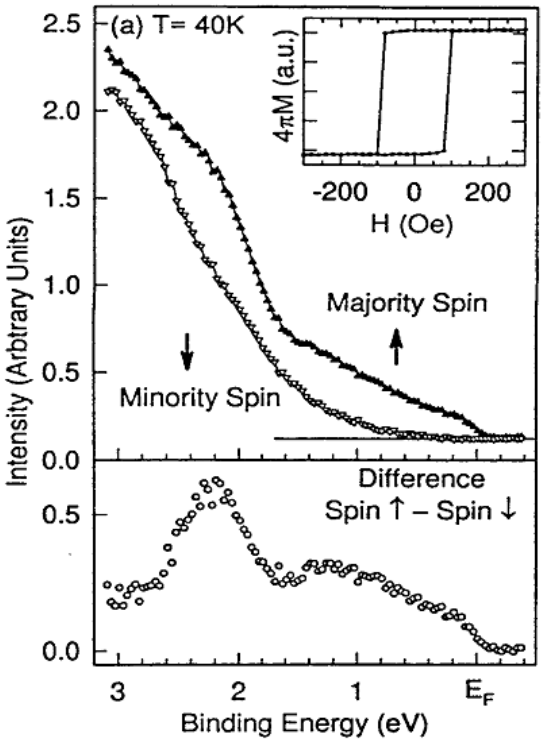

Figure 1.10: *The spin-resolved photoemission spectroscopy experiments reported by Park* et al. *on* $La_{0.7}Sr_{0.3}MnO_3$. *[23] In the top-panel the intensity of the emitted electrons is shown as function of their energy for spin up electrons and spin down electrons. For the majority spins the metallic Fermi cut-off is visible. Which means that emitted electrons can have any energy higher then the Fermi-level. The spin down electrons that are emitted have an energy of at least 0.6eV above the Fermi-level. This shows that there are no spin down electrons between the Fermi-level and 0.6 eV above the Fermi-level. The absence of spin down electrons around the Fermi-level shows that the* $La_{0.7}Sr_{0.3}MnO_3$ *is half-metallic.*

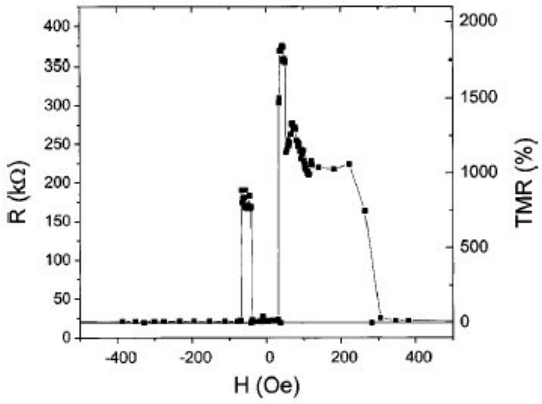

Figure 1.11: *Resistance and TMR as function of the applied magnetic field for a $La_{0.67}Sr_{0.33}MnO_3$ / $SrTiO_3$ / $La_{0.67}Sr_{0.33}MnO_3$ magnetic tunnel junction measured at 4.2 K. Reported by Bowen* et al.*[30]*

In 2002 Bowen *et al.*[30] measured 1800% TMR in $La_{0.67}Sr_{0.33}MnO_3$ / $SrTiO_3$ / $La_{0.67}Sr_{0.33}MnO_3$ magnetic tunnel junctions at 4.2 K. Figure 1.11 shows the junction resistance and TMR dependence on the field measured at 4.2 K. This gives a spin polarization of at least 95%. TMR was present up to 280 K despite the fact that the Curie temperature is 360 K. [31] This is believed to be due to a reduced high temperature spin polarization at the interface. [30, 32] The asymmetry in the curve is due to the pinning of one the electrodes by a CoO layer. This TMR was measured at 1 mV bias. The TMR decreases rapidly with increasing bias voltage.

Determination of the tunnel spin polarization of $La_{0.67}Sr_{0.33}MnO_3$ by the spin polarized tunneling technique of Meservey and Tedrow was first reported in 2000 by Worledge and Geballe. [33] They used $La_{0.67}Sr_{0.33}MnO_3$ /$SrTiO_3$ /Al tunnel junctions and determined a tunnel spin polarization of $La_{0.67}Sr_{0.33}MnO_3$ at the $SrTiO_3$ interface of 72%.

The magnetic tunnel junctions that we have addressed until now consist of two $La_{0.67}Sr_{0.33}MnO_3$ electrodes. In 1999 Sun *et al.* reported on magnetic tunnel junctions consisting of 60 nm $La_{0.67}Sr_{0.33}MnO_3$ as bottom electrode, 3 nm $SrTiO_3$ as tunnel barrier and 10 nm either Fe or $Co_{80}Fe_{20}$ as top electrode.[34, 35] The $La_{0.67}Sr_{0.33}MnO_3$ and $SrTiO_3$ thin film are grown by pulsed laser deposition at an oxygen pressure of 0.33 mbar and at a temperature of 780°C. A Nd-YAG laser (355 nm) is used at a frequency of 10 Hz. The energy density of the laser at the target was 2 J/cm^2 per pulse. The samples are then transferred to another vacuum system. Here the metal layers are deposited by sputtering after cleaning the surface in an oxygen plasma. 10 nm of

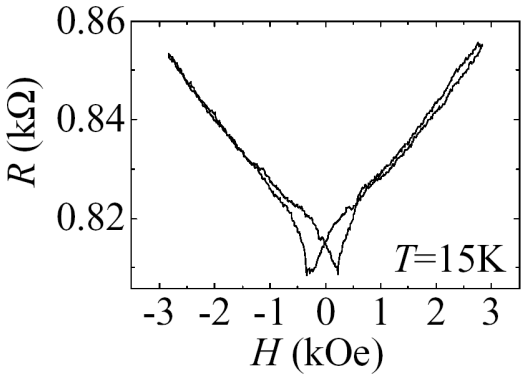

Figure 1.12: *Resistance as function of the applied field for a $La_{0.67}Sr_{0.33}MnO_3$ /$SrTiO_3$ /Fe magnetic tunnel junction at 15 K. Reported by Sun* et al.*[34]*

Ti is sputtered as a cap layer. Contact photolithography and Ar ion milling are used to define the Current Perpendicular to Plane (CPP) geometry. A curve of the field dependence of the resistance for a $La_{0.67}Sr_{0.33}MnO_3$ / $SrTiO_3$ / Fe magnetic tunnel junction is given in figure 1.12. The resistance change is present up to very high magnetic fields. This indicates that spins at the junction interface do not switch along with those in the bulk. Sun attributes that to an oxidized interface region between the $SrTiO_3$ and the metal. The temperature dependence that is found for the TMR and for the junction resistance in (anti)parallel alignment is given in figure 1.13 The curve shows that the maximum of junction resistance is around 200 K. The TMR becomes very small around 280 K. The reversal of TMR around 280 K is not real but caused by the fact that at these temperatures the condition that the base resistance should be 10 times higher then the sheet resistance [36] is not satisfied. This means that the current density through the barrier is inhomogeneous. This effect can seemingly enhance the TMR or even change the sign of the TMR. [36] Strong variations in junction behavior were also observed. Both positive and negative TMR are found in two junctions on the same chip at the same bias voltage. For a $La_{0.67}Sr_{0.33}MnO_3$ /$SrTiO_3$ /CoFe junction it was found that biasing up to 1 Volt could irreversibly reverse the TMR and increase junction resistance by factor of 20. These observations suggest that the junction MR is very sensitive to the interface condition. Another observation is that the shape of the R(H) curves depends on bias. This is attributed to inhomogeneous and non-linear conduction through the tunnel barrier.

De Teresa *et al.* studied magnetic tunnel junctions with an $La_{0.7}Sr_{0.3}MnO_3$ and a Co electrode separated by different kinds of tunnel barriers. [37, 38,

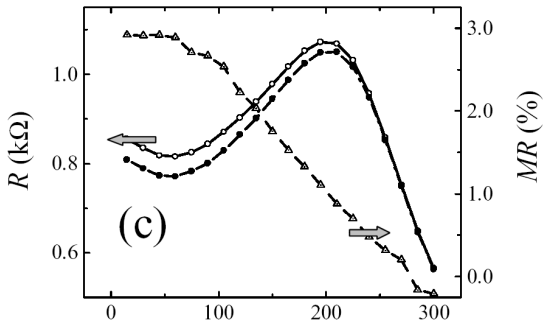

Figure 1.13: *Temperature dependence of resistance and TMR for a $La_{0.67}Sr_{0.33}MnO_3$ /$SrTiO_3$ /Fe magnetic tunnel junction. Reported by Sun* et al.*[34]*

39, 40] The insulating barriers used were Al_2O_3 (ALO), $SrTiO_3$ (STO), $Ce_{0.69}La_{0.31}O_{1.845}$ (CLO) and double ALO/STO barriers. The $SrTiO_3$ based magnetic tunnel junctions that they investigated consist of 35 nm of $La_{0.67}Sr_{0.33}MnO_3$ as bottom electrode, 2.5 nm of $SrTiO_3$ and 30 nm of Co as top electrode. For protection there is a 5 nm Au film. The $La_{0.67}Sr_{0.33}MnO_3$ and $SrTiO_3$ are grown by pulsed laser deposition at an oxygen pressure of 0.47 mbar and 700°C. The Co and Au films are grown by sputtering. The structures are etched using conventional lithography. The high resolution cross-sectional TEM image in figure 1.14 of a sample with an $SrTiO_3$ barrier shows sharp interfaces and it confirms that the $La_{0.67}Sr_{0.33}MnO_3$ film as well as the $SrTiO_3$ film is epitaxial. [41] The circles indicate the positions where Electron Energy Loss Spectroscopy (EELS) is performed. EELS spectra of the $La_{0.67}Sr_{0.33}MnO_3$ / $SrTiO_3$ interface show that the Mn atoms at the interface have the same valence as in the bulk, indicating that the MnO_2 layer is sandwiched between two $La_{0.67}Sr_{0.33}O$ layers rather then between one $La_{0.67}Sr_{0.33}O$ layer and a SrO layer. So the $La_{0.67}Sr_{0.33}MnO_3$ is $La_{0.67}Sr_{0.33}O$ terminated while TiO_2 is the last atomic plane of the $SrTiO_3$ at this interface. When ALO barriers are used the s-electrons of the cobalt are involved in the bonding between cobalt and ALO and the tunnel spin polarization is positive. Both tunneling spin polarizations are then positive giving a positive TMR. If the barrier material is $SrTiO_3$ a negative TMR is found at zero bias. So the tunnel spin polarization of the cobalt electrode on $SrTiO_3$ is negative, like the polarization of the d-electrons, coherent with the d-d bonding between Co and Ti. The dependence of resistance (TMR) on the applied field is given in figure 1.15. [39] This was measured at −400 mV bias and a temperature of 5 K. The $La_{0.67}Sr_{0.33}MnO_3$ switches around 3 mT. The Co starts switching around 40 mT. By changing the bias this TMR becomes positive. The bias dependence of the TMR is

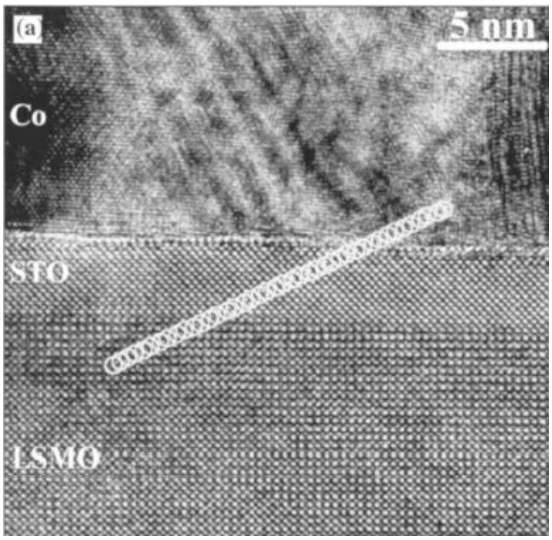

Figure 1.14: *High resolution cross-sectional TEM image of the* $La_{0.67}Sr_{0.33}MnO_3$ */*$SrTiO_3$ */Co junction. The circles indicate the positions where an Electron Energy Loss Spectroscopy (EELS) spectrum is recorded. Reported by Pailloux* et al.*[41]*

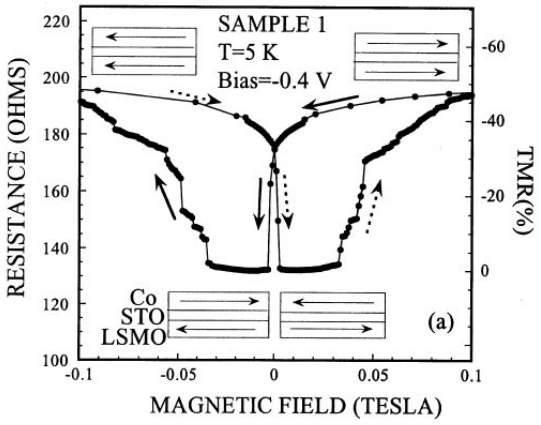

Figure 1.15: *Field dependence of the resistance and the TMR for a* $La_{0.67}Sr_{0.33}MnO_3$ */*$SrTiO_3$ */Co junction measured at 5 K at a bias voltage of 0.4 V. In the anti-parallel alignment the resistance finds its minimum, which gives a negative TMR. Reported by De Teresa* et al.*[39]*

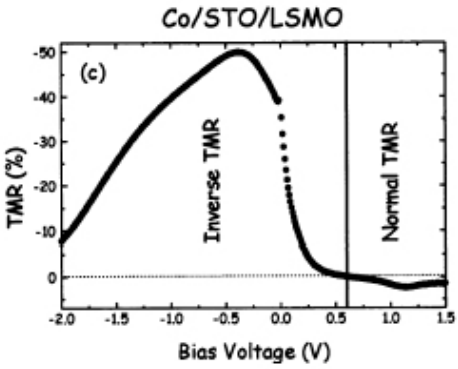

Figure 1.16: *TMR as function of the applied bias voltage for a $La_{0.67}Sr_{0.33}MnO_3$ /$SrTiO_3$ /Co junction measured at T=5 K. Reported by De Teresa* et al.*[39]*

shown in figure 1.16. This bias dependence closely resembles the polarization of the Co d-electron density of states that was calculated by Wang *et al.*[42] Positive bias means that the $La_{0.67}Sr_{0.33}MnO_3$ has a positive bias and electrons flow from the Co to the $La_{0.67}Sr_{0.33}MnO_3$. According to De Teresa *et al.*, this probes the Co density of states below the Fermi-level. [37] At negative bias the Co density of states above the Fermi-level is probed. This is shown in figure 1.17. At 0 V, the Fermi-level is probed and the density of states of the d-electrons clearly shows domination of the minority spins here, giving the negative tunnel spin polarization. The peak in the TMR at -0.4 volts corresponds to the maximum in spin imbalance at +0.4 eV in the Co d-electron density of states. Below the Fermi-level the spin imbalance changes sign and this results in a positive TMR above 0.6 volt. Insertion of Al_2O_3 to form a double barrier (Co/ALO/STO/LSMO) also gives a positive TMR while the ALO barrier is thinner then the STO barrier. This shows that the electronic structure at the Co/ALO interface determines the tunnel spin polarization rather then the propagation through the barrier.

Fert *et al.* find that the barrier resistance has a maximum at a certain temperature. For two different samples (The Co electrode for sample 1 has been sputtered while it has been evaporated (MBE) for sample 2) the temperature dependence of the junction resistance is shown in figure 1.18 [40] Sample 1 does not show a maximum below 300 K. Sample 2 finds the maximum of junction resistance at 280 K. For bulk $La_{0.67}Sr_{0.33}MnO_3$ the resistance finds a maximum at the Curie temperature. This is because in bulk $La_{0.67}Sr_{0.33}MnO_3$ the number of carriers decreases as the temperature increases from low temperature to the Curie temperature where it has its metal-insulator transition. The TMR as

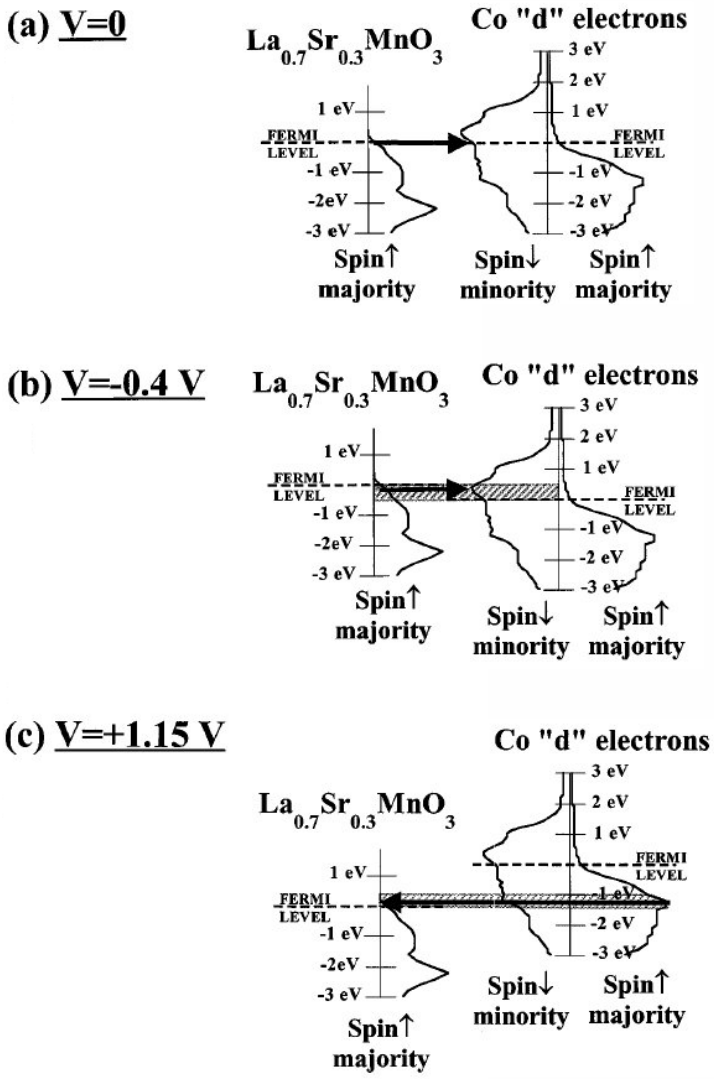

Figure 1.17: *Explanation of the bias dependence of the TMR for* $La_{0.67}Sr_{0.33}MnO_3$ */*$SrTiO_3$ */Co junctions based on the density of states of both electrodes. The arrow indicates the tunneling of the electrons with the highest tunneling rate. In case of a bias around 0 V (a) or a bias at -0.4 V (b) this route is between majority electrons in the* $La_{0.67}Sr_{0.33}MnO_3$ *and minority electrons on the Co in the anti-parallel configuration, giving a negative TMR. In case of a positive voltage of +1.15 V (c) this route is between the majority states of both electrodes, giving a positive TMR. Reported by De Teresa* et al.*[37]*

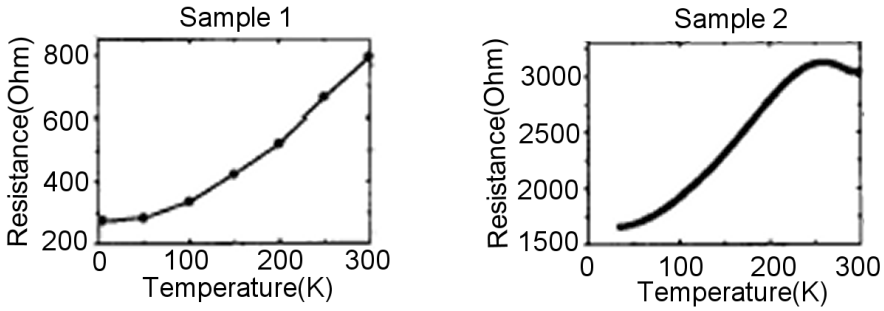

Figure 1.18: *Temperature dependence of the junction resistance for two $La_{0.67}Sr_{0.33}MnO_3$ /$SrTiO_3$ /$La_{0.67}Sr_{0.33}MnO_3$ magnetic tunnel junctions. The Co electrode for sample 1 has been deposited by sputtering, while it has been evaporated (MBE) for sample 2. Reported by Fert* et al.*[40]*

function of temperature is shown in figure 1.19. They define the temperature at which the TMR disappears as the Curie temperature of the interface, because at this temperature the spin polarization of the interface becomes zero.

Hayakawa *et al.* studied magnetic tunnel junctions consisting of $Co_{90}Fe_{10}$ / $SrTiO_3$ / $La_{0.7}Sr_{0.3}MnO_3$. [43, 44] MgO substrates are used and the materials are deposited by magnetron sputtering. The effect of oxygen deficiency in the $SrTiO_3$ barrier on the tunnel junction characteristics is studied. Depositing the $SrTiO_3$ barrier at 700°C in an atmosphere of Ar with 5% of O_2 gives an oxygen deficiency of 2% in the barrier (sample A). Deposition of the $SrTiO_3$ at 500°C in an atmosphere of pure Ar gives a oxygen deficiency of 10% in the barrier (sample B). Inverse TMR is found for both samples. The TMR of sample A was -22% at 4.2 K, while sample B gives -16%. The bias voltage dependence of the TMR of both samples is shown in figure 1.20. The TMR has a maximum at 0 Volt of bias. Higher bias decreases the TMR. For the strongly oxidized barriers, the bias dependence is asymmetric. For the oxygen deficient barriers the bias dependence is symmetric and much stronger(TMR drops faster with V). The temperature at which the TMR vanishes is for both samples lower then the Curie temperature of $La_{0.7}Sr_{0.3}MnO_3$. In figure 1.21 we see that the TMR vanishes at 160 K for the sample with high oxygen deficiency and at 200 K for the the sample with less oxygen deficiency. The explanation given for this is as follows: The oxygen deficiency in the barrier causes an oxygen deficiency in the $La_{0.7}Sr_{0.3}MnO_3$ interface, which reduces the spin polarization of the $La_{0.7}Sr_{0.3}MnO_3$ at the interface with the $SrTiO_3$. This explains the lower TMR for the oxygen deficient sample. Further the oxygen deficiency in the

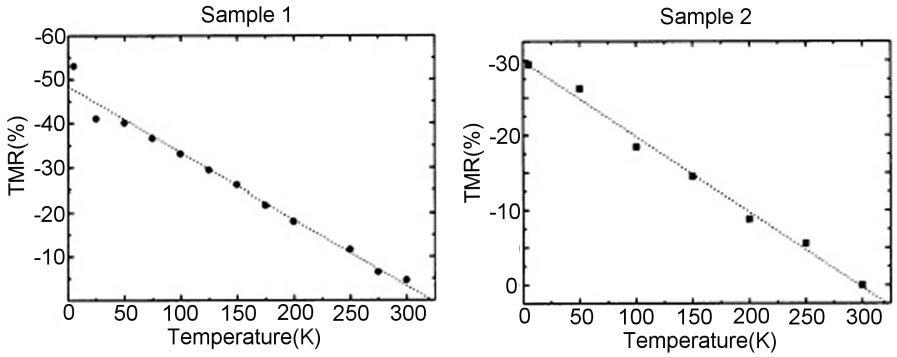

Figure 1.19: *Temperature dependence of the TMR for two* $La_{0.67}Sr_{0.33}MnO_3$ */*$SrTiO_3$ */*$La_{0.67}Sr_{0.33}MnO_3$ *magnetic tunnel junctions. The Co electrode for sample 1 has been deposited by sputtering, while it has been evaporated (MBE) for sample 2. Reported by Fert* et al.*[40]*

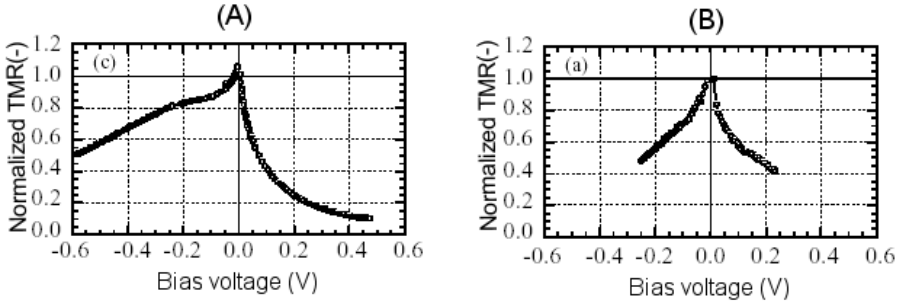

Figure 1.20: *Voltage dependence of the tunnel magneto-resistance for two* $Co_{90}Fe_{10}/SrTiO_3$ */*$La_{0.7}Sr_{0.3}MnO_3$ *magnetic tunnel junctions measured at 4.2 K. Sample B has a higher oxygen deficiency then sample A. Reported by Hayakawa* et al.*[43]*

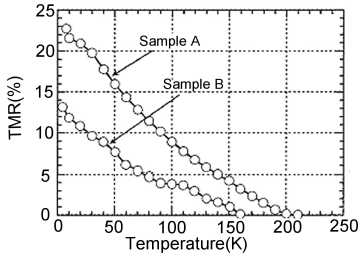

Figure 1.21: *Temperature dependence of the junction resistance for two $Co_{90}Fe_{10}/SrTiO_3$ /$La_{0.7}Sr_{0.3}MnO_3$ magnetic tunnel junctions. Sample B has a higher oxygen deficiency then sample A. Reported by Hayakawa* et al.*[43]*

barrier increases the electron scattering in the barrier and hence reduces the symmetry in the bias-voltage dependence of the TMR.

Thomas *et al.* studied the tunnel spin polarization of Co in combination with amorphous $SrTiO_3$ and TiO_2 tunnel barriers. [45] The $SrTiO_3$ and TiO_2 barriers are deposited by reactive evaporation onto a liquid nitrogen cooled substrate, which results in amorphous barriers. $Co/SrTiO_3/Co$ magnetic tunnel junctions show positive TMR of less then 3%. Positive TMR is to be expected as both electrodes are similar. The TMR decreases with increased bias and drops to zero at -0.35 V (+0.45 V). $Co/SrTiO_3$ /NiFe magnetic tunnel junctions also show positive TMR. So both the $Co/SrTiO_3$ and the $NiFe/SrTiO_3$ interface have the same sign for the tunnel spin polarization. From the spin polarized tunneling measurements [6] performed on $Co/SrTiO_3$ /Al junctions Thomas *et al.* deduce a positive spin polarization of $P_{Co} = 31\%$.

Oleynik, Tsymbal and Pettifor studied the atomic and electronic structure of the $Co/SrTiO_3$ interface using the first-principles density functional theory. [9, 46, 47, 48] The most stable interface crystal structure is found to be TiO_2-terminated with oxygen atoms (instead of Ti) on top of the Co atoms. This configuration is schematically depicted in figure 1.22 (A) (Crosscut) and 1.22(B) (Top-view). The interface local density of states (LDOS) calculated for this atomic structure is picture (C) in figure 1.22. Figure 1.22(D) and 1.22(E) are the contours of the density of charge and of spin for the $Co/SrTiO_3$ interface. Picture 1.22(F) shows the charge density of the minority electrons. Picture 1.22(E) shows that the Ti atoms at the surface with the Co have a magnetic moment. This moment is 0.25 Bohr magneton and is directed antiparallel to the magnetic moment of the Co film. Electrons that tunnel from these Ti atoms to the other electrode will therefore have a negative spin polarization. So this is a way to explain the negative spin polarization for the

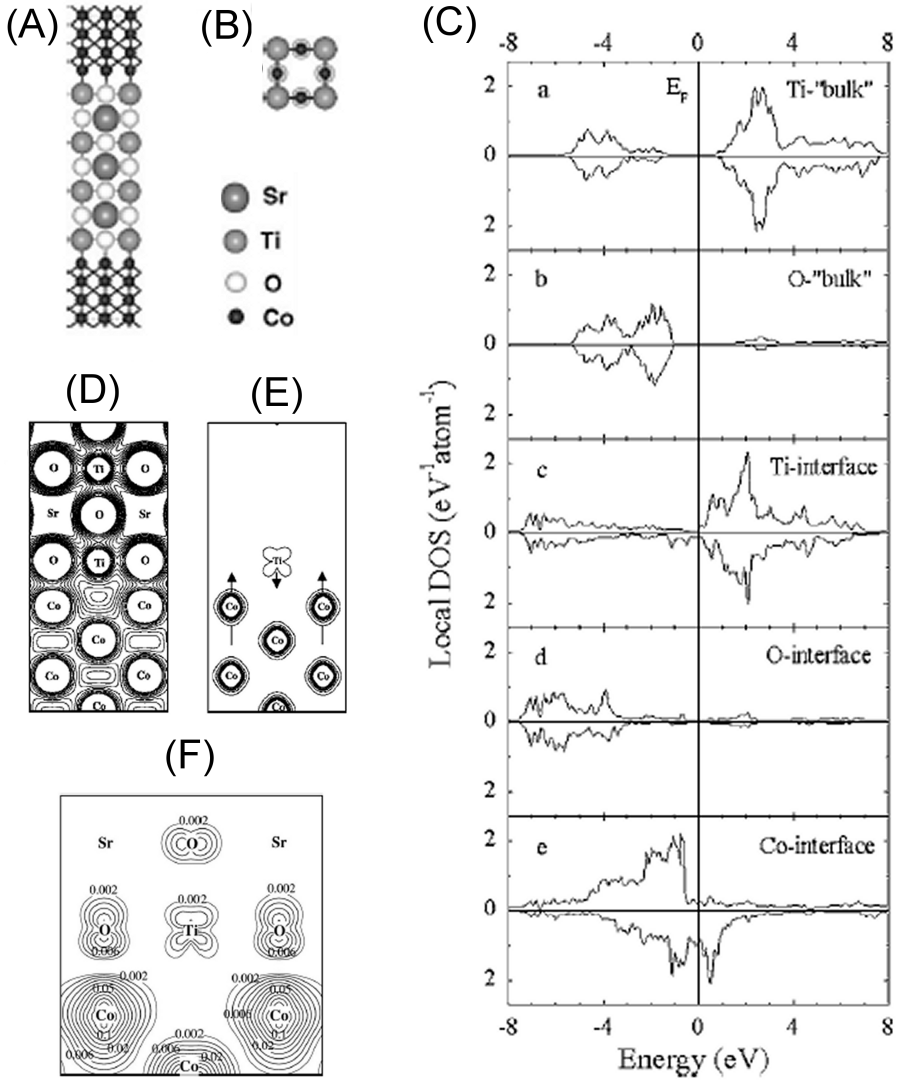

Figure 1.22: *Different schematic representations of the Co / $SrTiO_3$ interface: Most stable atomic structure (A)Cross-section and (B)Top-view. (C)Local density of states. (D)Contours of the density of charge. (E)Contours of the density of spin. (F)Density of charge of the minority electrons. Reported by Oleynik* et al.*[46]*

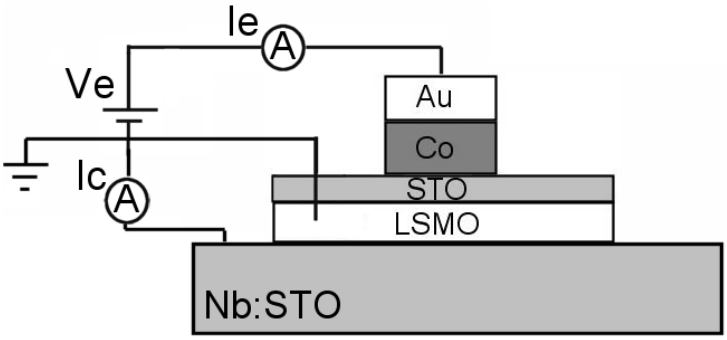

Figure 1.23: *Schematic view of the Magnetic Tunnel Transistor, that is discussed in this chapter.*

$Co/SrTiO_3$ interface.

In section 1.2 we have seen that electron tunneling from an electrode through a thin insulator barrier to another electrode is sensitive to the density of states of both electrodes. For magnetic electrodes this results in the TMR effect. We have seen that the TMR is sensitive to the spin polarization at the interface and that the barrier material also plays a part in the tunnel spin polarization of an electrode. In this section we showed that $La_{0.67}Sr_{0.33}MnO_3$ has a very high spin polarization and this can give a very high TMR at low temperatures. It was also shown that the TMR in $La_{0.67}Sr_{0.33}MnO_3$ based magnetic tunnel junctions at room temperature is low and that it vanishes well below the Curie temperature of $La_{0.67}Sr_{0.33}MnO_3$. This is attributed to a decreased spin polarization at the $La_{0.67}Sr_{0.33}MnO_3$ /tunnel barrier interface. The tunnel spin polarization of a Co electrode on a $SrTiO_3$ tunnel barrier is sometimes found positive and other times it is found to be negative. A discussion about the spin polarization of the $Co/SrTiO_3$ interface in the light of results presented in this thesis will be given in section 5.5 of chapter 5.

1.5 Motivation and thesis outline

The aim of the work presented in this thesis is to realize an epitaxial MTT based on $La_{0.67}Sr_{0.33}MnO_3$. A schematic view of this MTT is shown in figure 1.23. Half-metallic ferromagnets and in particular $La_{0.67}Sr_{0.33}MnO_3$ attract a lot of attention from the field of spintronics and information storage. Used in magnetic tunnel junctions in combination with $SrTiO_3$ tunnel barriers they give the largest tunnel magneto resistance ever reported. Unfortunately magnetic tunnel junctions are very sensitive to the condition of the interface between the

ferromagnet and the tunnel barrier and for the $La_{0.67}Sr_{0.33}MnO_3$ /$SrTiO_3$ interface the spin polarization is degraded at room temperature. Hence the huge TMR of these MTJ's only exists at low temperatures. The Curie temperature of $La_{0.67}Sr_{0.33}MnO_3$ is 360 K, so at room temperature it is still magnetic. It would therefore be highly interesting to use the spin polarization of bulk $La_{0.67}Sr_{0.33}MnO_3$ in a device instead of its spin polarization at the interface. SVT and MTT devices have shown large magneto-transport effects, even at room temperature, due to highly spin-dependent transmission of hot electrons through the metallic base of the transistor. Since it was shown[49] that interfaces contribute little to the spin dependence of hot-electron transmission, we anticipate that transistors using a half-metallic $La_{0.67}Sr_{0.33}MnO_3$ base should also operate at room temperature. Therefore we aim to realize an MTT with a $La_{0.67}Sr_{0.33}MnO_3$ base.

Magnetic tunnel transistors are among the first devices to combine spintronics with semiconductor electronics. The strength of the device is that it is based on the spin dependent scattering of hot electrons in magnetic films. But here also lies its weakness. The strong scattering in the base results in an output current that is 4 magnitudes in size lower then the input current. Increase of the output current can be expected when the scattering in the base is decreased. The most obvious way to do that is to decrease the number of layers in the base, to take base materials that have a long attenuation length for hot electrons and to use thin layers. It has been shown that an improve of the crystalline structure of the base material drastically increases the transfer ratio. [50] This is because the crystal boundaries form scattering centers. In epitaxial films, crystal boundaries will be rare or even absent. That is why we anticipate that the use of epitaxial films in the base of an MTT will have a positive result on the transfer ratio. In order to realize this, it is necessary to select a semiconductor / ferromagnet combination with a low lattice mismatch to facilitate the epitaxial growth of the ferromagnet. The combination also has to result in a Schottky barrier with a low reverse current that can serve as a filter for hot electrons. These demands drastically narrow down the options. We choose to use $La_{0.67}Sr_{0.33}MnO_3$ as the ferromagnet and niobium doped $SrTiO_3$ as the semiconductor.

A magnetic tunnel transistor with an epitaxial $La_{0.67}Sr_{0.33}MnO_3$ base is interesting for the reasons mentioned before and should in principle be feasible. Epitaxial $La_{0.67}Sr_{0.33}MnO_3$ is usually grown on $SrTiO_3$ substrates by pulsed laser deposition. Doping of the $SrTiO_3$ with Nb is a way to make it an n-type semiconductor. This doesn't change its lattice constant, so these doped substrates should still facilitate the epitaxial growth of $La_{0.67}Sr_{0.33}MnO_3$. For the tunnel barrier $SrTiO_3$ is chosen. $SrTiO_3$ has shown to result in high quality barriers. For the emitter electrode we choose Co because in order for the device to operate at room temperature, a high tunneling spin polarization of the emitter electrode at room temperature is necessary.

This introductory chapter will be followed by chapter 2, in which the experimental techniques used in this work will be addressed. We will show how the substrates are treated to achieve a TiO_2 termination. The chapter gives a short overview of the pulsed laser deposition technique that is used to grow the thin films. Also the high pressure reflective high energy electron diffraction (RHEED) technique used to follow the growth will be adressed. Other experimental techniques that we discuss here are the vibrating sample magnetometer (VSM) and the (low angle) X-ray diffraction (XRD). In chapter 3, we pay attention to the properties of single $La_{0.67}Sr_{0.33}MnO_3$ thin films. The structural, magnetic and electrical properties will be analyzed. In chapter 4 we focus on the diodes formed between the $La_{0.67}Sr_{0.33}MnO_3$ and the Nb doped $SrTiO_3$. We explain how the diodes are prepared and how the contacts are realized. These diodes are the first diodes to incorporate a half-metallic ferromagnet. The diodes are characterized and their applicability for use as a collector in an MTT is evaluated. The three top-layers in the MTT form a $La_{0.67}Sr_{0.33}MnO_3$ /$SrTiO_3$ /Co magnetic tunnel junction. These junctions are characterized and compared to similar junctions we find in literature. This topic is treated in chapter 5. In chapter 6 we discuss the preparation of the epitaxial MTT and the results that we obtained with these structures. The conclusions are presented in chapter 7.

Chapter 2

Experimental techniques

In this section we describe the experimental techniques that are used in this work. First a short overview of the development of the pulsed laser deposition (PLD) technique is given. Then we focus on the basic principles and the important characteristics of the PLD technique. The PLD setup that we use to grow the thin films as well as the Reflective High Energy Electron Diffraction (RHEED) that we use to monitor the growth are described. We also discuss the techniques that are used to characterize the thin films and the devices.

2.1 Pulsed laser deposition

Immediately when the laser was invented, there were studies on the interaction between laser beams and solid surfaces [51, 52], liquids and gaseous materials [53]. In 1965 it was demonstrated that the vaporization, observed in these experiments, can be used to deposit thin films. A breakthrough came in the mid-1970s when the electronic Q-switch was developed to deliver short pulses with very high peak power density, which broadened the selection of materials that could be deposited and allowed for congruent evaporation. The biggest breakthrough for PLD was the growth of high Tc superconducting films in 1987, led by Venkatesan. [54] The growth of these superconductors makes use of two important characteristics of PLD. The first one is that PLD allows all kinds of environments to deposit at because the energy source for the ablation is situated outside the vacuum-chamber. This enables the deposition of high Tc superconductors at the oxygen environment that is needed. In the growth of these films use is also being made of the single-crystalline growth characteristic of PLD, that can be obtained when depositing particles with a very high energy on a heated substrate. Also in the growth of other complex oxides like

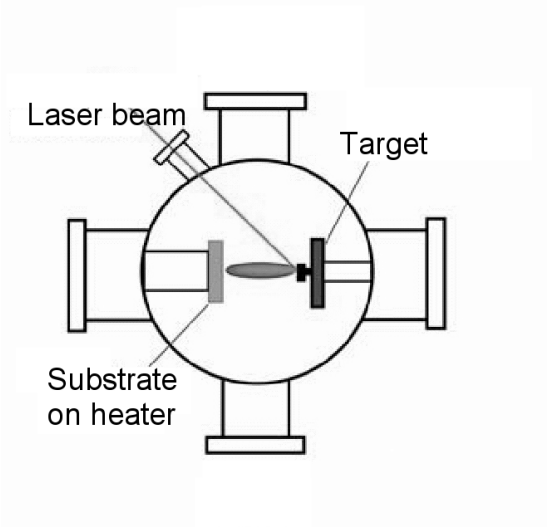

Figure 2.1: *Schematic view of a pulsed laser deposition setup. The laser beam enters the vacuum chamber through a window and intersects with the target. A plume is created that deposits on the heated substrate.*

ferroelectric oxides [55, 56, 57] and ferromagnetic oxides, PLD is used, for its stoichiometric deposition, the epitaxial growth and the possibility to deposit at an oxygen environment. Figure 2.1 shows a schematic diagram of a PLD setup. A Target and a substrate heater are mounted in a vacuum chamber. A high power laser is used as an energy source to vaporize the target material that deposits on the substrate. The laser is aimed and focused on the target by a set of mirrors and a lens. Although the PLD concept is simple, the laser-target interaction is a very complex physical phenomenon. The mechanism of the ablation of material depends on the properties of the laser and the target, and the theory combines equilibrium and non-equilibrium processes. Electromagnetic energy is absorbed by the target by means of electronic excitation. The absorbed energy is converted into thermal, chemical, and mechanical energy, which causes evaporation, ablation, excitation, plasma formation, and exfoliation. This results in the formation of a plume consisting of atoms, molecules, electrons, ions, clusters, micron sized particles and molten globules. In this complex process, target properties like density, absorption coefficient, thermal conductivity, surface morphology and melting temperature as well as laser characteristics like pulse duration, wavelength and beam profile, play an important role. Since the mean free path of the particles in this plume is very short the

plume rapidly expands into the chamber forming a plasma. The particles in the plasma have strong interaction with the ambient gas and deposit on the substrate. Important deposition parameters to influence the growth are the positioning of target and substrate, the energy and energy density of the laser beam on the target, the ambient pressure and the substrate temperature.

Advantages of PLD are that it can be used for any kind of material that absorbs laser light, and that it is possible to deposit in a reactive environment because the evaporation power source is outside the vacuum chamber so that there are no constraints imposed by an internally powered evaporation source. The characteristic that distinguishes PLD from other thin film techniques is the high kinetic energy that can be given to the particles arriving at the substrate and its high deposition rate during the laser pulse. The plume will contain neutral and charged particles and these charged particles can have an energy of up to 250 eV. This causes the particles in the plume to have very strong interaction with the ambient gas. The energy of the particles arriving on the substrate can be influenced by the deposition pressure and the target to substrate distance.

As was mentioned the energy of the ablated particles and the instantaneous deposition rate distinguish PLD from the other thin film growth techniques. In evaporation the target material is heated and evaporated by resistive heating or by an electron-gun. The vapor will expand in the vacuum chamber and condense on the substrate forming a condensed layer. The energy of the atoms in this vapor is a few tenths of eV and rates vary from 0.1 to 10 nm per minute. In sputtering, the target material is bombarded by ions. This bombardment will remove atoms or molecules from the target. These atoms and molecules will condense on the substrate that is close to this target. The ions can come from a plasma that is situated between the target and the substrate, or from a ion gun. The latter allows for lower pressures. Deposition rates are comparable to those obtained in evaporation. The energy of the atoms, that arrive on the substrate is a few eV.

For pulsed laser deposition, generally a laser with a wavelength between 200 and 400 nm is used. The absorption coefficient tends to increase at shorter wavelengths and the penetration depth is accordingly reduced. This is an advantage as thinner layers will be ablated and the threshold fluence will be lower. In this 200 to 400 nm range there are only a few commercially available lasers that can deliver the high energy. Generally, excimer lasers and Nd^{3+}:YAG lasers are used. Nd^{3+}:YAG lasers are solid state lasers. The neodymium ions serve as the active media. They are an impurity in the YAG (yttrium aluminium garnet) host. The Nd^{3+} ions are optically excited by a flashlamp. They will decay into a metastable state. From this state they will decay again, emitting light with a wavelength of 1064 nm. Since this is well beyond the usable range, a non linear crystal has to be used to double the frequency. This light can be mixed again with the 1064 nm light to attain an output at 355

Active excimer	Wavelength
F_2	157 nm
ArF	193 nm
KrCl	222 nm
KrF	248 nm
XeCl	308 nm
XeF	351 nm

Figure 2.2: *Wavelength of Excimer-gases used in lasers.*

or 266 nm. The efficiency at which these wavelengths can be produced is respectively 20% and 15%. Excimer lasers do not have this loss, because the wavelength is already in the right range. These systems can achieve repetition rates of several hundred hertz with energies of 1 J/pulse. That's why these lasers are usually used in PLD. These kind of lasers are gas lasers. In figure 2.2 a list of used excimer and their wavelength of emission is given. Among these the KrF laser is most used for its combination of a short wavelength with a high power. In an excimer laser the high energetic state has a very short lifetime, so the excimer will fall back to the lower state in about 10^{-13} second. This makes excimer lasers perfect for delivering a very short but high energy pulse. In the figure 2.3, the potential energy diagram of the KrF laser is shown. In excimer lasers the active material is excited to an excimer by an avalanche electric discharge excitation, although in some systems electron-beam excitation or microwave discharge excitation is used.

2.2 Growth characteristics of pulsed laser deposition

A high energy of incoming particles is especially welcome in the growth of epitaxial films. Due to this high energy the particles on the substrate surface have the high mobility that they need in order to find the position with the lowest energy. Due to the pulsed character of PLD, we should distinguish the average deposition rate from the deposition rate during and shortly after a laser pulse. For the perovskites that are deposited in this work we typically need about 10 pulses to grow 1 unit cell. That means that at a laser repetition rate of 1 Hz, the average deposition rate is around 0.4 Å/sec. But since this material is deposited in about 1 ms, the deposition rate during this millisecond is in the order of 40 nm/sec. This is one or two orders higher then in sputtering or evaporation, and can even be increased by two orders. When the substrate and ablated material are carefully chosen the ablated material can grow epitaxial, (following the crystal structure of the substrate) and a layer by layer growth mode can be imposed by the high supersaturation during the pulse. In the case

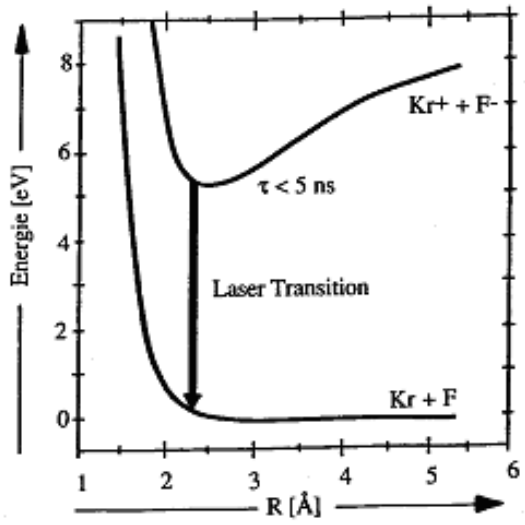

Figure 2.3: *The potential energy diagram of the transition of the KrF gas in the KrF excimer laser.*

of perovskites, the oxygen content in the film is of great importance. The oxygen content in the particles that arrive on the substrate will depend strongly on the oxygen deposition pressure, the target to substrate distance and the energy density of the ablating laser spot. The phase of the film that is grown will depend on the temperature and the stabilizing effect of the substrate as well. The pressure and target to substrate distance chosen is usually a trade-off between the phase-stability and the morphology. (high pressure and large target to substrate distance promotes the oxidation but decreases the mobility of the ad-atoms.)

Preservation of stoichiometry is also often referred to as an advantage that PLD has compared to other deposition techniques. In order to preserve the stoichiometry during mass transfer from the target to the substrate, the energy of the pulse should not have time to diffuse into the target. This means that the thermal diffusion length has to be shorter then the thickness of the material that is ablated every pulse. This thermal diffusion length is given by: $L = \sqrt{(2D\tau_p)} = \sqrt{\frac{2\kappa\tau_p}{\rho C_p}}$ in which D is the thermal diffusivity and τ_p is the duration of the laser pulse, κ is the thermal conductivity, ρ is the specific weight and C_p is the specific heat capacity at constant pressure. [58] The use of short high power pulses is therefore preferable to achieve congruent ablation. Disadvantages of the PLD technique are the presence of micron sized particles, and

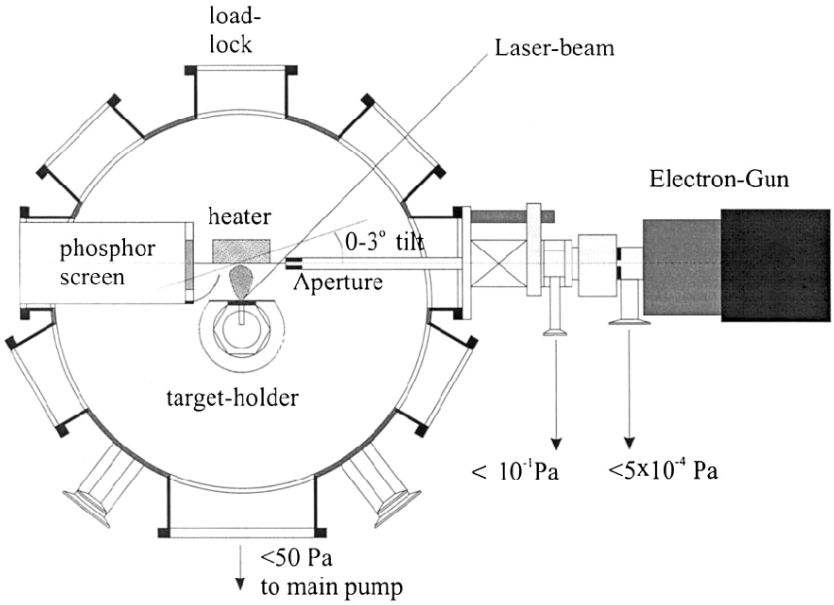

Figure 2.4: *Schematic view of a pulsed laser deposition setup with high pressure Reflective High Energy Electron Diffraction (RHEED) monitoring.*

the narrow forward angular distribution of the plume that makes deposition on large areas difficult.

The system is equipped with a Reflective High Energy Electron Diffraction (RHEED) setup. A schematic view of the system with the RHEED setup is shown in figure 2.4. RHEED is a technique that allows in situ monitoring of the substrate surface during the growth of a film. In this technique a beam of high energy (energy:10 - 50 keV, wavelength: 0.1 - 0.05 Å) electrons is reflected by the substrate surface and collected on a phosphorus screen where a diffraction pattern is formed. Due to the grazing angle of incidence (0.1 - 5 °), the technique is surface sensitive giving information about the crystal structure of the first 1-2 nm at the surface. The grazing angle also prevents the electron beam and the plume of deposited material from interfering with each other. The aspect of the RHEED technique that is exploited in this work is the intensity oscillations of the specular intensity during the growth of a film. These oscillations are observed when a layer is grown in a layer by layer growth mode. In this mode the step edge density oscillates during the growth. The surface has a low step edge density before the growth starts and at completion of an atomic layer. In these cases the only step edges are the terrace steps that are

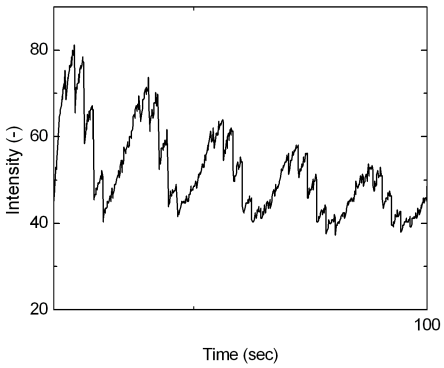

Figure 2.5: *Oscillations observed by in situ Reflective High Energy Electron Diffraction (RHEED) monitoring during the growth of an $La_{0.67}Sr_{0.33}MnO_3$ film onto a $SrTiO_3$ substrate.*

necessarily present because of the miscut of the substrate. When an atomic layer has been deposited partially, the terraces are covered by islands with a height of one unit cell. In that case the step edge density is larger, which causes stronger scattering of the electrons outside the specular beam on these edges. This causes the intensity of the specular beam to oscillate (see figure 2.5) and enables determination of the growth rate during the growth.

Whether or not this two dimensional growth is achieved, is governed by the kinetics of the deposited material and the interaction with the substrate surface. The kinetics have to be considered because the growing film is usually not in thermodynamic equilibrium. The nucleation of islands and the growth of these islands that determine the growth mode relate closely to the supersaturation of the vapor, the diffusion length of the adatoms, and thus to the substrate temperature.

2.3 The pulsed laser deposition setup

The laser that is used in our experiments is a KrF excimer laser (Compex 205, Lambda Physik). It has a pulse duration (FWHM) of about 25 ns. The incoming beam intersects with the target at an angle of 45°with respect to the target normal. A mask is placed in the laser beam in order to select that part of the beam in which the spatial energy density variation is limited to 5%. To control the energy density of the laser beam on the target, we adjust the laser power

and the demagnification of the optics. The energy of the laser beam before it enters the chamber is measured over a series of pulses, and a transmittance of the window of 90% is taken into account. The demagnification of the laser spot size is varied by changing the position of the mask and the lens.

The turbo molecular pump can pump the system down to 10^{-8} mbar. The oxygen pressure is controlled by a gas inlet through a brooks mass flow controller and a variable valve between the chamber and the turbo molecular pump to control the pump speed. 5 targets can be mounted on the target holder. This holder is loaded through a load-lock and by rotating this holder the targets are selected. Stepper motors move the target laterally, allowing the laser beam to scan a selected target area. The substrate holder includes a resistive heater and is also loaded through the load-lock. The heater is PID controlled and can reach temperatures of 800°C. The temperature of the heater is monitored by a K-type thermocouple situated inside the heater. The system is built by Twente Solid State Technology (TSST) B.V. A shutter between the target and the substrate holder allows preablation of the target without material being deposited on the substrate. To avoid removal of clusters from the target a high density target is preferable. With respect to density and compositional homogeneity, single crystal targets are superior. When these are not available, sintered pellets with the highest possible density are preferred. In this work a single crystal $SrTiO_3$ target and a sintered $La_{0.67}Sr_{0.33}MnO_3$ target are used. For the $La_{0.67}Sr_{0.33}MnO_3$ target hot isostatic pressing is used to reach a relative density of more than 95%.

The high pressures involved in the deposition of perovskites, causes two problems for a conventional RHEED system. The first one is a practical one and is caused by the fact that the e-gun operates at lower pressures. The source of electrons in an e-gun is generally a tungsten filament and these filaments are not resistent to the elevated pressures. The other problem is the attenuation of the electron beam. At high pressures the beam intensity decreases very fast so the path of the beam through the ambient gas should be minimized. This is achieved by application of a two-stage, differentially pumped RHEED system. (See figure 2.4) Due to this differential pump system a pressure of less then 10^{-4} Pa is realized in the e-gun and the pressure in the tube can be kept below 10^{-1} Pa. The tube is separated from the chamber by an aperture with a diameter of 0.5 mm. The tube allows the electron beam to enter the chamber at a distance of 5 cm from the substrate. The distance between the substrate and the phosphor screen is also 5 cm so that the path of the electrons through the ambient gas is reduced to 10 cm. For an oxygen pressure of 1 mbar the intensity loss of the beam in this path is estimated to be 99%. The E-gun that is used is RH-30 of STAIB instruments allowing an electron energy of 30 keV. A CCD camera is used to record the diffraction pattern. Acquisition software of K-space Associates is used to perform time-resolved intensity measurements.

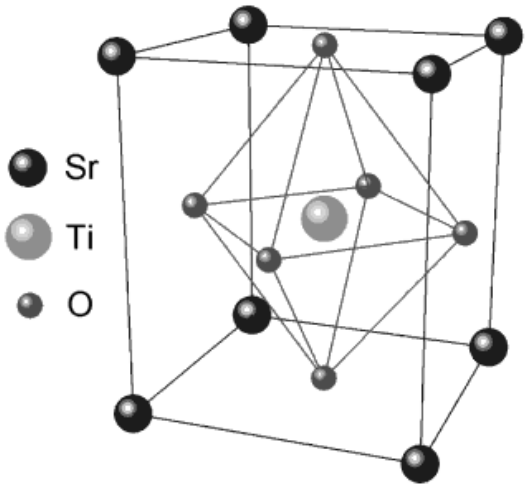

Figure 2.6: *Schematic view of the $SrTiO_3$ unit cell.*

2.4 Substrate preparation

$SrTiO_3$ single crystalline substrates are often chosen as substrate for the epitaxial growth of perovskite oxides. Figure 2.6 shows the unit cell of $SrTiO_3$. The crystal structure is cubic with a lattice parameter of 3.905 Å. $SrTiO_3$ consists of two sub-lattices of SrO and TiO_2 that are layered along all the principle axis. Both of these sublattices can be present at the surface. Figure 2.7 shows the (100) $SrTiO_3$ surface. On the left side, the surface is SrO terminated, on the right side the termination is TiO_2. An (100) substrate can be single terminated, which means that only one of the sublattices is present at the surface. In that case the step height of the terraces at the surface is 3.905Å

To facilitate epitaxial growth, the surface has to be crystalline and free of contaminants like water and carbon-oxides. A proper heat treatment is usually sufficient to remove these contaminants, but substrate surface properties like morphology and the termination of the substrate can influence the growth as well. In the as-received substrates these properties are not well defined. That is why we use a treatment to define these properties. In the as-received (100) substrates, both sub-lattices can be at the surface. Figure 2.8 shows an AFM image of the as received substrate surface. In the image we observe terrace steps. The height of these terrace steps is 4 Å. Since $SrTiO_3$ consists of a TiO_2 and a SrO sublattice, it is not clear which of the sub-lattices is at the surface.

In order to start the growth on a well defined surface however, a single termination of the substrate is preferred. Both a TiO_2 and a SrO single ter-

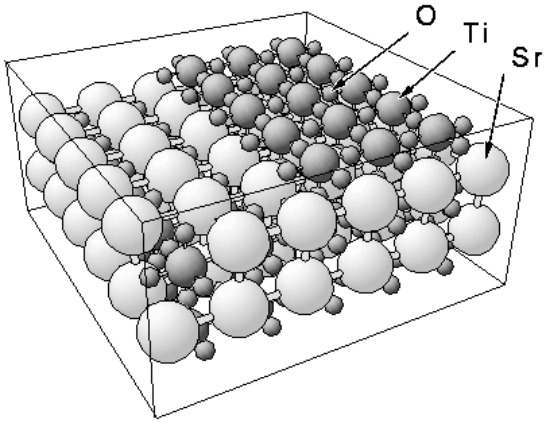

Figure 2.7: *Schematic view of the $SrTiO_3$ surface. The surface on the left side is SrO terminated, the part on the right side is TiO_2 terminated.*

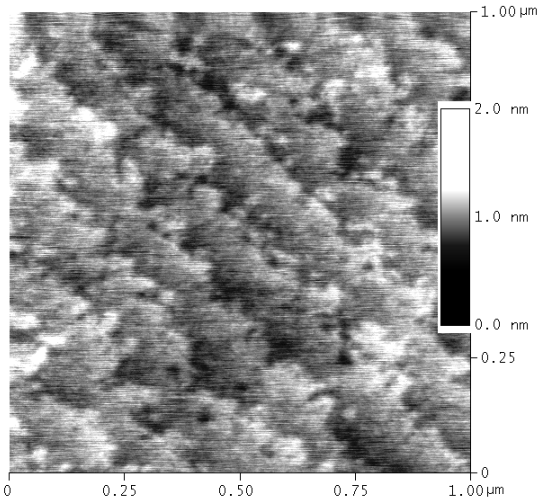

Figure 2.8: *AFM image of a $SrTiO_3$ substrate as received.*

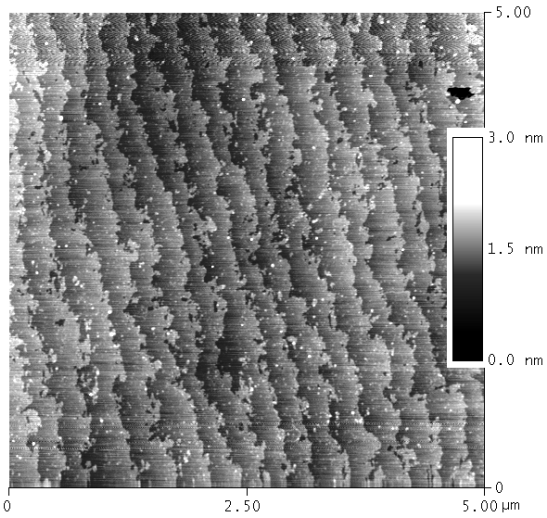

Figure 2.9: *AFM image of a $SrTiO_3$ substrate that is treated to achieve a TiO_2 termination. This substrate has not been annealed.*

mination can be achieved, but we choose TiO_2 because it is calculated to have the lowest surface energy and we now from the work by Shimizu *et al.*[59] that high quality Au/Nb:$SrTiO_3$ diodes have been attained using TiO_2 terminated Nb:$SrTiO_3$. Such a single termination can be achieved chemically by using the difference in solubility in acids between SrO and TiO_2. This difference is increased when the $SrTiO_3$ substrate is soaked in water allowing the SrO to form a $Sr(OH)_2$ hydrate. Using these chemical reactions, the treatment is performed as follows; First the $SrTiO_3$ substrate is placed in ultrasone ethanol to clean the surface. Then it is placed in ultrasone deionized (DI) water for 30 minutes. This hydrates the SrO planes at the surface ($SrO \rightarrow Sr(OH)_2$). This hydrate is removed by dipping it for 30 sec in ultrasone BHF. This is a buffered HF solution consisting of NH_4F and HF in the relation 7:1 with a PH of 5.5. Then the substrate is placed in ultrasone DI water for 20 minutes and rinsed with ethanol to remove residues. After this treatment the substrate has a TiO_2 termination. This treatment was reported by Koster *et al.* [60] Figure 2.9 shows an AFM image of the substrate surface after this treatment. The AFM image shows the terrace steps at the $SrTiO_3$ surface. The height of the terrace steps observed is around 4 Å, which corresponds the height of one unit cell. This shows that the substrate is single terminated. To obtain crystalline perfection of the surface, the substrates are annealed for half an hour at 950°C at an oxygen pressure of 1 bar. Figure 2.10 shows an image taken after the annealing step. The annealing causes the surface to relax by reducing the step edge density.

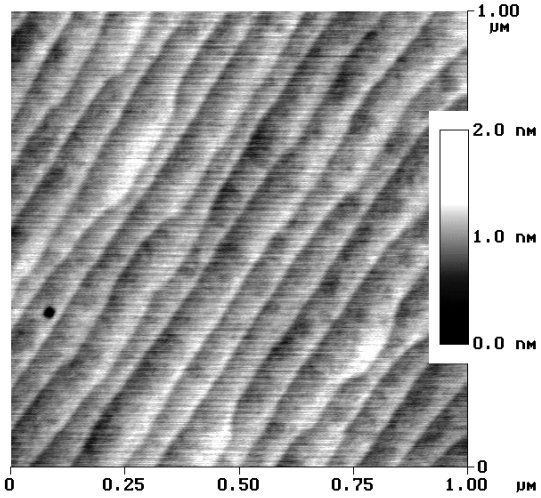

Figure 2.10: *AFM image of a $SrTiO_3$ substrate that was treated to achieve TiO_2 termination and annealed at 950 °C for one hour.*

2.5 Structural characterization

In this section the tools that are used for structural characterization of the deposited films are discussed. On the macroscopic scale, crystal structures are analyzed by X-ray diffraction. On the microscopic scale, transmission electron microscopy is used to analyze the crystal structure of the thin films and atomic force microscopy to analyze surfaces.

X-ray diffraction (XRD) is used to gain information on crystal structure, but it can also give information on layer-thickness, and interface roughness. X-ray diffraction uses the fact that a crystal lattice will act like an array of mirrors reflecting the X-rays. An X-ray source produces a coherent X-ray beam. This beam reflects on the different crystal planes, and since these planes are regularly spaced in the sample, this will cause diffraction. The type of measurement that is used in this research is a $\theta, 2\theta$ scan. In this scan, the angle of the incoming beam is swept while the detector is positioned to detect the reflected beam. Information can be extracted on the distance between the lattice planes that are parallel to the substrate surface. In analogy with light falling through a grating, the periodicity of the lattice planes and the wave-character of the X-ray beam result in a diffraction pattern. The angle θ under which there will be positive interference between the reflected beams obeys Bragg's law.

$$\sin(\Theta_{Bragg}) = \frac{n \cdot \lambda}{2d} \tag{2.1}$$

In which λ is the wavelength of the X-ray beam, n is the order of the reflection and d is the lattice constant perpendicular to the plane of the sample. The Cu-Kα X-ray source that is used generates an X-ray beam with a wavelength of 1.54 Å. Actually there two wavelengths present in the beam, one is 1.5406 Å, the other one is 1.5444 Å. So the peaks in the intensity in the $\theta, 2\theta$ scan can be correlated to a distance between the planes in the sample. The penetration depth of the X-ray beam is in the order of 100 μm. In case of a thin film, the interface plane and the surface plane can also form a set of reflecting planes. This can cause diffraction as well, but since the distance between these planes is larger then the distance between the crystal planes, this diffraction is at low angles of theta. Since $\frac{\lambda}{2d}$ is much smaller, the different orders of n result in oscillations of the intensity. For low angles, $\sin\Theta$ is approximated by Θ and Bragg's law can be adapted to give the relation between the layer thickness and the period of the oscillations:

$$t = \lambda/\Delta(2\theta) \tag{2.2}$$

In this way, low angle X-ray diffraction can be used to determine layer thickness in a thin film. The amplitude of the oscillation will give information about the sharpness of the interfaces. The X-ray Diffractometer that is used in this research is the Philips XRD model Expert system 1.

Atomic force microscopy (AFM) is a tool we use for analysis of surfaces of substrates or thin films. An AFM is a probe microscope. This means that a probe (a thin needle or tip) is scanned over the surface that is imaged. There are a couple of physical principles that can be used to measure interaction between the tip and the surface of the sample under investigation. In non contact AFM the interaction is the tapping of the tip on the surface. The cantilever, on which the tip is placed is brought in resonance directly above the substrate surface. When the tip touches the surface this frequency will change, this change in frequency will be the feedback signal that will change the height of the tip, getting it back to the height where it just touches the surface. In contact AFM the tip is not oscillated and it constantly touches the surface. The feedback signal is the deflection of the tip. The AFM that is used in this research is a Digital Instrument Nanoscope III A. This setup has the possibility to do both tapping mode AFM and contact AFM. For Tapping AFM, silicon Nanosensor non-contact tips, are used with a tip diameter of 5 to 10 nm. The resolution of the microscope in AFM mode is in the order of the size of the radius of the tip, so that is 5 to 10 nm.

For visualization of the microstructure of thin films we use cross-sectional Transmission Electron Microscopy (TEM). The TEM is a so called fixed beam instrument. A fixed electron beam will intersect with a cross section of the sample. This thickness of the cross section will be between 50 and 100 nm. The transmitted beam will form an image on the detector, so the image is always present as a whole. The transmittance of the beam will depend on the

electron density in the cross section. In general, use is made of electrons that have an energy of 100 to 200 keV. Although there are high voltage electron microscopes that use 3 MeV electrons. The wavelength of these electrons will be in the order of 10^{-12} meter. Unlike in an optical system, this does not mean that the resolution is also in this order. The resolution is limited by the lenses. But high energetic electrons do increase the resolution. The cross-sectional TEM pictures that are shown in this thesis are made at an electron energy of 260 to 300 keV. This results in a resolution of a couple of angstroms. The electrons that reach the substrate can transmit through the sample or be diffracted at an angle 2 Θ (Bragg condition; equation 2.1). This gives a diffraction pattern, that is Fourrier transformed back to real space to form the cross-sectional TEM image. It is possible to select parts of this diffraction pattern to be involved in the image formation. This gives the system different modes of operation. In the bright field mode, only the directly transmitted beam will be involved in the forming of the image. In this mode, the cross-sectional TEM image reflects the electron density in the cross section, although different crystal orientations will result in different intensities on the image as well because of the fact that the fraction of the electrons that is diffracted will depend on the orientation of the crystal. A dark field image is attained when only a diffracted spot of the diffraction pattern is used to form the image. In that way only the crystals with a certain orientation (from which the electrons will diffract into the spot used to make the image) will give a high intensity on the image. It is also possible to make an image of the diffraction pattern. This can give information about lattice spacings in the sample. The TEM that is used in this research is a Philips CM30 TWIN STEM, fitted with Kevex Delta Plus EDX and Gatan model 666 PEELS. It has a maximum accelerating voltage of 300 kV.

2.6 Magnetic characterization

The vibrating sample magneto-meter is the most used technique to characterize the macroscopic magnetic behavior of a sample. The sample is vibrated so that the magnetic moment of the sample creates an oscillating magnetic flux through the pick up coils. An oscillating voltage is induced over the coils, that is picked up by a set of lock in amplifiers, to filter out magnetic fluctuations that do not originate from the sample. We use two different VSM's. The first one is an Oxford VSM. This VSM can reach a magnetic field of 3 Tesla (2400 kA/m) with a step size of 10 μTesla (8 A/m) and is controlled by an Aerosonic 3001 VSM controller. It contains an Oxford sample cryostat, so that the temperature of the sample can be varied between 20 and 300 K. The sample can be rotated over 360 degrees with a step size of 0.1 degree. Two EG&G 5209 lock in amplifiers read out the pick up coils. This VSM can measure a magnetic moment from 5

nAm^2 to 1 Am^2 with an accuracy of 5%. The other one is the model 10 high field VSM of ADE technologies. It can reach a magnetic field of 2 T (1600 kA/m) with 10 nT (8 mA/m) resolution. It has a sensitivity of less then 5 nAm^2. The sample can be rotated 540°and the temperature of the sample can be varied between 120 and 700 K. The system includes a magneto resistive measurement setup.

Chapter 3

Epitaxial $La_{0.67}Sr_{0.33}MnO_3$ films

To fabricate a magnetic tunnel transistor with an epitaxial base, a ferromagnet and a semiconductor with matching crystal structure are essential. We choose to use a perovskite both for the ferromagnet and the semiconductor. Several perovskites show ferromagnetic behavior. We use $La_{0.67}Sr_{0.33}MnO_3$ because its Curie temperature is well above room temperature at 360 K. [31] We deposit the $La_{0.67}Sr_{0.33}MnO_3$ by pulsed laser deposition, because of the epitaxial growth characteristic that can be obtained by PLD. In this chapter, the deposition of the $La_{0.67}Sr_{0.33}MnO_3$ thin films by pulsed laser deposition is discussed. The procedure that we use to grow the thin films is described and we will show the effect of variation of the deposition parameters on the structural, magnetic and electronic properties of the films.

3.1 Introduction

In order to grow epitaxial films, the substrate and the film should have a low lattice mismatch. Bulk $La_{0.67}Sr_{0.33}MnO_3$ is rhombohedral. The pseudo-cubic unit cell has an angle of 89.74°and a lattice parameter of 3.873 Å. [61] $SrTiO_3$ is cubic and has a lattice parameter of 3.905 Å. This gives a very small lattice angle mismatch of 0.26°and a mismatch of the lattice constant of 0.8%. This allows epitaxial growth of $La_{0.67}Sr_{0.33}MnO_3$ on $SrTiO_3$ substrates.[26] For this reason we choose to use $SrTiO_3$ substrates.

Calculations by Picket and Singh in 1997 predicted a high spin polarization for $La_{2/3}A_{1/3}MnO_3$ (with A = Ca, Sr, or Ba) [20, 21]. Since then, much work has been performed on these materials. Park *et al.*[23, 24] found $La_{0.67}Sr_{0.33}MnO_3$ to be a half-metallic ferromagnet, which means that the electrons at the fermi level are 100% spin-polarized. A schematic view of the density

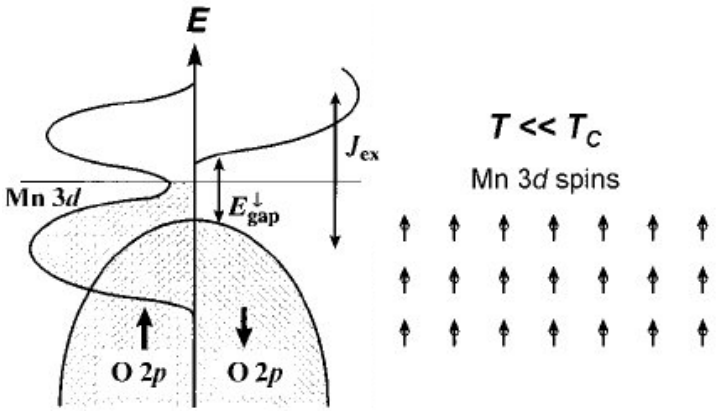

Figure 3.1: *Scematic view of the density of states of $La_{0.67}Sr_{0.33}MnO_3$. Source: J.H. Park [23]*

of states of $La_{0.67}Sr_{0.33}MnO_3$ is given in figure 3.1. Below the Curie temperature the Mn 3d spins are aligned parallel and the energy of the Manganese 3d-electrons is spin split. The difference in the energy between the spin up and spin down electrons, is the Hund rule exchange energy and is shown in the figure as J_{ex}. Spin up electrons are present at the Fermi-level, but the energy of the spin down electrons lies above the Fermi-level. This leaves an insulating bandgap at the Fermi-level for spin down electrons. This is denoted in the figure as E_{gap}. In devices that are based on spin dependent transport of electrons, materials with high spin polarization are useful building blocks. Applied in magnetic tunnel junctions $La_{0.67}Sr_{0.33}MnO_3$ has shown the highest TMR effect ever reported (1800% at 4.2 K). [30] Half-metallic ferromagnets like $La_{0.67}Sr_{0.33}MnO_3$ have been suggested as an emitter for spin injection into a semiconductor.[62] In these applications the spin polarization of electrons that travel from or to the interface of the material is exploited, but used in a magnetic tunnel transistor, the spin dependent transmission through the material can be studied. Since the growth of epitaxial $La_{0.67}Sr_{0.33}MnO_3$ films in a ferromagnetic phase is not straightforward, we discuss the growth in this chapter. In the next section we describe the procedure that we use to grow the thin films. Section 3.4 describes the deposition parameters that we varied and the effect of these variations on the structural, magnetic and electronic properties of the films. In situ monitoring of the growth is used to identify the mode in which the films grow. In section 3.5 and 3.6, we present a structural, magnetic and electrical characterization of two films that are grown with two different sets of deposition parameters. The reason that we present a detailed characterization

of these films is that the same two sets of deposition parameters are used to grow the magnetic tunnel junctions that will be described in chapter 5.

3.2 Preparation of $La_{0.67}Sr_{0.33}MnO_3$ thin films by pulsed laser deposition

In this section the preparation of the $La_{0.67}Sr_{0.33}MnO_3$ thin films is described. To facilitate the epitaxial growth of the $La_{0.67}Sr_{0.33}MnO_3$, we use $SrTiO_3$ substrates. The substrates are treated to achieve a TiO_2 termination and annealed for an hour at 950°C to decrease the step edge density. More details about the treatment and the annealing are given in section 2.4. Before each deposition run, we prepare a smooth target surface by polishing the surface with with sand-paper. The polishing removes the tracks that are formed by the ablation of material in the previous deposition run. The reason that we prefer a smooth target surface, is that a rough surface increases the chance of the ablation of large particles. The target is mounted in the target holder and loaded into the system through a load lock. In order to heat the $SrTiO_3$ substrate, it is thermally anchored to the heater with silver paste. This silver paste is heated for 5 minutes to harden out. The heater with substrate is loaded through a loadlock. In the deposition chamber the substrate is heated to 750°C. Then the laser is lined out and focused. A mask is placed in the laser beam to select the part of the beam in which the spatial energy density variation is limited to 5%. The slits in this mask have an area of 0.99 cm^2. A lens is used to demagnify the width and the height of the spot by a factor 0.12. Taking into account that the beam has an incident angle of 45°with the target, this results in a spot size of 0.020 cm^2 on the target. The intensity of the laser spot before it enters the chamber is measured and controlled to 65 mJ/pulse over a series of pulses. This energy has a standard deviation of typically 2 mJ. The transmittance of the window is 90% so that an energy density of 3.0 J/cm^2 is obtained. The energy density of 1.0 and 2.0 J/cm^2 is obtained by changing the position of the mask and the lens so that the demagnification is 0.21 or 0.17. When the laser is lined out and the base pressure is in the $1{\cdot}10^{-7}$mbar regime, the oxygen flow is started and the pressure is controlled to 0.3 or 0.35 mbar. A shutter is rotated between target and substrate so that the target can be preablated without depositing on the substrate. During this preablation the target is scanned horizontally by 1 cm, so that an area of 0.25 cm^2 is ablated for 3 minutes at a laser repetition rate of 3 Hz. This preablation is used to remove impurities from the target surface. After the preablation, the shutter is opened and the distance between the target and the substrate is set to 40 mm. Finally, the electron beam for the Reflective High Energy Electron Diffraction (RHEED) is lined out and the ablation is started.

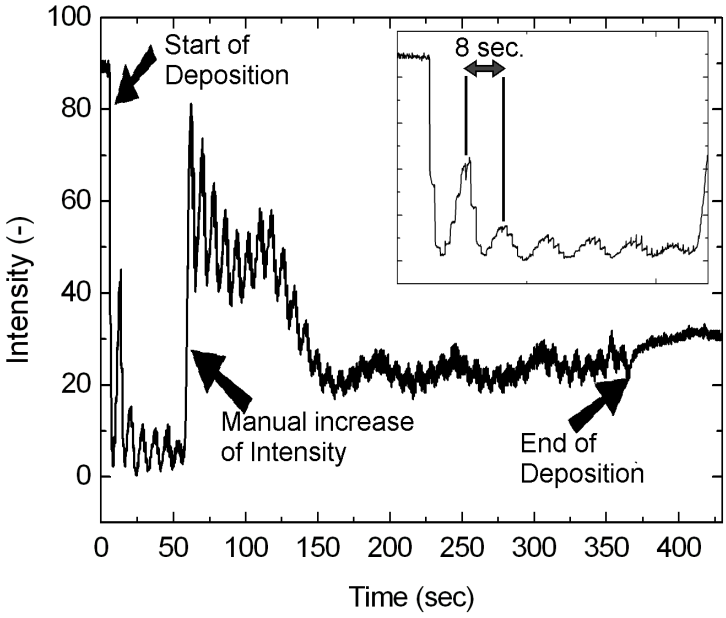

Figure 3.2: *RHEED pattern recorded during the growth of a $La_{0.67}Sr_{0.33}MnO_3$ film at a laser frequency of 1 Hz. The inset zooms in on the first six oscillations. At t=60 sec, the intensity of the electron beam is manually increased. The deposition is stopped at t=360 sec.*

3.3 In situ growth monitoring by Reflective High Energy Electron Diffraction (RHEED)

We use in situ RHEED to monitor the growth. It is possible to identify the layer by layer growth mode by RHEED. This growth mode should result in an oscillation of the RHEED intensity during the growth of the film. [63, 64] Figure 3.2 shows the RHEED intensity that is recorded during the growth of a $La_{0.67}Sr_{0.33}MnO_3$ film at a repetition rate of 1 Hz and a laser energy density of 1 J/cm^2. An oxygen deposition pressure of 0.3 mbar is used. The figure shows the intensity of the reflected electron beam as function of the time. The oscillations with a period of 8 seconds correspond to the deposition of 1 monolayer. [63, 64] At t=60 sec, the intensity of the e-beam is manually increased. The inset zooms in on the deposition of the first 6 monolayers. The peaks that are superposed on these oscillations are due to the material being

deposited every pulse. The oscillations are very clear even up to the deposition of the 45th and last monolayer at t=360 sec, when the thickness of the film has reached 17 nm. The oscillation with a period of about 1 minute, that show up after t=100 sec are due to the fact that the number of pulses necessary to grow a monolayer is not exactly 8. In the highest maxima the atomic layer has finished growing and the only steps at the surface are the steps that are there due to the miscut angle. In the lowest maxima, the atomic layer would need half the amount of material that is deposited in one pulse to finish growing and fill up the terrace steps. During the deposition, the intensity gradually decreases up to t=170 sec. After that, the intensity oscillates around a constant value. The gradual damping of the oscillations is due to the fact that the growth is not a true 2D growth. In true 2D growth, the adatoms that arrive on top of a 2D island will migrate to the step edge of the 2D islands and are incorporated at this edge. In that case, islands will not nucleate on top of a 2D island. However when the mobility of the adatoms is lower, or the deposition pressure is higher, nucleation can occur on top of a 2D island before the preceding layer is complete. That means that when one layer has finished growing the next has already started growing so the surface will not become as smooth as the surface, that is started with. This is called a multilevel growth. This repetitive process will cause the oscillations to be damped as the surface becomes statistically distributed over several incomplete atomic levels. [64] The nucleation is still a 2D nucleation and we can still speak about a 2D growth. [65]

3.4 Structural and magnetic characterization of the $La_{0.67}Sr_{0.33}MnO_3$ thin films

In this section, the influence of different deposition parameters on the structural, magnetic and electrical properties of the $La_{0.67}Sr_{0.33}MnO_3$ thin films is studied. An important deposition parameter in PLD is the energy density or fluence of the laser spot at the target. In literature, values ranging from 1 to 3 J/cm^2 are reported for the deposition of $La_{0.67}Sr_{0.33}MnO_3$. (1 J/cm^2[66], 2 J/cm^2[25, 66, 67], 3 J/cm^2[68, 69]) A fast way to characterize the influence of the laser fluence on the ablation process without deposition of a film is an investigation of the surface of the target after ablation. The target is ablated by 20 laser pulses in an oxygen environment of 0.3 mbar. Six different energy densities are used to investigate the effect of the energy density on the target surface. The target surface after ablation is visualized by Scanning Electron Microscopy (SEM). Figure 3.3 shows the surface of the target after ablation by 20 pulses with an energy density ranging from 0.5 to 3.0 J/cm^2. The images show that an energy density of 1.0 J/cm^2 leaves the smoothest surface. The increased roughness at higher densities is likely to be caused by particulates that are ablated from the target. The structures that are on the surface after

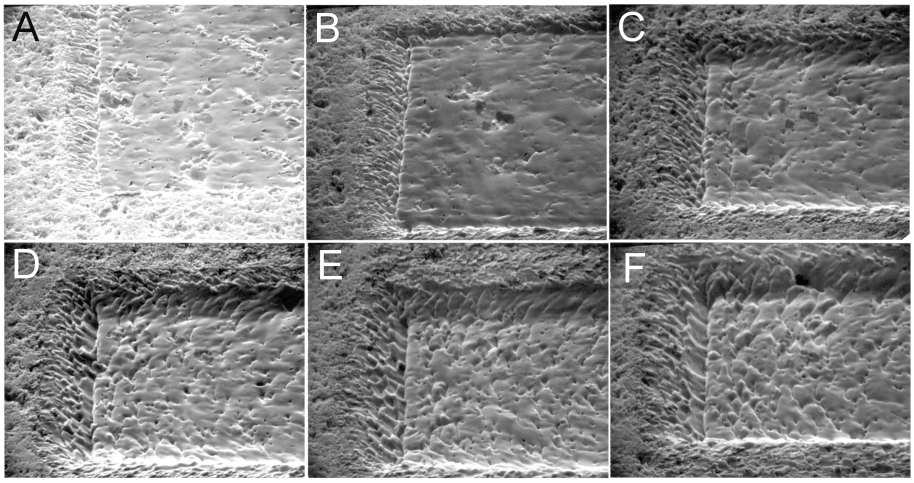

Figure 3.3: *SEM images of the $La_{0.67}Sr_{0.33}MnO_3$ target after ablation. The images show the surface after ablation in a rectangular area by 20 pulses with an energy density of (A)0.5, (B)1.0, (C)1.5, (D)2.0, (E)2.5 and (F)3.0 J/cm^2 respectively.*

ablation at 0.5 J/cm^2 are parts of the target that ablate less strong then the surrounding material. It shows that this energy density is close to the threshold. This should be avoided as well, as these parts can also be ablated as a particulate. So based on the ablated surface of the $La_{0.67}Sr_{0.33}MnO_3$ target we initially choose to use an energy density of 1.0 J/cm^2 for deposition of the films.

The repetition rate of the laser is an important parameter in PLD as well. A low repetition rate of the laser gives the deposited atoms the time to find the position with the lowest energy. In the case of $La_{0.67}Sr_{0.33}MnO_3$ on top of single crystalline $SrTiO_3$, this results in epitaxial growth. [26] Increase of the time between two pulses can allow the material to absorb oxygen. On the other hand the repetition should not be lower then necessary because this can allow deposition of polluting atoms that are in the ambient gas. To examine the influence of the repetition rate of the laser, we grow $La_{0.67}Sr_{0.33}MnO_3$ films with different repetition rates. These films are all grown at a substrate temperature of 750°C, a laser fluence of 1.0 J/cm^2 and an oxygen background pressure of 0.3 mbar. Figure 3.4 shows cross sectional Transmission Electron Microscopy (TEM) and Atomic Force Microscopy (AFM) images of these samples. The AFM and cross-sectional TEM image, that are shown for the repetition rate of 5 Hz (picture A and D) are both taken from the same sample. The cross-sectional TEM image shows that the thickness of this sample is about 14 nm.

The other four images are all taken from different samples. The AFM images E and F are taken from films with a thickness of respectively 45 and 21 nm. This thickness is determined by low angle X-Ray Diffraction (XRD). Cross-sectional TEM images B and C are taken from samples that consist of a Niobium doped $SrTiO_3$ substrate onto which a $La_{0.67}Sr_{0.33}MnO_3$ /$SrTiO_3$ /Co/Au multilayer is grown. In the images, only the $La_{0.67}Sr_{0.33}MnO_3$ film and the Nb:$SrTiO_3$ substrate is shown. The sample that is grown at a repetition rate of 3 Hz, shows an atomically smooth surface in the AFM image (image E). The image shows terrace steps. The height of these terrace steps is on the order of 4 Å, which corresponds to 1 unit cell. On top of the terrace steps we observe small (diameter 10 to 30 nm) islands and 2 larger (diameter 60 to 80 nm) holes (on the left side of image E). The height of the islands is about 1 unit cell and the holes are 1 unit cell deep. The fact that no structures higher then 1 unit cell are observed shows that a 2 dimensional growth-mode is achieved with these settings. Image F of the sample grown at a laser repetition rate of 1 Hz, shows terrace steps as well. The terrace steps are for a large part covered with islands with a height of one unit cell. The islands on top of the terraces in figure F are laterally larger then the islands in figure E. This can simply be caused by the moment at which the deposition is stopped. If the deposition is stopped in the middle of the growth of an atomic layer, the islands will be larger then if the deposition is stopped when the layer has just finished growing. With both settings we do not observe steps of more then one unit cell so the growth is 2 dimensional. Image D however shows that the film grown with a repetition rate of 5 Hz has a relatively rough surface. The AFM image shows a surface that is covered with islands that have an in plane diameter in the order of 25 nm and a height of about 4 nm. This shows that at a repetition of 5 Hz we no longer have a 2 dimensional growth mode. Instead the growth is best characterized by the island growth mode. All three cross-sectional TEM images show an epitaxial $La_{0.67}Sr_{0.33}MnO_3$ film and a sharp $SrTiO_3$ /$La_{0.67}Sr_{0.33}MnO_3$ interface. In the TEM images we do not see any significant difference in the crystal structure of the three $La_{0.67}Sr_{0.33}MnO_3$ films.

We prefer to use the atomically smooth surfaces achieved at a repetition rate of 1 and 3 Hz over the relatively rough surface that is observed at a repetition rate of 5 Hz. That is because, in this work we want the $La_{0.67}Sr_{0.33}MnO_3$ film to function as base in an MTT. Applied in an MTT, the $La_{0.67}Sr_{0.33}MnO_3$ film should facilitate the growth of the $SrTiO_3$ tunnel barrier. A homogeneous thickness and crystal structure is preferable for a tunnel barrier, as inhomogeneities can cause spots where the tunnel barrier can break down. So in order to grow epitaxial $SrTiO_3$ films with a homogeneous thickness, we will not use a frequency of more then 3 Hz to grow the $La_{0.67}Sr_{0.33}MnO_3$ films.

X-Ray Diffraction (XRD) measurements are performed on a sample on which a 7 nm $La_{0.67}Sr_{0.33}MnO_3$ film is grown with a laser repetition of 3 Hz, an energy density of 1.0 J/cm^2 and an oxygen pressure of 0.3 mbar. Fig-

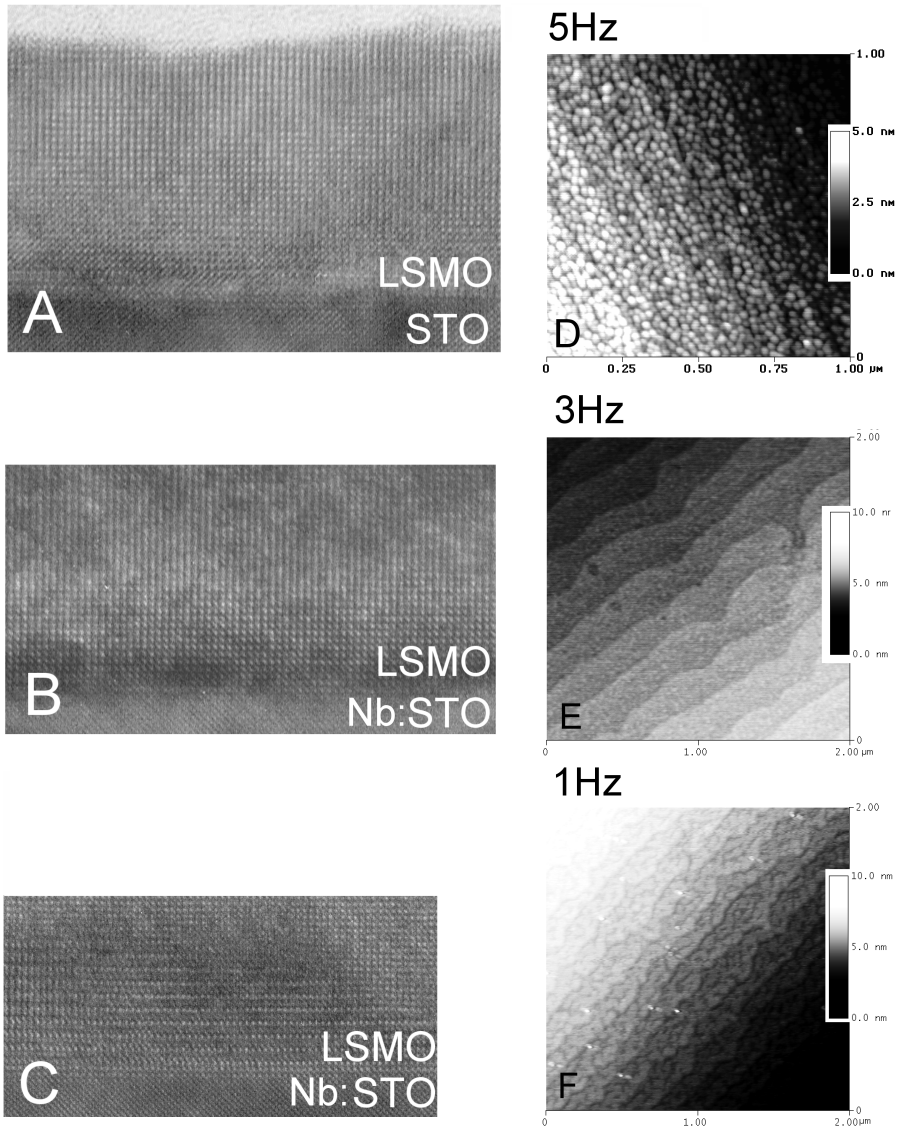

Figure 3.4: *Cross-sectional TEM and AFM images of $La_{0.67}Sr_{0.33}MnO_3$ thin films deposited with a laser repetition rate of 5 (A,D), 3 (B,E) and 1Hz. (C,F) All films are grown at substrate temperature of 750°C, a laser energy density of 1 J/cm^2 and an oxygen deposition pressure of 0.3 mbar.*

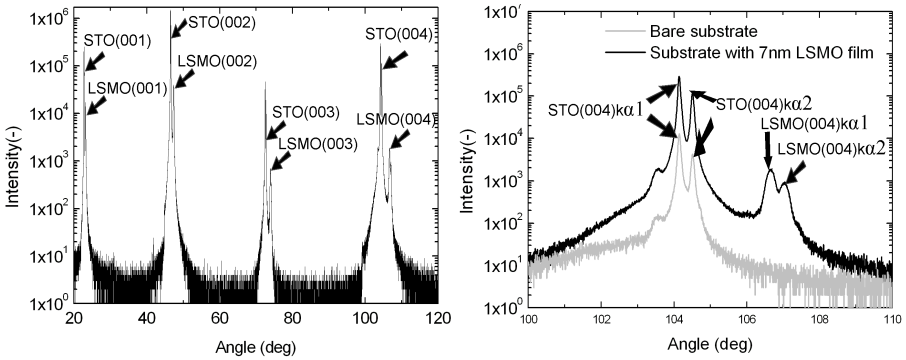

Figure 3.5: *XRD Θ,2Θ measurement of a 7 nm $La_{0.67}Sr_{0.33}MnO_3$ film on a $SrTiO_3$ substrate. The image on the right zooms in on the (004) peak. For comparison this image shows the measurement of a bare substrate as well.*

ure 3.5 shows the XRD measurement of this sample. In the picture on the left side we observe only (00l) peaks of both the substrate and the film. The absence of other peaks shows that no crystal orientations other then (001) are present in the film. The picture on the right zooms in on the (004) peak. For clarity the measurement on a bare $SrTiO_3$ substrate is added. We see that the $La_{0.67}Sr_{0.33}MnO_3$ film adds two extra intensity peaks. These are the Kα1 and Kα2 peaks, formed by diffraction by the two wavelengths (1.5406 resp. 1.5444 Å) in the X-ray beam. From the peaks, an out of plane lattice constant of 3.84 Å is deduced. For bulk $La_{0.67}Sr_{0.33}MnO_3$ the lattice parameter is 3.873 Å, [61] so the out of plane lattice constant reduced compared to bulk $La_{0.67}Sr_{0.33}MnO_3$. If the in plane lattice parameter of the $La_{0.67}Sr_{0.33}MnO_3$ would be the same as in bulk $La_{0.67}Sr_{0.33}MnO_3$, we would observe in the cross-sectional TEM images that due to the 0.8% lattice mismatch the crystal columns of the $La_{0.67}Sr_{0.33}MnO_3$ would become in and out of phase with the crystal columns of the $SrTiO_3$ with a period of 490 nm. In the TEM images we do not observe this. Instead the TEM images show that the crystal structure of the substrate is continued in the film. So we conclude that the in plane lattice parameter is adapted to that of the $SrTiO_3$ substrate. This gives the film a tensile stress. It is a well known effect in stressed films that an increase of the in plane lattice constant decreases the out of plane lattice constant to keep the volume of a unit cell equal to that in the bulk. This is called elastic deformation of the film. Konishi *et al.* have also reported this behavior for $La_{0.6}Sr_{0.4}MnO_3$ films on $SrTiO_3$ substrates.[70] When we calculate the volume of the unit cell in the film, we find 58.6 $Å^3$. Which is very close to the volume of a unit cell in the bulk (58.1 $Å^3$). [70] So we conclude that the films are under tensile stress

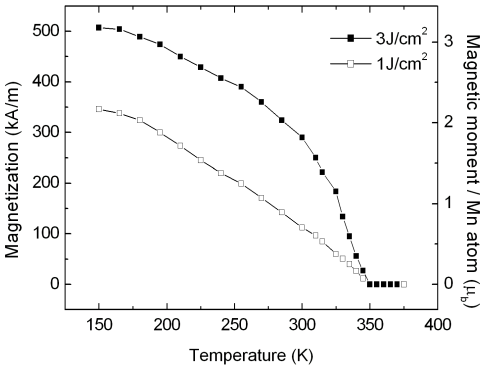

Figure 3.6: *Influence of the laser energy density on the magnetization of $La_{0.67}Sr_{0.33}MnO_3$ thin films. The graph shows the magnetization as function of temperature for films grown at 1.0 and 3.0 J/cm^2. The magnetic moment per Mn atom is shown on the vertical axis on the right side.*

and that this causes elastic deformation of the films.

In literature, laser energy densities ranging from 1 to 3 J/cm^2 are reported for the epitaxial growth of $La_{0.67}Sr_{0.33}MnO_3$. (1 J/cm^2[66], 2 J/cm^2[25, 66, 67], 3 J/cm^2[68, 69]) We study the effect of the laser energy density on the magnetic properties of the $La_{0.67}Sr_{0.33}MnO_3$ thin films. Energy densities of 1.0 and 3.0 J/cm^2 are used to deposit $La_{0.67}Sr_{0.33}MnO_3$ thin films. The saturation magnetization (M_s) is determined by measuring in plane magnetic hysteresis loops by Vibrating Sample Magnetometer (VSM) to determine the saturation magnetic moment (m_s) of the films. Low angle XRD is used to determine the thickness of the films. From these values and the area of the surface of the film, the saturation magnetization is determined. Figure 3.6 shows the magnetization of the films grown with a laser fluence of respectively 1.0 and 3.0 J/cm^2. These films are grown at an oxygen pressure of 0.35 mbar. The curves show the increase of M_s with increase of the laser energy density. The magnetic moment per Mn atom is shown on the vertical axis on the right side. The Curie temperature of the films is 350 K. The value of the magnetization for the sample grown with a laser fluence of 3 J/cm^2 at 150 K is 510 kA/m,which is 50 to 70 kA/m lower than what we find in literature. [25, 66, 71] The shape of the curve for this sample resembles a normal Curie-Weiss law, which is also what we find in literature. For the sample grown at 1 J/cm^2, a lower magnetization is found that decreases almost linear with the temperature. This temperature dependence indicates that different magnetic phases are present in the film.

	LSMO1	LSMO2
Laser frequency	1Hz	1Hz with intervals
Laser fluence	3J/cm^2	1J/cm^2
Oxygen pressure	0.35 mbar	0.3mbar
Substrate temperature	750°C	750°C
Target to substrate distance	40mm	40mm

Figure 3.7: *Deposition parameters for the samples LSMO 1 and LSMO 2. These deposition parameters are used to grow the magnetic tunnel junction discussed in chapter 5*

It is the oxygen content in the $La_{0.67}Sr_{0.33}MnO_3$ that has a strong effect on the double exchange mechanism that governs the ferromagnetic coupling. In Oxygen deficient $La_{0.67}Sr_{0.33}MnO_3$ the double exchange process is suppressed and the magnetization is reduced. [72] We observe an increase of the magnetization when the laser energy density is raised from 1 J/cm^2 to 3 J/cm^2. We believe that the increase of the laser fluence increases the oxygen content in the films. The higher laser fluence gives the particles in the plume a higher energy. This makes them more reactive, and increases the oxidation.

3.5 $La_{0.67}Sr_{0.33}MnO_3$ films with deposition parameters 1

We use two different sets of deposition parameters for the growth of the magnetic tunnel junctions that we describe in chapter 5. Therefore we will present a structural, electronic and magnetic characterization of two samples with $La_{0.67}Sr_{0.33}MnO_3$ films grown with the same set of deposition conditions as used for the junctions in chapter 5. These two sets of parameters are shown in the table in figure 3.7. In this section we discuss sample LSMO 1 in more detail. Figure 3.8 shows the XRD measurements for LSMO 1. From the measurement at low angle (shown in the left panel), we deduce a thickness of 21 nm. The large number of observed X-ray intensity maxima and the weak decay of the oscillations are evidence for a well defined $SrTiO_3$ /$La_{0.67}Sr_{0.33}MnO_3$ interface and a surface with very low roughness. [73] The second graph shows the Θ, 2Θ measurement for higher angle. We observe (00l) peaks of the substrate and the film. The absence of other peaks shows that only the (001) orientation is present in the film. Figure 3.9 shows an AFM image of LSMO 1. The figure shows the terrace steps with a height of one unit cell. This shows the high crystalline quality of the film and confirms the layer by layer growth mode. When the SEM images of the $La_{0.67}Sr_{0.33}MnO_3$ target were discussed in section 3.4, we noticed that a laser energy density of 3 J/cm^2 leaves a relatively

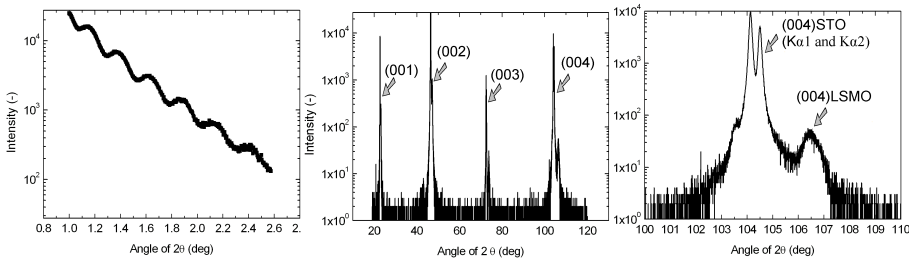

Figure 3.8: *X-ray diffraction measurements for sample LSMO 1. The film is deposited with a laser energy density of 3.0 J/cm^2. The graph of on the left side shows the XRD measurement at low angle from which a film thickness of 21 nm is derived. The second graph shows the XRD measurement for higher angle. The graph on the right zooms in on the (004) peak.*

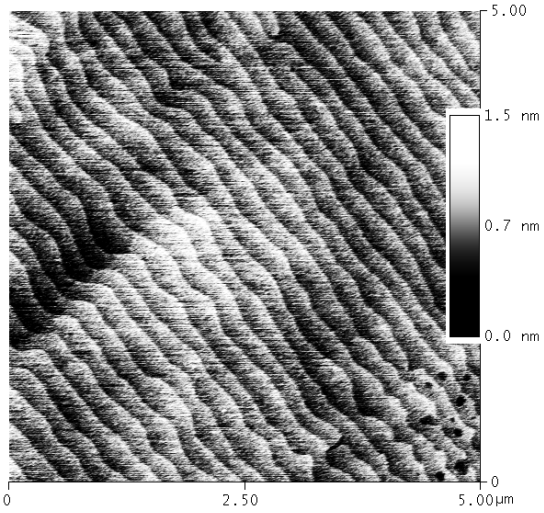

Figure 3.9: *AFM image of sample LSMO 1. The film is deposited with a laser energy density of 3.0 J/cm^2. The thickness of the film is 21 nm.*

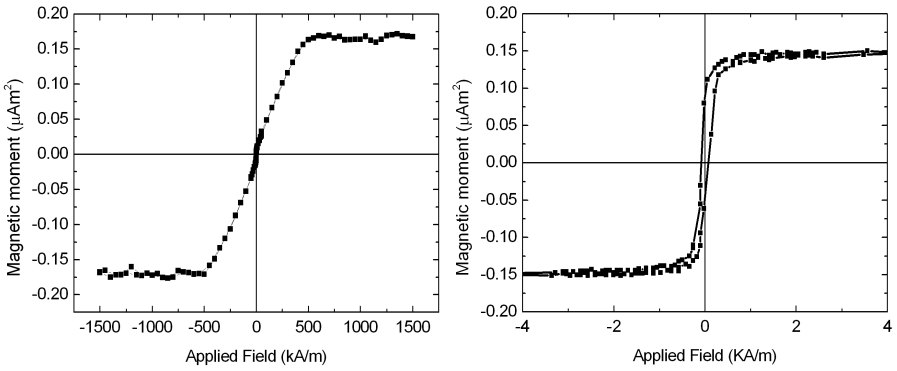

Figure 3.10: *Magnetic hysteresis loops for sample LSMO 1 (21 nm $La_{0.67}Sr_{0.33}MnO_3$ on $SrTiO_3$) at room temperature. The image on the left side shows the out of plane loop. The in plane loop is shown on the right. Note the different field range of both graphs*

rough target surface, which could cause ablation of large particles. However, we do not observe these particles in AFM images of the films. So we conclude that deposition of particles is either absent or negligible.

The saturation magnetization as function of the temperature was already shown in figure 3.6 and discussed in section 3.4. Figure 3.10 shows hysteresis loops measured at room temperature by VSM. The graph on the left shows the out of plane loop. In this measurement the field is applied perpendicular to the film plane. The curve is typical for a magnetic hysteresis loop in the hard direction of a ferromagnetic material. The field that is necessary to saturate the magnetic moment in the direction of this hard axis (the anisotropy field) is 500 kA/m. If the only anisotropy in the film would be caused by the shape of the film (which is a thin film), the anisotropy field would be given by the saturation magnetization of the film. From figure 3.6 however, we can read that the saturation magnetization of this film at room temperature is on the order of 300 kA/m. This shows that besides the shape anisotropy there is another anisotropy that favors an in plane magnetization. In the magnetic hysteresis loop on the right side of figure 3.10, the field is applied in plane. The loop shows sharp switching and the coercivity is about 100 A/m or 8 Oe. From these measurements we conclude that the film has in plane anisotropy, which is only partly caused by the shape. Figure 3.11 shows the resistivity of LSMO 1 as determined by four point measurements. The contacts to the film are realized by ultrasone wirebonding of Al wires. The resistivity is 33% lower then the resistivity that Yu Lu *et al.* report. [25]

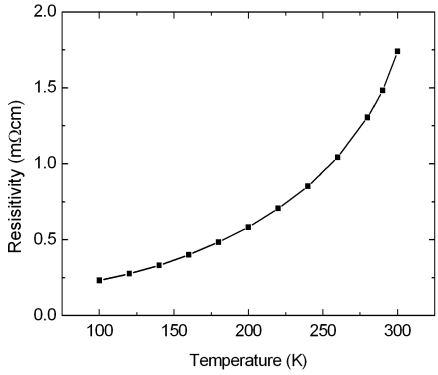

Figure 3.11: *Resistivity of LSMO 1 (21 nm $La_{0.67}Sr_{0.33}MnO_3$ on $SrTiO_3$) determined by four point measurement.*

3.6 $La_{0.67}Sr_{0.33}MnO_3$ films with deposition parameters 2

In chapter 5, a magnetic tunnel junction in which the $La_{0.67}Sr_{0.33}MnO_3$ film is deposited in intervals will be described. Therefore we will characterize a sample here that has a single $La_{0.67}Sr_{0.33}MnO_3$ film grown in the same way. We will name this sample LSMO 2. For the deposition, we use a pressure of 0.3 mbar and a laser energy density of 1 J/cm^2. (See table 3.7) The growth is monitored by RHEED so that we can identify the moment at which a complete monolayer has been deposited. The laser is operated at a repetition rate of 1 Hz. We stop the laser for about 30 seconds each time after deposition of 2 complete monolayers. We anticipate that this interval allows the $La_{0.67}Sr_{0.33}MnO_3$ to absorb oxygen. An example of a RHEED intensity that is recorded during such type of deposition is shown in figure 3.12. Figure 3.13 zooms in on the deposition of the first nine atomic layers. After two oscillations are observed, the laser is stopped for 30 seconds. In these 30 seconds the RHEED intensity increases. This shows that the step edge density at the surface decreases during these 30 seconds and that we should expect the introduced time intervals to have some effect on the growth.

The XRD measurements for LSMO 2 are shown in figure 3.14. The thickness of the film is determined by low angle XRD to be 16 nm. The XRD measurement for higher angles shows only (00l) peaks, which shows that the film is epitaxial.

Figure 3.15 shows an AFM image of the surface of LSMO 2. Again we observe terrace steps with a height of one unit cell, confirming the two dimensional growth mode of the film.

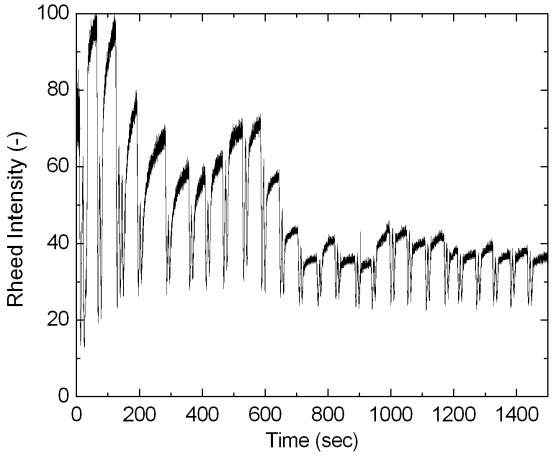

Figure 3.12: *RHEED oscillations recorded during the growth of an $La_{0.67}Sr_{0.33}MnO_3$ film onto a $SrTiO_3$ substrate. The laser energy density is 1 J/cm^2 and the frequency is 1 Hz.*

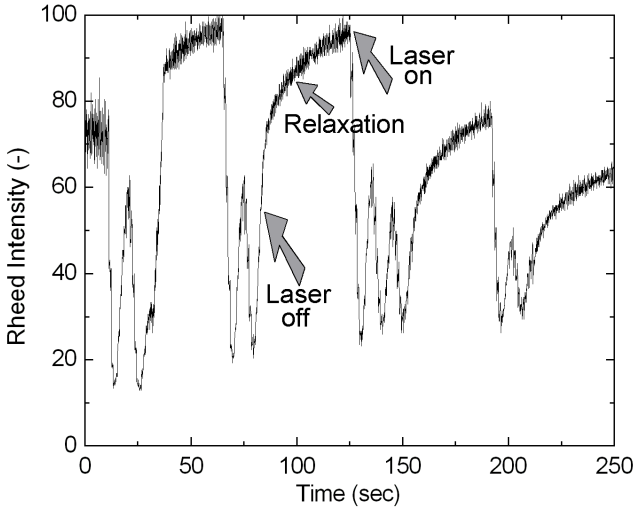

Figure 3.13: *Zoom in on figure 3.12; deposition of the first nine atomic layers. After deposition of two complete atomic layers, the laser is stopped for about 30 seconds. The figure also shows an interval in which three atomic layers are deposited. The arrows indicate when the laser is stopped and started and a 30 second time interval in which the atomic layer relaxes.*

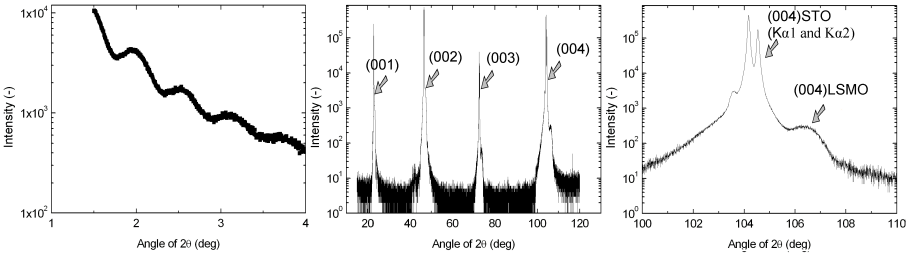

Figure 3.14: *X-ray diffraction for sample LSMO 2 (16 nm $La_{0.67}Sr_{0.33}MnO_3$ on $SrTiO_3$). The film is deposited with a laser energy density of 1.0 J/cm^2. Intervals are introduced during the deposition to allow oxidation of the film. The graph in the left panel shows the XRD measurement at low angle from which a film thickness of 16 nm is derived. The second graph shows the XRD measurement for higher angle. The graph on the right zooms in on the (004) peak.*

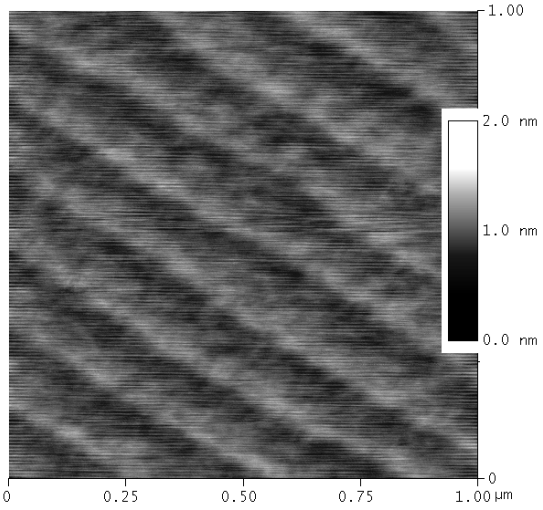

Figure 3.15: *AFM image of the surface of the $La_{0.67}Sr_{0.33}MnO_3$ film of sample LSMO 2 (16 nm $La_{0.67}Sr_{0.33}MnO_3$ on $SrTiO_3$). The film is deposited in intervals to allow relaxation and oxidation.*

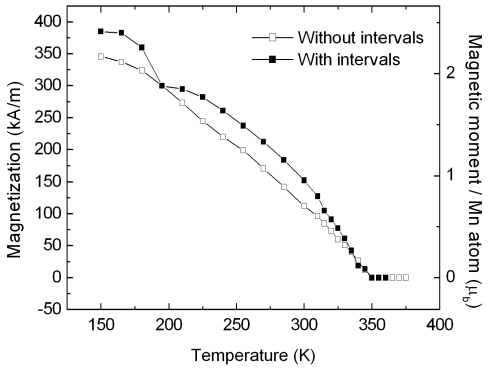

Figure 3.16: *Temperature dependence of the saturation magnetization of the $La_{0.67}Sr_{0.33}MnO_3$ film of sample LSMO 2 (16 nm of $La_{0.67}Sr_{0.33}MnO_3$ on $SrTiO_3$), that is grown in intervals. For comparison the magnetization of a film deposited with the same deposition conditions, but without using intervals is plotted as well. The magnetic moment per Mn atom is shown on the vertical axis on the right side.*

The saturation magnetization of this sample is plotted as function of the temperature in figure 3.16. The magnetic moment per Mn atom (in Bohr magneton), that is shown on the vertical axis on the right side, is calculated, using a unit cell volume of 58.6 $Å^3$. For comparison we also plot the saturation magnetization of a sample that is grown with the same deposition parameters, but without intervals. We can see that the magnetization is increased due to the intervals. We believe that the time intervals allow the film to absorb more oxygen. The in plane hysteresis loop for LSMO 2 is shown in figure 3.17. The coercivity is a 180 A/m or 14 Oe. For both LSMO 1 and LSMO 2, the temperature dependence of the saturation magnetization is plotted in the graph on the left side of figure 3.18. This graph also shows the magnetic moment per Mn atom. LSMO 1 shows a significantly higher magnetization, but for both samples the Curie temperature is 350 K. The curve for LSMO 2 does not resemble a curve that we expect for a homogeneous ferromagnetic film. Again we believe that different phases have formed in this film and that the film contains less oxygen then LSMO 1. So the time intervals that are introduced during the deposition do increase the oxygen content but not as much as the increase of the laser fluence from 1 to 3 J/cm^2 does.

Conductivity and magnetization in $La_{0.67}Sr_{0.33}MnO_3$ are closely related. Zener reports that, the double exchange process that is the mechanism for the conduction also insures the coupling that leads to ferromagnetism.[72] It

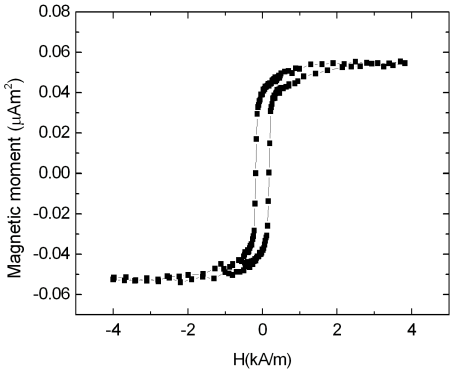

Figure 3.17: *In plane magnetic hysteresis loop of sample LSMO 2 (16 nm of $La_{0.67}Sr_{0.33}MnO_3$ on $SrTiO_3$) measured by VSM at room temperature. The field is applied in the easy axis of the film.*

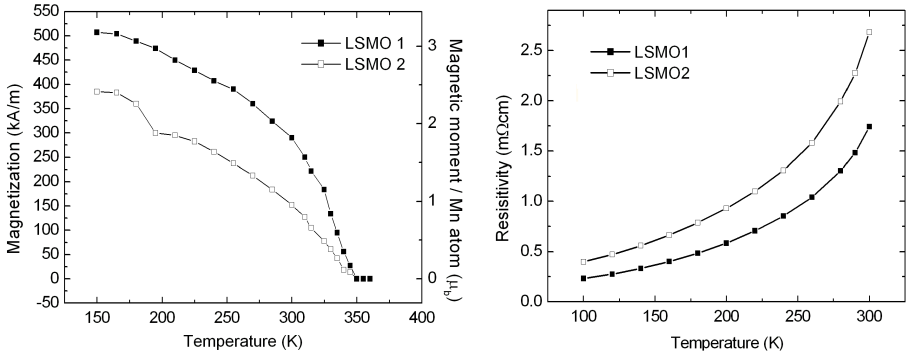

Figure 3.18: *Magnetization (left side) and resistivity (right side) of samples LSMO 1 and LSMO 2 as function of temperature. In the figure of the magnetization, the magnetic moment per Mn atom is shown on the vertical axis on the right side. The magnetization is determined from the saturation magnetic moment that is determined by VSM and the volume of the film. The thickness is determined by low angle XRD.*

is shown that, the lining up of the spins of adjacent incomplete d-shells of the Mn ions will be accompanied by an increase in the migration rate of the Mn4+ ions (the rate at which an electron jumps from a Mn^{3+} across an intervening O^{2-} ion to an adjacent Mn^{4+} ion) and hence an increase of the conductivity. So we expect LSMO 1 to have a lower resistivity then LSMO 2. We measure the resistivity of the samples by a four point measurement. Figure 3.18 shows the resistivity for LSMO 1 and 2 in the graph on the right side. Indeed we observe a lower resistivity for LSMO 1. But the value and the temperature dependence of the resistivity of LSMO 2 is in good agreement to the resistivity that is reported in literature,[25] while the resistivity of LSMO 1 is about 33% lower.

3.7 Conclusions

We have grown $La_{0.67}Sr_{0.33}MnO_3$ thin films onto single crystalline $SrTiO_3$ substrates by pulsed laser deposition. For deposition of the films we use a target to substrate distance of 40 mm, and a substrate temperature of 750°C. Initially we used a laser energy density of 1.0 J/cm^2 and a oxygen deposition pressure of 0.3 mbar. With these settings, the influence of the repetition rate of the laser on the roughness of the films was examined. We found that a repetition rate of 5 Hz results in an island growth and in a relatively rough surface. For repetition rates of 3 and 1 Hz, we find atomically smooth film surfaces, that indicate a 2D growth mode. cross-sectional TEM images of $La_{0.67}Sr_{0.33}MnO_3$ films grown with these settings show an epitaxial crystal structure regardless of the repetition rate. XRD measurements confirm that the films are epitaxial. From the XRD measurements we conclude that the out of plane lattice parameter of the film is lower than for bulk $La_{0.67}Sr_{0.33}MnO_3$. From the cross-sectional TEM images we conclude that the in plane lattice parameters of the film are adapted to the $SrTiO_3$ substrate. From these two observations it is concluded that the films are under tensile stress which causes elastic deformation.

We use high pressure RHEED for in situ growth monitoring. The oscillations that we observe in the RHEED intensity show that a layer by layer growth mode is obtained. As a result, the AFM images show that the films are atomically smooth. Cross sectional TEM images show the high crystalline quality of the films.

However, to achieve the magnetic and electrical properties that are reported in literature, [25, 66, 71] an epitaxial crystalline structure is not sufficient. We find that extra care should be taken to attain a high magnetization. In the films grown with a laser energy of 1.0 J/cm^2 the magnetization is found to be approximately 2/3 of the magnetization reported in literature for $La_{0.67}Sr_{0.33}MnO_3$ thin films. The Curie temperature of 350 K does correspond with the Curie temperature that is reported in literature. The magnetization in these films

decreases almost linearly with the temperature, which indicates that different ferromagnetic phases have formed in the $La_{0.67}Sr_{0.33}MnO_3$ film. Since the coupling of the magnetic moments relates to the oxygen content in the $La_{0.67}Sr_{0.33}MnO_3$ through the double exchange principle, we believe that the films are oxygen deficient. To increase oxygen content in the films, time intervals (in which the deposition is stopped for 30 seconds) are introduced during the deposition of the film each time two atomic layers are deposited. This increases the magnetization of the films. But the increase of the magnetization is even larger when the laser energy density is increased from 1.0 J/cm^2 to 3.0 J/cm^2. It is observed that films with a higher magnetization have a lower resistance. This confirms the calculations by Zener *et al.*, [72] that predict that the coupling of the magnetic moments on the manganese atoms in $La_{0.67}Sr_{0.33}MnO_3$ and the electronic conduction in $La_{0.67}Sr_{0.33}MnO_3$ are both governed by the same principle, the double exchange principle.

The highest magnetization that we measure (510 kA/m at 150 K) is still somewhat lower then reported by Yu Lu *et al.* (580 kA/m at 150 K)[25] or Haghiri-gosnet *et al.*(560 kA/m at 150 K) [66]. We believe that the oxygen content can be increased further by optimization of the deposition parameters.

Chapter 4

$La_{0.67}Sr_{0.33}MnO_3$ / Nb:$SrTiO_3$ epitaxial diodes

In this chapter the preparation and characterization of the epitaxial diodes consisting of the half-metallic ferromagnet $La_{0.67}Sr_{0.33}MnO_3$ and niobium doped $SrTiO_3$ will be discussed. A schematic view of such a diode is shown in figure 4.1. First the niobium doped $SrTiO_3$ substrates of different doping concentrations are electrically characterized. We explain how the diodes are prepared and how the contacts are realized. Then we characterize the diodes electrically. The results are compared to diodes of normal metals on Nb:$SrTiO_3$ that are reported in literature. We present a model that describes the electrical transport through the diode and we will evaluate the applicability of the diodes as collector in a magnetic tunnel transistor. Part of this work has been reported in the journal of applied physics. [74]

4.1 Introduction

The aim of the work described in this thesis is to prepare and study an epitaxial magnetic tunnel transistor with a half-metallic base. The diodes described in this chapter are to be used as a collector in this MTT. Mizushima *et al.* [14] use silicon, whereas Sato *et al.* [16] use gallium-arsenide as collector material in their MTT. These barriers collect hot electrons with energy and momentum selection. This selection makes the collector current extremely sensitive to the spin-dependent scattering in the base which is controlled by the relative orientation of the ferromagnetic layers. So prerequisite for a collector diode, is that the diode functions as an energy filter for electrons. Another demand is that, in order to detect the hot electrons, the reverse biased leakage current has to

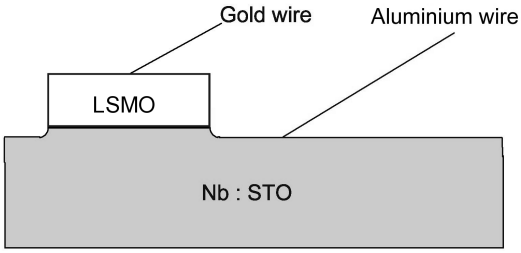

Figure 4.1: *Schematic view of a LSMO/Nb:STO diode. Ohmic contact to the LSMO / Nb:STO is realized by ultrasone wirebonding of gold / aluminium wires.*

be lower than or at least in the same order of magnitude as the collected hot electron current. In a positive estimate of a injected current in the order of a mA and a transfer ratio in the order of 10^{-4} this would mean a maximum leakage current in the order of 10^2 nA.

Whether or not the $La_{0.67}Sr_{0.33}MnO_3$ / Nb:$SrTiO_3$ combination actually results in a Schottky barrier and what Schottky barrier height and leakage current can be expected for such a system was unknown at the start of this work. That's why we need to investigate these diodes and establish the transport mechanism in them.

We want to use the $La_{0.67}Sr_{0.33}MnO_3$ /Nb:$SrTiO_3$ diode as a collector in a MTT, but a junction between a half-metallic ferromagnet and a semiconductor is an interesting one for other reasons as well. Spin injection into a semiconductor is an essential requirement to use the spin of an electron as an operational paradigm for electronic devices. [75, 76, 77] Calculations of Schmidt *et al.*[62] show that contacts of a ferromagnet on a semiconductor are not efficient spin injectors in the diffuse transport regime due to the large conductivity mismatch. In literature two different configurations are reported to show successful spin injection. Both are not in the diffusive transport regime but use the principle of tunneling. Hanbicki *et al.*[78] report on injection by tunneling through a reverse biased Schottky diode contact of a conventional ferromagnetic metal (Fe) on an n-type semiconductor. Motsnyi *et al.*[79] report spin injection by tunneling through a thin Al_2O_3 tunnel barrier inserted between the ferromagnet and the semiconductor. Half-metallic ferromagnets are interesting candidates for spin injection into a semiconductor as well. Schmidt *et al.*[62] suggest that a diode between a semiconductor and a half-metallic ferromagnet can be an efficient way to inject spin polarized electrons into a semiconductor. However, if transport is by tunneling, it will be interface sensitive and we may expect a degradation of the spin injection at higher temperature, much in the same way

as the decay of tunnel magnetoresistance in $La_{0.67}Sr_{0.33}MnO_3$-based magnetic tunnel junctions. [30] It is therefore highly relevant to study transport across interfaces between a half-metallic ferromagnet and a semiconductor and establish the transport mechanism.

In the next section we first describe the Nb-doped $SrTiO_3$ substrates. We have used three different doping concentrations. The conductivity and its dependence on temperature and doping concentration are analyzed and compared to literature. In section 4.3 the preparation of the diodes is described. The structuring into diodes as well as the realization of the contacts is explained. In section 4.4 the diodes are characterized electrically and the Schottky barrier height and the ideality factor are studied. We compare our findings to diodes that consist of Nb:$SrTiO_3$ and a normal metal, that we find in literature. Then the role of the permittivity of the $SrTiO_3$ is discussed. We present a model that explains the behavior of the Schottky barrier height and the ideality factor. In section 4.6 we conclude by evaluating the applicability of the diodes as collector in a MTT.

4.2 Niobium doped $SrTiO_3$ substrates

In this section the properties of the Nb-doped $SrTiO_3$ substrates will be discussed. We use [001] oriented Verneuil-type Nb-doped $SrTiO_3$ single crystal substrates. $SrTiO_3$ is an insulator with a bandgap of 3.3 eV [80]. The $SrTiO_3$ can be doped by replacing Ti atoms with Nb. Ti has 4 electrons in its outer core whereas Nb has 5, so the Nb will act as a shallow donor of 1 electron. This creates states in the bandgap, making the substrates n-type semiconducting. The Nb doping densities used are 0.1 weight percent (Wt%), 0.05 Wt% and 0.01 Wt%. Using the volume of a unit cell and the weight of the atoms, we can calculate that this corresponds to $SrTi_{(1-x)}Nb_xO_3$ with x=0.002, 0.001 and 0.0002, respectively. That means that a doping concentration of 0.1 Wt% corresponds to a doping concentration 0.2 atomic%. The substrates are chemically treated to achieve a TiO_2 termination. A detailed description of this treatment can be found in section 2.4. The 0.01 Wt% doped substrates are annealed at 950°C to reduce the energy in the terrace steps by reducing the length of the terrace steps. An AFM image of such an annealed substrate is shown in figure 4.2 on the left side. The result is an atomically smooth surface just like we observe for the undoped substrates. See figure 2.10. However when the substrates with a niobium doping concentration of 0.05 and 0.1 Wt% are annealed at 950°C the result is different. In the AFM images of these annealed substrates, we observe islands. This is shown on the right side of figure 4.2 for 0.1 Wt% doped substrate. On the surface, islands are observed with an in plane diameter of 15 to 60 nm and a height of up to 8 nm. Compositional analysis of these islands is not performed, but since these islands do not show up in

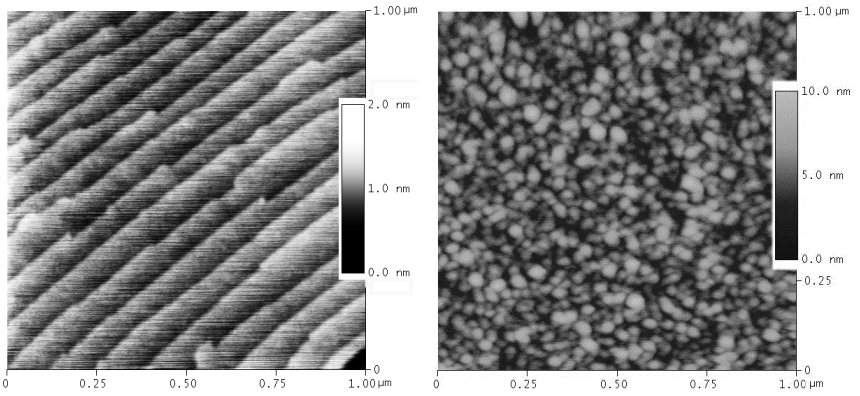

Figure 4.2: *AFM image of the surface of a 0.01 (left) and 0.1 wt % doped substrate (right) that are treated to achieve a TiO_2 termination and annealed for an hour at 950 °C. For the 0.1 Wt% doped substrates, the annealing causes the niobium to diffuse to the surface where it forms islands. For the 0.01 Wt% doped substrates, this is not observed.*

the undoped or in the low doped substrates and Niobium diffusion in $SrTiO_3$ has more often been reported in literature [81], we believe that the islands are formed by diffusion of Nb to the surface. It is obvious that this surface is not suited for epitaxial growth of the $La_{0.67}Sr_{0.33}MnO_3$ film. Therefore it was decided to not anneal the substrates with these doping concentrations. Since the $La_{0.67}Sr_{0.33}MnO_3$ is deposited at 750°C we are interested in whether or not this diffusion is also present at 750°C. To imitate the deposition condition, we annealed a 0.1 Wt % doped substrate at 750°C for an hour and imaged the surface by AFM. The AFM image is shown in figure 4.3. The islands that are observed for the substrates annealed at 950°C are not present in the substrates annealed at 750°C. The image shows the terrace steps at the $SrTiO_3$ surface. These steps have a height of about 3.9 Å, which corresponds to one unitcell. This shows that the surface is terminated by just one of the sublattices. The image also shows that the surface does not relax by decreasing the length of the terrace steps. The surface is basically the same as for a substrate that is not annealed. See figure 2.9.

To determine the resistivity of the substrates, four point measurements are performed. Ohmic contacts to the substrates are made by ultrasone wirebonding of aluminium wires. For all three doping concentrations the temperature dependence of the resistivity is given in figure 4.4. As anticipated, the resistivity decreases with increase of doping concentration. For all doping concentrations the resistivity increases with increase of temperature. For more

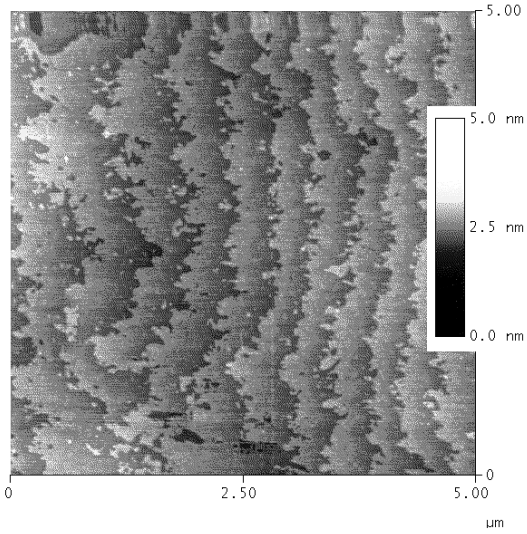

Figure 4.3: *AFM image of the surface of a 0.1 Wt% doped substrate that is treated to achieve a TiO_2 termination and annealed for an hour at 750 °C.*

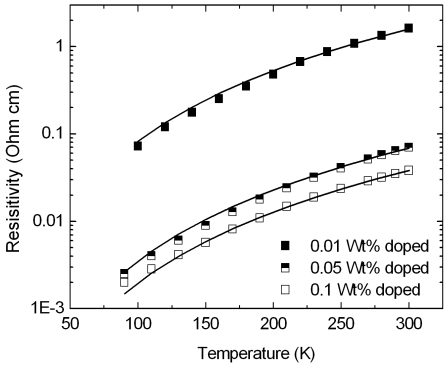

Figure 4.4: *Resistivity of $SrTiO_3$ substrates for Nb doping concentrations of 0.01, 0.05 and 0.1 Wt% as function of the temperature. The symbols represent the measured data points, the curves are a fit to $\rho(T) = \alpha \cdot T^{2.7}$.*

Nb doping concentration	Calculated carrier concentration	χ^2
0.01Wt%	$6.6{\cdot}10^{17} \pm 10^{16}$	$9{\cdot}10^{-4}$
0.05Wt%	$1.54{\cdot}10^{19} \pm 10^{17}$	$2{\cdot}10^{-6}$
0.1Wt%	$2.7{\cdot}10^{19} \pm 10^{18}$	$4{\cdot}10^{-8}$

Figure 4.5: *The resistivity as function of temperature for $SrTiO_3$ substrates with a Nb doping concentrations of 0.01, 0.05 and 0.1 Wt% are fitted to:$\rho(T) = \alpha \cdot T^{2.7}$ The table gives the calculated carrier concentration and the accuracy of the fit χ^2.*

conventional semiconductors like Si and GaAs the resistivity decreases with increasing temperature. In these conventional semiconductors the carrier concentration increases rapidly with increase of temperature. The resistivity of a material relates linearly to this carrier concentration by:

$$\sigma = \frac{1}{\rho} = \mu \cdot n \cdot q \tag{4.1}$$

where σ is the conductance, ρ is the resistivity, μ is the mobility of the carriers, n is the carrier concentration and q is the charge of an electron. So due to the temperature dependence of the carrier concentration, the resistance of Si and GaAs decreases with increase of temperature. For $SrTiO_3$ however a temperature independent carrier concentration is reported. Tufte *et al.* report this for reduced (oxygen deficient) $SrTiO_3$. [82] Shimizu *et al.* report this for Nb doped $SrTiO_3$. [59] Both use Hall measurements to study the conductance of $SrTiO_3$. So in $SrTiO_3$ the carrier concentration is determined by the doping concentration or by the concentration of oxygen deficiencies and therefore independent of temperature. Tufte *et al.* find that above 80 K the mobility is governed by $\mu = 2.9 \cdot 10^7 \cdot T^{-2.7} cm^2/(V \cdot sec)$. Shimizu *et al.* report a behavior that is almost the same. So the temperature dependence of the resistivity of $SrTiO_3$ is governed by the temperature dependence of the mobility of the electrons.

To determine the doping concentration in our substrates from the measured resistivity, we assume a temperature independent carrier concentration as well and a mobility of $2.9 \cdot 10^7 \cdot T^{-2.7} cm^2/(V \cdot sec)$. So we fit the $\rho(T)$ curves by $\rho(T) = \alpha \cdot T^{2.7}$ and from the fitting parameter α we deduce the carrier concentration of the substrates. The fitted curves are shown as black lines in figure 4.4. The calculated carrier concentration and the parameter that gives the accuracy of the fit χ^2 are given in table 4.5. The low value of χ^2 shows that the fitting is accurate and that the temperature dependence of the resistivity is in agreement with a temperature independent carrier concentration and a mobility that scales with $T^{-2.7}$. Now that we have calculated the carrier concentration, we can check whether or not this corresponds to what we expect

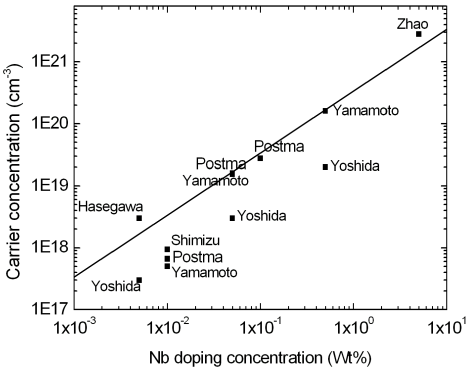

Figure 4.6: *Carrier concentration in Nb doped $SrTiO_3$ found by us and from literature. The line shows the calculated carrier concentration based on the fact that each Nb atom donates one electron. The scattered symbols are the values reported in literature, which are all determined by Hall measurements. The points that are labeled "Postma" are the values that we calculated for our substrates by analysis of the resistivity.*

on basis of the doping concentration. We assume that each Nb atom donates one free electron and we use a unitcell volume of 59.5 $Å^3$ to find the relation between the niobium doping concentration and the carrier concentration. This relation is plotted as a line in figure 4.6 along with our data points (labeled "Postma") and a series of data points that are reported in literature. The data reported in literature (Shimizu *et al.*[59], Yoshida *et al.*[83],Yamamoto *et al.*[84], Zhao *et al.*[85] and Hasegawa *et al.*[86]) are determined by Hall measurements. The carrier concentration that we calculate from the resistivity of the 0.1 Wt% doped substrates is 22% lower then calculated from the doping concentration. For the 0.05 Wt% doped substrates the difference is 8%. For the 0.01 Wt% doped substrates however, we find a factor of 5 difference between the carrier concentration determined from the doping concentration and that determined from the resistivity. The points that we extracted from literature show a wide spread and they also show large differences between the carrier concentration measured by Hall measurements and the carrier concentration calculated from the doping concentration. This large deviation is due to the fact that it is difficult to control the Nb concentration in $SrTiO_3$. For the low (0.01 Wt%) doped substrates, we not only find the doping concentration to deviate from what we expected, we also find that the doping concentration is not homogeneous. We observe that the doping concentrations of these sub-

strates deviates from one substrate to the other as well as in a single substrate. The inhomogeneity shows up in measurements of resistivity, but also in optical inspection there is a clear difference in the transparency of the substrates. Part of the substrates even show insulating behavior. Suppliers of $SrTiO_3$ substrates informed us that they can not guarantee a homogeneous doping concentration for 0.01 Wt% doped $SrTiO_3$. That means that the doping concentration of the 0.01 Wt% doped substrates is actually not well known.

4.3 Preparation of the diodes

We have seen now that the electrical properties of the substrates are governed by the doping concentration and that the substrates with a doping concentration 0.05 Wt% or higher do not allow annealing because of the diffusion of Nb to the surface. The electrical properties of the $La_{0.67}Sr_{0.33}MnO_3$ are influenced by the deposition conditions used to grow the films. To study the effect of these different properties on the diode characteristics we have to use all three doping concentration and two $La_{0.67}Sr_{0.33}MnO_3$ deposition conditions to create different diodes. In both deposition conditions the target to substrate distance is 40 mm, the repetition rate of the laser is 1 Hz and the deposition temperature is 750°C. One condition uses a laser fluence of 1 J/cm^2 and an oxygen pressure of 0.3 mbar and the other a laser fluence of 3 J/cm^2 and an oxygen pressure of 0.35 mbar. The deposition procedure of the $La_{0.67}Sr_{0.33}MnO_3$ is described in chapter 3. To pattern the $La_{0.67}Sr_{0.33}MnO_3$ films into 350 x 700 μm^2 rectangles to realize the structure shown in figure 4.1, standard photo-lithography and ion beam etching are used. The exact ion beam etching conditions are described in appendix A.2.

Electrical contacts from the $La_{0.67}Sr_{0.33}MnO_3$ to a printed circuit board (PCB) are made by ultrasone wire bonding. A problem could arise when this wire pierces through the $La_{0.67}Sr_{0.33}MnO_3$ film and makes ohmic contact to the substrate, thereby creating a shortcut of the diode. To prevent this, gold wires are used. Gold is a soft material that can be bonded using less power compared to bonding of aluminium wires. So using gold instead of aluminium wires decreases the chance of piercing through the $La_{0.67}Sr_{0.33}MnO_3$ during wirebonding. Another reason is that unlike aluminium, gold in contact with the Nb:$SrTiO_3$ will create a Schottky barrier. Shimizu *et al.* report a Schottky barrier height of 1.42 eV for Au/Nb:$SrTiO_3$ diodes. [87] So even when the gold pierces through the $La_{0.67}Sr_{0.33}MnO_3$, if the height of the Schottky barrier that is formed between $La_{0.67}Sr_{0.33}MnO_3$ and Nb:$SrTiO_3$ is lower then the one formed with gold, then the dominant current will flow over the barrier with the $La_{0.67}Sr_{0.33}MnO_3$ and the Au/Nb:$SrTiO_3$ contact will not form a shortcut. Ohmic contacts to the substrate are obtained by ultrasone wire bonding of aluminium wires. This is known to form an ohmic contact in combination with

Nb:$SrTiO_3$. [83, 87] To ensure that the interface that forms the Schottky diode is the $La_{0.67}Sr_{0.33}MnO_3$ /Nb:$SrTiO_3$ interface, we perform measurements to rule out that the Schottky barrier is at a different interface. When there are two aluminium wires bonded to the Nb:$SrTiO_3$ surface, and current flows from one bond through the substrate to the other, we find an ohmic I-V characteristic with a resistance in the order of 100 Ohm. This rules out that the Schottky barrier is at the Al/Nb:$SrTiO_3$ interface. It also confirms that wirebonding of aluminium wires on Nb:$SrTiO_3$ results in an ohmic contact. When two gold wires are bonded to the $La_{0.67}Sr_{0.33}MnO_3$ surface, we also find a low resistant ohmic I-V characteristic. This rules out that the Schottky barrier is formed at the Au/$La_{0.67}Sr_{0.33}MnO_3$ interface.

For the substrates with a doping concentration of 0.05 Wt% a dedicated sample to analyze the diodes was not made, instead the I-V characteristics of these diodes are extracted from samples that are processed to form a magnetic tunnel transistor. That means that the diode is 900 x 200 μm instead of 350 x 700 μm and that contact to the $La_{0.67}Sr_{0.33}MnO_3$ is not by wirebonding directly on the $La_{0.67}Sr_{0.33}MnO_3$. For diode 3 and 4, the contact to the $La_{0.67}Sr_{0.33}MnO_3$ is as follows. On top of the $La_{0.67}Sr_{0.33}MnO_3$ there is an $SrTiO_3$ tunnel barrier on which we have sputtered a Au contact pad that leads to a Cr/Au bond-pad on which an aluminium wire is bonded.

4.4 Electrical characterization of the diodes

In this section the current-voltage (I-V) characteristics of the diodes will be analyzed. Since this combination of materials has not been studied before, we are interested to see whether or not a Schottky barrier is formed. If this is the case, we want to analyze the conduction mechanism in the diodes and determine the height of the Schottky barrier.

Figure 4.7 shows the preparation conditions for the diodes that are analyzed and the I-V characteristics of these diodes for temperatures of 100, 200 and 300 K. On the Y-axis, the absolute value of the current is plotted on a log scale. Negative voltage means that the semiconductor has a negative bias and electrons flow from the Nb:$SrTiO_3$ to the $La_{0.67}Sr_{0.33}MnO_3$. The current voltage characteristics are highly rectifying. For all diodes, the direction of the rectification is in agreement with an n-type semiconductor Schottky diode. The high rectification is consistent with the $SrTiO_3$ being a wide band-gap semiconductor with a band-gap of 3.3 eV. [80] In the forward direction, the curves have a straight part, which shows that the current in this regime depends exponentially on the voltage. At large voltage the current saturates, this is because in this regime, the series resistance of the contacts limits the current.

The I-V characteristics for diode 1 are shown in figure 4.7A. The forward current depends exponentially on the voltage. At a bias of -1 V the current is

	Nb doping concentration	Laser fluence	Oxygen pressure	Substrate temperature	Target to substrate distance
Diode 1	0.01 Wt%	1.0J/cm^2	0.30 mbar	750°C	40 mm.
Diode 2	0.1 Wt%	1.0J/cm^2	0.30 mbar	750°C	40 mm.
Diode 3	0.05 Wt%	1.0J/cm^2	0.30 mbar	750°C	40 mm.
Diode 4	0.05 Wt%	3.0J/cm^2	0.35 mbar	750°C	40 mm.

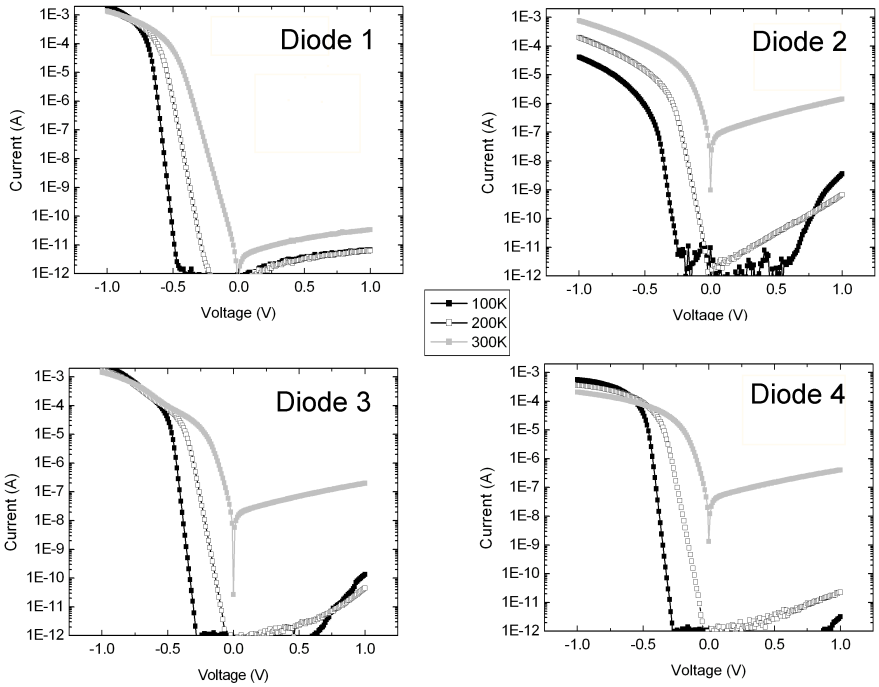

Figure 4.7: *I-V characteristics of the diodes for 100, 200 and 300 K. On the Y-axis the absolute value of the current is plotted on a log scale. Negative voltage means that the semiconductor has a negative bias and electrons flow from the $Nb:SrTiO_3$ to the $La_{0.67}Sr_{0.33}MnO_3$. The table shows the doping concentration of the substrate and the deposition conditions that are used to grow the $La_{0.67}Sr_{0.33}MnO_3$ film.*

limited by a series resistance of approximately 1 kΩ. The reverse bias current at +1 V is of the order of 10^{-11} A and the forward bias current at -1 V is more than seven orders of magnitude larger. Since the series resistance limits the forward current, a lower series resistance would result in a even higher rectification at 1 V. The reverse bias current gradually decreases upon decrease of the temperature.

For diode 2, the forward I-V characteristics (figure 4.7B)show a regime in which the current increases exponentially with the voltage as well, but the series resistance of the contacts limits the current stronger then in diode 1. This series resistance increases with decrease of temperature. An increase of a contact resistance with decreasing temperature can only be expected for the $Au/La_{0.67}Sr_{0.33}MnO_3$ contact because of the decrease of carrier concentration with temperature in $La_{0.67}Sr_{0.33}MnO_3$. So we believe that the high series resistance is caused by a poor contact of the Au wire to the $La_{0.67}Sr_{0.33}MnO_3$. The reverse biased current at +1 V at room temperature is in the order of $1{\cdot}10^{-6}$which is five decades higher than for diode 1. At 200 K the reverse current for diode 2 is decreased to $1{\cdot}10^{-8}$A, but upon cooling further to 100 K the current increases again at large bias.

Figure 4.7C shows the I-V characteristics for diode 3. The series resistance at -1 Volt is in the same order as that in diode 1, but limitation of the current by the series resistance starts at lower voltage and current. This indicates that this series resistance decreases with the applied voltage. This is in agreement with the fact that the contact contains a tunnel barrier. The reverse bias current at +1 V at room temperature is in the order of $1{\cdot}10^{-7}$and drops to $4{\cdot}10^{-11}$at 200 K. At 100 K the reverse current at +1 V has increased to $1{\cdot}10^{-10}$.

The $La_{0.67}Sr_{0.33}MnO_3$ films in diodes 1, 2 and 3 are deposited at 0.3 mbar of oxygen pressure and a laser fluence of 1 J/cm^2. To analyze the influence of the $La_{0.67}Sr_{0.33}MnO_3$ deposition parameters on the diode characteristics, a sample is made with $La_{0.67}Sr_{0.33}MnO_3$ deposited with a laser fluence of 3 J/cm^2 and a deposition pressure of 0.35 mbar (diode 4). The I-V characteristics of this junction are shown in figure 4.7D. The different deposition conditions for the $La_{0.67}Sr_{0.33}MnO_3$ do not cause any significant change in the I-V characteristics for forward bias compared to diode 3, which is on a substrate with the same doping concentration. The reverse current at low temperature however, is much lower then in diodes 2 and 3.

In the introduction of this chapter, the importance of a low reverse current for use of these diodes as collector in a MTT, was already explained. The diodes on the 0.01 Wt% doped substrates (diode1) show an extremely low reverse current, but diode 2, 3 and 4 have a reverse current at +1 V at room temperature that is higher then the estimated demand of $1{\cdot}10^{-7}$A. The reverse current at +1 V for all 4 diodes is plotted as function of temperature in figure 4.8. For diode 1 we see a gradual decrease of reverse current with temperature. For diode 2, the reverse current at +1 V decreases from $1{\cdot}10^{-6}$to $2{\cdot}10^{-10}$A when

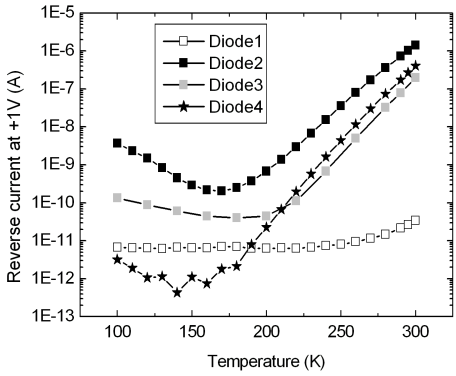

Figure 4.8: *Temperature dependence of the leakage current for the 4 diodes. The graph shows the leakage current as function temperature measured at a reverse bias voltage of +1 V.*

temperature decreases from room temperature to 170 K, but below 170 K the reverse current increases as the temperature decreases and reaches $4{\cdot}10^{-9}$at 100 K. For diode 3 the increase of leakage at +1 V with decrease of temperature is observed below 180 K, while for diode 4, this behavior is observed below 140 K. Above 200 K the reverse current at +1 V increases with increase of the doping concentration. Below 200 K we do not observe this as diode 4 has a lower reverse current then diode 1. In fact we believe that the reverse current at low temperatures is sensitive to the preparation. To explain this we show figure 4.9 of the temperature dependence of the reverse current at +1V of a series of diodes for which the $La_{0.67}Sr_{0.33}MnO_3$ is grown at the same condition as diode 4 (3 J/cm^2/0.35 mbar) and on substrates with the same doping concentration (0.05 Wt%) as diode 4. The figure shows a wide spread in the value for this reverse current at low temperatures. Diode 4 has the lowest reverse current at 1 V at low temperature. Other diodes show reverse currents that are 3 to 7 decades higher. The difference in the preparation between diode 4 and diode 5, 6, 7 and 8 is in the removal of the photoresist after ion beam etching of the diode structure. For all structures this is achieved by ultrasone cleaning in acetone, but for diodes 5, 6, 7 and 8 the substrates are cleaned for 15 minutes in acetone at room temperature, while diode 4 is cleaned for approximately 4 hours in acetone at 50°C. So the reverse current of the diode at low temperature decreases strongly by thorough cleaning after the ion beam etching step that defines the diode structure. The fact that the reverse current at 100 K can be reduced by thorough cleaning, indicates that this reverse current at low temperatures is caused by the presence of removable material at the edge of the

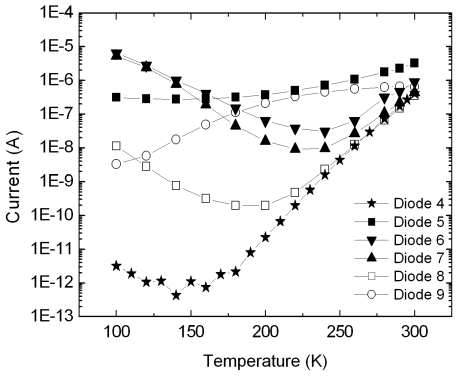

Figure 4.9: *Temperature dependence of the leakage current for a series of diodes that are grown on 0.05 Wt% doped $SrTiO_3$. The graph shows the leakage current as function temperature measured at a reverse bias voltage of 1V. Diode 4 is the same as the diode 4 in figure 4.8*

diode structure. This is likely to be material that is redeposited during the ion beam etching. The reverse current at higher temperatures however does not show this large dependence on the cleaning procedure. The leakage through the redeposited material at the diode edges increases strongly with decrease of temperature. This is not observed for more conventional diodes based on Si or GaAs. It may be caused by the lowering of the barrier at lower temperatures.

To determine whether or not thermionic emission dominates the current in the diodes, we fit the exponential part of the I-V curves for forward bias to the expression for the thermionic emission current density. [88, 89],

$$J = A^* T^2 \exp(\frac{-q\phi_b}{kT})[\exp(\frac{qV}{nKT}) - 1] \tag{4.2}$$

in which ϕ_b is the Schottky barrier height, n is the ideality factor and A^* is the Richardson constant. For $SrTiO_3$ this constant has a value of 156 A $cm^{-2}K^{-2}$. [59] If a good fit is found and this fit gives a ideality factor close to 1, this indicates that the thermionic emission model is an accurate model for describing the current through the diode. In that case, the fit will give the height of the Schottky barrier. If other transport mechanisms like tunneling through the barrier, minority injection (holes travel from the metal to the semiconductor) or recombination in the space charge region play a significant role in the transport, this will increase the value of the ideality factor. [89] Equation 4.2 allows the ideality factor to be calculated from the exponential

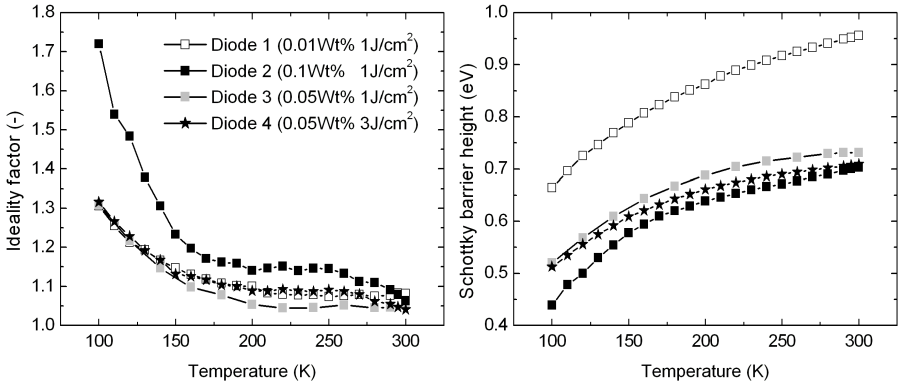

Figure 4.10: *Temperature dependence of the ideality factor and the Schottky barrier height of the diodes. The values are determined by fitting the forward current to the expression for the thermionic emission current density.*

part of the forward I-V curves by:

$$n = \frac{q}{kT}\frac{\delta V}{\delta \ln J} \tag{4.3}$$

The Schottky barrier height and ideality factor that we find in this way for diode 1-4 are shown in figure 4.10. Both the Schottky barrier height and the ideality factor depend significantly on temperature and doping concentration. For the Schottky barrier height of the diodes on the 0.01 Wt% doped substrates we find 0.96 eV at room temperature and 0.66 eV at 100 K. For the diodes on the 0.05 Wt% doped substrates, (diode 3) we find 0.73 eV at room temperature and 0.52 eV at 100 K. For the 0.1 Wt% doped substrates (diode 2) we find a height of 0.70 eV at room temperature and 0.44 eV at 100 K. When the the diodes on the 0.05 Wt% doped substrates with different $La_{0.67}Sr_{0.33}MnO_3$ deposition parameters (diode 3 and 4) are compared, we find only a very small differences. When we compare the height of the Schottky barrier of diodes 1,2 and 3 that have the same $La_{0.67}Sr_{0.33}MnO_3$ deposition conditions, the barrier height shows the trend to decrease with increasing doping concentration. The ideality factors for the diodes on the 0.05 and 0.01 Wt % doped substrates (diode 1, 3 and 4) do not deviate strongly from each other and are lower than 1.1 for temperatures above about 160 K. This shows that thermionic emission is an accurate model to describe the forward current in these diodes in this temperature regime. The ideality factor of diode 2 on the 0.1 Wt% doped substrate is significantly larger then in diodes 1, 3 and 4. With decrease of temperature the ideality factors show an increase and below about 160 K the

ideality factor becomes significantly larger then 1 which shows that the I-V characteristics deviate from the thermionic emission model.

4.5 Discussion

We find that the ideality factor and the Schottky barrier height of the diodes depend strongly on the temperature and on the doping concentration. This temperature dependence deviates significantly from what is reported for Si based Schottky diodes. Several groups have studied the dependence of the barrier height of Si based diodes and in no case was there any clear evidence of such a large variation of the barrier height with the doping concentration. [90, 91] The temperature dependence of the Schottky barrier height is either reported to absent or an order smaller than what we find. This temperature dependence is attributed to the temperature dependence of the energy gap in the semiconductor [92]and is therefore not only smaller but also of opposite sign (-3·10^{-4}eV/K) [93, 94] than what we find.

For $SrTiO_3$ a relative permittivity is reported that varies strongly with temperature. [95] The relative permittivity is reported to vary in an applied electric field as well.[96] For Si this not the case, so we expect that this is the cause of the temperature dependence of the Schottky barrier height.

Neville *et al.*[95] reported that the relative permittivity of $SrTiO_3$ can be characterized by the following Curie-Weiss law:

$$\varepsilon(T) = \frac{A}{T - T_c}\epsilon_0 \tag{4.4}$$

in which A=8.9·10^4K and T_c=30 K. This gives a relative permittivity for $SrTiO_3$ of about 300 at 300 K and 1160 at 100 K. How would this effect the Schottky barrier properties? The width of the Schottky barrier is given by:

$$W_s(T) = \sqrt{\frac{2\varepsilon_s(T)}{qN_d}(V_{bi}(T) - V - \frac{kT}{q})} \tag{4.5}$$

in which V_{bi} is the built in potential. So if all other parameters are constant, a permittivity that increases with decreasing temperature would cause the width of the depletion area to increase for decreasing T. A wider depletion area would decrease the tunneling probability through the barrier. Thermionic emission would dominate even stronger and this would give an ideality factor closer to one for low temperatures. Since this is not what we observe, the temperature dependence of the permittivity does not explain the observed behavior.

An increase of the ideality factor and a decrease of the Schottky barrier height with decreasing temperature are found in other diodes on Nb:$SrTiO_3$ as well. Shimizu *et al.*[59] report on diodes of Cu or Au on niobium doped $SrTiO_3$.

It is found that the capacitance of the diodes increases with decreasing temperature, in correspondence with an increase of the relative permittivity and the barrier width. This increase of the width of the Schottky barrier however, should result in a lower ideality factor and a larger effective Schottky barrier height. But the I-V characteristics of the diodes show, just like in our measurements, a Schottky barrier height that decreases and an ideality factor that increases towards lower temperature. Since the ideality factor is estimated by equation 4.3, the fact that the ideality factor is larger than 1 can be caused by a voltage dependent Schottky barrier height. When the applied voltage causes a reduction of the Schottky barrier height, the applied voltage will cause an increase in $\delta V/\delta \ln J$ and thus a higher ideality factor. Shimizu confirmed the voltage dependence of the Schottky barrier height by photo-electric measurements. In this technique the metal in contact with the semiconductor is irradiated by photons. When the energy of the photons exceeds the height of the Schottky barrier, electrons will have sufficient energy to cross the barrier and a photocurrent is created. [97] It is found that this threshold energy decreases when the applied reverse bias voltage is increased. This shows that the Schottky barrier height is voltage dependent. Computer simulations explain these phenomena only when an intrinsic low permittivity (ILP) layer is assumed to be present at the surface of the $SrTiO_3$. The computer simulations use a model in which a tunneling probability of one is assumed for this layer. The result is that the ILP layer absorbs part of the potential drop across the diode. Since the electrons can tunnel through this ILP layer, this lowers the effective Schottky barrier height and makes the height voltage dependent. The ratio of the thickness and the permittivity of the layer δ_i/ε_i is a fitting factor in the simulations. A value of 10.4 Vm^2C^{-1} is found for δ_i/ε_i. When ε_0 is taken for ε_i, the thickness of this ILP layer is in the order of an Å. Since ε_0 is a minimum value for ε_i, 1 Å is a minimum value for δ_i. The temperature and doping concentration dependence of the ideality factor and the Schottky barrier height that we find can also be explained qualitatively using the assumption of the intrinsic low permittivity layer. To elucidate the temperature dependence we show the energy diagrams of the Schottky barrier for 100 and 300 K in figure 4.11. The higher permittivity of the $SrTiO_3$ at 100 K compared to 300 K causes a larger part of the flat-band voltage to drop over the intrinsic low permittivity layer. This results in a lowering of the effective Schottky barrier height and it makes the Schottky barrier height depend stronger on the applied voltage, which causes the higher ideality factor. The effect of a higher doping concentration is the narrowing of the depletion area, which also causes a larger part of the flat-band voltage to drop over the ILP layer. Again this lowers the effective Schottky barrier height and increases its voltage dependence and the ideality factor.

Now that we found a model to describe the behavior of the Schottky barrier, we can evaluate the applicability of the diodes as collector in a magnetic tunnel

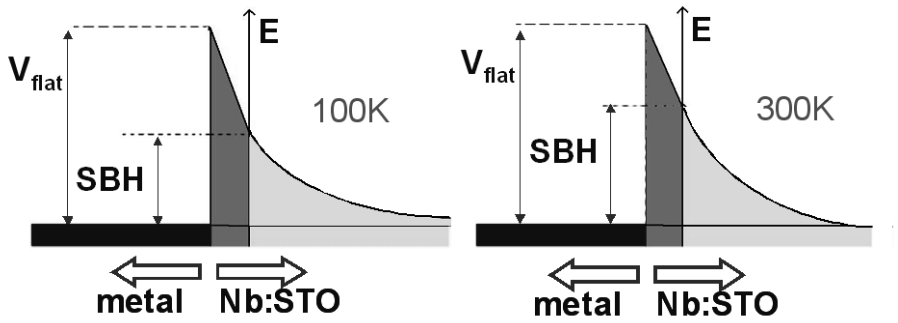

Figure 4.11: *Energy diagram of the Schottky barrier for 100 K (left) and 300 K (right). A part of the flatband voltage that drops over an intrinsic low permittivity (ILP) layer. Electrons can tunnel through this layer so that the effective Schottky barrier height is decreased. The voltage that drops over the ILP layer depends on the relative permittivity and the carrier concentration in the Nb:SrTiO$_3$.*

transistor structure. For the intrinsic low permittivity layer a value for δ_i/ε_i is found by simulations. This provides us with a minimum value in the order of 1 Å for the thickness of this layer. In forward bias the electrons tunnel through this layer, with a tunneling probability of 1. So the layer will not be much thicker then 1 nm. Unfortunately we do not know what the transmittance of this layer for hot electrons is, when the diode is applied as collector in an MTT. To evaluate the applicability of the diodes as collector in an MTT, we discuss two extreme cases. In the first case the ILP layer does not form a reflecting barrier for hot electrons and electrons with an energy higher then the effective Schottky barrier height will be collected. In that case the Schottky barrier can be used as collector in an MTT and the treshold of the energy filter can be tuned by the temperature and the doping concentration. In the second case the ILP layer is thicker and reflects hot electrons with an energy lower than the flatband voltage, regardless of temperature and doping concentration. Also in this case the diodes are applicable as collector in a MTT.

4.6 Conclusions

In conclusion, we have fabricated high-quality epitaxial Schottky diodes of a half-metallic ferromagnet ($La_{0.67}Sr_{0.33}MnO_3$) on semiconducting Nb:$SrTiO_3$ substrates of different doping densities. Electrical transport across the interface is dominated by thermionic emission. The diodes are highly rectifying and have a low reverse bias current. The effective Schottky barrier height decreases

as the doping concentration in the $SrTiO_3$ is increased. A decrease in temperature decreases the height of the Schottky barrier as well. The temperature dependence of the Schottky barrier height and the ideality factor are explained by an intrinsic low permittivity layer in the $SrTiO_3$ at the interface with the $La_{0.67}Sr_{0.33}MnO_3$. We do not know how strong this layer will reflect hot electrons when it is used as collector in a magnetic tunnel transistor, but in both extreme cases of a completely transparent and a completely reflecting layer, the diode can be used as collector in a magnetic tunnel transistor.

Chapter 5

$La_{0.67}Sr_{0.33}MnO_3$ /$SrTiO_3$ /Co magnetic tunnel junctions.

The top-layers of the magnetic tunnel transistor form a $La_{0.67}Sr_{0.33}MnO_3$ / $SrTiO_3$ / Co magnetic tunnel junction (MTJ). These junctions will be discussed in this section. The deposition of the $La_{0.67}Sr_{0.33}MnO_3$ was discussed in chapter 3, so we will start by describing the deposition of the $SrTiO_3$ tunnel barrier followed by its structural characterization. Then we focus on the cobalt thin film. Again the deposition is described and the structural and magnetic properties are analyzed. We will describe the processing steps that are performed to structure the stack into magnetic tunnel junctions that can be electrically characterized in a 4-point configuration. We report the temperature and voltage dependence of the tunnel magneto resistance (TMR) and the resistance for two different structures. The results are compared to what has been reported in literature for similar junctions.

5.1 Introduction

Since the mid 1990's magnetic tunnel junctions are extensively studied. The reproducible large TMR at room temperature reported by Moodera *et al.*[98] formed a breakthrough in the field of magnetic tunnel junctions. Magnetic tunnel junctions are interesting for study of the physics of spin dependent electron tunneling and for their application in the information storage as memory element in a magnetic random access memory (MRAM) or as magnetic field sensor. The relative change in the resistance that is induced by an applied magnetic field (TMR) depends strongly on the spin polarization of the electrodes. Therefore half-metallic ferromagnets like $La_{0.67}Sr_{0.33}MnO_3$ are promising can-

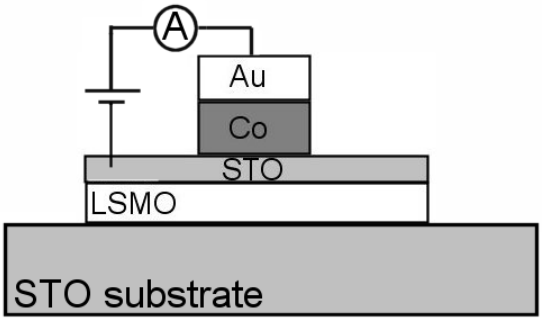

Figure 5.1: *Schematic view of the magnetic tunnel junctions.*

didates for the electrode material. A short overview on $La_{0.67}Sr_{0.33}MnO_3$ based MTJ's was given in section 1.2 of chapter 1. Despite the Curie temperature of 360 K,[31] the TMR of these junctions is diminished at room temperature due to the reduced spin polarization at the $La_{0.67}Sr_{0.33}MnO_3$ / $SrTiO_3$ interface. The function of these junctions in the magnetic tunnel transistor is to inject a spin polarized hot electron current into the $La_{0.67}Sr_{0.33}MnO_3$ base. Therefore Co is chosen as emitter electrode because we anticipate that Co will still have a reasonable tunnel spin polarization at room temperature. De Teresa *et al.* report a tunnel spin polarization of 25% for Co in combination with $SrTiO_3$ at 5 K. [37] Because of the high Curie temperature of cobalt (1112 to 1145 °C [99]), this shouldn't decrease drastically at room temperature. A schematic view of the magnetic tunnel junctions that are discussed in this chapter is given in figure 5.1. $SrTiO_3$ substrates are used to facilitate the epitaxial growth of the $La_{0.67}Sr_{0.33}MnO_3$ electrode. The tunnel barrier itself consists of $SrTiO_3$ and the top electrode is cobalt. A gold cap layer prevents the cobalt from oxidizing.

In section 5.2 the preparation and characterization of the $SrTiO_3$ tunnel barrier will be discussed. We will present the deposition conditions that we use to grow the $SrTiO_3$ epitaxially on the $La_{0.67}Sr_{0.33}MnO_3$ bottom electrode and the structural analysis performed by cross sectional Transmission Electron Microscopy (TEM). In section 5.3, the deposition of the cobalt electrode is described and the Co films are analyzed structurally and magnetically. Section 5.4 describes the processing steps that are applied to create the desired structure. In section 5.5, the magnetic tunnel junctions will be electrically characterized with a focus on the magnetic field dependence.

5.2 Preparation and characterization of the epitaxial $SrTiO_3$ tunnel barrier

Due to the small lattice mismatch, the $SrTiO_3$ tunnel barrier can be grown epitaxially on the $La_{0.67}Sr_{0.33}MnO_3$ electrode. The advantage of an epitaxial tunnel barrier is the high degree of order in epitaxial films. A perfect epitaxial tunnel barrier will not have any pinholes and a low defect density. We now describe how the stack of films is grown. Before loading, the targets are polished with sandpaper to remove tracks formed by the previous deposition run. Both the $La_{0.67}Sr_{0.33}MnO_3$ and the $SrTiO_3$ targets are loaded into the vacuum system. The $SrTiO_3$ substrates that we use are Nb doped, so that they can function as a Magnetic Tunnel Transistor (MTT) as well. These substrates are treated in the way described in section 2.4 to achieve a TiO_2 termination. The substrates are not annealed. The substrate is loaded through a loadlock and its temperature is raised to 750°C. Then we let the oxygen in and the $La_{0.67}Sr_{0.33}MnO_3$ is deposited as described in chapter 3. After the growth of the $La_{0.67}Sr_{0.33}MnO_3$ film, the temperature is kept constant at 750°C and the oxygen pressure is controlled to 0.3 or 0.4 mbar for deposition of the $SrTiO_3$ tunnel barrier. The KrF excimer laser is focused by a lens to obtain an energy density of 1.0 J/cm^2 at the $SrTiO_3$ target. The target to substrate distance is 40 mm. The $SrTiO_3$ target is poly crystalline and has a purity of at least 99.999 percent. It is in fact a poly crystalline part of the boule from which single crystalline substrates are cut. The crystallinity ensures a very high density of the target and therefore ablation without particulates. Before deposition, the $SrTiO_3$ target is pre-ablated for 2 minutes at 3 Hz. For the deposition the lowest repetition rate of 1 Hz is used to ablate the target. This is in order to give the deposited material more time to order itself in the crystal lattice as found in chapter 3 for $La_{0.67}Sr_{0.33}MnO_3$. We use Reflective High Energy Electron Diffraction (RHEED) to determine the deposition rate of the $SrTiO_3$. Figure 5.2 shows the RHEED oscillations that are recorded during the deposition of the $SrTiO_3$ tunnel barrier, grown at an oxygen pressure of 0.3 mbar, a laser fluence of 1.0 J/cm^2 and a target to substrate distance of 40 mm. The picture on the right zooms in on oscillations during the deposition of the first six atomic layers on top the $La_{0.67}Sr_{0.33}MnO_3$. At t=0, the deposition is started. The intensity shows oscillations with a period of 4 seconds. We observe 7 oscillations and the maximum of the 7^{th} oscillations is at t=28 sec. So a complete atomic layer of $SrTiO_3$ is grown every 4 seconds or every 4 laser pulses. This allows determination of the film thickness and the deposition rate (i.e. 1 Å/pulse) during the growth. At t=37 seconds, the intensity of the electron beam was manually increased. The laser is stopped at t=48 sec, from which we estimate a thickness of 12 atomic layers or 4.7 nm. The sharp changes in the intensity (one is indicated by the arrow in the figure on the right side) correspond to

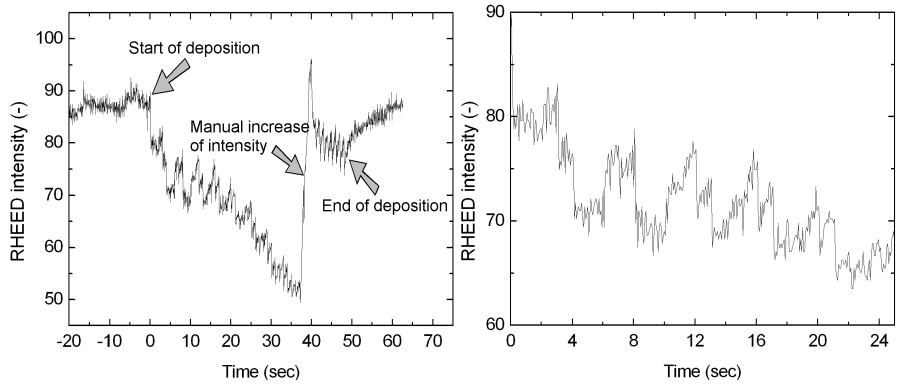

Figure 5.2: *RHEED oscillations, recorded during the deposition of $SrTiO_3$ onto $La_{0.67}Sr_{0.33}MnO_3$. The figure on the right zooms in on the deposition of the first six atomic layers. The arrows indicate the start and the end of the deposition and the moment at which the intensity of the incoming electron beam was manually increased.*

the material being deposited shortly after a laser pulse. After depositing the perovskites, the oxygen pressure is raised to 1 bar and the substrate is cooled down at a rate of 10 degrees per minute.

From this sample, cross-sectional transmission electron microscope (TEM) images are made to characterize the barrier structurally. Figure 5.3 shows the cross-sectional TEM image of this $SrTiO_3$ tunnel barrier. The $SrTiO_3$ is epitaxial and the interface with the $La_{0.67}Sr_{0.33}MnO_3$ film is sharp and abrupt. We do not observe stacking faults or pinholes. The $SrTiO_3$ barrier is about twelve atomic layers thick, which corresponds to what we expect from the RHEED oscillations. This makes the RHEED an accurate tool to estimate the film thickness during the deposition. Pailloux *et al.* simulated cross-sectional TEM images for the $SrTiO_3$ /$La_{0.67}Sr_{0.33}MnO_3$ interface and found that for a certain TEM setting, both the SrO and the TiO_2 planes of the $SrTiO_3$ are projected in the image, while for the $La_{0.67}Sr_{0.33}MnO_3$ film the MnO_2 planes are projected clearly while the projection of the $La_{0.67}Sr_{0.33}O$ planes is suppressed. Figure 5.4 shows a simulation of a cross-sectional TEM image obtained by Pailloux *et al.* This corresponds to what we observe in our cross-sectional TEM image as well. The spacing between the imaged lattice planes in the $La_{0.67}Sr_{0.33}MnO_3$ is twice the spacing between the $SrTiO_3$ planes, because the $La_{0.67}Sr_{0.33}O$ columns do not show up in the image. The difference in brightness between the SrO and the TiO_2 planes in our image is very small and does not allow discrimination between them on basis of their brightness. However the most stable configuration of the $La_{0.67}Sr_{0.33}MnO_3$ /$SrTiO_3$ interface is when the TiO_2 column

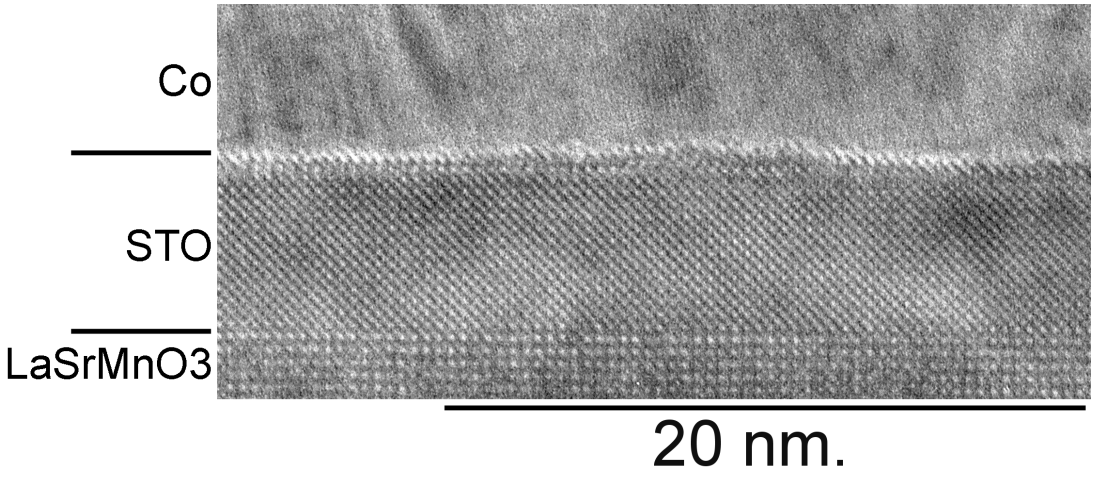

Figure 5.3: *Bright field cross-sectional TEM image of the* $La_{0.67}Sr_{0.33}MnO_3$ */*$SrTiO_3$ */Co magnetic tunnel junction.*

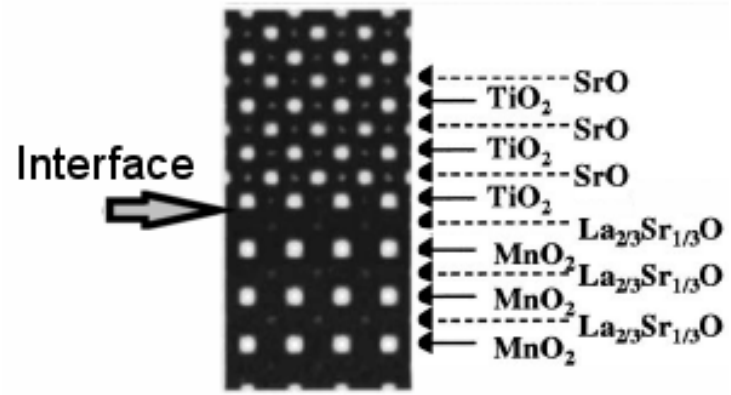

Figure 5.4: *Multislice contrast simulation of a* $SrTiO_3$ */*$La_{0.67}Sr_{0.33}MnO_3$ *interface by Pailloux* et al. *[41]*

is on top of the MnO_2 column. That means that the lattice column in the $SrTiO_3$ that is directly on top of the MnO_2 column has to be the TiO_2 column. Knowing which plane is which in the $SrTiO_3$ film, we can try to determine the termination of the $SrTiO_3$ on the Co side. Unfortunately the image is not clear enough at the Co/$SrTiO_3$ interface to draw conclusions about the termination. The interface will be discussed in more detail on page 93.

Electrical characterization of the $SrTiO_3$ barrier is included in section 5.5, where the magnetic tunnel junctions are characterized.

5.3 Preparation and characterization of the cobalt electrode

In order to inject spin polarized electrons over the tunnel barrier, we use Co as a magnetic emitter. In this section we describe how the Co thin film is deposited onto the $SrTiO_3$ tunnel barrier and we characterize a Co thin film grown on an $SrTiO_3$ substrate magnetically. After deposition of the $SrTiO_3$ tunnel barrier the sample is cooled down at an oxygen pressure of 1 bar. When the sample has reached room temperature, the vacuum chamber is pumped down to $1{\cdot}10^{-7}$mbar. The $La_{0.67}Sr_{0.33}MnO_3$ and $SrTiO_3$ target are unloaded and the cobalt and gold target are polished and loaded. Unlike De Teresa et.al., Sun et.al. and Hayakawa et.al. [35, 38, 43]we use PLD instead of Molecular Beam Epitaxy (MBE) or sputtering to deposit the Co electrode and the Au cap-layer. Since there was no possibility for evaporation in the same system, PLD was the only way to deposit Co on the $SrTiO_3$ tunnel barrier without exposing the sample to air, during a transfer of the sample to another system. Transport of the sample from one vacuum system to the other has to be avoided because a clean Co/$SrTiO_3$ interface is very important in both the MTJ and the MTT. The cobalt film is deposited at room temperature and a base pressure of $1{\cdot}10^{-7}$mbar. During the deposition the pressure rises to $1{\cdot}10^{-6}$mbar. The energy density of the ablating laser-spot is 6.0 J/cm^2 per pulse. The laser is operated at a repetition rate of 5 hz.

To investigate the properties of the cobalt film, a film is grown on an $SrTiO_3$ substrate. The film is grown by depositing for 30 minutes at a laser repetition rate of 5 Hz. The thickness of the film is determined by low angle X-ray diffraction. This measurement is shown in figure 5.5. The figure shows the intensity of the reflected beam as a function of the angle 2Θ. The oscillations in 2Θ have a period of $0.15 \pm 0.01^\circ$ from which a thickness of 59 ± 1 nm and a deposition rate of 0.07 Å/pulse is deduced. Figure 5.6 shows the magnetic hysteresis loops measured by vibrating sample magnetometer (VSM) at room temperature for in plane configuration. In the picture on the right, the field scale is reduced. The easy axis of magnetization is in plane. The coercivity of the Co film as measured in plane is 13 Oe, but it takes a field of 5 kOe to fully saturate the film in the in plane direction. The magnetic moment of the Co film

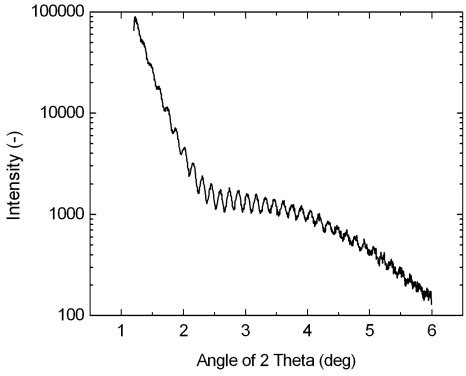

Figure 5.5: *Low angle X-ray diffraction of 59 nm cobalt film on $SrTiO_3$.*

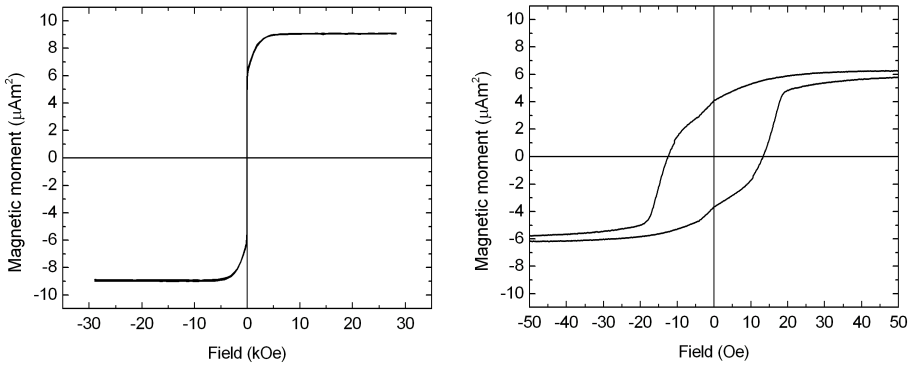

Figure 5.6: *Magnetic hysteresis loop of a 59 nm cobalt film on $SrTiO_3$, measured by VSM. The field is applied in plane. The graph on the right is the same data as the graph on the left, but it has a smaller scale for the applied field.*

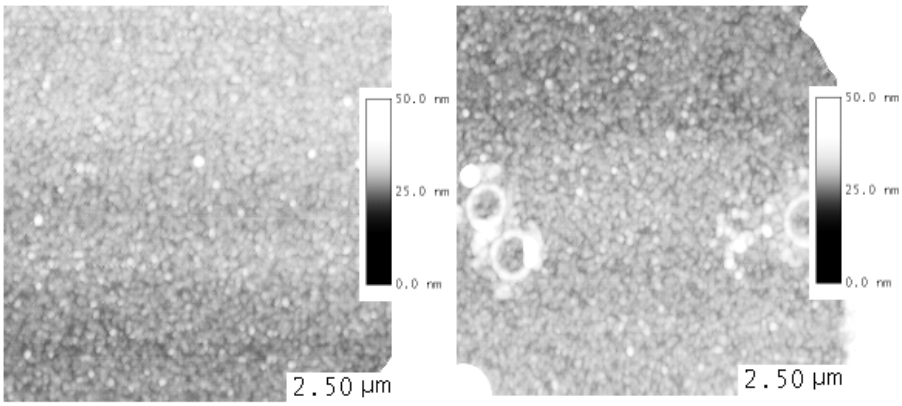

Figure 5.7: *AFM images of a cobalt film grown on $SrTiO_3$ by PLD. Most of the surface surface looks like the image on the right. The image on the right shows a part where we observe crater-like structures that are formed due to the ablation of droplets from the target.*

saturates at 9.0 μAm^2. The volume of this film is 1 $cm^2 \cdot 59nm = 5.9 \cdot 10^{-12} m^3$, so we can calculate a magnetization for the cobalt of $1.5 \cdot 10^2$kA/m. This is close to the magnetization of Co at 300 K of $1.42 \cdot 10^2$kA/m [100]. We use Atomic Force Microscopy (AFM) to examine the surface of the Co film. Figure 5.7 shows two AFM images of the surface of the Co film. Most of the surface of the Co film looks like in the picture on the left. The surface shows islands with a height of 2 to 3 nm and a diameter of about 9 nm. Parts of the surface show crater-like structures. These structures are shown in the picture on the right side. This effect is due to Co droplets that arrive on the surface. Droplet formation is a well known phenomenon in pulsed laser deposition of metal films, that is difficult to prevent.

Cross-sectional TEM allows structural characterization of the Co film. Figure 5.8 shows a cross-sectional TEM image of the complete stack of films that we use to fabricate the MTT. Figure 5.9 shows a dark field cross-sectional TEM image of the same sample, taken at a different position. The Co film shown in these cross-sectional TEM images is grown in 5 minutes at a laser repetition rate of 5 Hz. Grains with different orientations of the Co lattice planes can be seen in both images. This shows the poly-crystalline nature of the Co film. From the cross-sectional TEM image we can deduce a thickness of $15 \pm 1nm$ for the Co film. From this thickness, we can deduce a deposition rate of 0.10 Å/pulse. The difference compared to the deposition rate determined from the single Co film is 30% which is quite large. This does not cause a serious problem, as the thickness of the Co is not a very critical parameter for

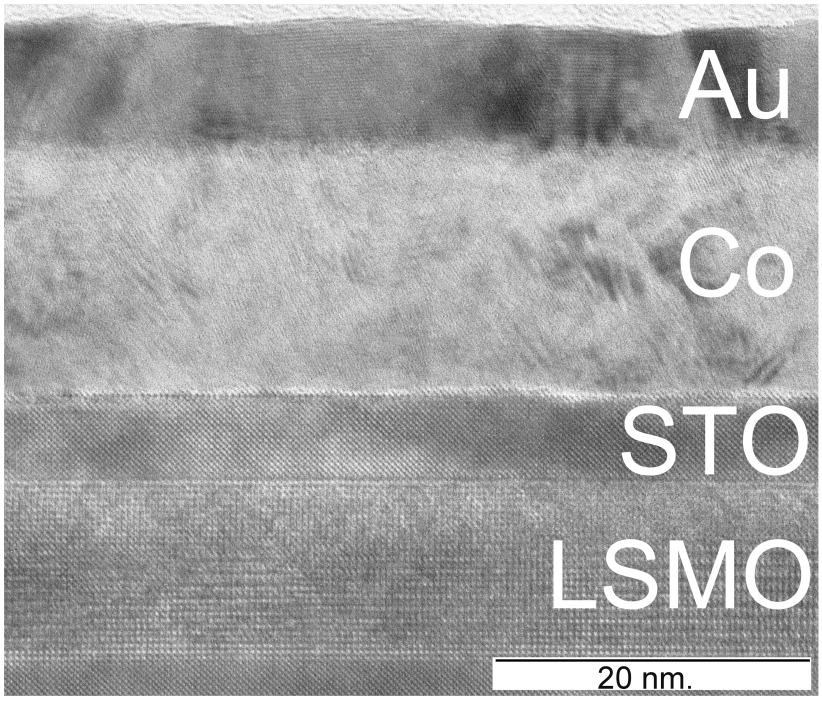

Figure 5.8: *Cross-sectional TEM image of the* $La_{0.67}Sr_{0.33}MnO_3$ */*$SrTiO_3$ */Co/Au stack grown by PLD on 0.05 Wt% Nb-doped* $SrTiO_3$*. Both the Co and Au are grown with laser fluence of 6.0* J/cm^2 *and a laser repetition rate of 5Hz.*

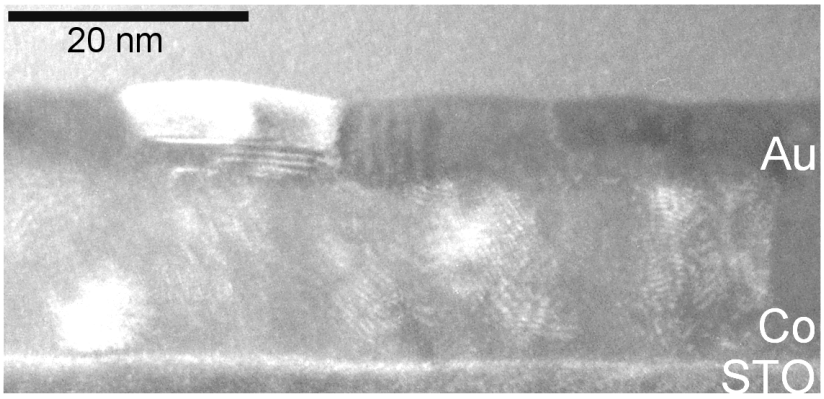

Figure 5.9: *Dark field cross-sectional TEM image of the same sample as shown in figure 5.8, at a different position. Only the $SrTiO_3$, the Co and Au film are shown in the picture.*

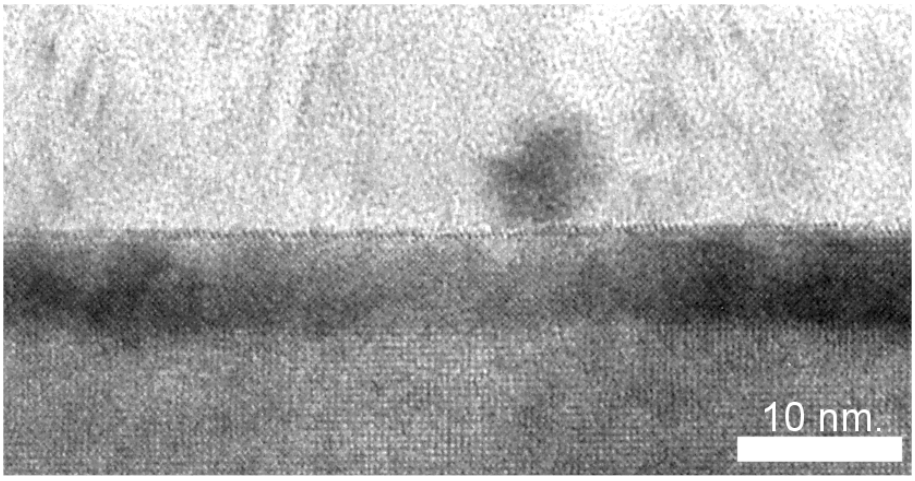

Figure 5.10: *Cross-sectional TEM image of the same $La_{0.67}Sr_{0.33}MnO_3$ / $SrTiO_3$ / Co stack. With these TEM settings, the $SrTiO_3$ / Co interface does not show a white line.*

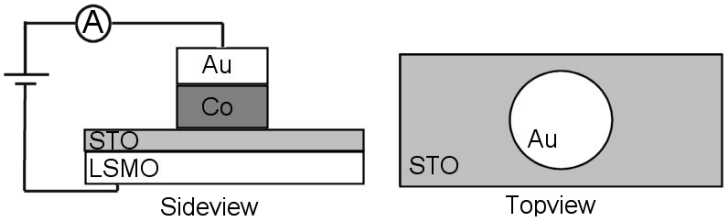

Figure 5.11: *Schematic view of the magnetic tunnel junction.*

the functioning of the MTT. The cross-sectional TEM images 5.2, 5.9 and 5.8 show a bright line at the $SrTiO_3$ /Co interface. This interface is extremely important as it determines the spin polarization of the injected electrons. So the question rises what it is that we see at this interface. Such a bright line could in principle be induced by a layer with a lower electron density such as cobalt-oxide, that transmits the electrons strongly. But when the TEM settings are changed, so that the interface shows up more clear (see image 5.10), the $SrTiO_3$ /Co interface does not show a bright, but a somewhat darker line. So the white line is not caused by a strongly transmitting region. The cross-sectional TEM images do not allow us to identify the crystal structure or composition at the $SrTiO_3$ /Co interface.

5.4 Processing of the magnetic tunnel junction

In this section we explain how the stack of films is processed into structures that allow a 4 point electrical measurement of the magnetic tunnel junctions. Details about why we use these processing steps and what other processing we investigated are described in the appendix. We define the top electrode first by standard photolithography and wet etching. We use a diluted gold etchant to etch both the Au and the Co top layers. This etchant does not etch the $SrTiO_3$ tunnel barrier providing a convenient etch stop. For more detail see appendix A.1 Standard photolithography and ion beam etching define the bottom $La_{0.67}Sr_{0.33}MnO_3$ electrode (with the $SrTiO_3$ tunnel barrier on top). The ions bombard the surface under an angle of 20°with the surface normal. We use an accelerator Voltage of 100 V to achieve an etch rate of 1.4±0.2 nm per minute. More details are described in appendix A.2.

The electrodes are now defined. Figure 5.11 shows a schematic view of the electrodes and the tunnel barrier. The $La_{0.67}Sr_{0.33}MnO_3$ bottom electrode has a rectangular shape of 900 x 200 μm^2. The top electrode is circular. We use different diameters. Each sample contains 41 junctions. Of the junctions with a diameter of 150, 100, 50, 25 and 10 μm, there are each 7. There are 6 junctions

with a diameter of 5 μm.

After the definition of the bottom and top electrode, the contact leads are prepared. A schematic view of the processing steps that are used to realize the contacts is shown in figure 5.12. First a 400 nm sputtered SiO_2 film is deposited to serve as electrical insulation between the bottom electrode and the contact to the top electrode. The holes in this SiO_2 layer that allow contact to both electrodes are defined by lift off using a negative tapered photo-resist. Appendix A.3 describes other routes that we have investigated to realize an insulator layer. A bilayer of 15 nm chromium and 500 nm gold is deposited by sputtering, and lifted off to form the bond pads. A 40 nm gold film is used as contact leads between the electrodes of the magnetic tunnel junction and the bond-pads. This layer is also sputtered and structured by lift-off. We have investigated other ways to realize the contacts. This is described in Appendix A.4. Finally wire-bonding serves to make electrical contact to a printed circuit board.

5.5 Electrical characterization of the magnetic tunnel junction

In this section we will show the results, that we obtained for the magnetic tunnel junctions. Table 5.13 shows the deposition parameters that are used to grow the $La_{0.67}Sr_{0.33}MnO_3$ and the $SrTiO_3$ films of the magnetic tunnel junctions that are discussed in this chapter. Characteristic properties of the magnetic tunnel junctions like the temperature dependence of the TMR and the resistance and the bias dependence of the TMR are discussed and compared to similar junctions that are reported in literature.

5.5.1 Junctions with negative TMR

In the first junction that we discuss, the $La_{0.67}Sr_{0.33}MnO_3$ and the $SrTiO_3$ are both grown with a laser energy density of 1.0 J/cm^2 at an oxygen pressure of 0.3 mbar. For both layers, we stopped the laser for 30 seconds after each deposition of two atomic layers. We will call this junction MTJ 1. The thickness of the $La_{0.67}Sr_{0.33}MnO_3$ ($SrTiO_3$) film is 20 nm (4 nm) as determined by RHEED during growth. The Co top electrode is circular in shape and has a diameter of 150 μm. Figure 5.14 shows the resistance and the TMR for a bias of -100 mV as function of the applied field at 82 K. Negative voltage means that the $La_{0.67}Sr_{0.33}MnO_3$ electrode is at a negative voltage so that electrons tunnel from the $La_{0.67}Sr_{0.33}MnO_3$ to the Co. The arrows indicate the direction in which the magnetic field is varied. The curve shows sharp switching behavior of one of the magnetic layers at 8 Oe. In the figure, we do not only observe the resistance to change when the field is increased, but also in a de-

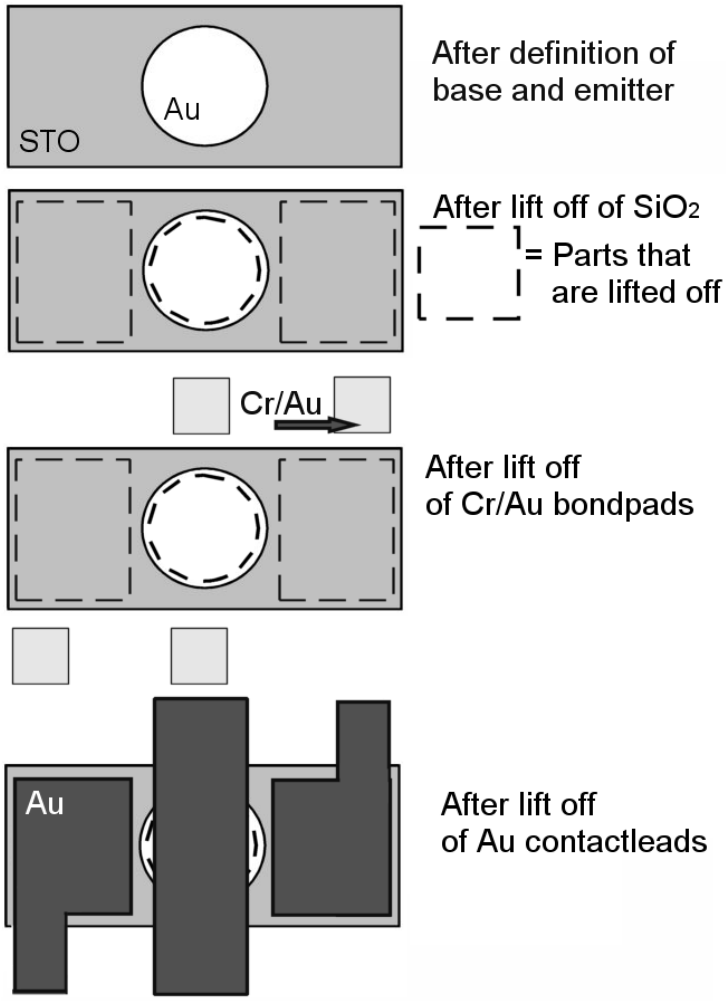

Figure 5.12: *Schematic view of the processing steps that are used to form the contacts to the magnetic tunnel junction.*

	MTJ 1	MTJ 2
LSMO Deposition Parameters		
Oxygen Pressure	0.3 mbar	0.35 mbar
Laser Fluence	1.0 J/cm^2	3.0 J/cm^2
Laser Frequency	1 Hz. with intervals	1 Hz.
Target to Substrate Distance	40 mm.	40 mm.
Temperature	750°C	750°C
LSMO Thickness	20 nm.	10 nm.
STO Deposition Parameters		
Oxygen Pressure	0.3 mbar	0.3mbar
Laser Fluence	1.0 J/cm^2	1.0 J/cm^2
Laser Frequency	1 Hz. with intervals	1 Hz
Target to Substrate distance	40 mm.	40 mm.
Temperature	750°C	750°C
STO Thickness	4 nm.	5 nm.

Figure 5.13: *Table of the deposition parameters used for the growth of the $La_{0.67}Sr_{0.33}MnO_3$ and the $SrTiO_3$ layer of the magnetic tunnel junctions MTJ 1 and MTJ 2*

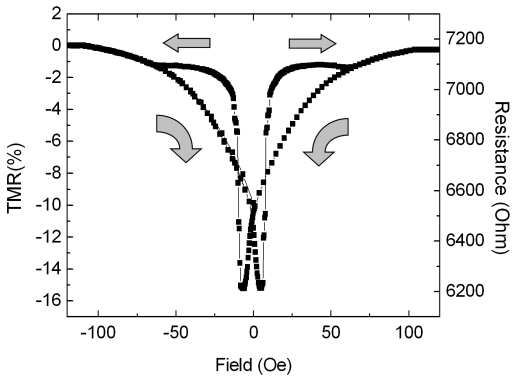

Figure 5.14: *Negative TMR measured in MTJ 1 at a bias voltage of -100 mV at 82 K. The junction diameter is 150 μm. Only one layer shows sharp switching behavior.*

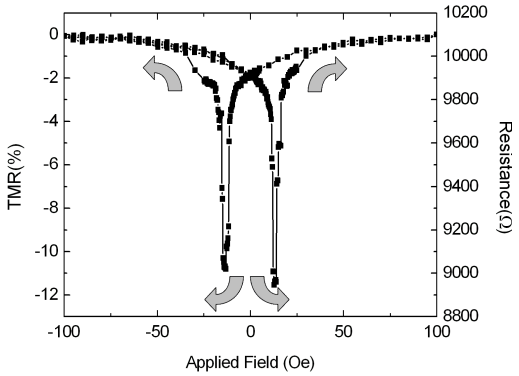

Figure 5.15: *Negative TMR measured in MTJ 1 at a bias voltage of -20 mV at 85 K. In this field direction both layers show sharp switching behavior.*

creasing field we observe a gradual change of the resistance, which shows that the magnetization in one of the layers changes. This means that the field is not applied in the easy direction of one of the films. It also means that a good anti-parallel alignment is possibly not reached in this measurement. The figure shows that the resistance has a maximum when the magnetization of the films is aligned parallel. This is called a negative TMR, because it is opposite to what is usually found in more conventional magnetic tunnel junctions based on transition metal ferromagnets and AlO_x tunnel barriers. Figure 5.15 shows the field dependence of the resistance when the field is applied in a different in plane direction. In this measurement the applied voltage is -20 mV and the temperature is 85 K. In a decreasing field the resistance decreases a little and when the field is increased from zero, we observe a sharp peak towards a lower resistance. This indicates a sharp switching of the magnetization of both of the ferromagnetic layers. The switching fields of both layers are very close to each other so that we do not observe a clear plateau of constant resistance at anti-parallel alignment. It is possible that the switching of the layers is not separated and that a good anti-parallel alignment is not achieved in this measurement either. There are several origins of in plane anisotropy. Research on this topic is in process in our group and will be reported in a later stage.

Figure 5.16 shows two Current-Voltage (I-V) characteristics for MTJ 1. Both are measured at 82 K. For one curve (Parallel) a field of 150 Oe is applied to align the magnetization of both electrodes parallel. In the other measurement a field of 10 Oe is applied to achieve the low resistant state that is shown in figure 5.14. Although this is probably not a perfectly anti-parallel state, this

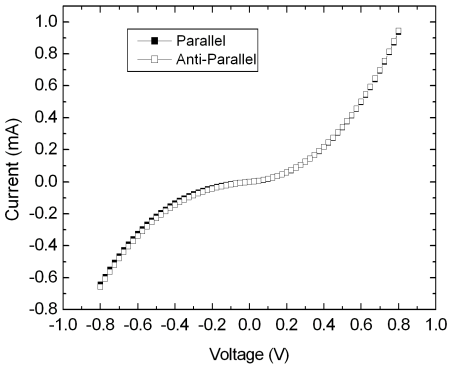

Figure 5.16: *I-V characteristics for MTJ 1. One curve is measured at an applied field of 100 Oe when the magnetization of the layers is parallel. The other curve is measured at the low resistant state. Both are measured at 82 K.*

curve is labeled "anti-parallel". The non linear I-V characteristics are typical for a tunnel barrier. From these characteristics the bias dependence of the TMR is determined. Two of these curves are given in fig 5.17. One is measured at 82 K the other one at 170 K. The figure shows that we find negative TMR and a maximum TMR of -15% at a bias voltage of -100 mV. The voltage at which the TMR finds its maximum does not change with temperature. The decay of the TMR is asymmetric. We will discuss the voltage dependence of the TMR in more detail in section 5.6

Figure 5.18 shows the temperature dependence of the TMR at a bias of -115 mV in the graph in the lower panel. It shows that the TMR decreases with increase of temperature. The TMR is present well above 250 K. In fact a small TMR is measurable up to 300 K. The temperature dependence of the junction resistance measured at +20 mV is given in the upper panel of figure 5.18. The curve shows a resistance maximum at 200 K. The issue of the temperature dependence will be discussed in more detail in section 5.6.

The junction resistance that is measured is only the correct tunnel barrier resistance if the current density through the barrier is homogeneous.[36] As a rule of thumb the resistance of the tunnel barrier should be at least 10 times larger then the lead resistance of the electrodes in the tunnel junction area to regard the current density as homogeneous. An inhomogeneous current density can cause a deviation between the measured resistance and and the real resistance. This causes an incorrect determination of the TMR and can even cause the sign of the TMR to be determined incorrect. To evaluate the homogeneity

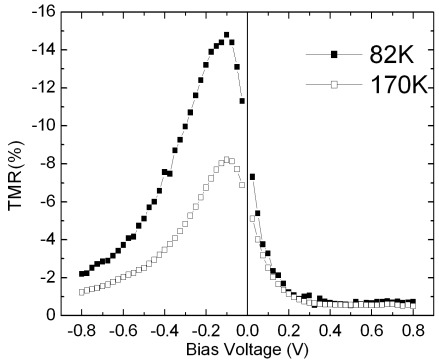

Figure 5.17: *Bias dependance of the TMR of MTJ 1, measured at 82 K and 170 K. Negative voltage means that the $La_{0.67}Sr_{0.33}MnO_3$ electrode is at a negative voltage so that electrons tunnel from the $La_{0.67}Sr_{0.33}MnO_3$ to the Co.*

of the current density through the tunnel barrier of MTJ 1, we start by estimating the sheet resistance of the $La_{0.67}Sr_{0.33}MnO_3$ film in MTJ 1. In chapter 3 we determined the resistivity of the $La_{0.67}Sr_{0.33}MnO_3$ film of sample LSMO2. (see figure 3.18) This film is grown with the same deposition conditions as the $La_{0.67}Sr_{0.33}MnO_3$ film in MTJ1 and the thickness is comparable (16 nm). For the $La_{0.67}Sr_{0.33}MnO_3$ film of sample LSMO 2 we determined a resistivity of 0.4 mΩcm at 100 K. When we use this resistivity and equation 5.1, we estimate a sheet resistance of 200 Ohm for the 20 nm $La_{0.67}Sr_{0.33}MnO_3$ film in sample MTJ 1 at 100 K.

$$R_{lead} = \frac{\rho}{t} = 200\Omega \tag{5.1}$$

The resistance of the top electrode is much lower so we will compare the resistance of the $La_{0.67}Sr_{0.33}MnO_3$ electrode to that of the tunnel barrier. Figure 5.19 shows the tunnel barrier resistance as function of the applied voltage at 82 K. The horizontal line represents 10 times the lead resistance at 100 K. (i.e. $10 \cdot 200\Omega$) (At 82 K this will be somewhat lower, but we use 200 Ohm as an estimate) The figure shows that when the voltage range is between -550 and +350 mV, the tunnel barrier resistance is more then ten times the lead resistance of the $La_{0.67}Sr_{0.33}MnO_3$ and the current density through the tunnel barrier can be regarded homogeneous. At +0.8 (-0.8)V the ratio between the tunnel barrier resistance and the lead resistance (R_{TB}/R_{lead}) is 4(6), in which case some effect of an inhomogeneous current density may be present.

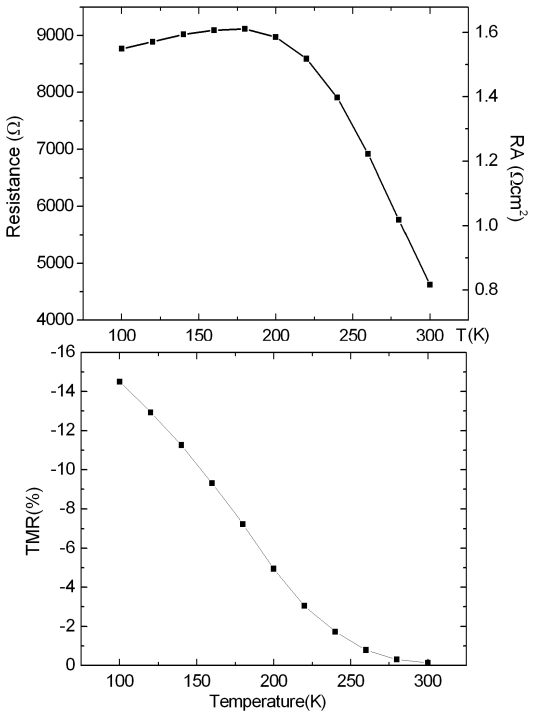

Figure 5.18: *Top: Temperature dependence of the resistance of the tunnel barrier of MTJ 1 at 20mV. Bottom: Temperature dependence of the TMR of MTJ 1, measured at a bias voltage of -115mV.*

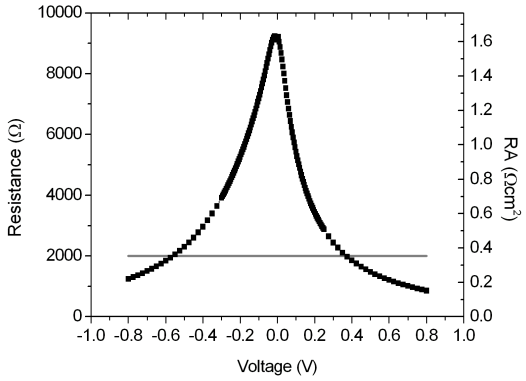

Figure 5.19: *Resistivity of MTJ 1 at 82 K. The horizontal line represents 10 times the sheet resistance.*

5.5.2 Junctions with positive TMR

We did not find negative TMR in all the magnetic tunnel junctions. Positive TMR is found as well in a few junctions. For example we found positive TMR in a junction for which the $La_{0.67}Sr_{0.33}MnO_3$ is grown at a laser fluence of 3.0 J/cm^2 and an oxygen deposition pressure of 0.35 mbar. We will call this junction MTJ 2. We do not correlate the positive TMR to the deposition conditions that are used, as we also found negative TMR in junctions that are grown with the same deposition parameters. The thickness of the $La_{0.67}Sr_{0.33}MnO_3$ film in MTJ 2 is 10 nm. Like in MTJ 1 the $SrTiO_3$ tunnel barrier is deposited with a laser energy density of 1.0 J/cm^2 and at an oxygen pressure of 0.3 mbar. The geometry of both electrodes is identical to that in MTJ 1. The deposition parameters for MTJ 2 are listed in figure 5.13. We observed that the behavior of the barrier is unstable. The resistance of the barrier changed due to the voltage that we applied over the junction. Figure 5.20 shows the TMR as function of the applied field at a bias of -50 mV at 100 K. The parallel configuration has the lower resistance, so the TMR is positive. An inhomogeneous current density through the tunnel barrier could in principle lead to an apparent reversal of the TMR, so we need to verify that the current density through the barrier is indeed homogeneous. To estimate the sheet resistance, we use the resistivity that we find in chapter 3 for LSMO 1, as this $La_{0.67}Sr_{0.33}MnO_3$ film is also grown with a laser energy density of 3 J/cm^2 and an oxygen pressure 0.35 mbar. We found a resistivity of 0.23 mΩcm for sample LSMO 1 at 100 K. Using equation 5.1 and a $La_{0.67}Sr_{0.33}MnO_3$ thickness of 10 nm, we estimate a sheet resistance of 230 Ω for the $La_{0.67}Sr_{0.33}MnO_3$ electrode. So in the mea-

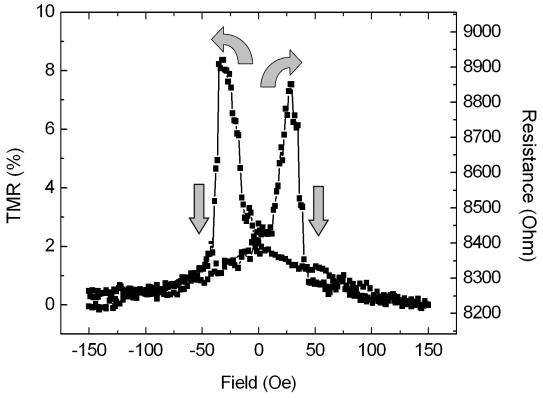

Figure 5.20: *Field dependence of the TMR of MTJ 2 at a bias voltage of -50 mV at 100 K.*

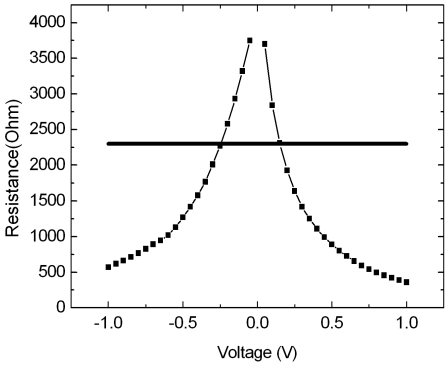

Figure 5.21: *Resistivity of the MTJ 2 at 100 K. The horizontal line is the resistance above which the tunnel current density can be regarded as homogeneous.*

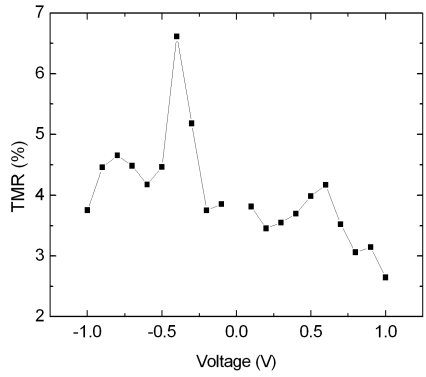

Figure 5.22: *Bias dependance of the TMR of MTJ 2 at 100 K.*

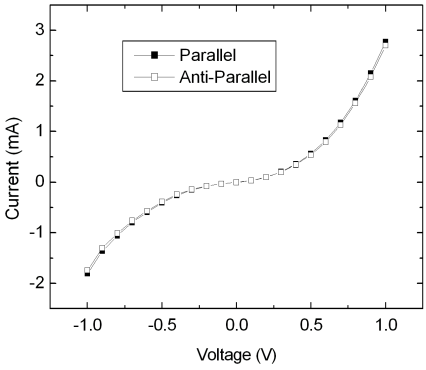

Figure 5.23: *I-V characteristics for MTJ 2 for parallel and anti-parallel alignment of the magnetization in the electrodes at 100 K.*

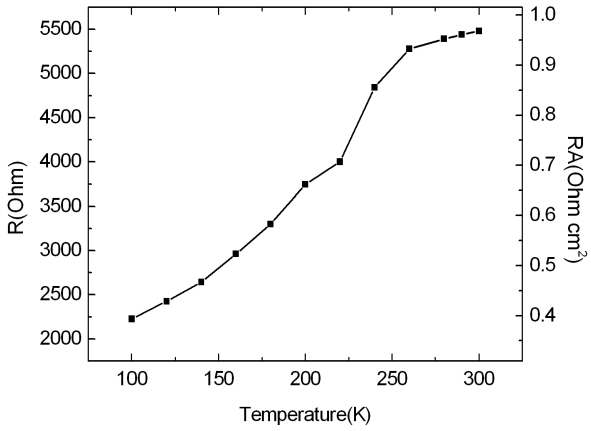

Figure 5.24: *Temperature dependence of the resistance of MTJ 2 at 20 mV.*

surement shown in figure 5.20, the barrier resistance is more then 35 times the sheet resistance of the $La_{0.67}Sr_{0.33}MnO_3$ film, so that a homogeneous current density can be expected. Figure 5.23 shows the I-V characteristics for parallel and anti-parallel alignment of the magnetization of the electrodes at 100 K. Figure 5.21 shows the resistance of the tunnel barrier as function of the applied voltage at 100 K that is deduced from the I-V characteristic at parallel alignment. The fact that this resistance does not correspond to the resistance shown in figure 5.20 is due to the instability of the tunnel barrier. Again, we added a line that represents 10 times the lead resistance of the $La_{0.67}Sr_{0.33}MnO_3$ electrode. Between -250 mV and +150 mV the current through the barrier can be regarded as homogeneous.

From the I-V curves at parallel and anti-parallel configuration we derive the bias dependence of the TMR. Figure 5.22 shows that we find positive TMR for a bias voltage from -1 to +1 volt, but since the homogeneity of the current density is only guaranteed for the voltage range from -250 to + 150 mV, we cannot rely on the measured TMR for higher voltages. Due to the instability of the barrier we could not measure the TMR for a series of temperatures, but a small effect is still observed at a bias of 50 mV at 280 K. The temperature dependence of the junction resistance measured at 100 mV is given in figure 5.24. The resistance increases with increasing temperature and unlike the resistance of MTJ 1 (5.18), it does not reach a maximum up to 300 K.

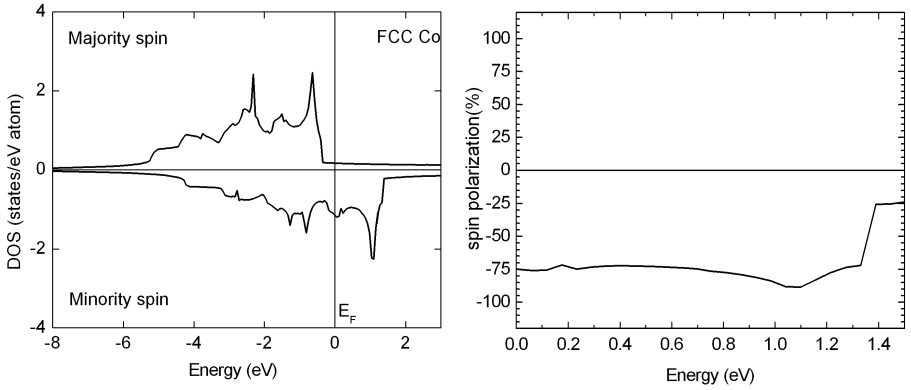

Figure 5.25: *Left panel: Total density of states for FCC Co. Right panel: The total spin polarization for FCC Co, derived from the total density of states shown on the right. [101]*

5.6 Discussion

In section 1.2 of chapter 1 we discussed the behavior of $La_{0.67}Sr_{0.33}MnO_3$ /$SrTiO_3$ /3d-ferromagnet tunnel junctions that are reported in literature. We will discuss our results in comparison to the reported data. MTJ 1 shows much resemblance with the $La_{0.67}Sr_{0.33}MnO_3$ /$SrTiO_3$ /Co junctions reported by De Teresa *et al.* [37] MTJ 1 also shows negative TMR and a maximum of TMR at non zero negative bias. However there are differences too. We find this maximum at a bias voltage of -100 mV instead of -400 mV. They find a sign reversal of the TMR at a bias voltage of +0.8 V. We do not observe the sign reversal at positive bias. The maximum of TMR that we find at 82 K is -15% while they report about -37% around 75 K. [40]

We will now verify if we can indeed correlate the bias dependence of the TMR to the relevant densities of states. In figure 5.25 we show the total density of states for FCC Co in the left panel. [101] The spin polarization that we deduce from this is shown in the right panel. So from the density of states of Co we expect a maximum in the TMR for negative bias at -1.1 V and not at -100 or -400 mV. However the density of states that is shown here is for bulk Co, and the TMR is sensitive to the tunnel spin polarization at the Co/$SrTiO_3$ interface. We do not have the density of states for the Co/$SrTiO_3$ interface available but we do have a density of states for the Co/vacuum interface. [42] It was shown in figure 1.17 in chapter 1. At the interface with vacuum, the maximum of the spin polarization is shifted to 400 mV, in correspondence with the maximum in TMR at -400 mV found by De Teresa *et al.* In section 1.2 of chapter 1 we showed that Fert *et al.* explained the sign reversal of the TMR

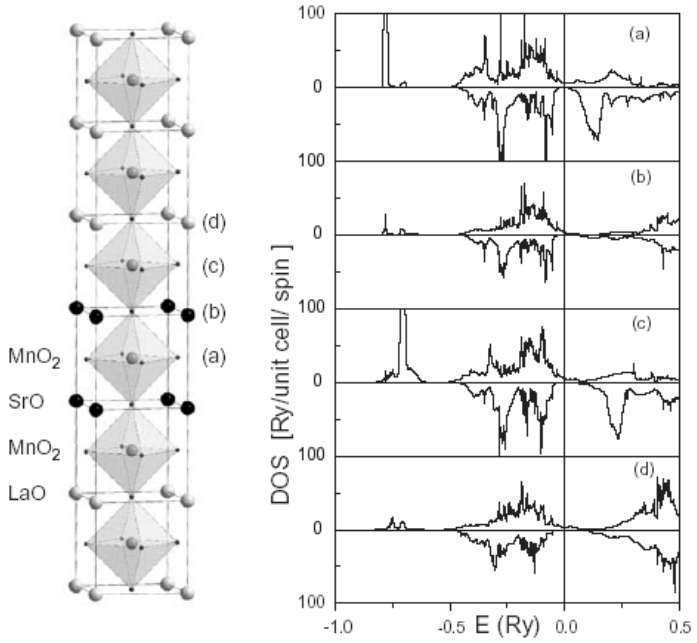

Figure 5.26: *Partial density of states for $La_{0.67}Sr_{0.33}MnO_3$: A: MnO_2 plane between 2 SrO planes, B: SrO plane, C: MnO_2 plane between SrO and LaO plane D: LaO plane. [102]*

for a positive bias voltage by spin polarization of the $La_{0.67}Sr_{0.33}MnO_3$ at the Fermi-level and the spin polarization of the Co below the Fermi-level. (See figure 1.17) However, we would expect the current for this bias to be dominated by electrons that tunnel from the Co Fermi-level to the empty $La_{0.67}Sr_{0.33}MnO_3$ states situated above the Fermi-level. The electrons at the fermi level in the Co layer have more energy then the electrons below the fermi-level of the Co, which gives them a higher tunnel probability and are therefore more likely to dominate the tunnel current at positive bias. In fact magnetic tunnel transistors would not function the way they do if the electrons would tunnel like in figure 1.17, because it would not be possible to create hot electrons by tunneling. So we expect that the $La_{0.67}Sr_{0.33}MnO_3$ density of states above the Fermi-level is probed at positive bias and not the Co density of states below the Fermi-level. The spin polarization for the d-electrons of Co near the Fermi-level is negative. The partial densities of states for $La_{0.67}Sr_{0.33}MnO_3$ are shown in figure 5.26.[102] Slightly above the fermi-level, all partial densities of states for $La_{0.67}Sr_{0.33}MnO_3$ show a positive spin polarization. So due to the negative spin polarization of cobalt at the Fermi-level this gives a negative TMR. At a higher energy we see that the spin polarization of all partial densities of states for $La_{0.67}Sr_{0.33}MnO_3$ change sign which should give a positive TMR.

We find a maximum of TMR of -15% at 82 K. If we assume a spin polarization of 100% for the tunnel spin polarization of the $La_{0.67}Sr_{0.33}MnO_3$ /$SrTiO_3$ interface then -15% TMR corresponds to a tunnel spin polarization of Co of -7.0%, according to equation 5.2

$$TMR = \frac{\Delta R}{R} = \frac{R_{AP} - R_P}{R_{min}} = \frac{2P_1P_2}{1 + |P_1P_2|} \tag{5.2}$$

This is much lower then the spin polarization of Co either in the bulk or at the interface with vacuum.

There are a number of possible explanations for the low TMR and the deviations in the voltage dependence of the TMR that we mentioned. The first explanation is in the fact that the magnetization of the layers does not reach a complete anti-parallel state in the measurements that are performed. This would explain the lower TMR but not the difference in the bias dependence of the TMR. A second explanation is that the deviations are caused by point defects (structural imperfections) in the $SrTiO_3$ tunnel barrier. Point defects in a tunnel barrier can form a conductive path for the tunneling electrons. This is known to cause the TMR to drop with increase of the bias voltage. Increase of the density of the point defects will thus cause the TMR to drop faster with the applied bias voltage.[43] Since this effect combined with the density of states will determine the bias dependence of the TMR, an increase of the density of the point defects in the tunnel barrier, will cause the maximum in the TMR to occur at a lower bias voltage. It can also explain the fact that the TMR that we find is lower. Another explanation for the deviation in the

bias dependence, is that our measurement is performed at 82 K instead of 5 K. At elevated temperatures the energy of the tunneling electrons is distributed and this distribution widens as T increases. That means that correlation of the bias dependence of the TMR to the density of states of both electrons should include an energy distribution. This effect will smear out sharp peaks in the density of states. An explanation for the absence of the sign reversal of the TMR could be that this reversal of the sign is reported to be at +0.8 V and we have seen that at this voltage we cannot guarantee that the current through the tunnel barrier is homogeneous as the ratio of tunnel barrier and the sheet resistance of the $La_{0.67}Sr_{0.33}MnO_3$ electrode is about 4.

Another explanation can be found in the fact that the exact composition at the $SrTiO_3$ /Co interface is undefined. In this chapter we showed four cross-sectional TEM images 5.3, 5.8, 5.9 and 5.10. None of them allow us to identify the structure or stoichiometry at the Co/$SrTiO_3$ interface. It is possible that the Co has formed an oxide or an alloy and that the TMR cannot be related to the density of states of Co at all. For the junctions reported De Teresa *et al.*, it could be determined that the TiO_2 plane is the sublattice that is present at the Co/$SrTiO_3$ interface. [41] We believe that formation of a cobalt-oxide or another cobalt phase, is more likely to occur in our structures then in their structures because we grow the Co by PLD instead of sputtering which gives the arriving Co atoms a higher energy and reactivity. This explanation would make all the other explanations obsolete.

In MTJ 2, we observe a positive tunnel magneto resistance. Positive TMR has not been reported in literature so far for $La_{0.67}Sr_{0.33}MnO_3$ /$SrTiO_3$ /Co magnetic tunnel junctions. This positive TMR means that both electrodes have the same sign for the tunnel spin polarization at the interface. All the partial densities of states for the $La_{0.67}Sr_{0.33}MnO_3$ show a positive spin polarization near the Fermi-level, (see Figure 5.26) so we do not expect a negative spin polarization for the $La_{0.67}Sr_{0.33}MnO_3$ /$SrTiO_3$ interface. For cobalt however, the sign of the spin polarization is less straightforward. In section 1.2 of chapter 1 we discussed two explanations for the negative spin polarization of the cobalt/$SrTiO_3$ interface: One is that the d-electrons of the Co are involved in the bonding with the TiO_2 sublattice and the d-electrons show negative spin polarization. [37] (If the s- and p-electrons are involved in the bonding to the $SrTiO_3$ we can expect a positive spin polarization at the Co/$SrTiO_3$ interface and hence a positive TMR.) The second explanation for the negative spin polarization of the Co/$SrTiO_3$ interface is given by Oleynik *et al.*[46]. It is calculated, that the interface with cobalt induces a magnetic moment on the Ti atoms in a TiO_2 terminated $SrTiO_3$ barrier. The direction of this magnetic moment is opposite to the magnetization of the Co electrode which explains the negative spin polarization. Oleynik *et al.* performed these calculation for a TiO_2 terminated barrier. So both explanations for the negative spin polarization of the Co/$SrTiO_3$ interface are for a TiO_2 terminated barrier. (Pailloux

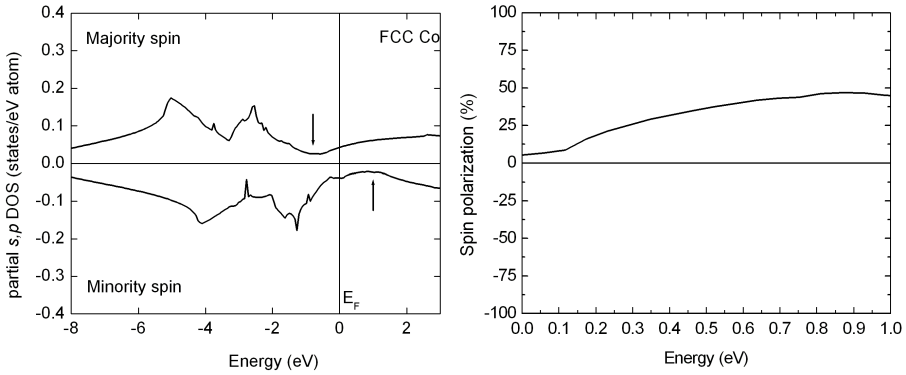

Figure 5.27: *Left panel: Density of states of the s- and p- electrons in FCC Co. Right panel: the spin polarization,that is deduced from this density of states. [101]*

et al.[41] observed this termination by cross-sectional TEM, for the junctions reported by De Teresa *et al.*. Oleynik *et al.* assume a TiO_2 termination and start the calculations with this assumption.) In principle it is possible that a SrO terminated barrier gives a different sign for the tunnel spin polarization although no calculations have been reported for this interface. This could mean that the Co s- or p-electrons are involved in the bonding with the SrO sublattice. This is also observed for the Co/AlO_x interface. The positive spin polarization for the s- and p electrons follows from the partial density of states for the s-and p- electrons, which is shown in figure 5.27 [101]

A positive tunnel spin polarization has been reported for the $Co/SrTiO_3$ interface before. Thomas *et al.*[45] find a positive tunneling spin polarization in spin polarized tunneling experiments on $Co/SrTiO_3$ /Al junctions. In these experiments the $SrTiO_3$ barrier is grown by reactive evaporation and the $SrTiO_3$ is amorphous instead of single crystalline. They propose two possible explanations for the fact that an amorphous $SrTiO_3$ barrier gives a positive tunneling spin polarization in combination with cobalt. Either the selection of the d-electrons is due to the fact that the barrier is epitaxial and therefore absent in the amorphous barriers, or the amorphous barriers have a mixed SrO and TiO_2 termination, instead of single TiO_2 termination, so that the interface deviates from the interfaces reported De Teresa *et al.* and calculated by Oleynik *et al.* In our structures we find positive TMR in junctions with epitaxial barriers. This excludes the first explanation.

So we believe that a possible explanation for the positive tunnel spin polarization of the $Co/SrTiO_3$ interface, is that the tunnel barrier deviates from a TiO_2 terminated $SrTiO_3$ barrier with pure Co on top. Either the $SrTiO_3$

barrier is not TiO_2 terminated or the Co has formed an oxide or another phase with Sr or Ti.

Another behavior that is characteristic for $La_{0.67}Sr_{0.33}MnO_3$ based tunnel junctions is the temperature dependence of the tunnel resistance. The increase of the resistance (see figure 5.18and 5.24) with increasing temperature is attributed to the decrease of the carrier concentration in the $La_{0.67}Sr_{0.33}MnO_3$ when the temperature is increased from 0 K to the temperature at which the metal-insulator transition occurs (360 K). For MTJ 1 we find a maximum at 200 K while the resistance of MTJ 2 increases up to the highest temperature that we measured (300 K). We consider two effects that determine the temperature dependence of the junction resistance. A drop of resistance with increasing temperature is expected for a tunnel junction in general, because at higher temperature there will be electrons with more energy and these have a higher tunneling probability. The effect that the carrier concentration in $La_{0.67}Sr_{0.33}MnO_3$ decreases as the temperature increases to Tc, gives an opposite contribution to the temperature dependence of the junction resistance (i.e. an increase of the junction resistance with increasing temperature). When the temperature dependence of the junction resistance is governed by these two phenomena, a stronger temperature dependence of the carrier concentration in the $La_{0.67}Sr_{0.33}MnO_3$ will shift the junction resistance maximum to a higher temperature. In chapter 3 figure 3.18 it is shown that for temperatures between 220 K and 300 K the magnetization and the conductance of $La_{0.67}Sr_{0.33}MnO_3$ as function of temperature show a larger slope for $La_{0.67}Sr_{0.33}MnO_3$ deposited at 3.0 J/cm^2 (LSMO 1 and MTJ 2) than for $La_{0.67}Sr_{0.33}MnO_3$ deposited at 1.0 J/cm^2 with intervals (LSMO 2 and MTJ 1). Since carrier concentration, conductance and magnetization in $La_{0.67}Sr_{0.33}MnO_3$ are closely related, we also expect a stronger slope in the carrier concentration as function of temperature. So the fact that the temperature at which the resistance finds its maximum is higher in MTJ 2 then in MTJ 1 is explained by the different $La_{0.67}Sr_{0.33}MnO_3$ deposition parameters that influences the temperature dependence of the carrier concentration of the $La_{0.67}Sr_{0.33}MnO_3$.

We do not find the temperature of maximum junction resistance to correlate with the temperature at which the TMR vanishes. Like us, Noh *et al.*[103] also find a maximum in the junction resistance for $La_{0.67}Sr_{0.33}MnO_3$ /$SrTiO_3$ /$La_{0.67}Sr_{0.33}MnO_3$ junctions, at a temperature (180 K) that does not correlate with the temperature at which the TMR vanishes (300 K). Fert *et al.*find that the temperature of maximum tunnel barrier resistance correlates to the Curie temperature of the interface, because at this temperature the TMR vanishes in these junctions.

5.7 Conclusions

We have developed a process to prepare $La_{0.67}Sr_{0.33}MnO_3$ / $SrTiO_3$ / Co magnetic tunnel junctions. The top electrode is defined by wet etching, while the bottom electrode is defined by ion beam etching. SiO_x is sputtered and lifted off to form an electrical insulation layer. In contrast to $La_{0.67}Sr_{0.33}MnO_3$ /$SrTiO_3$ /Co magnetic tunneljunctions that are reported in literature,[37] we use PLD to deposit the cobalt electrode. We observe negative TMR of -15% at a temperature of 82 K in some junctions. The negative TMR for a negative bias voltage is explained by the positive spin polarization of $La_{0.67}Sr_{0.33}MnO_3$ around the Fermi-level and the negative spin polarization of the Co above the Fermi-level. The negative TMR for positive bias is explained by the negative spin polarization of the Co around the Fermi-level and the positive spin polarization of the $La_{0.67}Sr_{0.33}MnO_3$ above the fermi level. In these junctions, the TMR decreases with increase of temperature and becomes about 1% at 260 K, but it can still be observed up to 300K. The maximum of TMR is observed at a bias voltage of -100 mV. When the behavior of these junctions is compared to the behavior of the $La_{0.67}Sr_{0.33}MnO_3$ /$SrTiO_3$ /Co magnetic tunnel junctions reported by De Teresa *et al.*, we find that the TMR, that we observe is significantly lower. (-15% at 82 K vs. -37% at 75 K) We also observe differences in the bias dependence of the TMR. We observe the maximum of the TMR at negative bias at a lower voltage. (-100 mV vs. -400 mV) Further, we do not observe the reversal of the sign of the TMR at positive bias.

A possible explanation for the lower TMR is that we did not attain a complete anti-parallel alignment of the magnetization of both electrodes in our measurements. However, this would not explain the deviations in the bias dependence of the TMR. A higher density of point defects in our $SrTiO_3$ tunnel barriers would explain the lower TMR as well as the deviations in the bias dependence of the TMR. Another possible explanation for the deviations in the bias dependence of the TMR, is that we measured this at 82 K while the measurement by De Teresa *et al.* is performed at 5 K. An explanation for the absence of the reversal of the sign of the TMR could be incorrect determination of the barrier resistance due to an inhomogeneous current density through the barrier at a positive bias of 0.8 V. ($R_{TB}/R_{SheetLSMO} = 4$)

We also observe positive TMR in some junctions. Positive TMR indicates that the tunnel spin polarization of both electrode/tunnelbarrier interfaces is of the same sign. We believe that the tunnel spin polarization of the $Co/SrTiO_3$ interface is positive for these junctions. The reason is twofold. The first is that, none of the partial densities of states of $La_{0.67}Sr_{0.33}MnO_3$ shows a negative spin polarization (see figure 5.26, so that we expect the tunnel spin polarization of $La_{0.67}Sr_{0.33}MnO_3$ to be positive. The second is that the tunnel spin polarization of Co is known to depend on the tunnel barrier. (Co in combination with an AlO_x barrier gives a positive tunnel spin polarization. Co in combination with

TiO_2 terminated $SrTiO_3$ barriers gives a negative spin polarization.[37, 46]) The negative tunnel spin polarization for the Co/$SrTiO_3$ interface is only reported for tunnel barriers with a TiO_2 termination at the Co interface. So in principle it is possible that a SrO termination of the $SrTiO_3$ barrier gives a positive tunnel spin polarization. When we investigate the Co/$SrTiO_3$ interfaces by transmission electron microscopy, we do not observe a sharp interface and we cannot determine the exact composition or structure of the interface. The fact that the interface is not very sharp could indicate that the Co has formed an oxide or another phase at the interface with the $SrTiO_3$. The chance that this is so, is increased by the fact that the PLD growth technique gives the Co particles that arrive on the surface a high energy compared to the sputter technique.

The junctions in which the $La_{0.67}Sr_{0.33}MnO_3$ is deposited at 3.0 J/cm^2 show a resistance that increases with temperature up to at least 300 K, while the resistance of the junction with the $La_{0.67}Sr_{0.33}MnO_3$ deposited at 1.0 J/cm^2 shows a maximum at 200 K. The resistance of a tunnel barrier in general, decreases with increase of temperature. The increase of the resistance with increasing temperature observed for $La_{0.67}Sr_{0.33}MnO_3$ based magnetic tunnel junctions is due to temperature dependence of the carrier concentration in $La_{0.67}Sr_{0.33}MnO_3$. This carrier concentration increases if the temperature is increased from 0 K to the temperature at which the metal insulator transition occurs. This is at the Curie temperature of $La_{0.67}Sr_{0.33}MnO_3$ at 360 K. We observed that for temperatures between 220 and 300 K the decrease of the carrier concentration with temperature is stronger for $La_{0.67}Sr_{0.33}MnO_3$ films grown with a laser fluence of 3 J/cm^2 then for films grown with a laser fluence of 1 J/cm^2. So the temperature at which the resistance finds its maximum can be correlated to the temperature dependence of the carrier concentration in the $La_{0.67}Sr_{0.33}MnO_3$ electrode.

Chapter 6

Epitaxial oxide-based magnetic tunnel transistor

In this chapter the results obtained with the magnetic tunnel transistor are presented. In chapter 4 the diode characteristics of the $La_{0.67}Sr_{0.33}MnO_3$ / Nb:$SrTiO_3$ junctions have been described. It is found that thermionic emission dominates the current in these diodes and that the reverse leakage current is in the order of a nano-ampere. In chapter 5 the $La_{0.67}Sr_{0.33}MnO_3$ / $SrTiO_3$ / Co magnetic tunnel junctions have been described. They show TMR and are stable up to voltages of at least 1 Volt. These are two important ingredients that are necessary to form a magnetic tunnel transistor (MTT). Figure 6.1 shows a schematic view of the MTT that is presented in this chapter. The preparation techniques that are used to realize this structure, will be discussed in this chapter. Then the results that are obtained will be presented, followed by discussion of these results and recommendations.

6.1 Introduction

The magnetic tunnel transistor was first suggested by Monsma *et al.*[10] Figure 6.2 shows an energy diagram of a MTT. Hot electrons are injected over a tunnel barrier into the base of the MTT. As these hot electrons travel through the base, the scattering in the base causes a change of their momentum and k-vector. Electrons that have traversed the base and still have enough energy and the right k-vector to overcome the Schottky barrier, will be collected. This Schottky barrier is called the collector. Since the scattering in the base depends on the relative alignment of both ferromagnets, the collector current becomes highly field dependent. In state of art MTT's the ratio between the collector

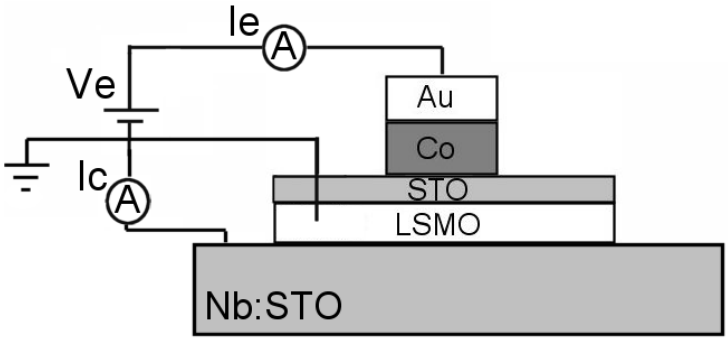

Figure 6.1: *Schematic view of the Magnetic Tunnel Transistor, that is discussed in this chapter.*

current and the emitter current (transfer ratio) is in the order of 10^{-3}. This transfer ratio is a strong limitation for the applicability of an MTT as memory element or magnetic field sensor. The transfer ratio can be increased by decreasing the scattering in the base. This can be achieved by decreasing the thickness of the base layer(s) or by selecting base-materials for which the hot electrons have a long attenuation length. Crystal boundaries are a source for hot electron scattering. It has been shown that an improvement of the crystalline structure of the base material drastically increases the transfer ratio. [50] We anticipate that the use of an epitaxial base will result in an increase of the attenuation length of hot electrons and hence an increased transfer ratio. This is the reason that an epitaxial MTT is pursued in this work. For the base layer, we choose to use $La_{0.67}Sr_{0.33}MnO_3$, as this is a ferromagnet with a Curie temperature well above room temperature (Tc=360 K) for which a lattice matching semiconductor can be found, that allows epitaxial growth. Park *et al.* report that $La_{0.67}Sr_{0.33}MnO_3$ is a half metallic ferromagnet.[23] This makes the material a useful building block for spintronic devices in which the spin of an electron is exploited. $La_{0.67}Sr_{0.33}MnO_3$ based Magnetic Tunnel Junctions (MTJ's) have shown the highest TMR ever reported. (1800% at 4 K [30]) MTJ's in general, are sensitive to the spin polarization of the electrodes at the interface with the tunnel barrier. So $La_{0.67}Sr_{0.33}MnO_3$ based MTJ's are sensitive to the spin polarization of the electrons at the $La_{0.67}Sr_{0.33}MnO_3$ interface. Unfortunately the spin polarization at the $La_{0.67}Sr_{0.33}MnO_3$ interface diminishes well below the Curie temperature of $La_{0.67}Sr_{0.33}MnO_3$. That is why the TMR is not present up to the Curie temperature of the $La_{0.67}Sr_{0.33}MnO_3$. In an MTT however, it is not the spin polarization at the interface that is probed, but the (spin dependent) transmission of hot electrons through the complete film. That means that a field dependence can be expected up to the

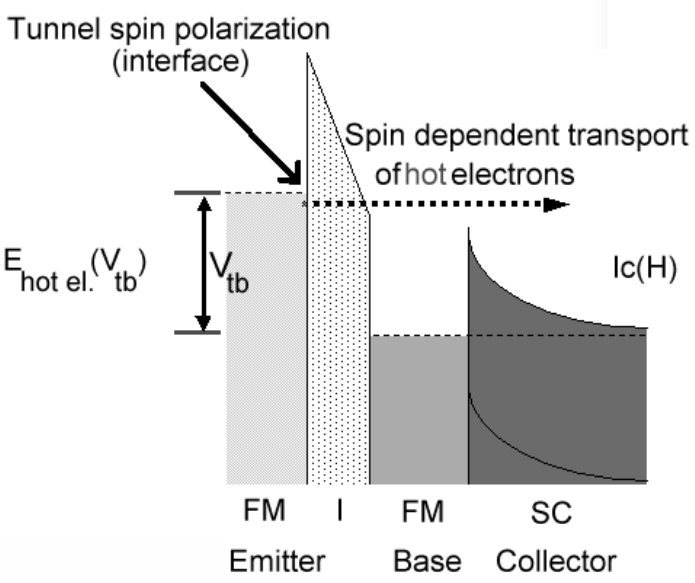

Figure 6.2: *Energy diagram of a MTT with a magnetic emitter. This is the type of MTT that is presented in this chapter. Spin polarized hot electrons are injected in the ferromagnetic base. As these hot electrons travel through the base, the scattering in the base causes a change of their momentum and k-vector. Electrons that have traversed the base and still have enough energy and the right k-vector to overcome the Schottky barrier, will be collected.*

Curie temperature of the $La_{0.67}Sr_{0.33}MnO_3$. This is another reason that this $La_{0.67}Sr_{0.33}MnO_3$ based MTT is an interesting one.

The MTT knows two different configurations. One uses a magnetic emitter to inject spin polarized hot electrons. In the other configuration, non polarized hot electrons are injected by a non magnetic emitter. The first MTT's were reported in 1997 by Mizushima *et al.*[14] They were of the type with a non-magnetic emitter. In that configuration the base contains two ferromagnetic layers separated by a non-magnetic spacer layer. The MTT with a magnetic emitter was reported in 1998. [15] It has the advantage of having only one or two layers in the base, which reduces scattering at interfaces in the base. On the other hand the polarization of the injected electrons is limited to the tunnel spin polarization of the emitter/tunnel barrier combination. [13]

The attenuation length of hot electrons in $La_{0.67}Sr_{0.33}MnO_3$ has not been reported so far. So to increase the chance of detecting hot electrons, we prefer to use the configuration in which we can expect the largest transfer ratio. This is the reason that we choose to use the configuration with a magnetic emitter to realize an epitaxial MTT.

In chapter 3 the growth of the $La_{0.67}Sr_{0.33}MnO_3$ films by Pulsed Laser Deposition (PLD) has been presented. The films can be grown in a 2 dimensional growth mode, which results in epitaxial $La_{0.67}Sr_{0.33}MnO_3$ films that have an atomically smooth surface. In chapter 4 the $La_{0.67}Sr_{0.33}MnO_3$ / $Nb:SrTiO_3$ diodes have been presented. Thermionic emission dominates the current in these diodes and the reverse current is in the order of a nA. The $La_{0.67}Sr_{0.33}MnO_3$ /$SrTiO_3$ /Co Magnetic tunnel junctions have been presented in chapter 5. The MTJ's exhibit TMR and are stable upto voltages of at least 1 V. We aim to realize an epitaxial MTT with these building blocks. A cross-sectional TEM image of the complete stack of layers is shown in figure 6.3 The image shows the niobium doped $SrTiO_3$ substrate with the epitaxial $La_{0.67}Sr_{0.33}MnO_3$ film and $SrTiO_3$ film on top. The cobalt film on top of the $SrTiO_3$ film as well as the gold film are poly-crystalline.

Section 6.2 describes the preparation of the devices. We focus on the contacts to the base and the collector contact to the substrate as much of the processing has already been described in chapter 5. Two different structures in which a hot electron current is collected are presented in section 6.3. The results are discussed in section 6.4

6.2 Preparation of the magnetic tunnel transistor

The first step in the preparation of the MTT is the definition of the base and the emitter, as shown in figure 6.5 A. The magnetic tunnel transistor that we aim to fabricate is basically a magnetic tunnel junction on a semiconducting substrate. The bottom electrode in the MTJ's discussed in chapter 5 becomes

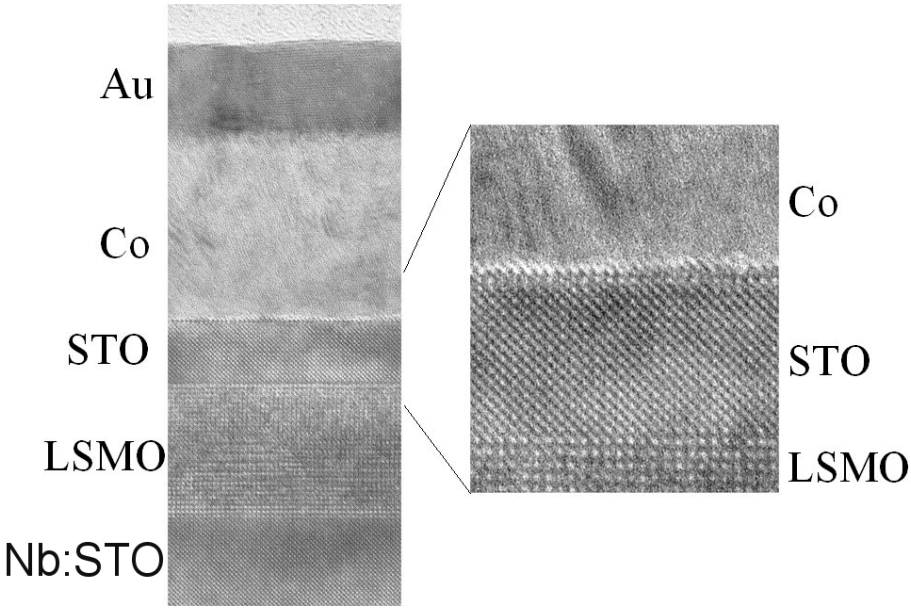

Figure 6.3: *Cross-sectional TEM image of the complete stack of films that will form the epitaxial MTT. From top to bottom the image shows the Au cap layer, the Co emitter, the $SrTiO_3$ tunnel barrier, the $La_{0.67}Sr_{0.33}MnO_3$ base layer and the single crystalline niobium doped $SrTiO_3$ substrate.*

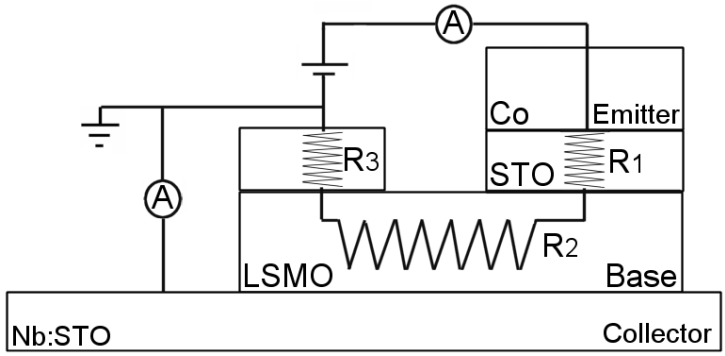

Figure 6.4: *Electrical scheme of the magnetic tunnel transistor. For clarity, the figure shows the situation in which the tunnel barrier is connected for a two point measurement. R1, R2 and R3 are the resistances of the tunnel barrier, the base and the contact to the base.*

the base and the top electrode becomes the emitter. Hence, the base and the emitter are defined in the same way as the bottom and top electrode in chapter 5. That means that the emitter is defined by wet etching and the $La_{0.67}Sr_{0.33}MnO_3$ base by ion beam etching. For the MTT however, it is important to define the emitter before defining the base, so that the ion beam etch step that defines the base only etches the base and tunnel barrier layer. When the base is defined first, the ion beam etching has to remove the Co and the Au layer as well as the $SrTiO_3$ tunnel barrier and the $La_{0.67}Sr_{0.33}MnO_3$ base. We found that in that case the diodes show a large reverse current, which is probably due to redeposition on the edges of the diode area.

For the magnetic tunnel junctions described in chapter 5, the resistance of the contacts to the top electrode and the bottom electrode are not critical as a 4 point measurement is used to characterize the tunnel junction. For a magnetic tunnel transistor however it is important to have a low resistant contact to the base-layer. Figure 6.4 is shown to explain this. Sending a current through the base causes a voltage drop across the base resistances (R2 and R3) proportional to the base current. This causes the base potential to deviate from ground. As a result, a bias voltage develops across the $La_{0.67}Sr_{0.33}MnO_3$ / Nb:$SrTiO_3$ collector Schottky diode. Under the conditions of negative bias on the emitter electrode, the voltage that develops corresponds to a reverse bias of the collector diode. This causes a reverse bias current across the collector diode, even if no transmitted hot-electron current is present. The induced current, here referred to as "diode leakage current" is proportional to the base resistances R2 and R3, and to the base current, and thereby also to the emitter current and voltage. Therefore, it can be interpreted erroneously as a hot-electron current,

and thus needs to be minimized. This can be done by using high quality diodes which have low reverse bias leakage even when biased, and/or by proper choice of the resistances, i.e. R1 $\gg$ R2+R3. While R1 and R2 are determined by the thickness of the $SrTiO_3$ tunnel barrier and the $La_{0.67}Sr_{0.33}MnO_3$ base layer, respectively, R3 depends on the method used to fabricate the base contact.

Therefore, different processing schemes have been examined to realize a low resistant contact to the $La_{0.67}Sr_{0.33}MnO_3$ base. One route is to wet etch the Co and Au from the $SrTiO_3$ tunnel barrier followed by ion beam etching to remove the $SrTiO_3$ tunnel barrier. The processing scheme is shown in figure 6.5. Picture A shows the device after the emitter has been wet etched and the base has been defined by ion beam etching. This step is followed by 4 minutes of ion beam etching through the $SrTiO_3$ tunnel barrier to expose the $La_{0.67}Sr_{0.33}MnO_3$ base for good electrical contact. The settings described in appendix A.2 are used for the ion beam etching. A schematic view of the device after the ion beam etching of the holes in the $SrTiO_3$ is given in the picture B in figure 6.5. Like in the MTJ's discussed in chapter 5 the base is 900 μm x 200 μm. The spacing between the hole created by the ion beam etching and the edge of the base is 10 μm. The spacing between this hole and the emitter is 10 μm as well. The 400 nm SiO_2 layer that electrically insulates the emitter contact lead from the bottom electrode and the substrate is deposited by sputtering. We use lift off to define the holes that allow contact to base and emitter. The holes in the SiO_2 that allow contact to the base are smaller then the holes in the $SrTiO_3$. The spacing between the edge of the hole in the SiO_2 and the edge of the base is 20 μm. This phase is schematically depicted in picture C of figure 6.5. The Cr(15 nm)/Au(500 nm) bond pads are shown in picture D of this figure. These bond pads are deposited by sputtering and structured by lift off. Picture E of the figure, shows the final structure after deposition and lift off of the 40 nm thick, Au contact leads. More details about the bond pads and the contact leads are given in appendix A.4. This type of contact is called type 1. Note that in this case, the contact to the base consists of a Au film sputtered on top of the $La_{0.67}Sr_{0.33}MnO_3$ film of which the surface has been exposed to the ion beam etching.

Another way of making contact is to leave the $SrTiO_3$ tunnel barrier and the Co and Au films intact. The contact is then formed by a $La_{0.67}Sr_{0.33}MnO_3$ /$SrTiO_3$ /Co/Au stack. The processing scheme to realize this, is given in figure 6.6. A different mask is used for the step to wet etch the emitter. This leaves the Co and Au films at the position of the base contacts. (see figure 6.6A) The SiO_2 insulation layer, the Cr/Au bond pads and the Au contact leads are deposited and defined in the same way as for the type 1 processing. Pictures taken by microscope of devices after each of these process steps are shown in the appendix. This type of contact is called type 2.

To characterize the contact resistance for the two different types of base contacts, I-V characteristics are measured from one base contact to the other. We

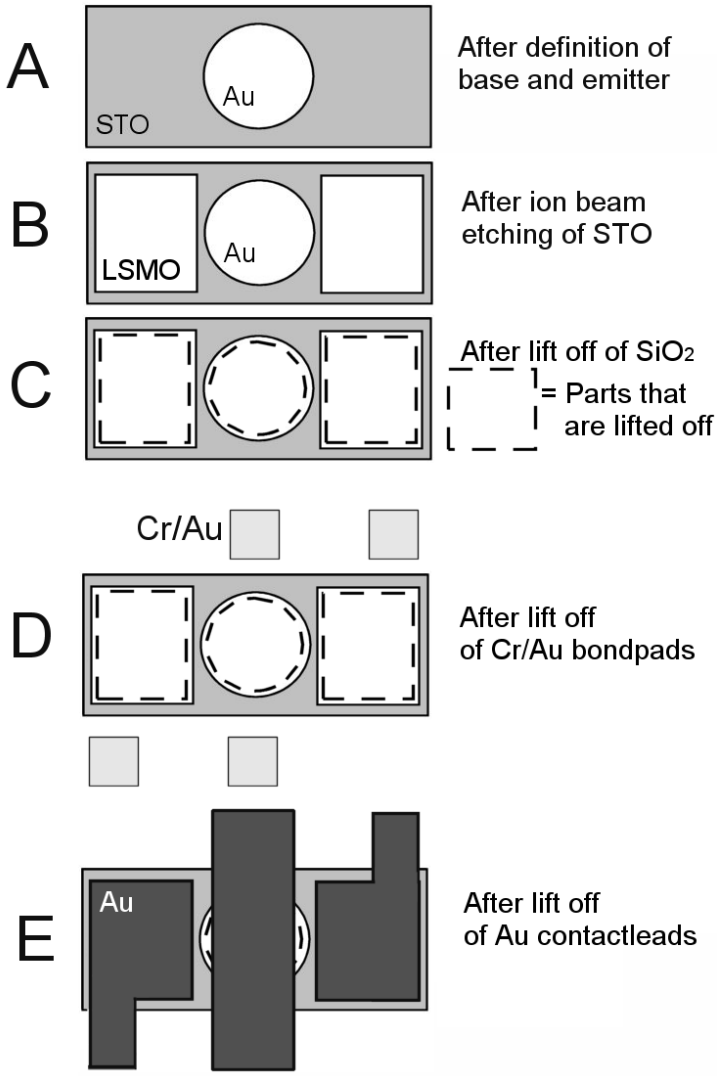

Figure 6.5: *Processing scheme to realize the MTT structure. In this processing scheme, contact to the base is realized by removal of the Au and Co by wet etching and removal of the $SrTiO_3$ tunnel barrier by ion beam etching. On top of the exposed $La_{0.67}Sr_{0.33}MnO_3$ base, a gold contact lead is sputtered that leads to a Cr/Au bond pad.*

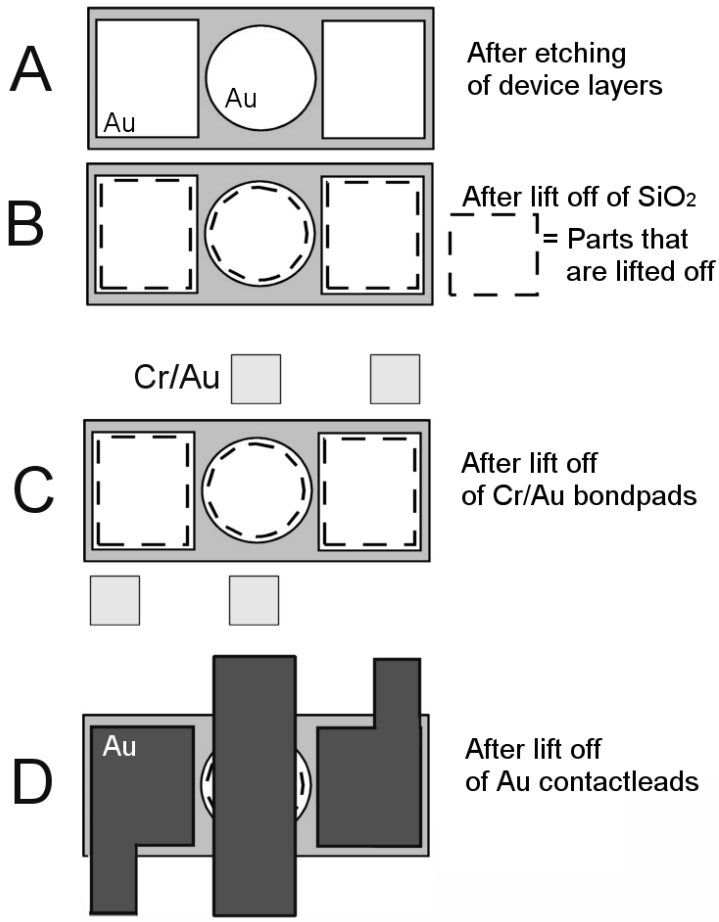

Figure 6.6: *Processing scheme to realize the MTT structure. For this processing scheme the contact to the base consists of the* $La_{0.67}Sr_{0.33}MnO_3$ */*$SrTiO_3$ */Co/Au stack that is deposited by PLD onto which a gold contact lead is sputtered that leads to the Cr/Au bondpads.*

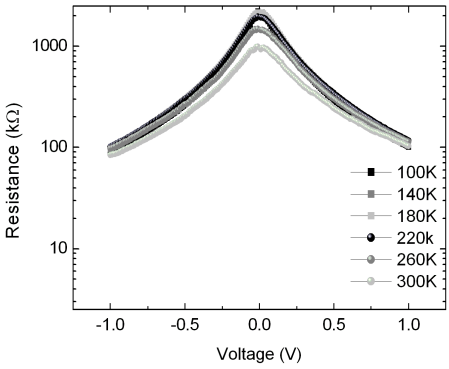

Figure 6.7: *Base to base resistance of a 15 nm thick base when the base contacts are formed by ion beam etching through the $SrTiO_3$ barrier, using the process shown in figure 6.5*

name the resistance that is measured in this way, the base to base resistance. So this base to base resistance should be approximately twice the resistance of the base and the base contact (2·[R2+R3]) that are shown in figure 6.4. (deviations from this can be expected when the current through the base contacts or through the tunnel barrier is inhomogeneous or when the current through the substrate is not negligible)

The first type of base contact, is the one in which the tunnel barrier is removed by ion beam etching. The sample that we discuss has a $La_{0.67}Sr_{0.33}MnO_3$ base with a thickness of 15 nm. The $La_{0.67}Sr_{0.33}MnO_3$ is grown with a laser fluence of 3 J/cm^2 and a repetition rate of 1 Hz at an oxygen pressure of 0.35 mbar. These are the same set of deposition settings as used for LSMO 1 in chapter 3. The $SrTiO_3$ barrier of this sample is about 5 nm thick. We use 4 minutes of ion beam etching time to remove the tunnelbarrier. At an etch rate of 1.4 ± 0.1 nm, this should be sufficient to remove the tunnel barrier and 1 ± 0.4 nm of the $La_{0.67}Sr_{0.33}MnO_3$. From the I-V characteristic measured from base contact to base contact we determine the base to base resistance. This resistance is shown in figure 6.7. The base to base resistance is in the order of a MΩ around zero voltage and decreases with increase of voltage. When the voltage is in the order of 1V the resistance reduces to about 100 kΩ. The resistance increases with decreasing temperature. From the resistivity of the $La_{0.67}Sr_{0.33}MnO_3$ and the size of the $La_{0.67}Sr_{0.33}MnO_3$ strip we expect a resistance for the $La_{0.67}Sr_{0.33}MnO_3$ strip between the base contacts in the order of $1{\cdot}10^2\Omega$ at 100 K and 1kΩ at room temperature. So the resistance that we measure from base to base is much higher then the the resistance that we ex-

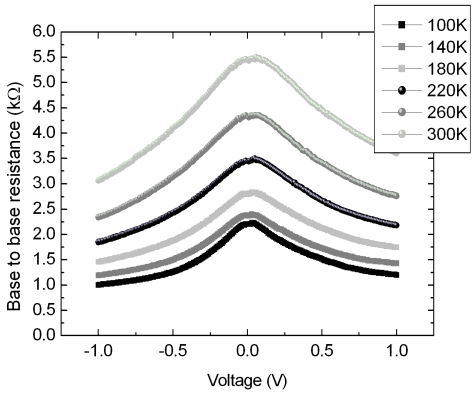

Figure 6.8: *Base to base resistance of a 10 nm thick base when the $La_{0.67}Sr_{0.33}MnO_3$ / $SrTiO_3$ / Co/ Au stack forms the base contact. This is contact type 2; the processing scheme to realize this is shown in figure 6.6*

pect for the $La_{0.67}Sr_{0.33}MnO_3$ strip. This shows that the sputtered Au contact to the $La_{0.67}Sr_{0.33}MnO_3$ has a very high resistance. It has been reported that ion beam etching can destroy the crystal lattice and the stoichiometry of a perovskite surface thereby drastically changing the resistance of that surface.[104] We believe that the ion beam etching has drastically increased the resistance of the $La_{0.67}Sr_{0.33}MnO_3$ surface in our case as well.

In order to avoid damage by the ion beam etching, we choose not to wet etch the Co and Au gold film and use the $SrTiO_3$ /Co /Au stack as base contact. This type of contacts was discussed as type 2. (Processing scheme shown in figure 6.6) When we make the area of the base-contacts ($6.7{\cdot}10^4 \mu m^2$ for 150 μm emitter) much larger than the area of the emitter ($1.7{\cdot}10^4 \mu m^2$ for 150 μm emitter) we should expect a base contact resistance that is lower (a factor of 4 for 150 μm emitters and a larger factor for smaller emitters) than the resistance of the emitter tunnel barrier. The sample, that we discuss here is processed in the way shown in figure 6.6. The 10 nm $La_{0.67}Sr_{0.33}MnO_3$ base is deposited with the same deposition parameters as the previously discussed sample. The tunnel barrier is about 5 nm thick. The base to base resistance that we find is shown in figure 6.8. The resistance is 2 to 3 orders lower then for the ion beam etched contacts. The resistance drops with decreasing temperature. Due to the inhomogeneity of the current through the emitter tunnel barrier and the base contact tunnel barrier, the resistance is difficult to interpret, but it is clear that this type of contact has a much lower resistance than the ion beam etched contact and is therefore preferable.

For one of the MTT's that will be discussed in the next section, another type of contact is used. We call this contact type 3. In this case, the contact is realized by wet etching of the Co and Au emitter layers to expose the $SrTiO_3$ tunnel barrier. Then a Au film is sputtered on top of the $SrTiO_3$ and wire bonds are placed on top of this Au film. (not on the bond pad but on top of the base itself) So this contact consists of $La_{0.67}Sr_{0.33}MnO_3$ /$SrTiO_3$ (both deposited by PLD) on which a Au layer is sputtered. So like in contact type 2 the perovskites have not been exposed to ion beam etching and the tunnel barrier is intact, but in this case the Co and Au, that have been deposited by PLD have been removed by wet etching. The processing scheme is identical to that shown in figure 6.5 but the ion beam etch step of the $SrTiO_3$ tunnel barrier is omitted.

6.3 Characterization of the magnetic tunnel transistor

In this section, the electrical behavior of the epitaxial magnetic tunnel transistors will be discussed. The first MTT, that we will discuss is grown on a 0.05 Wt% doped $SrTiO_3$ substrate and consists of a 10 nm $La_{0.67}Sr_{0.33}MnO_3$ base layer and a 4.7 nm $SrTiO_3$ tunnel barrier. The Co emitter and the Au cap layer are about 7 nm each. We will name this magnetic tunnel transistor MTT 1. Both the $La_{0.67}Sr_{0.33}MnO_3$ and $SrTiO_3$ film are grown with a laser energy density of 1 J/cm^2 and a repetition rate of 1 Hz. The oxygen deposition pressure is 0.3 mbar. The emitter has a diameter of 100 μm. Further deposition conditions are shown in table 6.9. The contact to the base is the contact type 3, discussed in the previous section.

First we will discuss the behavior of this structure at a temperature of 100 K. Figure 6.10 (a) shows the emitter current as function of the emitter voltage as measured in a 4 point geometry. Negative emitter bias means that electrons are injected from the emitter over the tunnel barrier into the base. (Note that this definition for the polarity is opposite to the one used in chapter 5) The emitter current shows the non linear dependence on the voltage that is expected for the tunnel barrier. The resistance of the tunnel barrier for a temperature of 90 K is plotted in figure 6.11. The resistance is an order higher then the junctions discussed in chapter 5. From the resistivity of the $La_{0.67}Sr_{0.33}MnO_3$ and from the thickness of the $La_{0.67}Sr_{0.33}MnO_3$ film, we calculate a sheet resistance of 400 Ω at 100 K. Using the criterium that the current density through the tunnel barrier can be regarded homogeneous when the tunnel barrier resistance is more then ten times the sheet resistance of the electrodes, we can conclude that we can expect a homogeneous current density through the tunnel barrier for an emitter voltage of up to -0.9 V. In addition to the emitter current, the collector current is measured. This measurement is shown in figure 6.10 (b). The collector current is below $5{\cdot}10^{-12}$A up to an emitter voltage of -600 mV.

Description of samples.		MTT1	MTT2
Nb doping concentration of substrate		0.05 Wt%	0.1Wt%
Diameterof emitter		100 µm	150 µm
LSMO Thickness		10 nm	10nm
LSMO deposition conditions	Oxygen pressure	0.3mbar	0.3 mbar
	Substrate temperature	750°C	750°C
	Laser frequency	1 Hz.	1 Hz
	Laser energy density	1.0 J/cm^2	1.0 J/cm^2
	Target to substrate distance	40mm	40mm
STO Thickness		4.7 nm.	4.7 nm.
STO deposition conditions	Oxygen pressure	0.3mbar	0.3mbar
	Substrate temperature	750°C	750°C
	Laser frequency	1 Hz.	1 Hz.
	Laser energy density	1.0 J/cm^2	1.0 J/cm^2
	Target to substrate distance	40mm	40mm
Cobalt thickness		7 nm.	No cobalt
Cobalt deposition conditions	Pressure	10^{-7} mbar	
	Substrate temperature	RT	
	Laser frequency	5 Hz.	
	Laser energy density	6.0 J/cm^2	
	Target to substrate distance	40mm	
Gold thickness		7 nm.	20 nm.
Gold deposition conditions	Pressure	10^{-7} mbar	10^{-7} mbar
	Substrate temperature	RT	RT
	Laser frequency	5 Hz.	5 Hz.
	Laser energy density	6.0 J/cm^2	6.0 J/cm^2
	Target to substrate distance	40mm	40mm

Figure 6.9: *Description of the samples MTT 1 and MTT 2.*

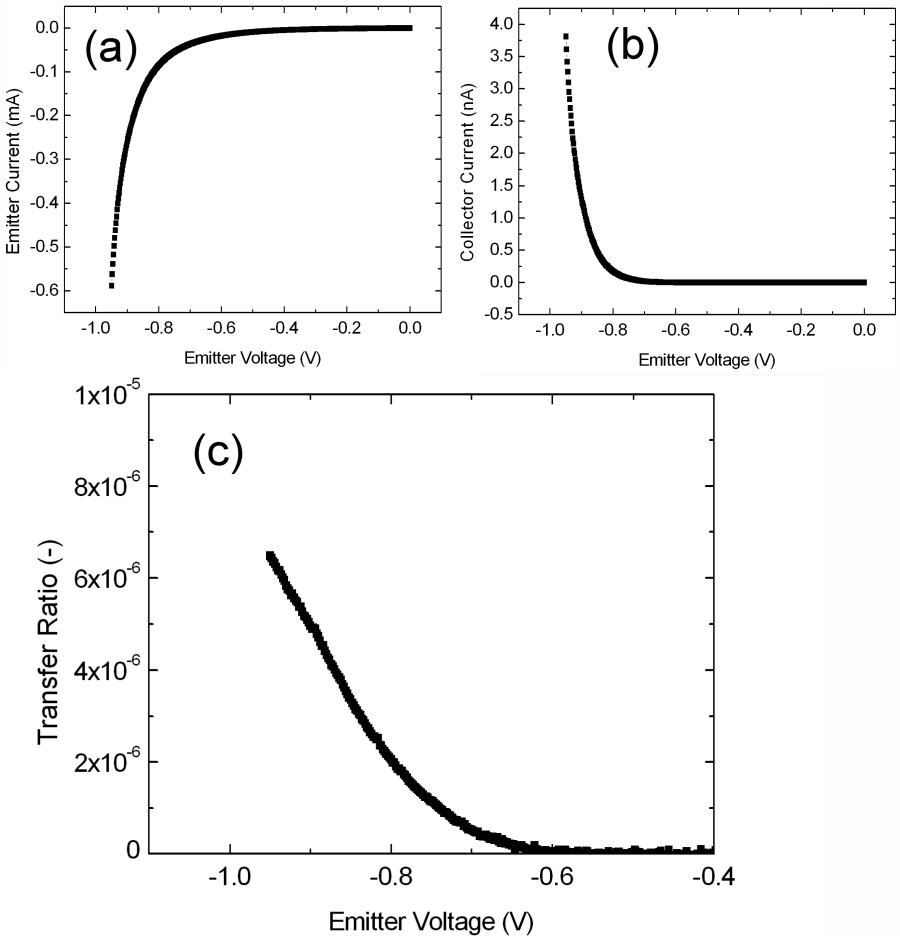

Figure 6.10: *Emitter current (a), collector current (b), and their ratio (Ic/Ie) (c) as function of the emitter voltage, measured at 100 K for MTT 1 (Nb:$SrTiO_3$ / $La_{0.67}Sr_{0.33}MnO_3$ / $SrTiO_3$ / Co/ Au). No voltage is applied between base and collector.*

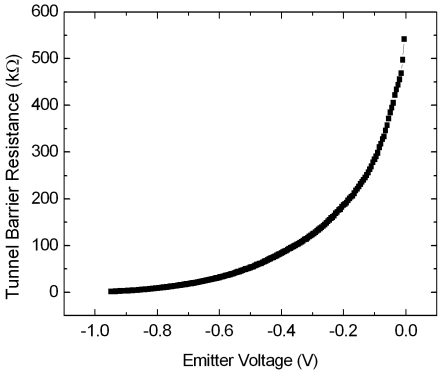

Figure 6.11: *Tunnel barrier resistance at 90 K for MTT 1 (Nb:$SrTiO_3$ / $La_{0.67}Sr_{0.33}MnO_3$ / $SrTiO_3$ / Co/ Au).*

Around -650 mV a collector current is observed. The current increases rapidly with increase of emitter voltage to reach 4.4 nA at -950 mV. The collector current is divided by the emitter current to obtain the transfer ratio of the injected electrons. This transfer ratio is shown in figure 6.10 (c). At -950 mV we observe a transfer ratio of $6.5 \cdot 10^{-6}$.

Before concluding that the observed collector current is due to collection of hot electrons, that have traversed the base and the $La_{0.67}Sr_{0.33}MnO_3$ / Nb:$SrTiO_3$ Schottky barrier, other possible causes have to be considered. The collector current could in principle be the leakage current of the diode instead of a hot electron current. The diode characteristic and the voltage that is created over the base during the measurement are investigated to determine the leakage current through the diode. Since the tunnel barrier is connected in a four point configuration, both the sense voltage and the source voltage are attained. Figure 6.12 shows an electrical scheme for the MTT measurement, in which the tunnel barrier is connected in the four point geometry. The source voltage is the voltage that is applied by the voltage source. If we assume that the current through the tunnel barrier is homogeneous, then the sense voltage is the voltage that drops over the tunnel barrier. If we assume that the tunnel barrier resistance, the base resistance and the resistance of the contact to the base (R1, R2 and R3 in figure 6.4) are the dominating resistances, then we can calculate the voltage that drops over the base and the base contact by subtracting the sense voltage from the source voltage. (V_{base}=V_{source}-V_{sense}). The voltage that drops over the base and the base contact is shown in figure 6.13 as function of the emitter voltage for a temperature of 90 K. In the figure we see that

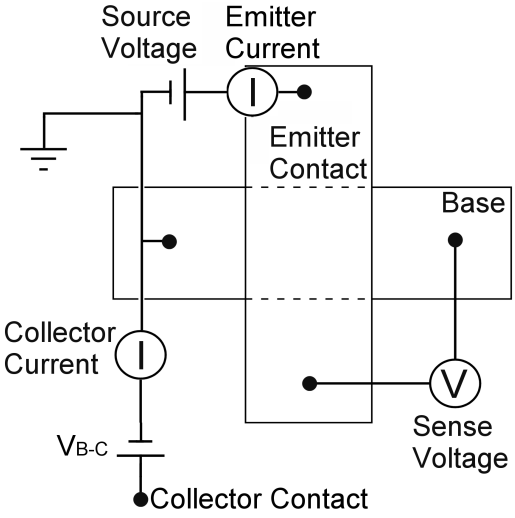

Figure 6.12: *Electrical scheme for the MTT measurement in which the tunnel barrier is connected in a four point geometry. (V_{B-C} is the voltage, that is applied between base and collector.*

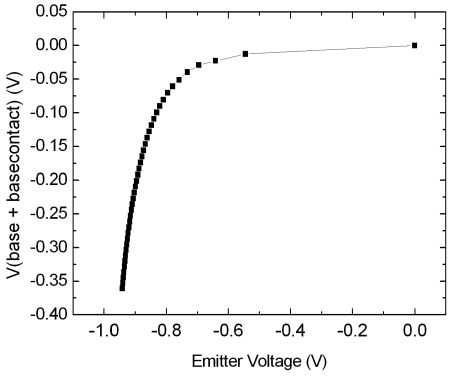

Figure 6.13: *Voltage drop over the base and the base contact for MTT 1 ($Nb{:}SrTiO_3$ / $La_{0.67}Sr_{0.33}MnO_3$ / $SrTiO_3$ / Co / Au) at 90 K.*

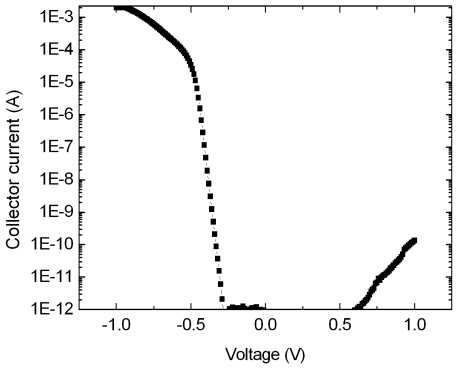

Figure 6.14: *I-V characteristic of collector diode for MTT 1 (Nb:$SrTiO_3$ / $La_{0.67}Sr_{0.33}MnO_3$ / $SrTiO_3$ / Co / Au) at 100 K.*

at a sense voltage of 950 mV, the source voltage is 360 mV higher. So we can estimate the voltage that drops over the base leg (the one that is connected as source), to be 360 mV. Figure 6.14 shows the I-V characteristic of the diode at 100 K. The curve shows that the reverse current through the diode at 360 mV is below $1{\cdot}10^{-12}$A. For a leakage current of 4.4 nA, the diode would have to be biased at more than 1 V. So the leakage current that is expected at a sense voltage of 950 mV is three orders lower than the collector current that we measure. Therefore, we conclude that the collector current that we observe is not caused by leakage in the diode, but by collection of hot electrons.

Figure 6.15 shows the emitter current (a), collector current (b) and transfer ratio (c) for a temperature range from 90 to 150 K. For all temperatures we observe a collector current above 650 mV. The curves for the transfer ratio for 90 K up to 130 K, show much resemblance. The transfer ratio decreases with increase of temperature. Some of the curves show a two level fluctuation. This fluctuation is not observed in the emitter current, but in the collector current at a current of approximately 1.5 nA. It is caused by the current meter that measures the collector current. This meter switches its range back and forth when the collector current is about 1.5 nA. For 140 K and more noticeable for 150 K, (see figure 6.16) the transfer ratio rises sharply above a certain threshold voltage. (indicated with an arrow in figure 6.15) This is due to thermal leakage in the reverse biased diode. The diode characteristic and the voltage drop over the base for a temperature at 150 K indicate this. The voltage that drops over the base leg that is connected as source, is shown in figure 6.17. The figure shows that, when a voltage of 940 mV is applied over the emitter,

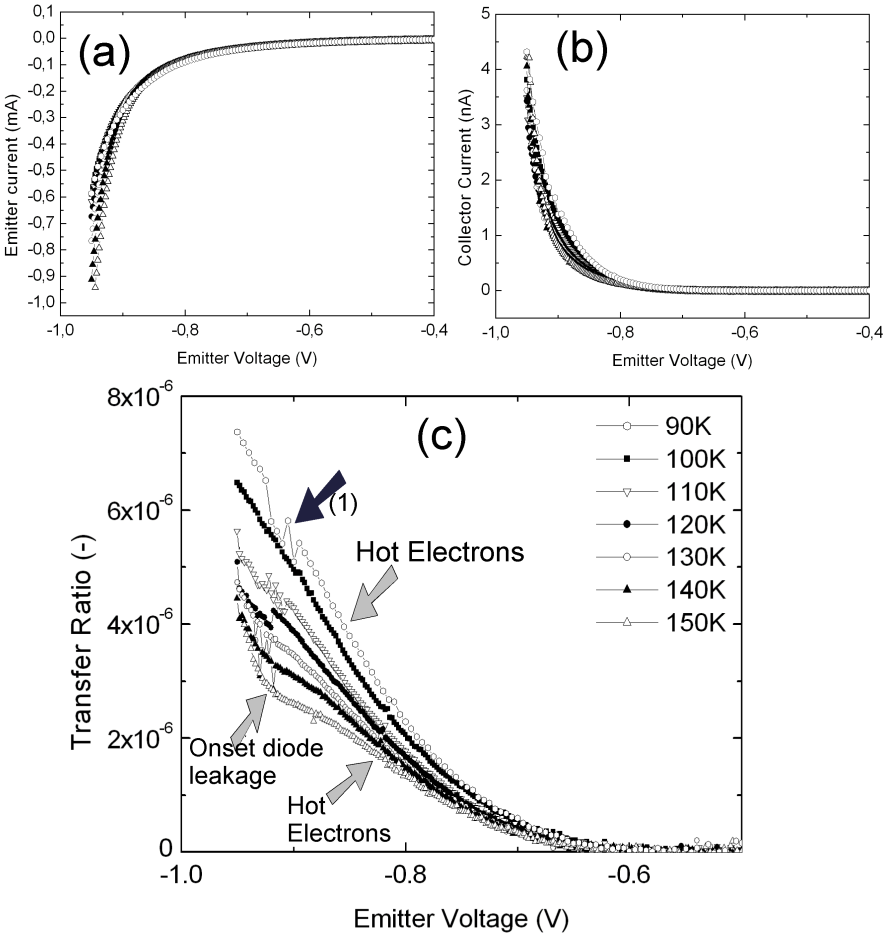

Figure 6.15: *Transfer ratio for a temperature range from 100 to 150 K for MTT 1 ($Nb{:}SrTiO_3$ / $La_{0.67}Sr_{0.33}MnO_3$ / $SrTiO_3$ / Co / Au). Arrows indicate the parts of the curves for which the collector current is identified as a hot electron current, and the onset of the leakage of the diode. The arrow indicated with (1) shows a two level fluctuation, that is caused by switching of the range of the current meter that measures the collector current.*

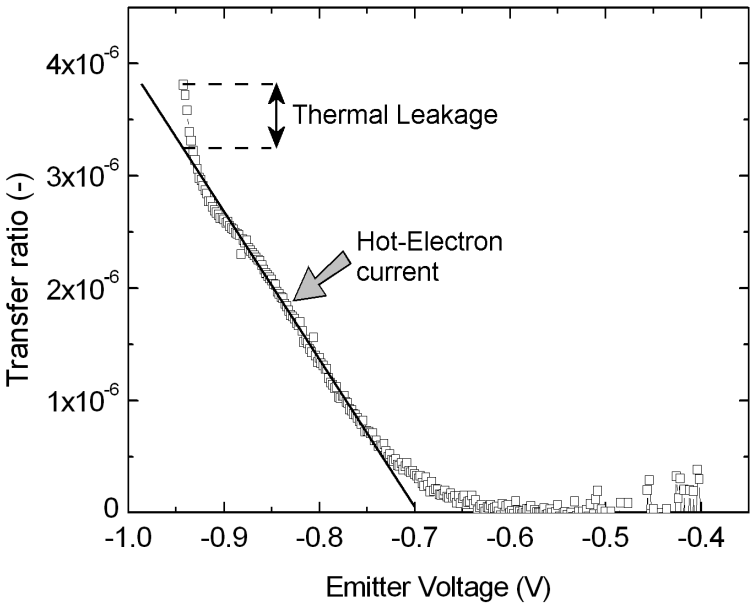

Figure 6.16: *Transfer ratio for a temperature of 150 K for MTT 1 (Nb:$SrTiO_3$ / $La_{0.67}Sr_{0.33}MnO_3$ / $SrTiO_3$ / Co / Au).*

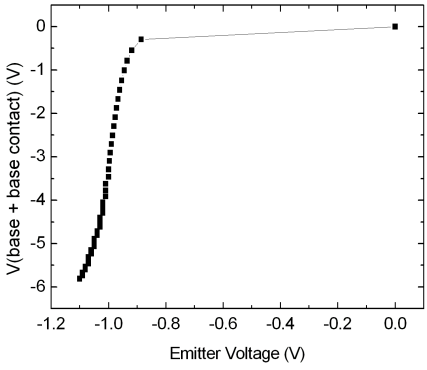

Figure 6.17: *Voltage drop over the base for MTT 1 (Nb:$SrTiO_3$ / $La_{0.67}Sr_{0.33}MnO_3$ / $SrTiO_3$ / Co / Au) at 150 K.*

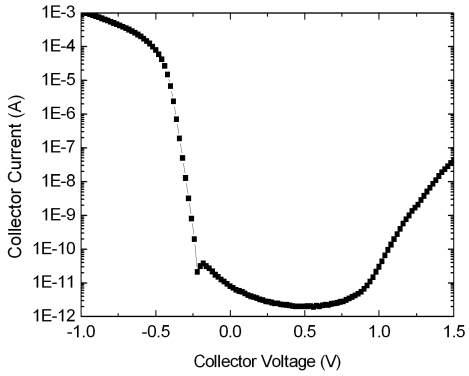

Figure 6.18: *I-V characteristic of the collector diode for MTT 1 ($Nb:SrTiO_3$ / $La_{0.67}Sr_{0.33}MnO_3$ / $SrTiO_3$ / Co / Au) at 150 K.*

the voltage drop over the base is 1.0 V. This voltage drop over the base and the base contact increases rapidly as the emitter voltage increases. Figure 6.18 shows the I-V characteristic of the collector diode at 150 K. The figure shows a strong increase in the reverse current around 1 V. We find a reverse current of 0.5 nA at 1150 mV, which increases to 4 nA at 1300 mV. So is this reverse current of the size that it explains the knee that is observed for the transfer ratio? Figure 6.16 shows that the transfer ratio at 150 K at 940 mV is $3.7{\cdot}10^{-6}$. When we extent the straight part of this curve to -940 mv, we find that the transfer ratio would be $3.3{\cdot}10^{-6}$if this knee would be absent. This difference in the transfer ratio corresponds to an extra collector current of 3nA. This is in the same order as the reverse current of the diode at 1100 mV. So the non-linear increase of the transfer ratio for T=150 K at an emitter voltage close to -1 V can be identified as a reverse current through the diode due to the bias voltage over the diode.

At higher temperatures the voltage drop over the base as well as the reverse current through the diode increase. In figure 6.19, we see that the leakage current through the diode obscures the collected hot electron current for higher temperatures. So the voltage range, in which the hot electron current is not obscured by a leakage current through the diode, is gradually reduced with increasing temperature.

The next step is to apply a magnetic field to analyze the spin dependence of the hot electron transport. Figure 6.20 (a) shows the dependence of the emitter current on the applied field, measured at a temperature of 90 K. When the field is swept form -140 Oe to 0 a gradual decrease of the emitter current

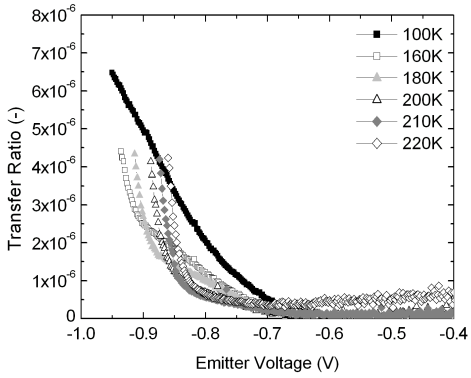

Figure 6.19: *Transfer ratio for a series of temperatures for MTT 1 (Nb:$SrTiO_3$ / $La_{0.67}Sr_{0.33}MnO_3$ / $SrTiO_3$ / Co / Au).*

is observed. As the field is increased in the opposite direction, the emitter current decreases up to a field of 17 Oe. Upon further increase of the field, the emitter current gradually increases. At large field, when the magnetization of the magnetic layers is aligned parallel, the emitter current is higher then at anti-parallel configuration. So the TMR is positive. The TMR is about +2.3%. We do not observe sharp switching of the layers. When the field is swept back from 140 Oe to -140 Oe, the peak is observed at -13 Oe and the TMR is about +2.8%. Around -43 Oe there is a jump in the emitter current, that is probably caused by an instability of the tunnel barrier. For both directions of the field sweep, we observe a change of emitter current when the field is decreased to zero. This shows that the magnetization of the layers changes in a decreasing field. So either the field is not applied in the magnetic easy direction of the layers or the layers are magnetically coupled.

The collector current also shows a field dependence. The collector current for a field sweep from -140 to +140 Oe is shown in figure 6.20 (b). The collector current shows the same field dependence as the emitter current. It also shows a minimum at 17 Oe. The relative change in the collector current is 2% just like the relative change of the emitter current. That means that the change in the collector is not caused by the spin dependence of the transport through the base, but simply due to the field dependence of the emitter current. The field dependence of the transfer ratio in figure 6.20 (c), shows that indeed the transfer ratio does not relate to the switching behavior of the magnetic layers. The measurement suffers from noise. The transfer ratio has a signal to noise ratio of about 3%. So we can conclude that if there is any dependence of the

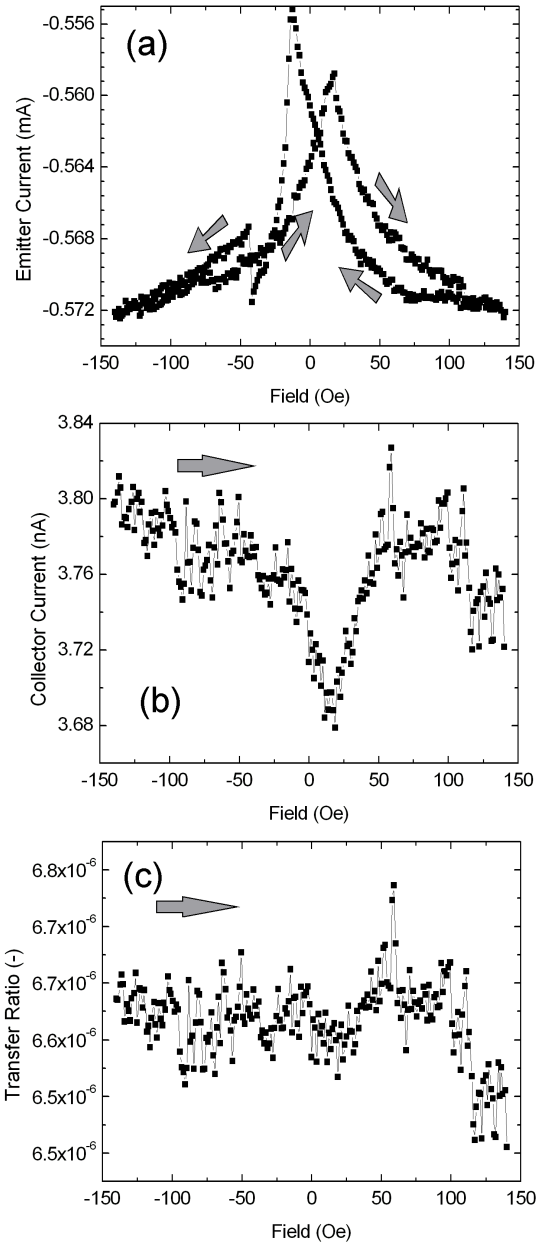

Figure 6.20: *Emitter current (a), collector current (b) and transfer ratio (c) as function of the applied field for MTT 1 (Nb:$SrTiO_3$ / $La_{0.67}Sr_{0.33}MnO_3$ / $SrTiO_3$ / Co / Au) at an emitter bias of -950 mV and a temperature of 90 K. The arrows denote the direction in which the magnetic field is varied.*

transfer ratio on the applied field, it is less then 3%

The next sample that we describe is a transistor that has a non magnetic emitter of gold. We name this transistor MTT 2. The substrate is 0.1 Wt% doped. The $La_{0.67}Sr_{0.33}MnO_3$ film is 25 atomic layers (10nm) thick as determined by RHEED. The $SrTiO_3$ thickness is determined by RHEED, to be 12 atomic layers (4.7 nm). The Au emitter is about 20 nm thick and has a diameter of 150 μm. More details are given in table 6.9. Figure 6.21 shows the emitter current, collector current and transfer ratio for MTT 2. The characteristics resemble those measured for MTT 1.

Analysis of the Metal Base Transistor (MBT) measurement is another way to verify that the collector current is a hot electron current. In this measurement, the collector current is measured while a constant current is applied through the tunnel barrier and the voltage over the diodes is swept. At zero emitter current this will result in the I-V characteristic of the diode. The way in which an applied emitter current changes this characteristic can give information about the origin of the collector current. Figure 6.22 shows the MBT measurement for MTT 2 measured at 150 K. The curve for zero emitter current is the I-V characteristic of the diode. If an applied emitter current does not change the bias over the diode (negligible resistance of base and base contact), but only causes collection of hot electrons, then the effect of increasing the emitter current is to add a current to the I-V curve. In other words: to move the I-V curves along the current axis. If the resistance of the base and the base contact is not negligible, then the emitter current creates a voltage drop over the diode. (see figure 6.4) If no hot electrons are collected and this is the only effect of the emitter current on the diode current, the I-V curve moves along the voltage axis when an emitter current is applied. The MBT measurement shows that an increase of the emitter current, increases the collector current and that this is due to both a shift over the current axis and a shift over the voltage axis. So both effects are present for MTT 2. The collector current from the MBT measurement at zero collector voltage corresponds to the collector current shown in figure 6.21. For an emitter current of 0.5 mA (emitter voltage of -950 mV, collector current of 1 nA) and 1 mA we see that the increased collector current is not caused by the shift of the I-V characteristic of the diode along the voltage axis, but by a shift along the current axis. This shows that the collector current that is measured at 150 K for an emitter current of up to 1 mA can be identified as a hot electron current. For higher emitter current, the collector current for zero applied collector voltage is formed by a combination of hot electrons and leakage current through the diode.

Just like for MTT 1, figure 6.21 shows that the transfer ratio increases with an increase of the applied emitter voltage. The onset at which the collector current is observed however, is about 750 mV and does not depend significantly on the temperature. So the onset is about 100 mV higher than for MTT 1. Like in MTT 1, the transfer ratio decreases with increase of the temperature.

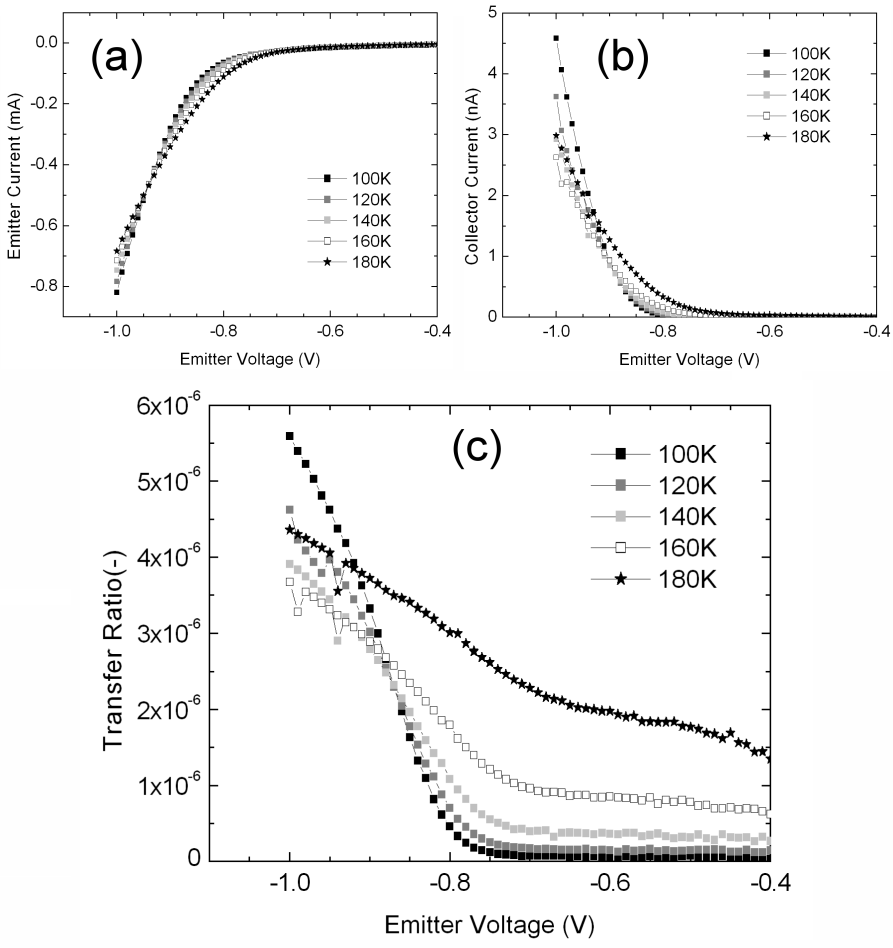

Figure 6.21: *Emitter current (a), collector current (b) and transfer ratio (c) for MTT 2 (Nb:$SrTiO_3$ / $La_{0.67}Sr_{0.33}MnO_3$ / $SrTiO_3$ / Au).*

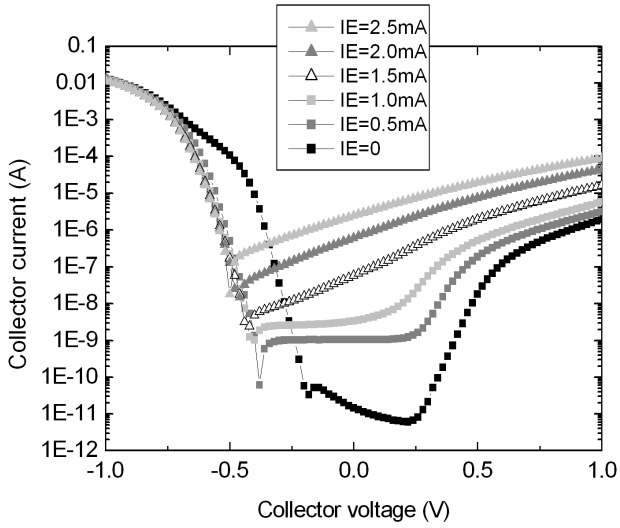

Figure 6.22: *Metal Base Transistor (MBT) measurement for MTT 2 (Nb:$SrTiO_3$ / $La_{0.67}Sr_{0.33}MnO_3$ / $SrTiO_3$ / Au) at 150 K. In this measurement the collector current is measured, while the collector voltage is swept and a constant emitter current is applied.*

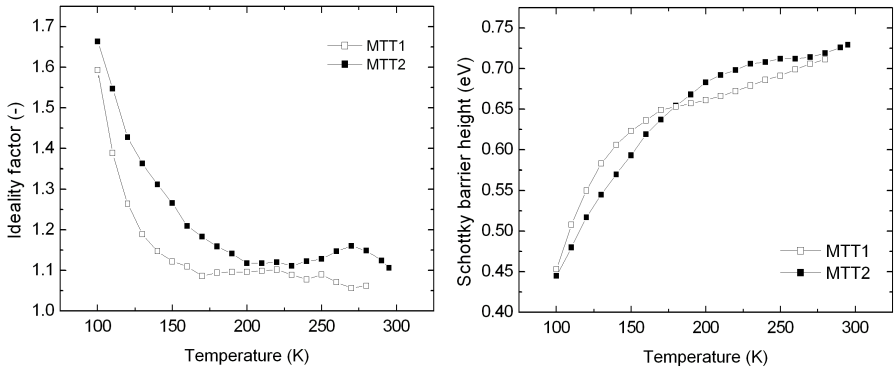

Figure 6.23: *Diode characteristics for the collector diodes in MTT 1 (Nb:$SrTiO_3$ / $La_{0.67}Sr_{0.33}MnO_3$ / $SrTiO_3$ / Co/ Au) and MTT 2 (Nb:$SrTiO_3$ / $La_{0.67}Sr_{0.33}MnO_3$ / $SrTiO_3$ / Au). The left panel shows the temperature dependence of the ideality factor. The right panel shows the temperature dependence of the Schottky barrier height.*

6.4 Discussion

For both MTT structures we observed collection of hot electrons. This hot electron current is observed when the emitter voltage exceeds a certain value. Since the emitter voltage determines the energy (q·V) of the injected hot electrons, the onset correlates to the energy above which hot electrons are collected. In chapter 4, section 4.5 we discussed the role of the low permittivity layer on the collection of the electrons. Two extreme cases were discussed. In one case the hot electrons would be blocked by the low permittivity layer, and the collector would collect electrons with an energy above the flatband voltage of the diode. In the other case the low permittivity layer would be transparent for hot electrons and the electrons with a energy above the effective Schottky barrier height would be collected. The Schottky barrier height and ideality factor, that are determined (by fitting the forward current to the expression for thermionic emission in Schottky diodes) for the diodes in these two structures are shown in figure 6.23. The Schottky barrier height for both diodes show almost similar temperature dependence. When the temperature increases from 100 to 150 K, we find the Schottky barrier height to increase from 450 mV to roughly 600 mV. For MTT1 (MTT2) however, the onset is 650 mV (750 mV) and does not depend significantly on the temperature for temperatures of 100 to 150 K. So the onset for collection of hot electrons is higher then the effective Schottky barrier height and does not show the temperature dependence that the effective Schottky barrier height shows. So from the observation that the

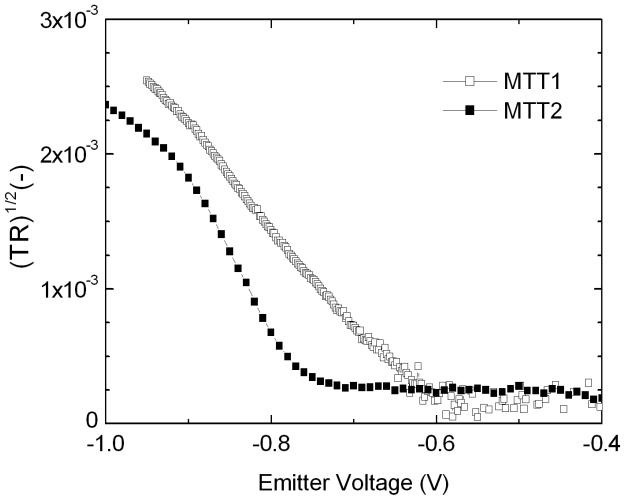

Figure 6.24: *Square root of the transfer ratio for MTT 1 (Nb:$SrTiO_3$ / $La_{0.67}Sr_{0.33}MnO_3$ / $SrTiO_3$ / Co/ Au) and MTT 2 (Nb:$SrTiO_3$ / $La_{0.67}Sr_{0.33}MnO_3$ / $SrTiO_3$ / Au) at 100 K. The onset for collection of hot electrons in MTT 2 is 100 mV higher then for MTT 1*

onset for collection of hot electrons is higher then the effective Schottky barrier height, we conclude that the low permittivity layer blocks hot electrons. However the Schottky barrier height that was determined for the 0.01 Wt% doped substrates was found to be 950 mV at room temperature. From this, we expect the flatband voltage to be higher then 950 mV. So the onset does not correspond with the flatband voltage either. From this we conclude that the low permittivity layer does block hot electrons but not to the extent that the onset for collection, is defined by the flatband voltage.

When the samples MTT 1 and MTT 2 are compared, the striking difference is the difference that we find in the onset of the collector current. For clarity the square root of the transfer ratio for MTT 1 and MTT 2 at 100 K is plotted in figure 6.24. For MTT 2, this onset is about 100 mV higher than for MTT 1. Since this onset is correlated to the blocking of hot electrons by the Schottky barrier, the blocking energy of this diode seems to be 100 meV higher than for the diode in MTT 1. Figure 6.23 however, shows that the difference in the Schottky barrier height between both diodes, is less then 30 mV. In the temperature range in which hot electrons are observed the Schottky barrier of MTT 1 is somewhat higher than the barrier of MTT 2. So the properties

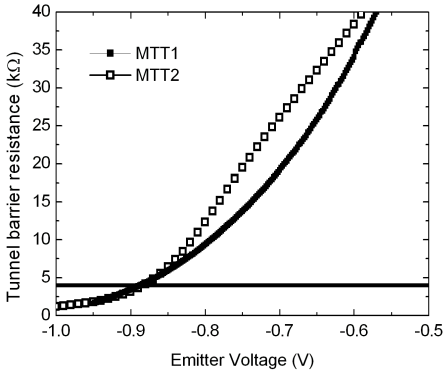

Figure 6.25: *Tunnel barrier resistance of MTT 1 (Nb:$SrTiO_3$ / $La_{0.67}Sr_{0.33}MnO_3$ / $SrTiO_3$ / Co/ Au) and MTT 2 (Nb:$SrTiO_3$ / $La_{0.67}Sr_{0.33}MnO_3$ / $SrTiO_3$ / Au) at 100 K.*

of the collector diode do not explain the difference in the onset that we find. The difference in the onset could be explained if the current in MTT 1 is more homogeneous than in MTT 2. The average voltage over the tunnel barrier in MTT 2 would be higher than the voltage in MTT 1 at the same sense voltage. Figure 6.25 shows that the resistance MTT 2 is a little higher than that of MTT 1. The $La_{0.67}Sr_{0.33}MnO_3$ bases of both samples have the same thickness and are grown under the same conditions, so we expect the same sheet resistance of 400 Ω at 100 K. At -750 mV the resistance of both tunnel barriers is more than 35 times the sheet resistance, so we can expect a homogeneous current through the tunnel barriers of both samples around 750 mV. The difference that we find in the onset in both samples can therefore not be explained by an inhomogeneous current density.

We observe collection of hot electrons in both samples. In both samples the regime in which we are able to observe the hot electrons is limited by a high reverse current in the diodes and a significant base resistance which creates a reverse voltage over the diodes. Nevertheless, there is a regime in which the hot electron current is not obscured by the reverse current in the diode. In this regime we observe that the transfer ratio decreases with increase of temperature. This is behavior that is expected for an MTT, as increase of temperature increases the scattering of the hot electrons in the base. In case of the MTT's discussed here, the dependence of the Schottky barrier on the temperature can also play a role in the temperature dependence of the transfer ratio. We also observe that an increase of energy of the injected electrons increases the transfer ratio. For both samples the $La_{0.67}Sr_{0.33}MnO_3$ is 10 nm thick. That means

that we do not have information on the dependence of the transfer ratio on the base thickness. The transfer ratio is determined by the scattering in the base and the efficiency of collection. The lack of information on the dependence of the transfer ratio on the thickness of the base makes it impossible to discriminate between the influence of the collection efficiency and that of the scattering on the transfer ratio. As a result of that we cannot estimate a value for the attenuation length of hot electrons in the $La_{0.67}Sr_{0.33}MnO_3$.

One of these MTT's has a ferromagnetic emitter. The magnetic tunnel junction of this MTT shows +2.8% TMR at an emitter voltage of -950 mV at 90 K. However we do not observe the transfer ratio of the MTT to depend on the relative orientation of the magnetization. There are a number of possible explanations for this.

1. It is possible that the difference of attenuation lengths for spin up and spin down hot electrons in $La_{0.67}Sr_{0.33}MnO_3$ is small. A high spin polarization at the Fermi-level does not guarantee that the attenuation length of hot electrons depends strongly on the spin orientation. It is also possible that the difference between the attenuation length of both types of electrons is small because the $La_{0.67}Sr_{0.33}MnO_3$ film is not grown with the optimized settings and is probably oxygen deficient.
2. Another possibility is, that the transfer ratio that is found, is mostly determined by a low collector efficiency and that the attenuation length of the hot electrons is longer than the thickness of the base so that there is little scattering in the base and thus also little spin dependence of the transport through the base. A low collector efficiency could be caused by the presence of the ILP layer. The energy of the hot electrons that are injected in the base is lower than the height of the ILP layer so the layer might reflect or scatter a large part of the hot electrons. It is possible that when the energy of the injected electrons is raised above the height of the ILP layer, the collector efficiency is drastically increased. Unfortunately if we apply higher emitter bias in the MTT structure that we prepared, the leakage current through the diodes obscures the hot electron current.
3. The TMR in the tunnel junction is only 2.8%. This could mean that both the $La_{0.67}Sr_{0.33}MnO_3$ /$SrTiO_3$ interface as well as the Co/$SrTiO_3$ interface have a low spin polarization. In that case the spin polarization of the injected electrons is low, which prevents a high field dependence of the collector current. When the low TMR is caused by a low spin polarization of the Co/$SrTiO_3$ interface, and the spin polarization of the $La_{0.67}Sr_{0.33}MnO_3$ /$SrTiO_3$ interface (above the Fermi-level) is reasonable, the tunnel current can still have a reasonable spin polarization. But in that case the spin polarization of the injected hot electron current is determined by the magnetization direction of the base and the dependence of the scattering in the base on the relative orientation of the magnetization of the electrodes would be small.

6.5 Conclusions

Collection of hot electrons is observed in epitaxial Nb:$SrTiO_3$ / $La_{0.67}Sr_{0.33}MnO_3$ / $SrTiO_3$ / Co magnetic tunnel transistors. The finite resistance of the base and the contact to the base cause a reverse bias of the collector diode when the electrons are injected. At temperatures above 150 K, this reverse bias causes a significant reverse current through the diode, which obscures the hot electron current.

Below 150 K there is a voltage regime in which the reverse leakage current is significantly lower than the collector current so that the collector current can be identified as a hot electron current. Hot electrons are collected when the emitter current exceeds a certain threshold voltage. For the MTT on the 0.05 Wt% doped substrate this voltage is about 650 mV, while for the MTT on the 0.1 Wt% doped substrate this threshold is about 750 mV. In conventional MTT's the onset of the hot electron current (emitter voltage above which hot electrons are collected) correlates with the height of the Schottky barrier of the collector diode. In the Nb:$SrTiO_3$ /$La_{0.67}Sr_{0.33}MnO_3$ diodes however, we have seen (chapter 4) that an Intrinsic Low Permittivity (ILP) layer forms at the diode interface. We find that the onset for the detection of hot electrons is higher then the effective Schottky barrier height. That means that the ILP layer partially reflects hot electrons.

When the voltage is increased, the transfer ratio increases. This due to the increase of the energy of the injected hot electrons. This causes an increase of the collector efficiency.
The transfer ratio decreases with increase of temperature. This is expected for an MTT in general, because the attenuation length of the hot electrons decreases with increase of temperature. In this MTT, the effective Schottky barrier height of the diode increases with increase of T, so a second explanation for the temperature dependence of the transfer ratio, could be that the collector efficiency decreases with increasing temperature.

For the MTT on the 0.05 Wt% (0.1Wt%) doped substrate, the transfer ratio is $7.4{\cdot}10^{-6}(4.6{\cdot}10^{-6})$ at an emitter bias of 950 mV and a temperature of 90 K (100 K). At this temperature and bias the collector current is a hot electron current. This transfer ratio is not only determined by the scattering of the hot electrons in the base, but also by the collection efficiency of the collector diode. We observe a hot electron current in two structures that have the same base thickness (10 nm). That means that it is not possible to determine the dependence of the transfer ratio on the base thickness in order to determine the attenuation length for hot electrons in $La_{0.67}Sr_{0.33}MnO_3$.

A dependence of the transfer ratio, on the relative orientation of the magnetization of the two ferromagnetic layers, is not observed. There are a number of possible explanations for this.

1. The attenuation length of the hot electrons is not strongly spin dependent.
2. The attenuation length of the hot electrons is large compared to the base thickness, so that there is only little scattering in the base.
3. The spin polarization of the injected electrons is either low or determined by the magnetic orientation of the $La_{0.67}Sr_{0.33}MnO_3$ base.

Insight in this subject can be attained when samples are prepared that have a different base thickness. This can give information about the attenuation length of the hot electrons in $La_{0.67}Sr_{0.33}MnO_3$.

The $La_{0.67}Sr_{0.33}MnO_3$ films in the MTT structures that have been discussed in this chapter have not been grown with the optimized settings for the $La_{0.67}Sr_{0.33}MnO_3$. Improvement can be expected when these optimized settings are used.

The hot electron current in the MTT's is obscured by a leakage current through the diodes. This current can be decreased by decreasing the voltage that drops over the base and the base contacts. This can be achieved by decreasing the resistance of the contacts to the base or by increasing the resistance of the tunnel barrier by either making it thicker or by decreasing the diameter. For a drastic decrease of the diameter, the wet etch step that is used for the definition of the emitter would have to be abandoned because of the under-etching. The leakage can also be decreased by improving the diode characteristics.

When the spin polarization of the injected electrons is low, it can be increased by choosing another material for the emitter and/or tunnel barrier. When this spin polarization is determined by the magnetization direction of the base, a non magnetic layer could be inserted between the base and the tunnel barrier.

The fact that the data about these MTT's is limited leaves much possibilities open. Further investigations are necessary to determine the correct explanation for the absence of the field dependence of the transfer ratio.

The results presented in this chapter show that hot electrons can be injected into an epitaxial thin $La_{0.67}Sr_{0.33}MnO_3$ film and that after these hot electrons have traversed the base, they can be selectively collected by using a Nb:$SrTiO_3$ / $La_{0.67}Sr_{0.33}MnO_3$ diode as an energy and momentum filter. This creates the possibility to study the spin dependent transport of hot electrons in $La_{0.67}Sr_{0.33}MnO_3$.

Chapter 7

Conclusions

The aim of the work presented in this thesis is to fabricate an epitaxial magnetic tunnel transistor (MTT) with a half-metallic $La_{0.67}Sr_{0.33}MnO_3$ base. half-metallic ferromagnets are promising materials for spintronic devices, in which the spin of electrons is exploited for the functionality of devices. In half-metallic materials, the spin polarization of the electrons at the fermi level is 100%. Magnetic tunnel junctions (MTJ's) based on $La_{0.67}Sr_{0.33}MnO_3$ have shown the highest TMR (1800%) reported so far. This TMR is measured at 4.2 K. Despite the $La_{0.67}Sr_{0.33}MnO_3$ Curie temperature of 360 K, the TMR of $La_{0.67}Sr_{0.33}MnO_3$ based MTJ's at room temperature is strongly reduced. This is due to the reduced spin polarization of the electrons at the $La_{0.67}Sr_{0.33}MnO_3$ interface and the interface sensitivity of the tunneling process. An MTT is sensitive to the spin polarization at the emitter interface and the spin dependence of the hot electron transport through the base. This means that an MTT with a $La_{0.67}Sr_{0.33}MnO_3$ base does not rely on the spin polarization at the $La_{0.67}Sr_{0.33}MnO_3$ /$SrTiO_3$ interface and that such an MTT should in principle function at room temperature.

The use of such a ferromagnetic oxide gives the possibility to create a MTT with an epitaxial base. In current magnetic tunnel transistors the base consists of poly crystalline layers. We anticipate that the absence of crystal boundaries in the base of an epitaxial MTT decreases the scattering of hot electrons in the base and thus increases the transmission and output current of the MTT.

To realize an epitaxial MTT, we have selected niobium doped $SrTiO_3$ substrates as an n-type semiconductor. $SrTiO_3$ is cubic and has a lattice parameter of 3.905 Å. Bulk $La_{0.67}Sr_{0.33}MnO_3$ is rhombohedral. The pseudo-cubic unit cell has an angle of 89.74°and a lattice parameter of 3.873 Å. This gives a very small lattice angle mismatch of 0.26°and a mismatch of the lattice constant of 0.8%, which allows epitaxial growth of $La_{0.67}Sr_{0.33}MnO_3$ on $SrTiO_3$ substrates. We

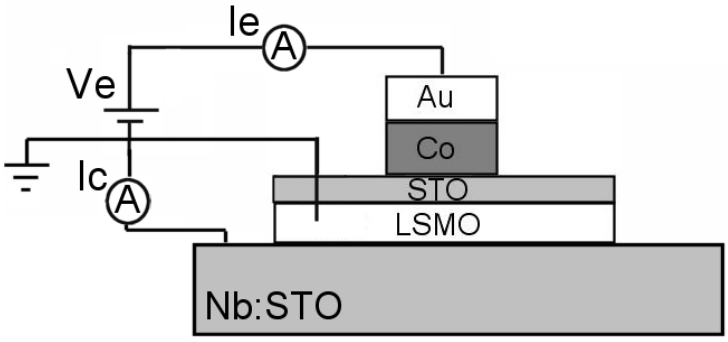

Figure 7.1: *Schematic view of the Magnetic Tunnel.*

selected $SrTiO_3$ as material for the tunnel barrier and Co as material for the emitter. A schematic view of the epitaxial magnetic tunnel transistor studied in this thesis is given in figure 7.1.

To realize this epitaxial MTT, the growth of the $La_{0.67}Sr_{0.33}MnO_3$ films by pulsed laser deposition was first investigated. The single crystal $SrTiO_3$ substrates that we use to grow the $La_{0.67}Sr_{0.33}MnO_3$ films on, are chemically treated to achieve a TiO_2 termination. Annealing of the substrates for an hour at 950°C results in relaxation of the substrate surface by decrease of the step edge density. In situ high pressure Reflective High Energy Electron Diffraction (RHEED) allows monitoring of the growth of the $La_{0.67}Sr_{0.33}MnO_3$ film. The RHEED indicates that the film grows in a layer by layer mode. Accordingly, atomic force microscopy (AFM) shows atomically smooth surfaces of the $La_{0.67}Sr_{0.33}MnO_3$ films. Transmission Electron Microscopy (TEM) images of the deposited films,(see figure 7.2) as well as X-ray diffraction (XRD) measurements, confirm that the films are epitaxial. We find that deposition of epitaxial films by imposing a layer by layer growth, is not extremely sensitive to deposition conditions, as we observed this for a wide range of deposition parameters. We do find the resistivity and magnetization of the films to depend strongly on the deposition parameters. Increase of magnetization goes hand in hand with a decrease of resistivity. Both the conductance and the coupling of the magnetic moments in $La_{0.67}Sr_{0.33}MnO_3$ is governed by the double exchange principle. This double exchange is suppressed in oxygen deficient films. Indeed we observed that if oxidation is promoted by increasing the energy density of the ablating laser spot, or by introducing time intervals during the deposition in which the deposition is paused, both the magnetization and the conductance are increased. For the $La_{0.67}Sr_{0.33}MnO_3$ films with the highest magnetization, the measured saturation magnetization (510 kA/m at 150 K) is close to what

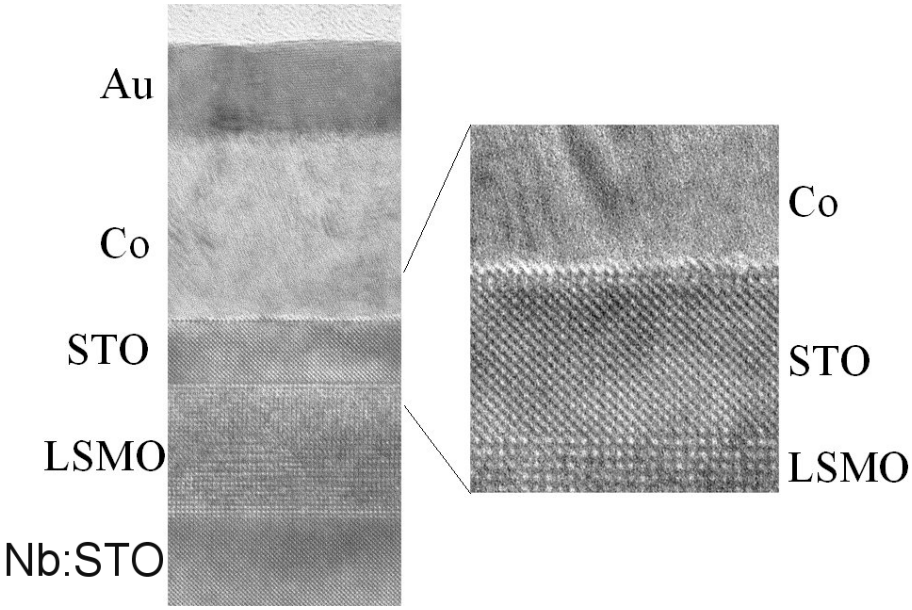

Figure 7.2: *Cross-sectional TEM image of the Magnetic Tunnel Transistor. From top to bottom the figure shows the Au cap layer, the Co emitter layer, the $SrTiO_3$ tunnel barrier layer and the $La_{0.67}Sr_{0.33}MnO_3$ base layer on top of the Nb doped $SrTiO_3$ substrate. The inset zooms in on the $La_{0.67}Sr_{0.33}MnO_3$ /$SrTiO_3$ /Co stack.*

is reported in literature (560-580) kA/m at 150 K). These films are deposited at an oxygen pressure of 0.35 mbar, a substrate temperature of 750°C, and a target to substrate distance of 40 mm. A laser energy density of 3.0 J/cm^2 is used and the laser is operated at a repetition rate of 1 Hz.

Whereas $SrTiO_3$ is an insulator, doping with Nb makes the $SrTiO_3$ an n-type semiconductor. The chemical treatment to achieve the TiO_2 termination can still be applied on the Nb doped single crystal substrates. But for niobium doping concentrations of 0.05 Wt% and higher we observe that annealing at 950°C causes the formation of islands on the substrate surface. Since these islands are not formed on undoped substrates, these islands are likely to be formed by niobium that diffuses to the surface. Therefore, the substrates with a doping concentration of 0.05 Wt% and higher are not annealed. From electrical four point measurements of the substrates we determine the resistivity of the substrates. The temperature dependence of the resistivity is in agreement with a temperature independent doping concentration and a $T^{-2.7}$ dependence of the mobility, as reported in literature. From the resistivity and the reported mobility, we calculate the carrier concentration in the substrates. For the 0.05 and 0.1 Wt% doped substrates, we find that the carrier concentration has approximately the same value as the niobium doping concentration, which confirms that the replacement of a Ti atom by Nb donates one free electron. For the 0.01 Wt% doped substrates we find a inhomogeneous doping concentration. The doping concentration in these substrates varies from substrate to substrate as well as within a single substrate, making reproducible experiments more difficult.

In order to realize the MTT a Schottky barrier is needed between the $La_{0.67}Sr_{0.33}MnO_3$ base and and the Nb doped $SrTiO_3$. However at the start of this project, no information was available on Schottky barriers between $La_{0.67}Sr_{0.33}MnO_3$ and Nb:$SrTiO_3$. Therefore we need to determine wether or not a Schottky barrier forms and what the height of this Schottky barrier is. That is why diodes of $La_{0.67}Sr_{0.33}MnO_3$ on Nb:$SrTiO_3$ are prepared to investigate their electrical properties. These are the first diodes reported to contain a half-metallic ferromagnet. Figure 7.3 shows I-V characteristics of diodes for three different doping concentrations (0.01, 0.05 and 0.1 Wt%) of the $SrTiO_3$ substrate. The diodes show high rectification and low reverse currents. For the substrates with a doping concentration of approximately 0.01 Wt% we find a reverse current in the order of $1{\cdot}10^{-10}$A, and a rectification of more than 10^8 for a voltage of 1 V. For diodes on the 0.05 Wt% doped substrates, we observe that the reverse current at room temperature is in the order of a μA at 1 V. This reverse current at 1 V drops to a nA around 230 K. At lower temperatures we observe a strong increase of the reverse current at 1 V with decreasing temperature. We are able to reduce this reverse current by drastically increasing the time that we use to clean the sample after the ion beam etching of the diode. So we believe that this part of the reverse current is

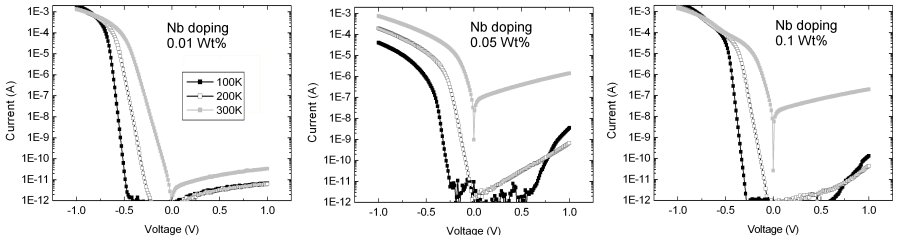

Figure 7.3: *I-V characteristics at 100, 200 and 300 K for $La_{0.67}Sr_{0.33}MnO_3$ /Nb:$SrTiO_3$ diodes on substrates with a doping concentration of 0.01, 0.05 and 0.1 Wt%.*

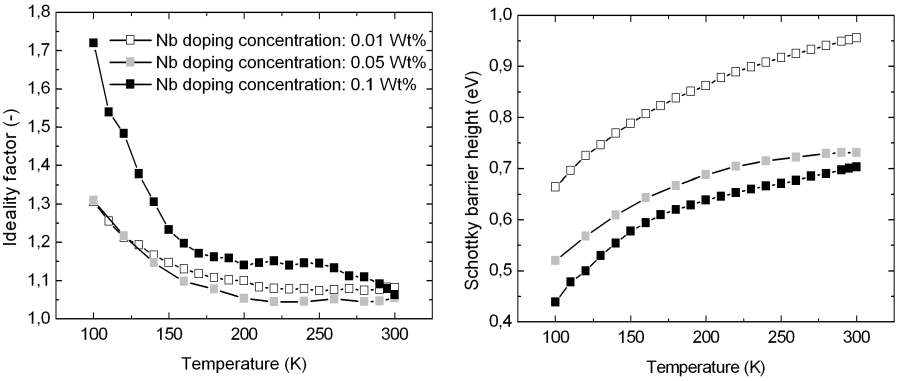

Figure 7.4: *Temperature dependence of the ideality factor and the Schottky barrier height for $La_{0.67}Sr_{0.33}MnO_3$ /Nb:$SrTiO_3$ diodes on substrates with a doping concentration of 0.01, 0.05 and 0.1 Wt%..*

caused by leakage at the edges of the diode. The forward I-V characteristics of the diodes show an exponential dependence of the current on the voltage. When we fit the exponential part of the I-V characteristic for forward bias to the expression for thermionic emission current density in a Schottky barrier, we obtain the ideality factor and a Schottky barrier height. Both are shown in figure 7.4. Both the ideality factor and the Schottky barrier height depend strongly on the temperature and on the doping concentration of the substrate. For the Schottky barrier height of the diodes on the 0.01 Wt% doped substrates we find 0.96 eV at room temperature and 0.66 eV at 100 K. For the diodes on the 0.05 Wt% doped substrates we find 0.73 eV at room temperature and 0.52 eV at 100 K. For the 0.1 Wt% doped substrates we find a height of 0.70 eV at room temperature and 0.44 eV at 100 K. So the barrier height decreases

with increasing doping concentration. The ideality factors for the diodes on the 0.05 and 0.01 Wt % doped substrates do not deviate strongly from each other and are lower than 1.1 for temperatures above about 160 K. This shows that thermionic emission is an accurate model to describe the forward current in these diodes in this temperature regime. The ideality factor of diodes on 0.1 Wt% doped substrates is significantly larger. With decrease of temperature the ideality factors show an increase and below about 160 K the ideality factor becomes significantly larger then 1 which shows that the I-V characteristics deviate from the thermionic emission model. Such dependence of the ideality factor and the Schottky barrier height on temperature and doping concentration, is reported for Au/Nb:$SrTiO_3$ diodes as well but is not observed for example for Si based diodes. Therefore it is related to the specific properties of the Nb:$SrTiO_3$ semiconductor. The dependence is caused by an intrinsic low permittivity (ILP) layer, that is formed at the surface of the $SrTiO_3$. This layer functions as a narrow insulating layer over which part of the flatband voltage drops. In forward bias, electrons tunnel through this ILP layer which lowers the effective Schottky barrier height of the diodes. The part of the flatband voltage that drops over this ILP layer depends on the carrier concentration of the substrate and on the permittivity of the ILP layer and the $SrTiO_3$. Since the permittivity of the $SrTiO_3$ depends strongly on temperature, the effective Schottky barrier height depends on temperature as well. The permittivity of $SrTiO_3$ also depends on the electric field and thus on the applied voltage. This causes the Schottky barrier height to depend on the applied voltage. A voltage dependent Schottky barrier height explains the high ideality factor that we find for temperatures below 150 K. The height of the Schottky barrier and the low reverse current make the diodes applicable as collector in a MTT.

In the MTT, we use a $SrTiO_3$ tunnel barrier and a Co emitter to facilitate the injection of spin polarized hot electrons into the $La_{0.67}Sr_{0.33}MnO_3$ base. In situ RHEED monitoring of the growth of the $SrTiO_3$ film by PLD shows that, like the $La_{0.67}Sr_{0.33}MnO_3$, the $SrTiO_3$ grows in a layer by layer growth mode. Cross-sectional TEM images of the $SrTiO_3$ film on top of the epitaxial $La_{0.67}Sr_{0.33}MnO_3$ film, (see figure 7.2) indicate that the $SrTiO_3$ film is epitaxial.

The cobalt film is magnetically characterized and we conclude that the cobalt behaves like a thin magnetic film with in plane shape anisotropy. Cross-sectional TEM images of the Nb:$SrTiO_3$ /$La_{0.67}Sr_{0.33}MnO_3$ /$SrTiO_3$ /Co/Au stack, (see figure 7.2) show that the cobalt film is poly crystalline. The cross-sectional TEM images of the $SrTiO_3$ /Co interface do not allow us to determine the precise composition or structure at the $SrTiO_3$ /Co interface, but it appears that the interface is structurally disordered.

The next step towards the development of the MTT is to electrically characterize the $La_{0.67}Sr_{0.33}MnO_3$ /$SrTiO_3$ /Co Magnetic Tunnel Junctions (MTJ). In most of the junctions, we observe a negative TMR with a maximum at a

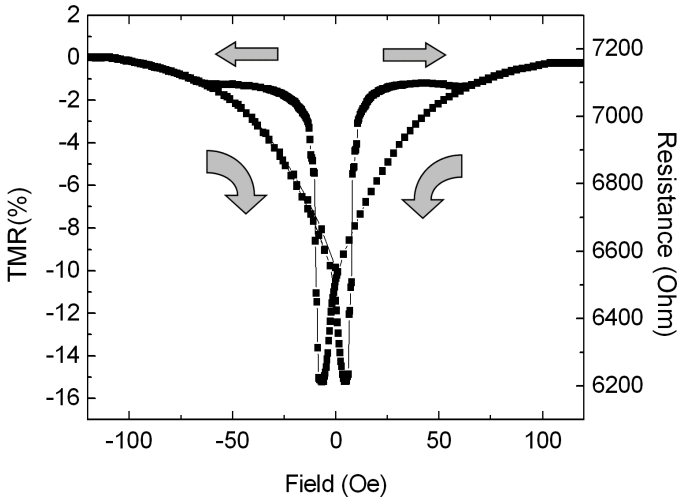

Figure 7.5: *Field dependence of the resistance of a $La_{0.67}Sr_{0.33}MnO_3$ /$SrTiO_3$ /Co magnetic tunnel junction at a bias of -100 mV and a temperature of 82 K.*

bias voltage of -100 mV. Negative voltage means that the $La_{0.67}Sr_{0.33}MnO_3$ is negatively biased and that electrons tunnel from the $La_{0.67}Sr_{0.33}MnO_3$ to the Co. The maximum TMR that we find is -15% at the lowest temperature that we measured (82 K).(see figure 7.5) The fact that the TMR is negative can be correlated to the density of states of the electrode materials (positive spin polarization for $La_{0.67}Sr_{0.33}MnO_3$ and negative spin polarization for Co). The value of the TMR is lower than the values reported by De Teresa *et al.* in literature for similar junctions(-37% at 75 K). The bias dependence of the TMR also deviates from the dependence that they report (maximum of TMR at a bias of -400 mV). Since the TMR is sensitive to the interfaces of the barrier with the electrodes and the cross-sectional TEM images did not show a well defined Co/$SrTiO_3$ interface, we believe that the interface is slightly different from theirs. The reason might be that we grow the Co by PLD instead of sputtering, which increases the reactivity of the arriving Co atoms. The TMR decreases with increase of temperature and diminishes around 280 K.

In other junctions we find a positive TMR of 8%. Positive TMR can be observed when both electrode interfaces have the same sign for the tunneling spin polarization. For $La_{0.67}Sr_{0.33}MnO_3$ we expect a positive spin polarization as all partial densities of states show positive spin polarization. For Co

however, both positive and negative tunneling spin polarization have been reported, depending on the insulator. Negative spin polarization is reported for Co in combination with epitaxial $SrTiO_3$ barriers with TiO_2 as terminating sublattice at the interface with the Co electrode. Positive tunneling spin polarization is reported for the Co/ AlO_x interface. One explanation for the fact that the tunneling spin polarization of Co is negative for TiO_2 terminated $SrTiO_3$ barriers and positive for AlO_x barriers, is that the TiO_2 terminated $SrTiO_3$ barriers select the d-electrons, while the AlO_x barriers select the s- and p-electrons for the tunneling process. Another explanation for the negative spin polarization of the Co/TiO_2 interface is that a magnetic moment is induced on the Ti atoms at the interface, which is anti-parallel to the magnetization in the Co. A positive spin polarization is reported for Co in combination with an AlO_x or an amorphous $SrTiO_3$ barrier. Since the sign of the spin polarization of the Co is sensitive to the interface conditions, we assume that it is the exact composition and structure of the interface that determines the sign of the TMR in our junctions.

We observed a maximum in the tunnel barrier resistance around 200 K for the junctions with an $La_{0.67}Sr_{0.33}MnO_3$ film that is presumably oxygen deficient. For the junctions in which the $La_{0.67}Sr_{0.33}MnO_3$ is assumed to have a higher oxygen content (because they have a higher magnetization and conductivity), we observed the resistance of the tunnel barriers to increase with increasing temperature without reaching a maximum below 300 K. The resistance of tunnel barriers in general decreases with increase of temperature. The temperature dependence of the resistance of these tunnel junctions is related to the carrier concentration in the $La_{0.67}Sr_{0.33}MnO_3$. This carrier concentration decreases as the temperature is increased from 0 K to the temperature (360 K) at which the metal-insulator transition occurs. A strong dependence of the carrier concentration on the temperature causes a decrease of the temperature at which the resistance of the tunnel barrier finds its maximum.

We investigate the Nb:$SrTiO_3$ / $La_{0.67}Sr_{0.33}MnO_3$ / $SrTiO_3$ / Co magnetic tunnel transistors to characterize their electrical behavior. In two structures, a collector current is measured that can be identified as a hot electron current. For both transistors the $La_{0.67}Sr_{0.33}MnO_3$ base has a thickness of 10 nm. The substrates are 0.05 and 0.1 Wt% Nb doped. The transistor on the 0.05 (0.1) Wt% doped substrate shows a transfer ratio (I_c/I_e) of $7{\cdot}10^{-6}(6{\cdot}10^{-6})$ around 100 K for an emitter bias of 950 mV. The transfer ratio decreases with increasing temperature (see figure 7.6). This is well known behavior for MTT's as an increase in temperature increases the scattering in the base. Another reason for the decrease of the transfer ratio with increasing temperature for this particular MTT, can be found in the temperature dependence of the effective Schottky barrier height of the diodes. In conventional MTT's the onset of the hot electron current (emitter voltage above which hot electrons are collected) correlates with the height of the Schottky barrier of the collector diode. In

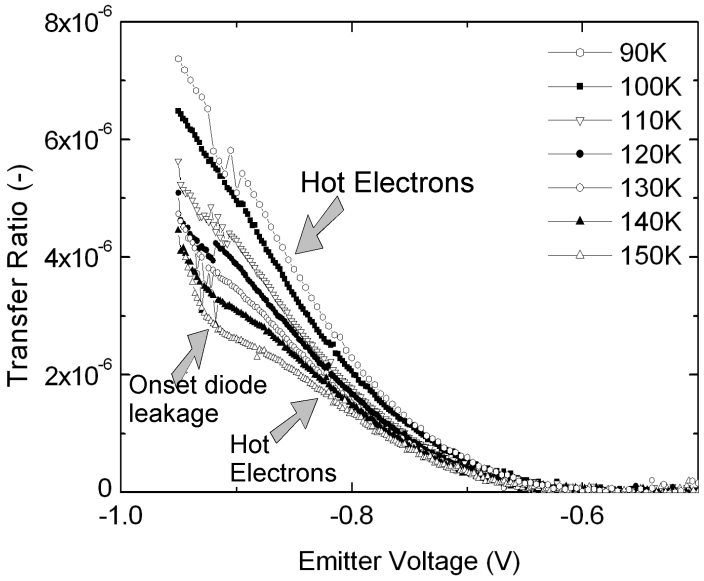

Figure 7.6: *Voltage dependence of the transfer ratio for an Nb:$SrTiO_3$ /$La_{0.67}Sr_{0.33}MnO_3$ /$SrTiO_3$ /Co magnetic tunnel junction.*

the Nb:$SrTiO_3$ /$La_{0.67}Sr_{0.33}MnO_3$ diodes however, we have seen that a layer with a low permittivity forms at the diode interface. We find that the onset for the detection of hot electrons in the MTT is higher then the effective Schottky barrier height. That means that the ILP layer partially reflects hot electrons. We observe a hot electron current in two structures that have the same base thickness. That means that we cannot determine the attenuation length for hot electrons in $La_{0.67}Sr_{0.33}MnO_3$.

The temperature and emitter voltage regime for which the collector current is dominated by collected hot electrons is limited by a leakage current through the diode. This leakage current can be decreased by improving the quality of the diode, or by reducing the voltage drop over the diode, when the emitter is biased. The latter can be realized by a reduction of the resistance of the base and the contact to the base, or by increasing the resistance of the tunnel barrier either by increasing its thickness or reducing its diameter. A drastic reduction of the diameter of the emitter is not possible with the wet etching step that we use for the emitter definition. This step would have to be replaced by for instance a dry etch step or by lift off.

For a MTT with a ferromagnetic emitter, the magnetic tunnel junction shows +2.8% TMR at an emitter voltage of -950 mV at 90 K. However we do not observe the transfer ratio of the MTT to depend on the relative orientation

of the magnetization. There are a number of possible explanations for this.
1. It is possible that the difference of the attenuation length for spin up and spin down hot electrons in $La_{0.67}Sr_{0.33}MnO_3$ is small. A high spin polarization at the Fermi-level does not guarantee that the attenuation length of hot electrons depends strongly on the spin orientation. It is also possible that the difference between the attenuation lengths of both types of electrons depends critically on the deposition conditions. If indeed the attenuation length of the hot electrons in $La_{0.67}Sr_{0.33}MnO_3$ does not depend strongly on the spin of the electrons, then there is little room for improvement.
2. Another possibility is that the transfer ratio that is found, is mostly determined by a large reflection probability at the $La_{0.67}Sr_{0.33}MnO_3$ /Nb:$SrTiO_3$ interface, while the attenuation length of the hot electrons is longer then the thickness of the base. In that case there is little scattering in the base and thus also little spin dependence of the transport through the base. This large reflection probability could be caused by the presence of the ILP layer. The energy of the hot electrons that are injected in the base is lower then the height of the ILP layer so the layer might reflect or scatter a large part of the hot electrons. It is possible that when the energy of the injected electrons is raised above the height of the ILP layer, the collector efficiency is drastically increased. Unfortunately if we apply higher emitter bias in the MTT structure that we prepared, the leakage current through the diodes obscures the hot electron current.

If the attenuation length is indeed longer then the thickness of the base and the Schottky barrier has a large reflection probability, then the base can be made significantly thicker to increase the scattering in the base. Decrease of the reflection probability can probably be realized by increasing the energy of the injected electrons. In this case the MTT with a non magnetic emitter can also be an option.
3. The TMR in the tunnel junction is only 2.8%. This could mean that both the $La_{0.67}Sr_{0.33}MnO_3$ /$SrTiO_3$ interface as well as the Co/$SrTiO_3$ interface have a low spin polarization. In that case the spin polarization of the injected hot electrons is low, which prevents a high field dependence of the collector current. When the low TMR is caused by a low spin polarization of the Co/$SrTiO_3$ interface, while the spin polarization of the $La_{0.67}Sr_{0.33}MnO_3$ /$SrTiO_3$ interface (above the Fermi-level) is reasonable, the tunnel current can still have a reasonable spin polarization. But in that case the spin polarization of the injected hot electron current is determined by the magnetization direction of the base and the dependence of the scattering in the base on the relative orientation of the magnetization of the electrodes would be small.

If the spin polarization of the injected electrons is low due to a low tunnel spin polarization of the Co/$SrTiO_3$ interface, this interface should be improved or a different material for the emitter and/or tunnel barrier should be chosen.

When this spin polarization of the injected hot electrons, is determined by the magnetization direction of the base, insertion of a non magnetic layer be-

tween the base and the tunnel barrier would solve the problem.

The results presented in this thesis show that hot electrons can be injected into an epitaxial thin $La_{0.67}Sr_{0.33}MnO_3$ film and that these hot electrons can be selectively collected after they have traversed the base by using a Nb:$SrTiO_3$ / $La_{0.67}Sr_{0.33}MnO_3$ diode as an energy and momentum filter. This creates the possibility to study the spin dependent transport of hot electrons in $La_{0.67}Sr_{0.33}MnO_3$. Further, this thesis provides a solid basis to optimize the output of the epitaxial $La_{0.67}Sr_{0.33}MnO_3$ based MTT.

Bibliography

[1] E. Grochowski. "www.hitachigst.com/hdd/technolo/overview/chart02.html". (2005).

[2] E. Y. Tsymbal, O. N. Mryasov and P. R. LeClair. "Spin dependent tunneling in magnetic tunnel junctions". *J. Phys. Cond. Matt.* **15**, R109–R142 (2003).

[3] J. G. Simmons. "Generalized formula for the electric tunnel effect between similar electrodes seperated by a thin insulating film". *J. Appl. Phys.* **34**, 1793–1803 (1963).

[4] W. F. Brinkman, R. C. Dynes and J. M. Rowell. "Tunneling conductance of asymmetrical barriers". *J. Appl. Phys.* **41**, 1915–1921 (1970).

[5] I. Giaever. "Energy gap in superconductors measured by electron tunneling". *Phys. Rev. Lett.* **5**, 147–148 (1960).

[6] P. M. Tedrow and R. Meservey. "Spin dependent tunneling into ferromagnetic nickel". *Phys. Rev. Lett.* **26**, 192–195 (1971).

[7] J. S. Moodera, J. Nowak, L. R. Kinder, P. M. Tedrow, R. J. M. van de Veerdonk, B. A. Smits, M. van Kampen, J. M. van Swagten and W. J. M. de Jonge. "Quantum well states in spin-dependent tunnel structures". *Phys. Rev. Lett.* **83**, 3029–3032 (1999).

[8] P. M. Tedrow and R. Meservey. "Critical thickness for ferromagnetism and the range of spin-polarized electrons tunneling into Co". *Solid State comm.* **16**, 71–74 (1975).

[9] E. Y. Tsymbal and D. G. Pettifor. "Modelling of spin-polarized electron tunneling from 3d ferromagnets". *J. Phys. Cond. Matt.* **9**, L411–L417 (1997).

[10] D. J. Monsma, J. C. Lodder, Th. J. A. Popma and B. Dieny. "Perpendiculal hot electron transport in a new magnetic field sensor: the spin valve transistor". *Phys. Rev. Lett.* **74**, 5260–5263 (1995).

[11] O. M. J. van't Erve, R. Vlutters, P. S. Anil Kumar, S. D. Kim, F. M. Postma and R. Jansen. "Transfer ratio of the spin-valve transistor". *Appl. Phys. Lett.* **80**, 3787–3789 (2002).

[12] R. Jansen. "The spin-valve transistor: a review and outlook". *J. Phys. D* **36**, R289–R308 (2003).

[13] T. Yamauchi and K. Mizushima. "Theoretical approach to the spin-dependent hot-electron transport in a spin valve". *Phys. Rev. B* **58**, 1934–1939 (1998).

[14] K. Mizushima, T. Kinno, T. Yamauchi and K. Tanaka. "Energy-dependent hot electron transport across a spin-valve". *IEEE Trans. on Mag.* **33**, 3500–3504 (1997).

[15] K. Mizushima, T. Kinno, K. Tanaka and T. Yamauchi. "Strong increase of the effective polarization of the tunnel current in $Fe/AlO_x/Al$ junctions with decreasing Fe layer thickness". *Phys. Rev. B* **58**, 4660–4665 (1998).

[16] R. Sato and K. Mizushima. "Spin-valve transistor with an Fe/Au/Fe(001) base". *Appl. Phys. Lett.* **79**, 1157–1159 (2001).

[17] S. van Dijken, X. Jiang and S. S. P. Parkin. "Room temperature operation of a high output current magnetic tunnel transistor". *Appl. Phys. Lett.* **80**, 3364–3366 (2002).

[18] S. van Dijken, X. Jiang and S. S. P. Parkin. "Spin-dependent hot electron transport in $Ni_{81}Fe_{19}$ and $Co_{84}Fe_{16}$ films on GaAs(001)". *Phys. Rev. B* **66**, 094417 (2002).

[19] S. van Dijken, X. Jiang and S. S. P. Parkin. "Comparison of magnetocurrent and transfer ratio in magnetic tunnel transistors with spin-valve bases containing Cu and Au spacer layers". *Appl. Phys. Lett.* **82**, 775–777 (2003).

[20] W. E. Picket and D. J. Singh. "Electronic structure and half-metallic transport in the $La_{1-x}Ca_xMnO_3$ system". *Phys. Rev. B.* **53**, 1146–1160 (1996).

[21] W. E. Picket and D. J. Singh. "Transport and femiology of the ferromagnetic phase of $La_{\frac{2}{3}}A_{\frac{1}{3}}MnO_3$(A=Ca,Sr,Ba)". *J. Mag. Mag. Mater.* **172**, 237–246 (1997).

[22] R. J. Soulen, J. M. Byers, M. S. Osofsky, B. Nadgorny, T. Ambrose, S. F. Cheng, P. R. Broussard, C. T. Tanaka, J. Nowak, J. S. Moodera, A. Barry and J. M. D. Coey. "Measuring the spin polarization of a metal with a superconducting point contact". *Science* pages 85–88 (1998).

[23] J. H. Park, E. Vescovo, H.-J. Kim, C. Kwon, R. Ramesh and T. Venkatesan. "Direct evidence for a half-metallic ferromagnet". *Lett to Nature* **392**, 794–796 (1998).

[24] J. H. Park, E. Vescovo, H.-J. Kim, C. Kwon, R. Ramesh and T. Venkatesan. "Magnetic properties at surface boundary of a half-metallic ferromagnet $La_{0.7}Sr_{0.3}MnO_3$". *Phys. Rev. Lett.* **81**, 1953–1956 (1998).

[25] Yu Lu, X. W. Li, G. Q. Gong, Gang Xiao, A. Gupta, P. Lecouer, J. Z. Sun, Y. Y. Wang and V. P. Dravid. "Large magnetotunneling effect at low magnetic fields in micrometer-scale epitaxial $La_{0.67}Sr_{0.33}MnO_3$ tunneljunctions". *Phys. Rev. B* **54**, 8357–8360 (1996).

[26] J. Z. Sun, W. J. Gallagher, P. R. ducombe, L. Krusin-elbaum, R. A. Altman, A. Gupta, Yu Lu, G. Q. Gong and Gang Xiao. "Observation of large low-field magnetoresistance in trilayer perpendicular transport devices made using doped manganate perovskites". *Appl. Phys. Lett* **69**, 3266–3268 (1996).

[27] J. Z. Sun, L. Krusin-elbaum, P. R. Ducombe, A. Gupta and R. B. Laibowitz. "Temperature dependent, non-ohmic magnetoresistance in doped perovskite manganate trilayer junctions". *Appl. Phys. Lett.* **70**, 1769–1771 (1997).

[28] M. Viret, M. Drouet, J. Nassar, J. P. Contour, C. Fermon and A. Fert. "Low field colossal magnetoresistance in manganite tunnel spin valves". *Europhys. Lett* **39**, 545–549 (1997).

[29] M. Viret, J. Nassar, M. Drouet, J. P. Contour, C. Fermon and A. Fert. "Spin polarized tunneling as a probe of half metallic ferromagnetism in mixed-valance manganites". *J of Mag. and Mag. Mater.* **198-199**, 1–5 (1999).

[30] M. Bowen, M. Bibes, A. Barthelemy, J. P. Contour, A. Anane, Y. Lemaitre and A. Fert. "Nearly total spin polarization in $La_{\frac{2}{3}}Sr_{\frac{1}{3}}MnO_3$ from tunneling experiments". *Appl. Phys. Lett.* **82**, 233–235 (2003).

[31] A. Urushibara, Y. Motitomo, T. Arima, A. Asamitsu, G. Kido and Y. Tokura. "Insulator-metal transition and giant magnetoresistance in $La_{1-x}Sr_xMnO_3$". *Phys. Rev. B* **51**, 14103–14109 (1995).

[32] M. Bibes, S. Valencia, Ll. Balcells, B. Martnez, J. Fontcuberta, M. Wojcik, S. Nadolski and E. Jedryka. "Charge trapping in optimally doped epitaxial manganite thin films". *Phys. Rev. B* **66**, 134416 (2002).

[33] D. C. Worledge and T. H. Geballe. "Spin-polarized tunneling in $La_{0.67}Sr_{0.33}MnO_3$". *Appl. Phys. Lett.* **76**, 900–902 (2000).

[34] J. Z. Sun, K. P. Roche and S. S. P. Parkin. "Interface stability in hybrid transition metal-oxide magnetic junctions". In *Proc. for MRS symposium spring* volume 1 pages 1–6 (1999).

[35] J. Z. Sun, K. P. Roche and S. S. P. Parkin. "Interface stability in hybrid transition metal-oxide magnetic trilayer junctions". *Phys. Rev. B* **61**, 11244–11247 (2000).

[36] J. S. Moodera, L. R. Kinder, J. Nowak, P. Leclair and R. Meservey. "Geometrically enhanced magnetoresistance in ferromagnet-insulator-ferromagnet tunnel junctions". *Appl. Phys. Lett.* **69**, 708–710 (1996).

[37] J. M. De Teresa, A. Barthelemy, A. Fert, J. P. Contour, R. Lyonnet, F. Montaigne, P. Seneor and A. Vaures. "Inverse tunnel magnetoresistance in $Co/SrTiO_3$ /$La_{0.67}Sr_{0.33}MnO_3$: New ideas on spin-polarized tunneling". *Phys. Rev. Lett.* **82**, 4288–4291 (1999).

[38] J. M. De Teresa, A. Barthelemy, A. Fert, J. P. Contour, F. Montaigne and P. Seneor. "Role of metal-oxide interface in determining the spin polarization of magnetic tunnel junctions". *Science* **286**, 507–509 (1999).

[39] J. M. De Teresa, A. Barthelemy, A. Fert, J. P. Contour, R. Lyonnet, F. Montaigne, P. Seneor and A. Vaures. "Manganite-based magnetic tunnel junctions: new ideas on spin-polarized tunneling". *J. of Mag. and Mag. Mater.* **211**, 160–166 (2000).

[40] A. Fert, A. Barthelemy, J. B. Youssef, J. P. Contour, V. Cros, J. M. De Teresa, A. Hamzic, J. M. George, G. Faini, J. Grollier, H. Jaffres, H. Le Gall, F. Montaigne, F. Pailloux and F. Petroff. "Review of recent results on spin polarized tunneling and magnetic switching by spin injection". *Mat. Sc and Eng.* **B84**, 1–9 (2001).

[41] F. Pailloux, D. Imhoff, T. Sikora, A. Barthelemy, J. L. Maurice, J. P. Contour, C. Colliex and A. Fert. "Nanoscale analysis of a $SrTiO_3$ / $La_{0.67}Sr_{0.33}MnO_3$ interface". *Phys. Rev. B* **66**, 014417 (2002).

[42] K. Wang. "Thesis". PhD thesis New York University (1999).

[43] J. Hayakawa, K. Ito, S. Kokado, M. Ichimura, A. Sakuma, M. Sugiyama, H. Asano and M. Matsui. "The origin of bias-voltage dependence in CoFe/ $SrTiO_3$ / $La_{0.67}Sr_{0.33}MnO_3$ magnetic tunnel junctions". *Jpn. J. of Appl. Phys.* **91**, 8792–8794 (2002).

[44] J. Hayakawa, S. Kokado, K. Ito, M. Sugiyama, H. Asano, M. Matsui, A. Sakuma and M. Ichimura. "Bias voltage dependence of tunnel magnetoresistance effect in spin-valve type MnIr/ NiFe/ $Co_{90}Fe_{10}$/ $SrTiO_3$ / $La_{0.7}Sr_{0.3}MnO_3$ tunnel junctions". *Jpn. J. of Appl. Phys.* **41**, 1340–1342 (2002).

[45] A. Thomas, J. S. Moodera and B. Satpati. "Evidence for positve spin-polarization in Co with $SrTiO_3$ barriers". *J Appl. Phys.* **97**, 10C908 1–3 (2005).

[46] I. I. Oleynik, E. Y. Tsymbal and D. G. Pettifor. "Metal-oxide interfaces in magnetic tunnel junctions". *Int. Sc.* **12**, 105–116 (2004).

[47] I. I. Oleynik, E. Y. Tsymbal and D. G. Pettifor. "Atomic and electronic structure of $Co/SrTiO_3$ /Co magnetic tunnel junctions". *Phys. Rev. B.* **65**, 020401 (2001).

[48] I. I. Oleynik and E. Y. Tsymbal. "Atomic, electronic and magnetic properties of magnetic tunnel junctions". *J. Appl. Phys* **93**, 6429–6431 (2003).

[49] R. Vlutters, O.M. J. van't Erve, S. D. Kim, R. Jansen and J. C. Lodder. "Interface, volume and thermal attenuation of hot-electron spins in $Ni_{80}F_{20}$e and Co". *Phys. Rev. Lett* **88**, 027202 (2002).

[50] S. van Dijken, X. Jiang and S. S. P. Parkin. "The influence of nonmagnetic seed layers on the magnetotransport properties of magnetic tunnel transistors with a silicon collector.". *J. Appl. Phys.* **97**, 043712 (2005).

[51] J. F. Ready. "Development of plume of material vaporized by giant-pulse laser". *Appl. Phys. Lett.* **3**, 11–12 (1963).

[52] R. M. White. "Generation of elastic waves by transient surface heating". *J. Appl. Phys.* **34**, 3559–3567 (1963).

[53] R. G. Meyerand and A. F. Haught. "Gas breakdown at optical frequencies". *Phys. Rev. Lett.* **11**, 401–403 (1963).

[54] D. Dijkkamp, T. Venkatesan, X. D. Wu, S. A. Shaheen, N. Jisrawi, Y. H. Min-Lee, W. L. McLean and M. Croft. "Preparation of Y-Ba-Cu oxide superconductor thin films using pulsed laser evaporation from high T_c bulk material". *Appl. Phys. Lett.* **51**, 619–621 (1987).

[55] H. Schwartz and H. A. Tourtelotte. "Vacuum deposition by high-energy laser with emphasis on barium titanate films". *J. Vac. Sci. Technol.* **6**, 373–378 (1969).

[56] J. S.Horwitz, K. S. Grabowski, D. B. Chrisey and R. E. Leuchtner. "In situ deposition of epitaxial $PbZr_xTi_{1-x}O_3$ thin films by pulsed laser deposition". *Appl. Phys. Lett.* **59**, 1565–1567 (1991).

[57] R. Ramesh, K. Luther, B. Wilkens, D. L. Hart and J. M. Tarascon. "Epitaxial growth of ferroelectric bismuth titanate thin films by pulsed laser deposition". *Appl. Phys. Lett.* **57**, 1505–1507 (1990).

[58] D. B. Chrisey and G. K. Hubler. "Pulsed Laser Deposition of Thin Films". John Wiley and sons Inc., New York (1994).

[59] T. Shimizu and H. Okushi. "Intrinsic electrical properties of $Au/SrTiO_3$ Schottky junctions". *J. of Appl. Phys.* **85**, 7244–7251 (1999).

[60] G. Koster, B. L. Kropman, G. J. H. M. Rijnders, D. H. A. Blank and H. Rogalla. "Quasi-ideal strontium titanate crystal surfaces through formation of strontium hydroxide". *Appl. Phys. Lett.* **73**, 2920–2922 (1998).

[61] A. Hammouche, E. Siebert and A. Hammon. "Crystallographic, thermal and electrochemical properties of the system $La_{1-x}Sr_xMnO_3$ for high temperature solid electrolyte fuel cells". *Mat. Res. Bull.* **24**, 367–380 (1989).

[62] G. Schmidt, D. Ferrand, L. W. Molenkamp, A.T. Filip and B. J. van Wees. "Fundamental obstacle for electrical spin injection from a ferromegnetic metal into a diffusive semiconductor". *Phys. Rev. B* **62**, 4790–4793 (2000).

[63] J. J. Harris, B. A. Joyce, P. J. Dobson and N. Norton. "Oscillations in the surface structure of Sn-doped GaAs during growth by MBE". *Surf. Sci.* **103**, L90–L96 (1981).

[64] J. H. Neave, B. A. Joyce, P. J. Dobson and N. Norton. "Dynamics of film growth of GaAs by MBE from RHEED observations". *Appl. Phys. A* **31**, 1–8 (1983).

[65] A. J. H. M. Rijnders. "The initial growth of complex oxides: study and manipulation". PhD thesis University of Twente (2001).

[66] A. M. Haghiri-Gosnet, J. Wolfman, B. Mercey, Ch. Simon, P. Lecouer, M. Korzenski, M. Hervieu, R. Desfeux and G. Baldinozzi. "Microstructure and magnetic properties of strained $La_{0.7}Sr_{0.3}MnO_3$ thin films". *J. of Appl. Phys.* **88**, 4257–4264 (2000).

[67] Yan Wu, Y. Suzuki, U. Ruediger, J. Yu, A. D. Kent and T. K. Nath C.B. Eom. "Magnetotransport and magnetic domain structure in compressively strained colossal magnetoresistance films". *Appl. Phys. Lett.* **75**, 2295–2297 (1999).

[68] Y. Suzuki and H. Y. Hwang. "anisotropy of magnetoresistance in (110) $La_{0.7}Sr_{0.3}MnO_3$ ". *J. Appl. Phys.* **85**, 4797–4799 (1999).

[69] F. Ott, M. Viret, R. Borges, R. Lyonnet, E. Jacquet, C. Fermon and J. P. Contour. "Interface magnetism of $La_{0.7}Sr_{0.3}MnO_3$ thin films studied by neutron reflectometry". *J. Magn. Magn. Mat.* **211**, 200–205 (2000).

[70] Y. Konishi, M. Kasai, M. Izumi, M. Kawasaki and Y. Tokura. "Epitaxial growth and strain manganite thin films". *Mat. Sc. and Eng.* **B56**, 158–163 (1998).

[71] O. J. Gonzalez, G. Bistue, E. Castano and F. J. Gracia. "Room temperature colossal magnetoresistance in nanocrystalline $La_{0.67}Sr_{0.33}MnO_3$ sputtered thin films". *J. Magn. Magn. Mat.* **222**, 199–206 (2000).

[72] C. Zener. "Interaction between the d-shells in the transition metals. II. Ferromagnetic compounds of manganese with perovskite structure". *Phys. Rev.* **82**, 403–405 (1951).

[73] S. K. Sinha. "X-ray diffuse scattering as a probe for thin film and interface structure". *J. Phys. III* **4**, 1543–1557 (1994).

[74] F. M. Postma, R. Ramaneti, T. Banerjee, H. Gokcan, E. Haq, D. H. A. Blank, R. Jansen and J. C. Lodder. "Epitaxial diodes of a half-metallic ferromagnet on an oxide semiconductor". *J. Appl. Phys.* **95**, 7324–7326 (2004).

[75] I. Zutic, J. Fabian and S. Das Sarma. "Spin injection through the depletion layer: A theory of spin-polarized p-n junctions and solar cells". *Phys. Rev. B.* **64**, 121201 (2000).

[76] M. E. Flatte and G. Vignale. "Unipolar spin diodes and transistors". *Appl. Phys. Lett.* **78**, 1273–1275 (2001).

[77] M. Oestreich. "Injecting spin into electronics". *Nature* **402**, 735–736 (1999).

[78] A. T. Hanbicki, B.T. Jonker, G. Itskos, G. Kioseoglou and A. Petrou. "Efficient electrical spin injection from a magnetic metal/tunnel barrier contact into a semiconductor". *Appl. Phys. Lett.* **80**, 1240–1242 (2002).

[79] V. F. Motsnyi, J. De Boeck, W. Van Roy, G. Borghs, E. Goovaerts and V. I. Safarov. "Electrical spin injection ina ferromagnet/ tunnelbarrier/ semiconductor heterostructure". *Appl. Phys. Lett.* **81**, 265–267 (2002).

[80] D. Goldschmidt and H. L. Tuller. "Fundamental absorption edge of $SrTiO_3$ at high temperatures". *Phys. Rev. B* **35**, 4360–4364 (1987).

[81] H. Hasegawa, T. Fukazawa and T. Aida. "Contact between high-T_c superconductor and semiconducting niobium-doped $SrTiO_3$ ". *Jap. J. Appl. Phys.* **28**, L2210–L2212 (1989).

[82] O. N. Tufte and P. W. Chapman. "Electron mobility in semiconducting strontium titanate". *Phys. Rev. B* **155**, 796–802 (1967).

[83] A. Yoshida, H. Tamura, K. Gotoh, H. Takauchi and S. Hasuo. "Electrical properties of Au/ and $YBa_2Cu_3O_{7-x}/SrTi_{1-y}Nb_yO_3$ diodes". *J. Appl. Phys.* **60**, 4976–4981 (1991).

[84] T. Yamamoto, S. Suzuki, H. Suzuki, K. Kawakuchi, K. Takahashi and Y. Yoshisato. "Effect of the field dependent permittivity and interfacial layer on $Ba_{1-x}K_xBiO_3$/Nb-doped $SrTiO_3$ Schottky junctions". *Jap. J. Appl. Phys.* **36**, L390–L393 (1997).

[85] T. Zhao, H. Lu, F. Chen, S. Dai, G. Yang and Z. Chen. "Highly conductive Nb doped $SrTiO_3$ epitaxial thin films grown by laser molecular beam epitaxy". *J. of Cr. Growth* **212**, 451–455 (2000).

[86] H. Hasegawa and T. Nishino. "Electrical properties of Au/Nb-doped-$SrTiO_3$ contact". *J. Appl. Phys.* **69**, 1501–1505 (1990).

[87] T. Shimizu and H. Okushi. "The properties of a metal/oxide semiconductor prepared using a high-purity ozone surface treatment". *Appl. Phys. Lett.* **67**, 1411–1413 (1995).

[88] S. M. Sze. "Physics of semiconductor devices". John Wiley and sons Inc., New York (1981).

[89] B. L. Sharma. "Metal semiconductor Schottky barrier junctions and their applications". Plenum press (1984).

[90] D. Kahng. "Properties of the Au-n-type-Si Schottky barrier". *Solid-st electron.* **6**, 281–295 (1963).

[91] J. L. Saltich. "Ohmic contacts to semiconductors". Electrochemical society, New York (1969).

[92] C. R. Crowell, S. M. Sze and W. G. Spitzer. "Equality of the temperature dependence of the gold-silicon surface barrier and the silicon energy gap in Au n-type Si diodes". *Appl. Phys. Lett.* **4**, 91–92 (1964).

[93] S. M. Sze, C. R. Crowell and D. Kahng. "Photoelectric determination of the image force dielectric constant for hot electrons in Schottky barriers". *J. Appl.Phys.* **35**, 2534–2536 (1964).

[94] T. Arizumi and M. Hirose. "Transport properties of metal-silicon Schottky barriers". *Jap. J. Appl. Phys.* **8**, 749–754 (1969).

[95] R. C. Neville and C. A. Mead. "Surface barrier energies on strontium titanate". *J. Appl. Phys.* **43**, 4657–4663 (1972).

[96] R. A. van der Berg, P. W. M. Blom, J. F. M. Cillessen and R. M. Wolf. "Field dependent permittivity in metal-semiconducting $SrTiO_3$ Schottky diodes". *Appl. Phys. Lett.* **66**, 697–699 (1995).

[97] E. H. Rhoderick and R. H. Williams. "Metal-semiconductor contacts 2nd ed.". Clarendon press Oxford (1988).

[98] J. S. Moodera, L. R. Kinder, T. M. Wong and R. Meservey. "Large magnetoresistance at room temperature in ferromagnetic thin film tunnel junctions". *Phys. Rev. Lett.* **74**, 3273–3276 (1995).

[99] R. M. Bozorth. "Ferromagnetism". D. van Nostrand Company (1963).

[100] D. Jiles. "Introduction to magnetism and magnetic materials. second ed.". Chapman & Hall (1998).

[101] "Electronic structure calculations for Co performed by M. Talanana, M. Zwierzycki and P. Kelly, using an ab initio method similar to that used in: K. Xia *et al.*, Phys Rev B., vol. 63, pp. 064407, 2001".

[102] G. Banach, R. Tyler and W. M. Temmerman. "Study of half-metallicity in LSMO". *J. of Mag. and Mag. Mater.* **272-276**, 1963–1964 (2004).

[103] J. S. Noh, T. K. Nath, C. B. Eom, J. Z. Sun, W. Tian and X. Q. Pan. "Magnetotransport in manganite trilayer junctions grown by 90°off-axis sputtering". *Appl. Phys. Lett.* **79**, 233–235 (2001).

[104] H. Smilde, H. Hilgenkamp, G. Rijnders, H. Rogalla and D. H. A. Blank. "Enhanced transparacy ramp-type Josephson contacts through interlayer deposition". *Appl. Phys. Lett.* **80**, 4579–4581 (2002).

Appendix A: Processing of the magnetic tunnel transistor.

In this appendix the individual process steps for the preparation of the magnetic tunnel transistor (chapter6) are discussed in more detail.

A.1 Structuring of the emitter

The first processing step in the fabrication of the MTT is the definition of the emitter. To define the emitters initially standard photolithography is used followed by ion beam etching. Ion beam etching is performed with a beam of Argon ions. A voltage of 350 V is used to accelerate the ions in the direction of the sample. A neutralizer grid discharges the ions in order to avoid charging up of the sample. The beam has an incident angle of 20 degrees with the surface normal of the sample. During the etching the sample is rotated. With these settings the etch rate is between 2 and 2.5 nm/minute both for the Au and the Co films. We find that when emitters are defined by ion beam etching the tunnel junctions are shorted. A well known effect in ion beam etching is sidewall re-deposition. Material that is etched from the sample will redeposit on the side of the photo-resist pattern and on the side of the etched structures. That means that we can also expect re-deposition on the side of the tunnel barrier and this redeposited material will create a conduction path between the two electrodes thereby shorting the tunnel junction. Therefore, the use of ion beam etching for definition of the emitters is abandoned.

Instead, the use of wet etching instead of ion beam etching is investigated. Etching of the Au and the Co top layers is done using a KI solution prepared by mixing 34 gr of KI, 4.5 gr of I_2, 150 ml of glycerol and 300 ml of water. We find that this etchant etches the 7 nm Au films in a couple of seconds. This gives

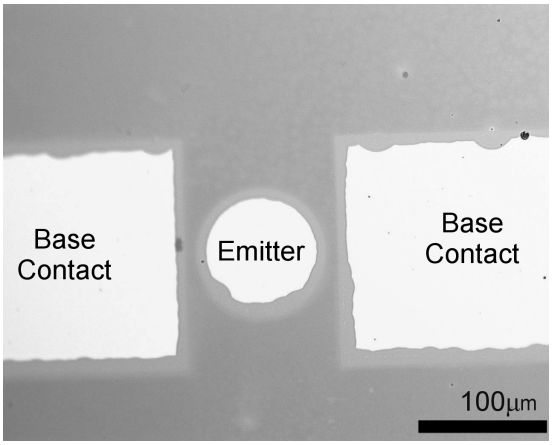

Figure A.1: *Photograph of the surface of the sample after 2 minutes of wet etching. The photo-resist pattern used here, is a circle with a diameter of 100 μm.*

a large and uncontrollable under-etching of the Au film. To decrease the etch rate we further dilute this etchant by taking 3 parts of this etchant and adding 5 parts of glycerol and 10 parts of water. Tests are performed to investigate the effect of the etchant on the $SrTiO_3$. A photo-resist pattern is applied on an $SrTiO_3$ substrate before subjecting to the etchant for 2 hours. After removal of the photo-resist, the substrate surface is investigated by AFM. The AFM images show that the photo-resist pattern has not transferred to the surface and that the etchant does not change the $SrTiO_3$ surface. This provides a convenient etch-stop. Due to the fact that the $SrTiO_3$ tunnel barrier is not etched, problems with re-deposition on the side of the tunnel barrier, that can in principle occur with wet etching as well, are overcome. A disadvantage of defining the emitter by wet etching is the under-etching that occurs. This becomes especially cumbersome because the gold etches much faster then the cobalt. The Co film is etched in 10 to 15 minutes. At the time that the cobalt layer has completely etched, the under-etching of the gold is about 40 micron, which means that on the large emitters (100 and 150 micron) there is only a small area of gold left whereas on the smaller emitters all the gold has etched. This problem is solved by wet etching in two steps. First the photo-resist is applied followed by wet etching until the Au is completely removed at the parts where there is no photo-resist. This takes about 2 minutes. Then the photo-resist is removed. The gold film shows under-etching of 10 to 20 micron as shown in figure A.1. The picture shows the circular emitter in the middle and the base contacts on both sides. The cobalt film has started to etch, but

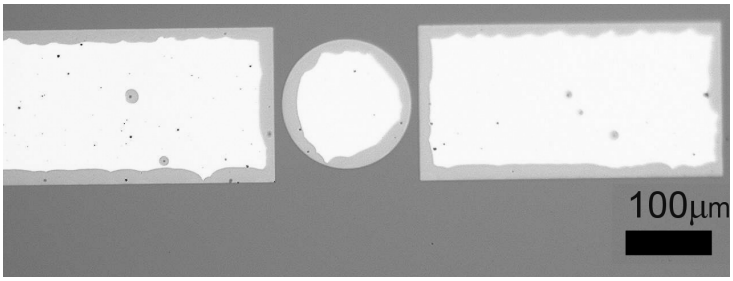

Figure A.2: *Photograph of a structure with a 150 µm emitter after re-applying the photo-resist and performing the second wet-etch step.*

is still present, so the same photo-resist pattern is applied again and the wet etching is continued. The gold film is no longer in contact with the etchant and doesn't etch. The cobalt film is etched in 10 to 15 minutes. Figure A.2 shows a structure with a 150 micron emitter after the second wet etch step. The picture shows that the under-etching of the gold film has not increased and that the cobalt film is etched without significant under-etching.

A.2 Structuring of the bottom electrode

After the emitter definition is completed, the next step is to define the base. For defining the base, standard photo-lithography and ion beam etching is used. The ion beam etching is almost the same as described in the previous section, but we now use an accelerator voltage of 100 V as we find that at this voltage there is less re-deposition. With these settings the etch-rate for $La_{0.67}Sr_{0.33}MnO_3$ base is 1.1 ± 0.1 nm/min and 1.4 ± 0.1 nm/min for $SrTiO_3$ tunnel barrier. To assure that all $La_{0.67}Sr_{0.33}MnO_3$ is removed, we time the etching to etch 2 or 3 nm into the Nb:$SrTiO_3$ substrate. After the ion beam etching, the photo-resist is removed in ultrasone acetone. For most structures we have used a cleaning time of 15 minutes. In section 4.4 of chapter 4 it is shown that a drastic increase of this cleaning time, strongly decreases the reverse current of the diodes. Figure A.3 shows a structure with a 150 micron emitter after definition of the base by ion beam etching.

A.3 Deposition and structuring of the silicon-oxide insulation layer

After the base definition, the next step is to deposit and structure a SiO_x insulator layer to electrically insulate the base from the emitter contact lead.

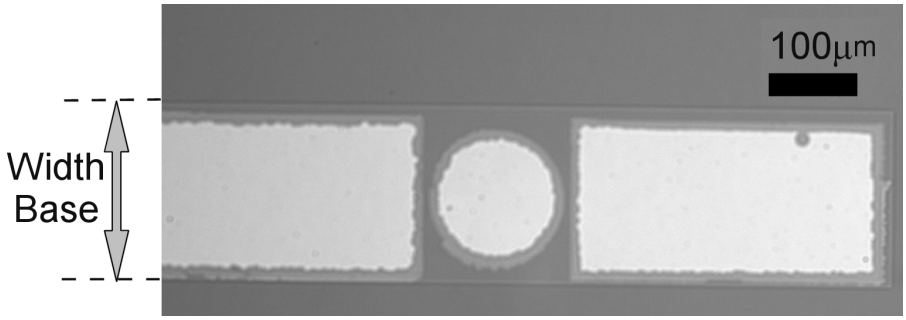

Figure A.3: *Structure with 150 micron emitter after Ion beam etching of the base.*

Different routes are taken to fabricate and structure the SiO_x film. The two deposition techniques that are available to us are RF diode sputtering and evaporation. For the RF diode sputtering a SiO_x target is used. The chamber is pumped down to $1 \cdot 10^{-7}$ mbar before the sputtering gases (argon and oxygen with a ratio of 4:1) are introduced to create a pressure of $2.5 \cdot 10^{-2}$ mbar. The RF sputtering in the system that is used, has the disadvantage of heating up the sample to at least 100°C. For evaporation of SiO_2, the vacuum chamber is pumped down to $1{\cdot}10^{-7}$mbar and an electron-gun serves to evaporate the SiO_2 in the crucible. During evaporation, the pressures increases to $1{\cdot}10^{-6}$mbar and the deposition rate is 6 nm/minute. Evaporation of SiO_2 doesn't heat the sample up significantly. We find that evaporated SiO_2 films, ranging in thickness from 100 to 400 nm, suffer from poor adhesion on $SrTiO_3$. Parts of the SiO_2 film are removed from the sample by the ultrasone cleaning in acetone in the subsequent processing step. Evaporation was abandoned to investigate the applicability of a 400 nm SiO_x film deposited by RF diode sputtering. The adhesion of a sputtered SiO_x film on $SrTiO_3$ however is good. For structuring of the contact holes in the SiO_x we have used both wet etching in BHF (buffered HF) and lift-off. Wet etching in BHF proved to be difficult. The etch rate is not homogeneous over the sample, so that for one contact hole the under-etching becomes too large while other contact holes are not opened up at all. When a positive photo-resist is used, the lift off of SiO_x is found to be incomplete. The larger contact holes (150 μm) open up partly but the silicon-oxide film on the smaller holes (< 25 μm) does not lift off. This is because the photo-resist becomes to hot during the silicon-oxide sputtering. The solution to this problem is to use an image reversal photo-resist. When such a negative tapered photo-resist is used, the silicon oxide is lifted off in ultrasone acetone in 5 minutes. Figure A.4 shows a structure after lift off of the SiO_x. At the emitter (base), a circular (rectangular) hole is created in the SiO_x. The Co

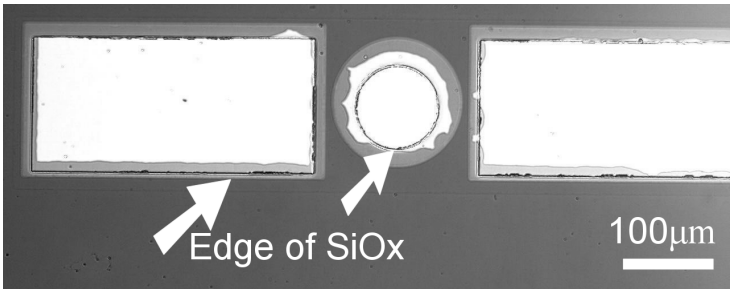

Figure A.4: *Structure with 150 micron emitter after lift off of silicon-oxide. The arrows indicate the edges of the SiO_x film*

and Au films are visible through the SiO_x film. The arrows indicate the edges of the SiO_x film.

A.4 Deposition and structuring of the contact leads and bond pads

The next step is to create emitter and base contact leads and bond pads for wirebonding. Because the Nb:$SrTiO_3$ substrate is not insulating, a conduction-path between the emitter strip and the substrate should be avoided. In order for the structures to function as a magnetic tunnel transistor, we also need to avoid forming ohmic conduction paths between the base contact and the substrate. In principle the SiO_x film serves as insulation. However when we deposit a thin (40 nm) Au film on the SiO_x and wire bond on it, the bond pierces through the SiO_2 film and create undesirable paths of conduction. That's why a Au film with a thickness of 500 nm is used for the bond pads. Lifting off such thick films requires a strong adhesion of the gold film with the SiO_2, to prevent the removal of the complete Au film during the lift off. That is why a 15 nm chromium adhesion film is used between the gold film and the SiO_2 film to promote the adhesion. The Cr(15 nm)/Au(500 nm) bilayer is deposited by sputtering and the bond-pads are defined by lift-off. Figure A.5 shows a structure after the lift-off of the Cr/Au. The two squares in the middle of the picture are the contact pads for the emitter, the squares on both sides are the bond pads for the base contacts.

We find that when chromium is deposited on top of the $La_{0.67}Sr_{0.33}MnO_3$ film to make base contacts, the $La_{0.67}Sr_{0.33}MnO_3$ / Nb:$SrTiO_3$ interface looses its diode characteristic. This is most likely due to the oxygen that is removed from the $La_{0.67}Sr_{0.33}MnO_3$ film by the chromium. The problem is solved by the use of Au contact leads with a thickness of 40 nm to connect the electrodes to

the bond-pads, so that contact of $La_{0.67}Sr_{0.33}MnO_3$ with the Cr adhesion-layer is avoided.

The 40 nm Au film that forms the contact leads is deposited by sputtering as well. Again lift-off defines the contact leads. Figure A.6 shows a structure after the contact leads have been deposited and defined. The picture shows the Al wires that lead to the printed circuit board as well. At this stage the sample is ready to be connected to the electronic measurement setup.

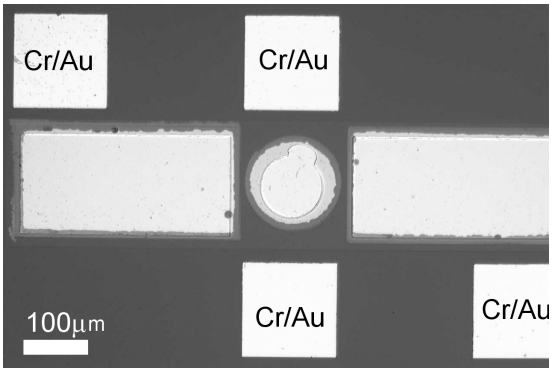

Figure A.5: *Structure with 150 micron emitter after lift off of the Cr/Au bond-pads.*

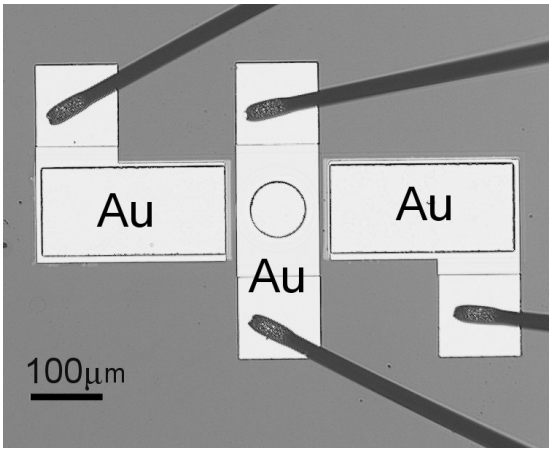

Figure A.6: *Structure with 150 micron emitter after lift off of the Au contact-leads. It also shows the wires that lead to a printed circuit board.*

Summary

The aim of the work presented in this thesis is to fabricate an epitaxial magnetic tunnel transistor (MTT) consisting of a Niobium doped $SrTiO_3$ collector, a $La_{0.67}Sr_{0.33}MnO_3$ base, a $SrTiO_3$ tunnel barrier and a Co emitter. The motivation is that this device is sensitive to the spin dependent scattering of hot electrons in a half-metallic ferromagnet. Further we anticipate that the high crystalline quality of the base will result in a large hot electron transmission.

First we studied the growth of $La_{0.67}Sr_{0.33}MnO_3$ onto single crystalline $SrTiO_3$ substrates by Pulsed Laser Deposition (PLD). For most deposition parameters that we used, the films grow in a layer by layer mode. Accordingly the films are epitaxial and the surface of the films is atomically smooth. The magnetization and conductivity of the films however does depend strongly on the deposition parameters, probably due to variations of the stoichiometry

To realize the MTT, a Schottky barrier between the $La_{0.67}Sr_{0.33}MnO_3$ and a semiconductor is necessary. To facilitate the epitaxial growth of the $La_{0.67}Sr_{0.33}MnO_3$, we choose to use lattice matching Niobium doped $SrTiO_3$ (Nb:$SrTiO_3$) single crystal substrates. We used $SrTiO_3$ substrates with different doping concentrations, and found that the $La_{0.67}Sr_{0.33}MnO_3$ / Nb:$SrTiO_3$ combination results in diodes, that show a low reverse current and a high rectification. The Schottky barrier height is determined by analysis of the diode current in the forward direction. The height of the barrier shows a strong dependence on the doping concentration of the semiconductor and on temperature. The dependence is related to an intrinsic low permittivity (ILP) layer that forms at the interface in combination with a $SrTiO_3$ permittivity that depends on the temperature and the electric field. The ILP layer absorbs part of the flatband voltage and when the diode is biased in the forward direction, electrons tunnel through this layer which effectively lowers the barrier height.

To inject spin polarized hot electrons into the $La_{0.67}Sr_{0.33}MnO_3$ we use a $SrTiO_3$ tunnel barrier and a cobalt emitter grown by PLD. The $SrTiO_3$ films

grow in a layer by layer mode as well. The $SrTiO_3$ is epitaxial, the Co is polycrystalline and the Co / $SrTiO_3$ interface is structurally disordered. The top layers of the MTT form a $La_{0.67}Sr_{0.33}MnO_3$ / $SrTiO_3$ / Co magnetic tunnel junction (MTJ). These MTJ's are electrically characterized. In most of the junctions a TMR of -15% is obtained at -100 mV bias at a temperature of 82 K. In some junctions positive TMR (+8%) is observed. Since it is well known that the sign of the tunnel spin polarization of Co depends strongly on the interface with the tunnel barrier and on the tunnel barrier material and the TEM images of the Co / $SrTiO_3$ interface show a disordered structure, we assume that it is the exact composition and structure of the Co / $SrTiO_3$ interface that determines the magnitude and sign of the TMR in our junctions.

The Nb:$SrTiO_3$ / $La_{0.67}Sr_{0.33}MnO_3$ / $SrTiO_3$ / Co MTT's with a 10 nm thick base show a collector current that can be identified as hot electrons that have traversed the base. For these structures the transfer ratio is about $7{\cdot}10^{-6}$at an emitter bias of 950 mV at 90 K. This transfer ratio decreases with increase of temperature. We observe that the onset for the collection of hot electrons is higher than the height of the Schottky barrier that we determine from the forward I-V characteristics of the diodes. This due to the ILP layer at the diode interface that partially reflects hot electrons.

We did not observe the transfer ratio of the MTT's to depend on the relative orientation of the magnetization of both ferromagnets. Their are a number of possible explanations for this. It is possible that the attenuation length of hot electrons in $La_{0.67}Sr_{0.33}MnO_3$ is not strongly spin dependent. If this is the correct explanation, there is little room for improvement of the performance of the MTT. Another possibility is that the attenuation length of hot electrons in $La_{0.67}Sr_{0.33}MnO_3$ is large compared to the thickness of the base. In that case an increase of the base thickness should improve the device performance. A third explanation can be found in the spin polarization of the injected hot electrons. If this is low due to a low spin polarization of the Co / $SrTiO_3$ interface, it can be increased by selecting different emitter and/or tunnel barrier materials. It is also possible that the spin polarization of the injected electrons is determined by the magnetization direction of the $La_{0.67}Sr_{0.33}MnO_3$ base. In that case insertion of a thin layer between the $La_{0.67}Sr_{0.33}MnO_3$ base and the $SrTiO_3$ tunnel barrier is a solution.

The results presented in this thesis show that hot electrons can be injected into an epitaxial thin $La_{0.67}Sr_{0.33}MnO_3$ film and that these hot electrons can be selectively collected after they have traversed the base by using a Nb:$SrTiO_3$ / $La_{0.67}Sr_{0.33}MnO_3$ diode as an energy and momentum filter. This creates the possibility to study the spin dependent transport of hot electrons in $La_{0.67}Sr_{0.33}MnO_3$. Further, the results presented in this thesis provide a solid basis to optimize the output of the epitaxial $La_{0.67}Sr_{0.33}MnO_3$ based MTT.

Samenvatting

Het doel van het werk dat in dit proefschrift wordt gepresenteerd is het fabriceren van een epitaxiale magnetische tunnel transistor (MTT) bestaand uit een niobium gedoopte $SrTiO_3$ collector, een $La_{0.67}Sr_{0.33}MnO_3$ basis, een $SrTiO_3$ tunnel barrière en een Co emitter. De motivatie is dat dit een device is dat gevoelig is voor de spin afhankelijke verstrooiïng van hete elektronen in een half-metallische ferromagneet. Verder anticiperen we dat de hoge kristallijne kwaliteit van de basis resulteert in een hoge hete elektronen transmissie.

We hebben eerst de groei van $La_{0.67}Sr_{0.33}MnO_3$ op èèn-kristallijne $SrTiO_3$ substraten d.m.v gepulste laser depositie (PLD) onderzocht. Voor de meeste depositie parameters groeit de film laag voor laag. De films zijn dan ook epitaxiaal en het oppervlak van de films is atomair glad. De magnetisatie en geleidbaarheid van de film hangen echter wel sterk af van de depositie parameters, waarschijnlijk door variaties in de stoichiometrie.

Om de MTT te realiseren is een Schottky barrière nodig tussen een halfgeleider en het $La_{0.67}Sr_{0.33}MnO_3$. Om epitaxiale groei van het $La_{0.67}Sr_{0.33}MnO_3$ mogelijk te maken, gebruiken we èèn-kristallijne Nb gedoopte $SrTiO_3$ substraten waarvan het kristal rooster sterk overeenkomt met het kristal rooster van $La_{0.67}Sr_{0.33}MnO_3$. We gebruiken substraten met verschillende doping concentraties en vinden dat de $La_{0.67}Sr_{0.33}MnO_3$ / Nb:$SrTiO_3$ combinatie resulteert in diodes met een lage sper stroom en een hoge rectificatie. De hoogte van de Schottky barrière wordt bepaald uit de diode stroom in de doorlaat richting. Deze hoogte hangt sterk af van de doping concentratie van de halfgeleider en de temperatuur. Die afhankelijkheid wordt verklaard door een intrinsieke laag met een lage permittiviteit (ILP laag), die vormt bij het interface in combinatie met een $SrTiO_3$ permittiviteit die van de temperatuur en het elektrische veld afhangt. Deze ILP laag absorbeert een deel van de flatband spanning en als er een spanning over de diode wordt gezet in de doorlaat richting dan tunnelen elektronen door die laag, hetgeen de effectieve hoogte van de barrière vermin-

dert.

Om spin gepolariseerde hete elektronen in de $La_{0.67}Sr_{0.33}MnO_3$ basis te injecteren gebruiken we een $SrTiO_3$ tunnel barrière en een cobalt emitter gegroeid d.m.v. PLD. De $SrTiO_3$ films groeien ook laag voor laag. Het $SrTiO_3$ is epitaxiaal, het Co is poly-kristallijn en het Co / $SrTiO_3$ interface is structureel ongeordend.

De bovenste films van de MTT vormen een $La_{0.67}Sr_{0.33}MnO_3$ / $SrTiO_3$ / Co magnetische tunnel junctie (MTJ). Deze MTJ's zijn elektrisch gekarakteriseerd. In de meeste juncties vinden we -15% TMR bij een spanning van -100 mV en een temperatuur van 82 K. In sommige juncties vinden we positief TMR (+8%). Aangezien het bekend is dat de tunnel spin polarisatie van Co sterk afhangt van het interface met de tunnel barrière en het materiaal, van de tunnel barrière en aangezien de TEM afbeeldingen van het Co / $SrTiO_3$ interface een ongeordende structuur tonen, gaan we ervan uit dat het de exacte samenstelling en kristal structuur van het Co / $SrTiO_3$ interface is dat de hoogte en het teken van de TMR in onze MTJ's bepaalt.

De Nb:$SrTiO_3$ / $La_{0.67}Sr_{0.33}MnO_3$ / $SrTiO_3$ / Co MTT's met een 10 nm dikke basis vertonen een collector stroom die we kunnen identificeren als hete elektronen die de basis zijn overgestoken. Voor deze structuren hebben we een transfer ratio bepaald van ongeveer $7{\cdot}10^{-6}$bij een emitter spanning 950 mV bij 90 K. De tranfer ratio vermindert bij hogere temperatuur. Voor deze MTT's zien we dat de onset voor detectie van hete elektronen hoger is dan de hoogte van de Schottky barrière die we bepalen uit de I-V karakteristiek van de diode in de doorlaat richting. Dat komt doordat de ILP laag gedeeltelijk elektronen reflecteert.

We hebben geen transfer ratio waargenomen die afhangt van de relatieve oriëntatie van de magnetisatie van beide ferromagneten. Er zijn een aantal mogelijke verklaringen hiervoor. Het is mogelijk dat de afval lengte van hete elektronen in $La_{0.67}Sr_{0.33}MnO_3$ niet sterk spin-afhankelijk is. Als dit de juiste verklaring is, dan is er weinig ruimte voor het verbeteren van de prestaties van het device. Een andere mogelijkheid is dat de afval lengte voor hete elektronen in $La_{0.67}Sr_{0.33}MnO_3$ lang is in vergelijking met de dikte van de basis. In dat geval zou het dikker maken van de basis, de prestaties van de MTT kunnen verbeteren. Een derde verklaring kan worden gevonden in de spin polarisatie van de geïnjecteerde elektronen. Als die laag is door een lage spin polarisatie van het Co / $SrTiO_3$ interface, dan kan het worden verhoogd door een ander materiaal voor emitter en/of tunnel barrière te kiezen. Verder is het mogelijk dat de spin polarisatie van de geïnjecteerde elektronen wordt bepaald door de magnetisatie richting van de $La_{0.67}Sr_{0.33}MnO_3$ basis. In dat geval zou het toevoegen van een dunne film tussen de $La_{0.67}Sr_{0.33}MnO_3$ basis en de $SrTiO_3$ tunnel barrière een oplossing zijn.

De resultaten die in dit proefschrift zijn gepresenteerd, tonen aan dat hete elektronen geïnjecteerd kunnen worden in een dunne $La_{0.67}Sr_{0.33}MnO_3$ film

en dat die hete elektronen selectief kunnen worden gecollecteerd door een Nb:$SrTiO_3$ / $La_{0.67}Sr_{0.33}MnO_3$ diode te gebruiken als energie en moment filter. Dit creëert de mogelijkheid om spin afhankelijk transport van hete elektronen in $La_{0.67}Sr_{0.33}MnO_3$ te bestuderen. Verder verstrekken de resultaten die in dit proefschrift zijn gepresenteerd een solide basis om de output van de epitaxiale $La_{0.67}Sr_{0.33}MnO_3$ gebaseerde MTT te optimaliseren.

Dankwoord

Graag zou ik nog de mensen bedanken, die hebben bijgedragen aan de totstandkoming van dit proefschrift. Veel van hen zijn werkzaam bij de leerstoel SMI, maar er is ook veel samenwerking geweest met collegae van de lage temperaturen groep en de anorganische materiaalkunde groep.

Allereerst wil ik Cock Lodder bedanken voor de ondersteuning en voor de promotieplaats bij de vakgroep SMI, maar ook voor sfeer in de groep. Dan natuurlijk Ronnie Jansen, die koste noch moeite gespaard heeft bij het begeleiden van het onderzoek. Ik heb veel respect voor zijn immense werklust en voor de manier waarop hij leiding geeft aan de spin valve groep. Onze tochten door de moerassen van Florida en de woestijn van Californië zal ik nooit vergeten.

Verder sta ik in het krijt bij Mercy Shaji, voor haar aandeel in de magnetische karakterisatie van de $La_{0.67}Sr_{0.33}MnO_3$ films. Frank Roesthuis wil ik bedanken voor zijn technische ondersteuning rond de PLD apparatuur. Het is altijd goed werken met tukkers. Verder is Martin Siekman's kennis van de AFM techniek onmisbaar gebleken bij de oppervlakte karakterisatie. Martin bedankt. Rico Keim, bedankt voor de TEM-analyses en Johnny Sanderink voor de bijdrage aan de karakterisatie van de SiO_2 films. Weer zo'n tukker waarmee het goed werken is. Ondanks zijn drukke agenda kon ik altijd bij Dave Blank terecht voor advies. Hartelijk bedankt Dave.

De spin valve groep is een sub-groep van de SMI leerstoel. De mensen in deze groep hebben altijd veel interesse getoond in mijn werk, en hebben altijd klaar gestaan met adviezen. Daarvoor ben ik ze allen zeer dankbaar. Ruud Vlutters en Olaf van't Erve, bedankt. Rajesh Ramaneti, Tamalika Banerjee, Byoung-Chul Min, Byong Guk Park, Ehtsham Ul Haq, Huseyin Gokcan, Sung Dong Kim and Kazunari Motohashi, thank you.

Mijn kamergenoten Mathieu Bolks, Arnout van den Bos en Ngocnga Dao, hebben gezorgd voor een plezierige werkomgeving. Met cichliden als gezamenlijke hobby, hadden Mathieu en ik gesprekstof in overvloed, zowel op de

werkplek als de rookplek als bij de drinkplaatsen. De drinkplaats werd consequent vrijdag 's middags door een groot deel van de leerstoel bezocht. Tot deze fanatieke tombraiders behoren Alexander, Arnout, Byoung Chul, Henry, Ite-jan, Jos, Martin, Mathieu, Mink, Olaf, Rogelio, Ronnie en Thijs. Ik kom nog wel een keer langs op vrijdag middag.

Het thuis front wil ik ook bedanken voor hun steun. Ramona en Nick, ik hou van jullie. Nu mijn proefschrift afgerond is zal ik niet meer 's avonds en in het weekend werken, zodat we weer leuke dingen kunnen gaan doen met z'n drieën. Mijn vader, mijn moeder en mijn broer en hebben ook altijd voor mij klaargestaan. Daarvoor wil ik jullie ontzettend bedanken, zonder jullie was dit nooit gelukt.

List of publications

Published articles:

- F. M. Postma, R. Ramaneti, T. Banerjee, H.Gokcan, E. Haq, D. H. A. Blank, R. Jansen and J. C. Lodder, "Epitaxial diodes of a half-metallic ferromagnet on an oxide semiconductor", *J. Appl. Phys.* **95**, 7324 (2004)

- E. Haq, H. Gokcan, T. Banerjee, F. M. Postma, M. H. Siekman, R. Jansen and J. C. Lodder, "Nanoscale magnetic hysteresis of $Ni_{80}Fe_{20}$/Au/Co trilayers using ballistic electron magnetic microscopy", *J. Appl. Phys.* **95**, 6930 (2004)

- R. Jansen, H. Gokcan, O. M. J. van't Erve, F. M. Postma and J. C. Lodder, "Spin-valve transistors with high magnetocurrent and 40 mA output current", *J. Appl. Phys.* **95**, 6927 (2004)

- R. Jansen, O. M. J. van't Erve, F. M. Postma and J. C. Lodder, "Comment on "Giant magnetocurrent exceeding 3400% in magnetic tunnel transistor with spin-valve base layers", [*Appl. Phys. Lett.* 83, 951 (2003)]", *Appl. Phys. Lett.* **84**, 4337 (2004)

- O. M. J. van't Erve, R. Vlutters, P. S. Anil Kumar, S. D. Kim, F. M. Postma, R. Jansen and J. C. Lodder, "Tranfer ratio of the spin-valve transistor", *Appl. Phys. Lett.* **80**, 3787 (2002)